

**Porous Catalyst Characterization Using
X-ray Nano Tomography and Pore Network Modeling**

**Karakterisering van poreuze katalysatoren met behulp van
Röntgen nanotomografie en porienetwerkmodellering**

(met een samenvatting in het Nederlands)

Proefschrift

ter verkrijging van de graad van doctor aan de
Universiteit Utrecht
op gezag van de
rector magnificus, prof.dr. H.R.B.M. Kummeling,
ingevolge het besluit van het college voor promoties
in het openbaar te verdedigen op

woensdag 6 juli 2022 des middags te 4.15 uur

door

Roozbeh Valadian

geboren op 22 mei 1989
te Teheran, Iran

Promotor:

Prof. dr. ir. B.M. Weckhuysen

Copromotor:

Dr. F. Meirer

This Ph.D. Thesis was accomplished with financial support from The Netherlands Organization for Scientific Research (NWO VIDI Grant, No. 723.015.007).

To my lovely parents, Ali Valadian and Shahin Khosravi

Author: Valadian, R.

Title: Porous Catalyst Characterization Using X-ray Nano Tomography and Pore Network Modeling

ISBN:

Printed By: - The Netherlands

Cover Design: Roozbeh Valadian

Table of Contents

1.	Introduction.....	8
1.1	Catalysis.....	9
1.1.1	Fluid Catalytic Cracking	9
1.1.2	Polymerization Catalysis.....	18
1.2	X-ray Microscopy.....	24
1.2.1	X-ray Microscope Instrumentation	25
1.2.2	Contrast Mechanisms in X-ray Microscopy.....	27
1.2.3	X-ray Holotomography	34
1.2.4	Correlative X-ray Ptychography and X-ray Fluorescence Tomography.....	36
1.2.5	Application of X-ray Microscopy in Catalysis.....	39
1.3	Pore Network Modeling.....	43
1.3.1	Application of X-ray Microscopy in Pore Network Modeling.....	47
1.4	Scope of the PhD Thesis	49
1.5	References	51
2.	Characterization of Coke Deposition within a Single Fluid Catalytic Cracking Catalyst.....	56
2.1	Introduction	58
2.2	Results and Discussion	64
2.2.1	Accessibility and Interconnectivity of the Catalyst's Pore Network.....	64
2.2.2	Correlation Between Electron Densities of Coke Deposits and Their Location	70
2.2.3	Origin of Coke Deposits.....	72
2.3	Conclusions	74
2.4	Experimental Section.....	75
2.4.1	Optical Microscopy of Spent Fluid Catalytic Cracking Catalyst Particles.....	75
2.4.2	Setup for Individual Catalyst Particle Calcination	76
2.4.3	X-ray Holotomography	77
2.4.4	X-ray Holotomography Spatial Resolution Estimation.....	78
2.4.5	Differential Contrast Holotomography	81
2.4.6	Registration of Two Datasets	82
2.4.7	Alignment Precision Assessment Using Scale-Invariant Feature Transform.....	84
2.4.8	Histograms of the Electron Density Before and After Calcination	86
2.4.9	Thresholding of Differential X-ray Holotomography Data to Determine the 3-D Coke Distribution	87
2.4.10	Radial Analysis	88
2.4.11	Coke Cluster Analysis.....	89
2.4.12	Powder X-ray Diffraction of a Spent Catalyst Particle Batch Before and After Calcination.....	94
2.4.13	In-situ Small- and Wide-angle Scattering Combined with Differential Scanning Calorimetry.....	95
2.4.14	X-ray Fluorescence Tomography.....	98
2.4.15	Simultaneous Thermogravimetric and Differential Thermal Analysis Combined with Mass Spectrometry	99
2.4.16	Single Particle Metrics and Porosity Profiles.....	100

2.4.17	Pore Network Model Generation	104
2.4.18	Effect of Pore Clogging by Means of Pore Network Analysis.....	105
2.4.19	Permeability Simulation.....	106
2.5	References	108
3.	Morphological Heterogeneity in Metallocene-Type Ethylene Polymerization Catalysts	110
3.1	Introduction	112
3.2	Results and Discussion	114
3.3	Conclusions	130
3.4	Experimental Section.....	131
3.4.1	Catalyst Synthesis	131
3.4.2	Catalyst Pre-polymerization.....	131
3.4.3	Focused Ion Beam - Scanning Electron Microscopy	132
3.4.4	Hard X-ray Holotomography	133
3.4.5	Phase Retrieval, Image Reconstruction and Segmentation	134
3.4.6	Estimation of Spatial Resolution.....	135
3.4.7	Pore Network Model.....	136
3.4.8	Dispersion Plots	137
3.5	References	138
4.	Heterogeneity in the Fragmentation of Ziegler-Type Ethylene Polymerization Catalysts.....	140
4.1	Introduction	142
4.2	Results and Discussion	145
4.3	Conclusions	160
4.4	Experimental Section.....	162
4.4.1	Synthesis of the Ziegler-Type Catalyst	162
4.4.2	Slurry-phase Ethylene Polymerization	163
4.4.3	Loading of Sample in Polyimide Capillary	166
4.4.4	Synchrotron Correlated X-ray Ptychography and Fluorescence Microscopy Set-up.....	167
4.4.5	Tomography Reconstruction of the Ptychography X-ray Computed Tomography and X-ray Fluorescence Datasets.....	168
4.4.6	Fourier Shell Correlation Estimation of the Achieved 3-D Spatial Resolution.....	174
4.4.7	Limited Information from the Ti X-ray Fluorescence Dataset.....	175
4.4.8	Marker-based Watershed Segmentation.....	177
4.4.9	Calculation of the Geometrical Parameters of Each Individual Ethylene Polymerized Catalyst Particle	181
4.4.10	K-Means Clustering Algorithm.....	182
4.4.11	Calculation and Comparison of Different Candidate Fragmentation Parameters	185
4.4.12	Radial and Disk Analysis to Study the Fragmentation Behavior	193
4.4.13	Estimating the Distribution of Particles in Fragmentation State	193
4.5	References	194
5.	Mass Transport Simulation in an Entire Fluid Catalytic Cracking Catalyst Particle	198

5.1	Introduction	200
5.2	Results and Discussion	204
5.3	Conclusions	216
5.4	Experimental Section.....	219
5.4.1	Correlative X-ray Ptychography and X-ray Fluorescence Tomography	219
5.4.2	Data Analysis and Image Processing	219
5.4.3	Estimation of 3-D Resolution of the Ptychography and X-ray Fluorescence Datasets	220
5.4.4	Radial Analysis	224
5.4.5	Zeolite Domain Sorting and Accessibility	225
5.4.6	Diffusion Simulation in the Catalyst Pore Network.....	226
5.5	References	229
6.	Summary, Future Perspectives, and Conclusions	232
6.1	Summary.....	233
6.2	Future Perspectives	238
6.3	Conclusions	241
6.4	References	241
	Back Matter	242
	Appendix A: Influence of 3-D Spatial Resolution on Image Analysis	243
	Appendix B: Nederlandse Samenvatting	250
	Appendix C: List of Abbreviations	257
	Appendix D: Publications and Presentations	261
	Appendix E: Acknowledgments	262
	Appendix F: Curriculum Vitae.....	268

1. Introduction

1.1 Catalysis

Catalysis is the process that the rate of a chemical reaction is accelerated by a substance called catalyst, which remains intact and is not consumed by the chemical reaction. Among all chemical processes, between 85%-90% of them includes at least one catalytic reaction^[1]. Catalysis has a wide range of applications in different industrial chemical processes, such as in oil refinery and the polymer industry. In this PhD Thesis, the focus is on the application of high-resolution X-ray microscopy (XRM) techniques combined with pore network (PN) modeling to study and characterize i) fluid catalytic cracking (FCC) catalyst used in the oil refinery industry and ii) Ziegler-type and metallocene-type catalysts used in olefin polymerization processes.

1.1.1 Fluid Catalytic Cracking

FCC units play a crucial role in oil refinery^[2,3] and convert high-molecular weight hydrocarbons to gasoline and propylene for polymer industry, with the recent promising trends to co-process biomass^[2] and/or plastic waste as alternative sources of fuel^[4-6]. Worldwide, approximately 350 FCC units are operated with an overall processing capacity of 14.7 million barrels per day and consuming 840,000 metric tons of FCC catalyst annually^[2,7]. The FCC catalyst represents an archetypical example of a rationally designed hierarchically porous material that is extensively employed in refinery industry to convert heavy gas oil (HGO), vacuum gas oil (VGO) or residue feedstocks composed mainly by naphthenes, aromatics and alkanes into more valuable lighter fractions, such as gasoline and propylene^[2,8,9]. In each unit, FCC catalyst particles with diameters between 50-150 μm experience 2500-10000 processing cycles with a 5000-cycle average. During each cycle of the FCC process, the feedstock is heated up and sent to the reactor where it comes in contact with the powdered catalyst (Figure 1.1). This catalyst is mainly composed of a microporous (pores $< 2 \text{ nm}$)^[10] zeolite active phase embedded in a mesoporous (pores between 2 and 50 nm)^[10] and macroporous (pores $> 50 \text{ nm}$) matrix of clay, silica, and alumina, as shown in Figure 1.2.

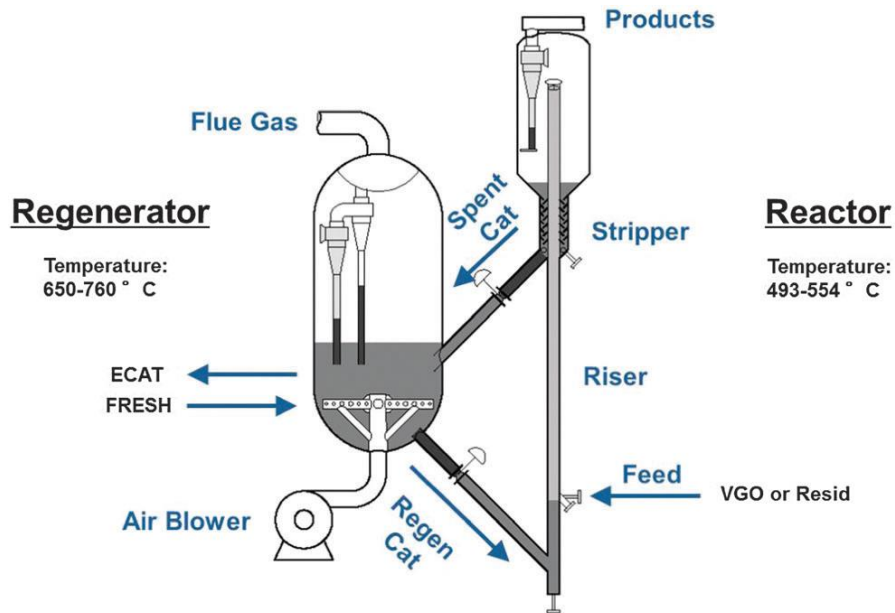


Figure 1.1 Schematic of the FCC unit operation. Figure is based on Vogt & Weckhuysen [2].

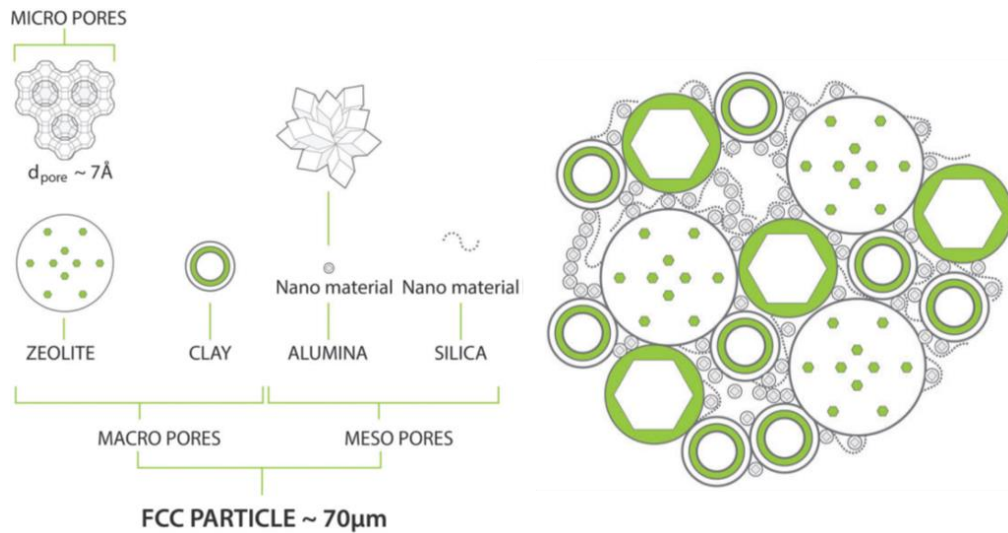


Figure 1.2 Schematic of an FCC catalyst particle composition. Figure is based on Vogt & Weckhuysen [2].

The alumina matrix plays an important role in the pre-cracking of heavy feedstock molecules for enabling feedstock accessibility to zeolite domains where the catalytic cracking reaction takes place, catalyzed by the presence of Brønsted acid sites^[11]. During operation the FCC catalyst is subjected to both reversible and irreversible deactivation (catalyst ageing)^[2,9,11,12]. Reversible deactivation is caused by the formation of a carbon-rich byproduct, termed

coke, that blocks pores and active sites. The coke is formed due to the cracking reactions related to the acidic sites of the catalyst. Dehydrogenation reactions, thermal reactions, and products formed during incomplete stripping in the regenerator can lead to an increase in the coke amount in FCC catalyst particles^[13]. This coke is burnt off in the regenerator and produces the heat used for warming the feedstock and in this way provides part of the energy necessary for the endothermic cracking reactions. However, deposition of coke produced in consecutive cracking cycles can contribute to catalyst deactivation^[14].

Irreversible deactivation is mainly dominated by two processes. The first process is metal poisoning due to the feedstock contaminations. The feedstock contains large molecules (e.g., organo-metallic compounds in the form of porphyrin) that can transport impurities, such as nickel, iron, and vanadium, which are typically the remainders from the plant and animal life forms or the result of the interaction of oil fractions with rock formations^[2]. The second process is the hydrothermal degradation of the zeolite phase due to harsh regeneration conditions (i.e., 700-800°C in the presence of steam) leading to zeolite dealumination and a reduced Brønsted acidity^[11,12,15-34]. For this reason, La is often added to ultra-stable Y zeolite (USY) to further improve the hydrothermal stability. Due to these deactivation processes, in order to preserve optimum steady-state behavior during operation, the FCC reactor is periodically fed with fresh catalyst to maintain a constant catalyst age distribution. The resulting mixture of fresh and aged catalyst in the reactor is therefore referred to as equilibrium catalyst (E-cat).

These two are in general the two main mechanisms leading to FCC catalyst deactivation. In the next two sections, both mechanisms will be explained briefly.

1.1.1.1 Catalyst Deactivation: Coke Deposition

More recently researchers have used various methods, such as carbon-13 nuclear magnetic resonance (¹³C NMR)^[13,35-39], supercritical fluid extraction (SFE)^[36], positron emission tomography (PET)^[40,41], electron paramagnetic resonance (EPR)^[42], electron energy loss spectroscopy (EELS)^[43], near edge

X-ray absorption fine structure (NEXAFS)^[44-46], X-ray photoelectron spectroscopy (XPS)^[36], matrix-assisted laser-desorption/ionization time-of-flight mass spectroscopy (MALDI-TOF-MS)^[35,47], temperature programmed hydrogenation (TPH) and temperature-programmed oxidation (TPO)^[48] to investigate the composition and structure of coke in catalytic processes. The coke in FCC catalysts can be classified into two main categories, i.e., coke produced in the catalytic reaction (aliphatic), and the coke that already exists in the feedstock (aromatic)^[12]. A distinction was made between the activity of catalysts obtained from two different cracking reactions, i.e., gas oil cracking (feedstock has no carbon residue) and residue feedstock (feedstock contains 4.3 wt% carbon residue) cracking^[49]. Therefore, the coked catalyst obtained from gas oil cracking contains mainly catalytic coke, while the one obtained from residue feedstock contains both catalytic coke and carbon residue coke. At the same coke content in the catalyst, the activity of the catalyst processed in gas oil cracking was much lower than the one processed in residue feedstock. The conclusion was therefore that the catalytic coke plays a more important role in catalyst deactivation compared to the residue carbon coke. It was speculated that during the residue cracking carbon deposition in large matrix pores near/on the particle surface causes less deactivation. In gas oil cracking on the other hand, carbon blocks the zeolite pores and leads to a faster deactivation and a more drastic decrease in catalyst activity^[49]. A lab-scaled (microriser reactor) investigation of the effect of coke deposition on catalyst activity was carried out in 1998^[50]. It was found that the coke deposition happens rapidly within the first 0.15 s, while the residence time (the average amount of time that a particle spends in the reactor) of the catalyst within the reactor is between 0 to 5 s. This means that the catalyst deactivation by coke deposition is not dependent on the residence time of the catalyst in the reactor, but it is function of the operating variable, such as catalyst-to-oil ratio (mass of catalyst injected to the reactor per unit mass of gas oil). Two mechanisms were suggested to explain how these coke deposits result in catalyst deactivation using a temporal analysis of products (TAP) transient experiment^[51]. In the first mechanism at low coke contents (<2.6 wt%), larger micro-pores (pore diameter>0.59nm) and the strongest acid sites of the catalyst get covered by carbon deposits leading to catalyst deactivation. In the second mechanism, at high coke contents (>2.6 wt%), the coke deposits

mainly on the exterior of zeolite crystallites and acts as a barrier for the diffusion of reactant inside the micro-pores.

A first study performing a characterization of coke deposited on two deactivated catalysts obtained from units with i) heavy feedstock and ii) hydrogenated vacuum gas oil (HVGO) using single pulse excitation (SPE) and cross-polarization (CP) ^{13}C NMR was carried out in 1995^[13]. The authors showed that there are more coke deposits with aromatic structure rather than those with an aliphatic structure. Three years later, in 1998, Jacobs et al.^[52] were one of the first who obtained information about the spatial distribution of different elements, including carbon, not only in the exterior part (i.e., surface) of the catalyst, but also within the particles using nuclear beam techniques. It was found that the carbon was distributed uniformly inside the FCC catalyst, while Ni showed a ring shape distribution at the surface of the FCC catalyst particles. This was interpreted as an indication that big molecules containing Ni were already converted into smaller molecules at the external surface of the particle. In a more recent publication^[53], a combination of solid-state NMR techniques supported by electron paramagnetic resonance (EPR) and scanning electron microscopy combined with energy dispersive X-rays spectroscopy (SEM-EDX) experiments were implemented to take a closer look at carbon deposition within FCC catalyst particles and the authors showed that the aromatic and aliphatic carbon species deposit in the outer regions and within the particle, respectively. Despite these important findings, a limitation of dynamic nuclear polarization enhanced NMR (DNP-NMR) is its inability to map the coke distribution within a single FCC catalyst particle at the macro-pore scale.

1.1.1.2 Catalyst Deactivation: Metal Deposition

Deactivation of the FCC catalyst by metals has received much attention in the past decade. The FCC feedstock contains different metals, such as iron, nickel, calcium and vanadium. The amount of metals is highly dependent on the crude oil source. Accumulation and deposition of metals on and in the FCC catalyst leads to catalyst deactivation. In heterogeneous catalysis, catalysts mainly deactivate in two distinct ways: via physical and chemical deactivation^[12]. Phenomena, like sintering, occlusion, and the lack of active

sites is considered physical deactivation. Chemical deactivation can happen because of reactions between the compounds (e.g., alkaline metals, steam, and vanadium) and the catalyst, which leads to the destruction of the active sites. Also, the deposition of nitrogen compounds, different metals (e.g., Fe, Ni, and V), and coke species on the surface or within the FCC catalyst leading to a reduction of catalyst activity is considered as chemical deactivation. For instance, three common stages of the decline in activity of a residue hydrotreating catalyst during hydrodemetallization (HDM) of residue oil can be seen in Figure 1.3.

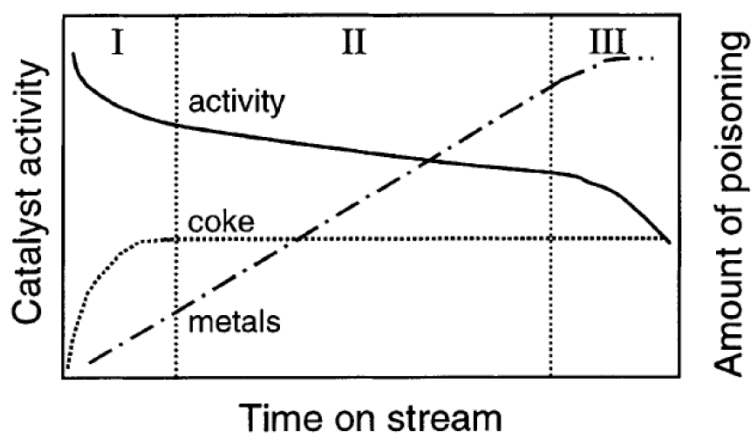


Figure 1.3 The schematic of a residue hydrotreating catalyst's activity decline and the amount of poisoning caused by metals and coke classified into three distinct time regimes. Figure is based on Moulijn et al.^[54].

As shown in Figure 1.3, catalyst activity decreases rapidly during the early stage of HDM (stage I) mainly due to the coke deposition with a minor contribution from metal accumulation. During HDM, the coke level (between 2-10 wt.%, depending on the initial acidity, feedstock characteristics, temperature and H₂ partial pressure) within the catalyst reaches equilibrium within a few hours and is assumed to be in a steady-state condition. In the second stage, coke deposition is saturated and the deactivation process slows down, with an increasing contribution from metal deposition. Finally, during the third stage, mainly the high amount of metal poisoning, with a minor contribution from coke deposition causes irreversible catalyst deactivation, *inter alia* due to the pore clogging.

In 1980, Mitchel^[55] suggested a new method to model catalyst deactivation by metals in the laboratory. The combination of a micro activity test unit (MAT) and a synthetic method of contaminating fresh FCC catalyst was a notable improvement in lab-scaled catalyst deactivation modeling over the old method that was limited to using lengthy studies with a pilot plant or inaccurate bench-scaled studies. The main weakness in their study was, however, that physical and catalytic properties of synthesized catalysts were not in line with the equilibrium catalysts obtained from the FCC operation. To overcome this limitation, an equilibrium catalyst obtained from a commercial FCC unit was analyzed for the first time by Kugler et al.^[56] to validate the observations acquired with laboratory samples. It was shown that during operation nickel has a much lower mobility in comparison to vanadium. Therefore, the age of the catalyst can be defined by considering the amount of nickel existing in the catalyst. However, the uniform distribution of nickel within the catalyst obtained in the laboratory was different from the one seen under real processing conditions.

In 2005, Whitcombe et al.^[57] determined the composition of key metals in the equilibrium and fresh FCC particles using SEM-EDX. In this experiment, the substantial difference between the surface of the fresh and E-cat particle was observed, as shown in Figure 1.4.

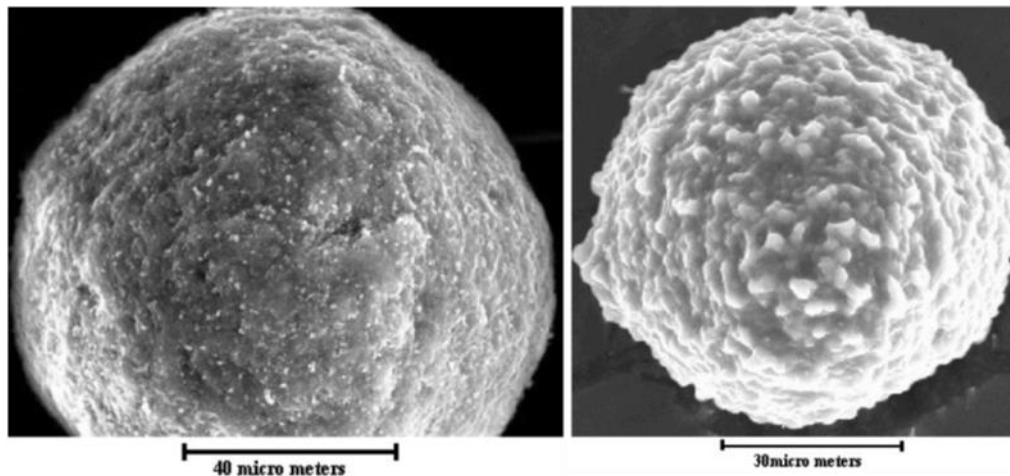


Figure 1.4 : Left: fresh catalyst surface, right: equilibrium catalyst surface. Figure is based on Whitcombe et al.^[57].

As shown in Figure 1.4, the backscatter image of the fresh catalyst has a relatively smoother surface compared to the E-cat surface. This rough layer on the E-cat surface is due to the deposition of impurities and metals. The authors also suggested mild abrasion that can remove metal deposits on the surface of the particle. Therefore, using low levels of attrition might lead to increase in catalyst activity despite of the material loss on the catalyst surface.

Among different poisoning metals, vanadium is known to degrade the zeolite phase by destroying the crystallinity of the zeolites embedded in the FCC catalyst particle. Various techniques, like X-ray powder diffraction^[58], secondary ion mass spectroscopy (SIMS)^[59], X-ray absorption spectroscopy (XAS)^[60], and electron micro-probe^[61,62], were used to show the crucial role of vanadium in destroying the active sites, mainly zeolites, of the catalyst. Etim et al.^[63] studied the substantial role of nickel in vanadium-poisoned FCC catalysts. They determined a threshold for vanadium concentration inside the lab-simulated E-cat using different techniques, like X-ray diffraction (XRD), Fourier-transform infrared spectroscopy (FTIR) spectroscopy, N₂ adsorption, magic-angle spinning solid state NMR (MAS-NMR), SEM and H₂-TPR. It was shown that the presence of vanadium at levels higher than the threshold in the catalyst may contribute to significant decrease in catalyst activity. They also proposed a mechanism that explains how the presence of nickel leads to a less destructive effect of vanadium on catalyst performance. For instance, for the catalyst with concentrations of more than 3000 mg/kg V, the activity was less than 50 percent, while in the presence of nickel with concentrations of 5400 mg/kg Ni (Ni 5.4 wt%), the activity was reduced less (79.1%). The XRD result confirming the destructive behavior of vanadium without the presence of nickel is shown in Figure 1.5.

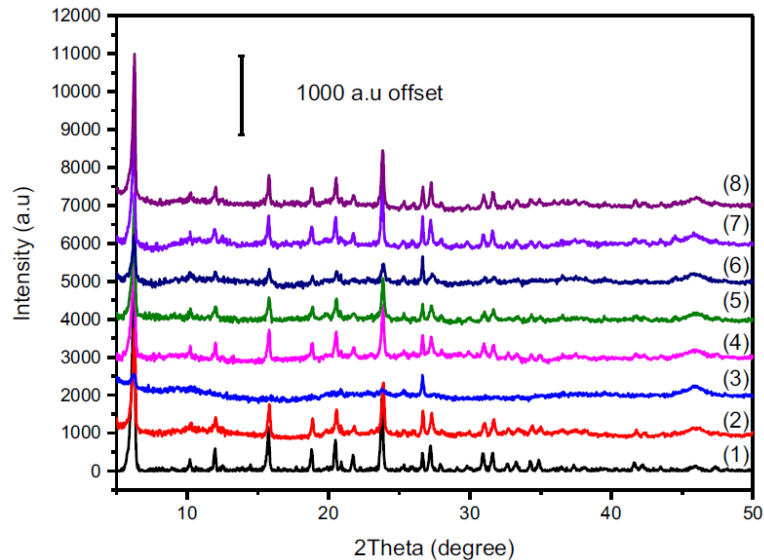


Figure 1.5 Results of the XRD measurements of FCC catalysts containing vanadium or nickel: (1) Fresh ST, (2) V₃ (3) V₅ (4) Ni_{5.4} (5) V₂Ni_{2.5} (6) V_{5.3}Ni_{3.9} (7) V₃Ni_{5.4} and (8) V₃Ni_{1.5}. Figure is based on Etim et al.^[63].

The main XRD peaks corresponding to the zeolite phase were either attenuated or completely disappeared in the samples deactivated by vanadium, while peaks remained almost intact when nickel was present together with vanadium. The commonly accepted mechanism explaining this behavior is as follows: the reaction between the V₂O₅ and the steam in the regenerator forms mobile vanadic acid, like H₃VO₄ and H₄V₂O₇. These acids in the proximity of the Aluminum (Al) can destroy the structure and reduce the active sites of the catalyst. In the presence of Ni, nickel can react with the mobile vanadic acids and retain the surface area, acid sites and activity of the catalyst.

Besides vanadium, iron also plays a crucial role in FCC catalyst deactivation. Different mechanisms for iron deposition on FCC catalyst particles were summarized and suggested by Wise et al.^[15]. The authors used soft X-ray ptychography to study cross-sections of E-cat particles at high spatial resolution (12.2-14.2 nm) and with chemical sensitivity towards the oxidation state of Fe. The first proposed mechanism explains iron deposition during the pre-cracking of large organic molecules that can transport atomic Fe into the pore space of the catalyst. The second deactivation mechanism is related to colloidal Fe or 'tramp Fe', which originates from soil contamination and/or reactor hardware. iron can influence the catalyst activity in three

ways^[28]. (i) in a low iron content catalyst (low contamination), the presence of iron can lead to a decrease in the overall acidity and activity of the catalyst. (ii) iron was shown to also lead to a clogging of the catalyst surface pores and, in this way, prevents the feedstock molecules from reaching the active sites. This phenomenon happens usually in catalysts with high iron contamination. (iii) In the last case, iron can also act as an active site for some other chemical reactions. For instance, iron can cause an increase in the hydrogen yield and coke selectivity in the cracking process. Apart from the iron poisoning effect on products of FCC operation, at high iron contamination, the catalyst also shows a reduced ability to fluidize in the reactor-regenerator system since its surface properties change (roughness, enhanced friction that can even lead to agglutination of particles) and after collision of particles with a rough layer of iron on the surface, the increased abrasion takes place. This causes increased amounts of fines to appear that endanger the FCC unit by reducing catalyst utilization efficiency, increasing the cost of the process, and causing problems in catalyst fluidization in the reactor-regeneration system^[64].

1.1.2 Polymerization Catalysis

Plastics revolutionized our daily lives and their remarkable versatility, durability, and adaptability result in a wide range of applications in different fields, such as food, agriculture, medical, and construction industries^[65,66]. More than 55000 companies in Europe produce plastics and have more than 350 billion euros turnover^[67]. Plastics can be classified into two main categories: i) thermoplastics, which are able to be reshaped (pliable or moldable) and ii) thermosets, which are not reshapable after their production^[68]. Among all diverse markets of plastic products, such as polycarbonate, polystyrene, and nylons, polyolefins have great importance and their annual production reached more than 180 million tons with a volume share of more than 60% to the world's thermoplastic market^[69-71]. Figure 1.6 shows the growing trend of polypropylene (PP), high-density polyethylene (HDPE) and low-density polyethylene (LDPE) global demand from 2008 to 2020.

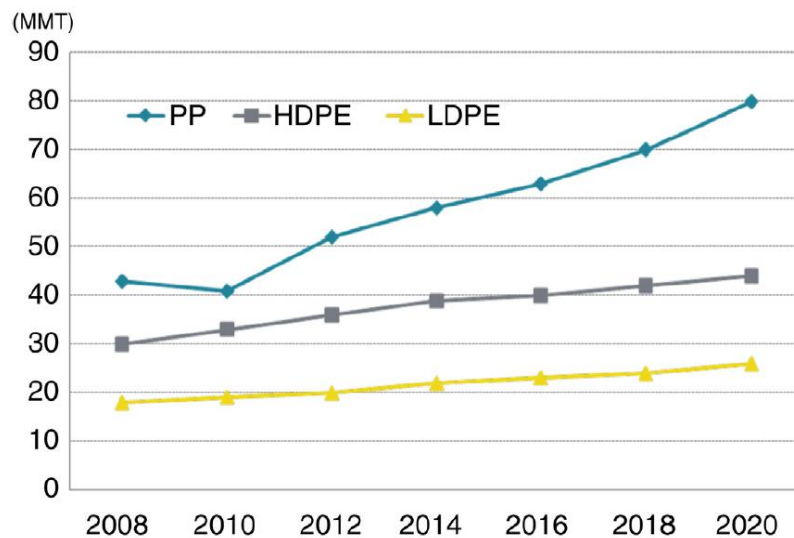


Figure 1.6 Trend of global demand of PP, HDPE, and LDPE (MMT= million metric tons. Figure is based on Posch^[72].

Within the polyolefin family, there are several grades of polyethylene, polypropylene, ethylene-propylene rubbers and higher α -olefins polymers, such as poly-1-butylene^[73,74]. These grades are produced by tuning the chain microstructures as well as the molecular mass distributions by choosing the proper reaction conditions and catalyst system during polymerization^[71].

In the polymerization process, once the monomer (α -olefin) reaches the catalyst's active sites, the polymer starts forming and accumulates inside the catalyst pore structure. The rapid growth of these polyolefins causes a pressure build-up and cracks within the catalyst framework^[75,76]. The catalyst starts to fragment, and both fragmentation and polymerization process continue inside the reactor until the whole catalyst particle is consumed and the final polymer particle is produced.

There are mainly three catalyst systems, which are used industrially due to their flexibility for production of polyolefins, namely i) Ziegler-type, ii) (post-) metallocene-type and iii) Philips-type catalysts. Design of these three classes of catalysts to optimize both polymerization process and product quality plays an important role in industry. In this PhD Thesis, the focus will be on the first two catalyst systems, i.e., Ziegler-type and (post-) metallocene-type, studying their heterogeneity and fragmentation behavior at different

stages of polymerization using high-resolution X-ray nano tomography and pore network modeling.

1.1.2.1 Ziegler-type Catalysts

Ziegler-type catalysts can be categorized based on their generation since their discovery in 1953. Table 1.1 shows the evolution and differences of various generations of Ziegler-type catalyst. The first and second generation of solid TiCl_3 catalyst was discovered by reduction of TiCl_4 with alkylaluminium as co-catalyst^[77,78]. The total polypropylene yield in the first and second generation catalysts was around ~4 kg PP/g catalyst and ~30 kg PP/g catalyst, respectively. These low yields are the indication of high concentration of catalyst phase in the final product. It was found that chemisorption of TiCl_4 on MgCl_2 as a support material due to its high surface area leads to a higher catalyst activity. Also, using particular external electron donors can increase the stereospecificity. These catalysts based on their composition and external electron donors are regarded as so-called third, fourth and fifth generation Ziegler-type catalyst^[79]. The new catalyst generation enabled the polymerization process to reach higher activity and isotacticity^[80].

The hierarchically complex Ziegler-type catalyst system remains one of the grand old workhorses of the polyethylene industry. It typically consists of a TiCl_4 pre-active site species epitaxially chemisorbed on a mechanically or chemically activated MgCl_2 support matrix and subsequently reduced and alkylated with a trialkylaluminium co-catalyst^[74]. This MgCl_2 matrix is formed by platelets, as small as 5 nm, referred to as the primary particles^[81,82]. These primary particles stack together due to ionic interactions to form the catalyst particles in the range of 5-30 μm ^[83]. Depending on the synthesis routes used, the physicochemical and mechanical properties of Ziegler-type catalysts, such as the pore size distribution, can be fine-tuned^[84,85]. For instance, precursors ranging from alkoxides, like $\text{Ti}(\text{OR})_4$, $\text{Mg}(\text{OR})_2$ and MgCl_2 alcohol adducts to MgRCl Grignard reagents, can be used^[86-89]. Furthermore, spray-drying of anhydrous MgCl_2 in a polar solvent or the deposition of MgCl_2 on a spherical and porous silica support matrix are

common industrial preparation routes providing high control over catalyst particle morphology, particle size distribution, and porosity^[90,91].

Year	Catalyst System	Productivity (kgPP/g cat)	I.I (%)	Mmmm (%)	M _w /M _n	Hydrogen Response	Generation
1954	$\delta - \text{TiCl}_3 \cdot 0.33\text{AlCl}_3 + \text{AlEt}_2\text{Cl}$	2–4	90–94			Low	1st
1970	$\delta - \text{TiCl}_3 + \text{AlEt}_2\text{Cl}$	10–15	94–97			Low	2nd
1968	$\text{MgCl}_2/\text{TiCl}_4 + \text{AlR}_3$	15	40	50–60		Low	3rd
1971	$\text{MgCl}_2/\text{TiCl}_4/\text{Benzonate} + \text{AlR}_3/\text{Benzonate}$	15–30	95–97	90–94	8–10	Medium	
1980	$\text{MgCl}_2/\text{TiCl}_4/\text{Phthalate} + \text{AlR}_3/\text{Silane}$	40–70	95–99	94–99	6.5–8	Very high	4th
1988	$\text{MgCl}_2/\text{TiCl}_4/\text{Diether} + \text{AlR}_3$ $\text{MgCl}_2/\text{TiCl}_4/\text{Diether} + \text{AlR}_3/\text{Silane}$	100–130 70–100	95–98 98–99	95–97 97–99	5–5.5 4.5–5	High	5th
1999	$\text{MgCl}_2/\text{TiCl}_4/\text{Succinate} + \text{AlR}_3/\text{Silane}$	40–70	95–99	95–99	10–15	Medium	6th

Table 1.1 Different generations of Ziegler-type catalysts. I.I (Isotactic index) shows the isotactic content of a polymer (the percentage of insoluble polymer sample in a hydrocarbon solvent such as boiling n-heptane). ‘Mmmm’ measures the isotactic sequence in a polymer chain. Here five stereocenters are considered. Table is based on Posch^[72].

1.1.2.2 Metallocene-Type Catalysts

Metallocene-type (MC) catalysts have been studied as one of the most important systems in polymerization catalysis in the last 30 years^[92]. In 1952, a MC catalyst, a π -bonded transition metal atom sandwiched between two cyclopentadienyl anions and bonded to two chlorine or alkyl ligands, was discovered first by Fisher and Wilkinson^[93,94]. Different types of MC catalysts can be synthesized by changing the transition metal and the structure of the ligands. The activity and selectivity of the catalyst is highly dependent on the chemical structure, shape and geometry of the ligand within the MC catalyst^[72].

In the beginning, the MC catalyst activity was significantly lower than that of ZN catalysts^[95]. Using methylaluminoxane (MAO) as a co-catalyst caused a significant change in catalyst activity during olefin polymerization. It also led to a rapid increase of production of linear low density polyethylene (LLDPE)^[96]. More than 5 million tons of different types of polyethylene was produced in 2010 using MAO as a co-catalyst^[96].

There are significant differences between MC-type and Ziegler-type catalysts as can be seen in Table 1.2. The noticeable difference is that the polymer produced by the MC-type catalyst has a narrower molecular weight distribution as well as lower molecular weight fraction compared to the polymer produced by the Ziegler-type catalyst. Moreover, having multiple active centers in Ziegler-type catalysts leads to the creation of different macromolecules with a broader molecular weight distribution compared to the MC-type catalysts, which is illustrated in Figure 1.7^[72].

	Ziegler–Natta	Metallocene
Catalyst	TiCl ₄	Zr-{Cp} _x
Metal	Titanium	Zirconium
Chemistry	Inorganic	Organometallic
Cocatalyst	TEAl	MAO or boron activators
Support	MgCl ₂	SiO ₂
Donor	Various	None
Active sites	Multiple	Single

Table 1.2 Differences between Ziegler-type and metallocene-type catalysts. Table is based on Posch^[72].

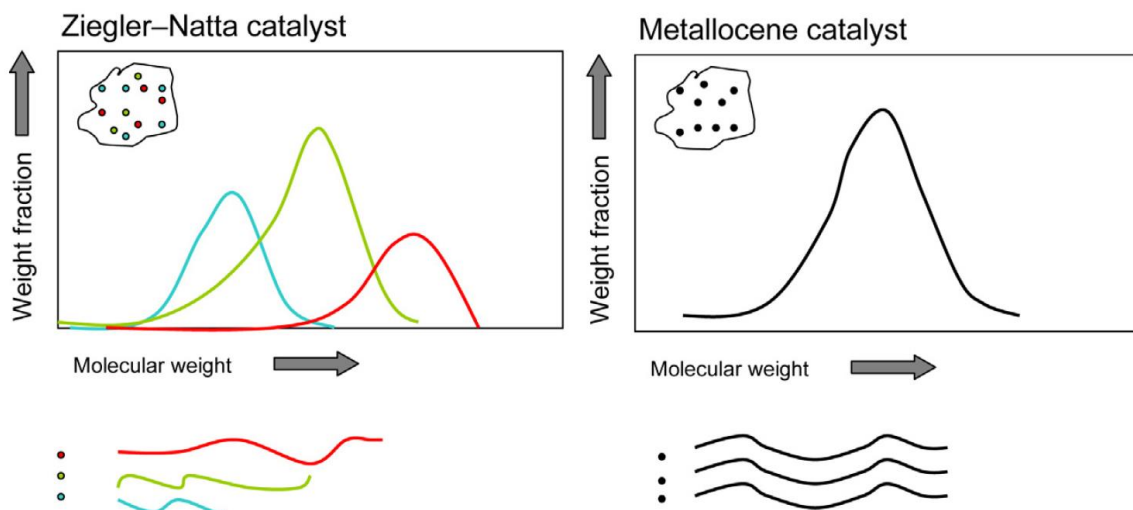


Figure 1.7 Different polymer structures produced by Ziegler-type and metallocene-type catalysts. Figure is based on Posch^[72].

The homogeneous MC-type catalyst is soluble by nature, and this can cause reactor fouling and lack of control over the polymer particle morphology while using heterogenous catalysts results in tunable polymer morphology. To overcome this issue, the MC-based catalysts can be supported by a carrier, such as SiO₂. Supported MC-type catalysts can be also used in the already existing olefin polymerization plants. They need less MAO to be activated and allow control over the morphology of the polymer^[97]. Although, due to the lower process stability and higher industrial costs of MC-type catalysts, their market is more limited compared to the use of Ziegler-type catalysts^[98].

1.1.2.3 Fragmentation in Polymerization Catalysts

The fragmentation process plays a crucial role in polymerization catalysis. Catalyst fragmentation leads to the exposure of previously non- or less accessible active sites in the catalyst to the monomer molecules. It also decreases the diffusion path for the monomers to reach the active site of the catalyst, which can avoid mass transport limitations during the polymerization reaction. Moreover, control over the fragmentation of the catalyst particles can prevent reactor fouling, which is caused by free migration of small catalyst fragments, so-called fines, in the reactor. The expensive damage caused by reactor fouling as well as costly cleaning procedure of the reactor emphasizes the economic importance of a smooth fragmentation of the catalysts during the polymerization process^[99]. Pre-polymerization of the catalyst particle in mild conditions is a key solution to control catalyst fragmentation. It also helps to insure that the final polymer catalyst shape resembles that of the pristine catalyst particle, which is called replication phenomenon^[100].

Fundamentally, there are two rather simplified fragmentation mechanisms proposed in literature^[101] (Figure 1.8): i) the shrinking core model where the catalyst fragments start peeling off from the surface of the particle while in ii) the continuous bisection model, long raptures cause the fragmentation of the catalyst into some larger fragments. Past studies have shown the simultaneous presence of both mechanisms during the actual fragmentation although

dominance of one model over the other depends on catalyst properties, polymer properties and reaction conditions^[83,101,102].

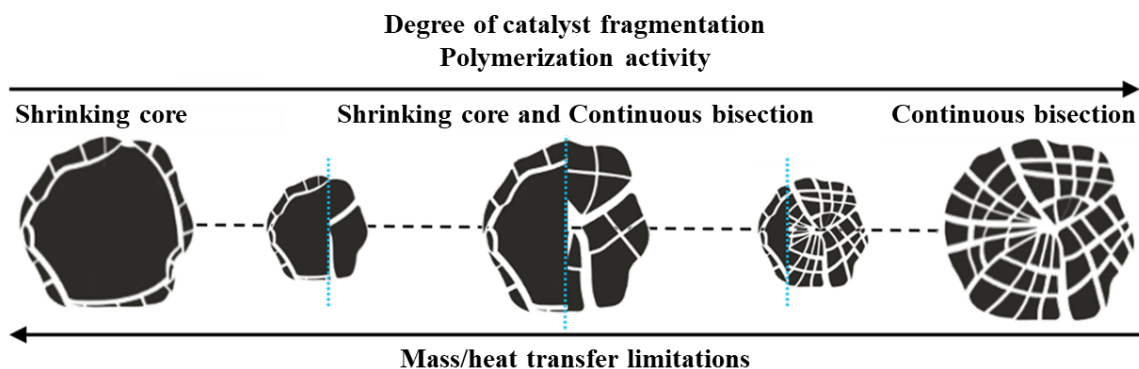


Figure 1.8 Schematic representation of the relationship between the two fragmentation mechanisms, namely, the shrinking core (left) and continuous bisection (right), versus the catalyst particle's polymerization activity, degree of catalyst fragmentation and mass/heat transfer limitations.

1.2 X-ray Microscopy

Microscopy was and still is the way to get insight about the 'micro-world'. Visible light was the main source for microscopes to illuminate an object and generate an image up to 1930. Based on the wavelength of the visible light, the resolution and penetration depth was and still is limited and a significant amount of information/detail can not be resolved with standard microscopy techniques^[103]. The introduction of electron microscopes in 1931 was therefore a great step forward enabling spatial resolutions of a few nanometers (~10 nm) that allowed capturing fine details of a macroscopic object. However, also in electron microscopy there were and are some limitations such as: i) the short penetration depth of electrons does not allow imaging of thick specimen, ii) the vacuum requirement due to the high attenuation of the electron beam in air and iii) a (depending on the exact method used more or less stringent) restriction to samples with metallic/metallized surfaces^[104,105].

Since the discovery of X-rays in the beginning of the 20th century our understanding of the nature of X-rays has significantly deepened. X-ray radiation has a three orders of magnitude shorter wavelength than visible light^[106], which makes X-ray microscopy (XRM) a potentially powerful tool

that can image relatively thick samples at high spatial resolution (sub-micron) providing a glimpse into the nano-world. Importantly, X-ray techniques offer a mostly non-destructive imaging of an object with the capability of measurements performed under non-high-vacuum conditions, e.g., in air or at elevated pressures and temperatures^[103], something that is much harder to achieve with electron microscopy, which, on the other hand offers unsurpassed spatial resolution.

In general, X-ray microscopes can be categorized in two groups: i) full-field microscopes and ii) scanning microscopes. In full-field microscopy, the object is imaged onto a detector either in simple projection obtained by single exposure (e.g., in holotomography) or by using an objective lens (e.g., in TXM). This can make the measurement time shorter and use the photon flux more effectively. In scanning microscopy, the specimen is raster-scanned via a focused X-ray beam (e.g., STXM, X-ray ptychography and X-ray fluorescence microscopy). Although microscopy in scanning mode is typically slower than full-field mode, scanning techniques allow obtaining a variety of information such as local structural information (e.g., in XANES imaging) and elemental composition (e.g., XRF imaging) at high spatial resolution.

1.2.1 X-ray Microscope Instrumentation

Different instruments and optics used in the experimental setup, explained in Sections 1.2.3 and 1.2.4, are now briefly explained.

Undulator: An insertion device consisting of a structure of periodic dipole magnets, which makes the emitted synchrotron radiation essentially (transversely) coherent. Typically, the electron beam oscillates as it passes through the undulator, which leads to the generation of a very intense short wavelength beam in the narrow band of energy in the form of X-rays. Then the generated X-ray beam is guided through different beamlines of the synchrotron.

Monochromator: An optical device that converts polychromatic light including wide range of wavelengths into a range of individual wavelengths. Typically, the polychromatic light enters the monochromator via the ‘entrance

slit' and is separated into its individual wavelengths by a dispersive element. Afterwards, the monochromatic light with the desired wavelength leaves the monochromator via the 'exit slit' and is directed onto the detector, sample, or other components of the experimental setup.

A double crystal monochromator (DCM) consisting of two silicon crystals is used for hard X-ray microscopy techniques (X-rays with energies from several keV up to ~ 100 keV^[8]). When the first crystal is illuminated by the polychromatic X-ray beam, only X-ray photons that meet the Bragg diffraction condition (Equation 1.1), that is those with the correct wavelength λ at the angle of incidence θ are diffracted and pass through, exiting at an angle 2θ . Then the second crystal changes the direction of the diffracted X-ray beam with the desired energy to be parallel with the incident beam ('fixed exit' geometry). This is important in XRM, because the beam position should not change during an energy scan, and this is guaranteed only when using a fixed exit geometry.

Waveguide: A fabricated thin film waveguide typically consists of a low Z layer (weak absorber acting as a core) sandwiched between two high Z layers (strong absorber acting as cladding). A waveguide helps to focus the radiation and i) causes a highly (spatially) divergent cone-beam, effectively making the exit of the wave guide a point source for the subsequent optical system and ii) generates coherent spherical wavefronts.

X-ray focusing optics: Many different X-ray optics exist and improving their efficiency is an active ongoing field of research. In this PhD Thesis, KB mirrors were used as a focusing optic in both XRM techniques described in Sections 1.2.3 and 1.2.4. Conventional mirrors used for focusing visible light do not work in the same way for X-rays because, unlike for visible light, the (complex) refraction index for X-rays is slightly smaller than 1. That means when mirrors should be used, total external reflection has to be used instead of total internal reflection. Paul Kirkpatrick and Albert Baez suggested using two concave orthogonal cylindrical mirrors in a crossed configuration to achieve 2-D focusing by reflecting the X-ray beam at small grazing angles (i.e. utilizing total external reflection)^[107]. Kirkpatrick-Baez (KB) mirrors have substantial advantages compared to other refractive (e.g., Compound

Refractive Lenses) and diffractive (e.g., Fresnel zone plate) optics due to their applicability over a wide range of energies (proper for hard X-rays), less beam intensity attenuation, and the possibility to produce nano-scale spot sizes down to 7 nm^[108].

1.2.2 Contrast Mechanisms in X-ray Microscopy

There are various types of contrast mechanisms, which enable the X-ray microscope to record an image, namely i) diffraction, ii) fluorescence, iii) absorption contrast and iv) phase contrast^[103].

Diffraction contrast is the basis of the crystallography and small angle scattering. If a crystalline material is illuminated by the X-ray beam with wavelength comparable to the lattice spacings (d) of a crystal, the radiation can be ‘Bragg reflected’. In this case, each plane of the crystal acts as weakly reflecting surface. But when the angle of incidence (θ) and crystal lattice spacings (d) meet the Bragg condition, the sum of those weak reflections can cause constructive interference. Otherwise, reflected waves cancel each other out leading to ‘destructive interference’. Bragg’s law can be written as

$$n\lambda = 2d\sin(\theta) \quad \text{Equation 1.1}$$

where θ is the angle of incidence, λ is the wavelength of the incident beam, d is the lattice spacing of the crystal, and n is the diffraction order. One can determine the 3-D molecular structure of a crystalline matter by collecting and processing the intensity of those diffraction patterns.

The second contrast mechanism is using the X-ray fluorescence (XRF) emitted from the material when being illuminated by the X-ray beam. When the energy of the incident X-ray beam is higher than the binding energy of a bound core-shell electron, the electron will be ejected from its atomic orbital. Then an electron from an orbital at higher energy level will fill the vacancy in the lower energy orbital and this electron transition goes along with the emission of a photon, that has an energy corresponding to the energy difference between the involved orbitals (Bohr frequency condition). The energy of this photon will be equal to the energy state gradient of those two orbitals, as shown in Figure 1.9. This energy difference between different

shell is dependent on the atomic number and is unique for each element. Moreover, the number of emitted photons will be directly proportional to the amount/concentration of that specific element within the sample. The quantitative elemental composition and distribution of the material can be measured using these X-ray fluorescence signals^[29,109,110].

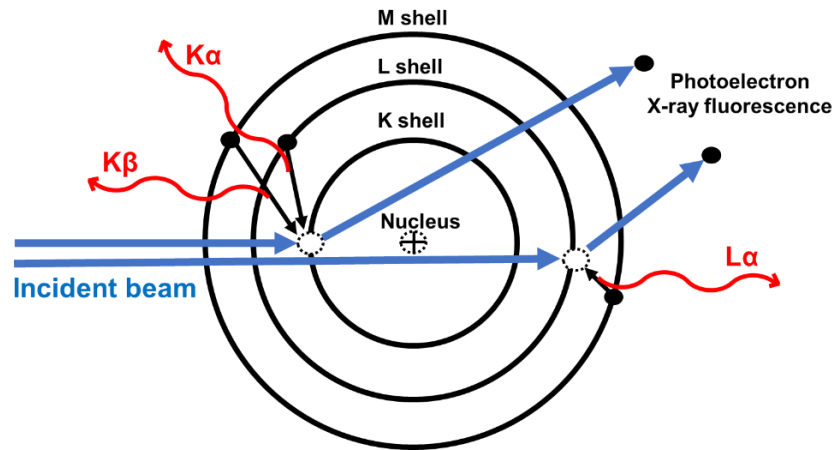


Figure 1.9 Schematic representation of fluorescence signal emission. The core electron of the atom is excited and released by the beam with the energy equal or greater than the binding energy of the respective electron. Then the vacant orbital is filled by a higher orbital electron which releases energy in the form of fluorescent photons (shown as $K\alpha$, $K\beta$ and $L\alpha$).

It is important also to mention an important effect in XRF tomography that is called self-absorption. This effect describes the situation when the fluorescence signal is absorbed by the sample itself. This happens, for example, when XRF originates from deeper inside a sample, which means that the emitted radiation needs to pass through a significant amount (thickness) of material of the sample itself before reaching the XRF detector. If the sample is strongly absorbing at the energy of the emitted XRF, this causes heterogenous absorption of the XRF, depending on the position of origin of the emitted radiation within the sample.

Collection of a full 360-degree set of projections can help to partially compensate the self-absorption effect. This means that the dataset can be reconstructed from two sets of projections, i.e., i) 0-180° projections, and ii) 181-360° projections. In principle these two data sets contain redundant information, but if self-absorption occurs one would notice a difference in the intensity profiles of the two reconstructed datasets (the intensity decreases on

one side of the particle) if the self-absorption effect is dominant. An alternative is to use two XRF detectors on both sides of the particle in the tomography setup - then one can obtain both sets of projections only by measuring angles from 0° to 180° . This effect is also extensively explained in reference^[17].

The third mechanism is absorption contrast. While the incident X-ray beam passes through the sample, the intensity of the beam is attenuated and can be described by Lambert-Beer Law:

$$I = I_0 \exp(-\mu t) \quad \text{Equation 1.2}$$

I_0 is the initial beam intensity, t is the thickness of the material and μ is the linear absorption coefficient, which is directly proportional to the third power of the wavelength λ^3 (or E^{-3} based on $E = \frac{hc}{\lambda}$) and the fourth power of the atomic number Z ^[111]. That is why the heavier elements with higher Z causes more noticeable X-ray attenuation than the lighter elements with lower Z . Figure 1.10 shows the correlation between the beam energy and absorption (attenuation) length (μm), which is the inverse μ in Equation 1.2. The absorption length of an element is the distance over which the X-ray beam intensity with a certain energy is decreased due to the absorption by a factor of $1/e$ (~ 0.37). For instance, based on Figure 1.10, Gold with higher Z is a stronger absorber than carbon as the absorption length of Gold at almost the whole range of energies is smaller than carbon.

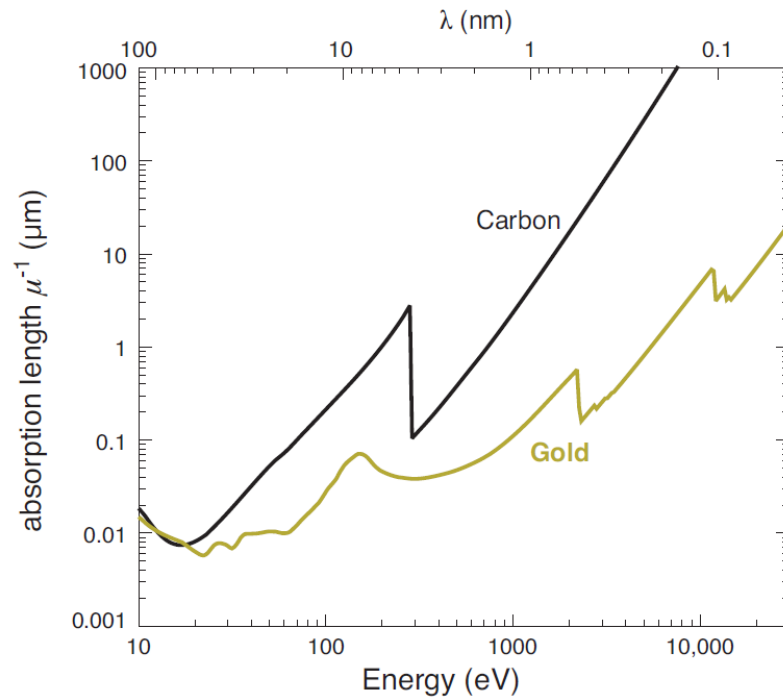


Figure 1.10 Correlation between absorption length and the wavelength (energy) of the X-ray beam for Gold and carbon. The assumed densities of Gold and carbon are 18.92 g/cm^3 and 2.26 g/cm^3 , respectively. Figure is based on Jacobsen^[111].

Therefore, absorption contrast works best for imaging dense materials, and/or samples containing strong absorbers, such as elements with higher atomic number Z ^[112–117]. Therefore, the main issue with techniques based on absorption contrast is that they are not ideal or even capable of imaging samples with low Z elements, such as carbon. Moreover, the achieved resolution for the techniques (either absorption or phase contrast) using focusing optics is mainly limited by the quality of the optics within the experimental setup. For instance, in full-field XRM techniques based on absorption contrast (e.g., TXM), an objective lens is used to form a magnified image of an object onto the detector or in scanning techniques (e.g., STXM), X-ray beam is focused via focusing optics and the sample is raster-scanned to map the sample's absorptivity.

To overcome the main issue, XRM techniques based on phase contrast such as Zernike phase contrast microscopy, X-ray holotomography, and X-ray ptychography provide a high contrast and sensitivity to map low absorptive samples (also high Z elements). The X-ray beam is refracted, and the phase and amplitude of the beam changes when it passes through a sample.

There are several approaches to determine the phase shift of the X-ray beam. For instance, Zernike phase contrast microscopy uses a ring aperture to illuminate a sample by X-ray beam. As the X-rays pass through the sample, a fraction of the beam is diffracted, and the rest is undiffracted. The interference pattern of the diffracted and undiffracted waves introduces the contrast in the image. In order to increase the contrast, a phase ring is used to impose a phase-shift of 90° (or 270° or 450° ...) on the undiffracted wave. Although Zernike phase contrast is a suitable technique to image low Z elements since it does not require any numerical (iterative) phase-retrieval calculation and a high-brilliance (determines the intensity and directionality of an X-ray beam) synchrotron source, the achieved resolution is still limited by the optics.

Coherent diffraction imaging (CDI) is an alternative method to determine the phase shift at high spatial resolution. CDI is based on the diffraction of a coherent X-ray beam passing through a specimen. In this case, the intensity of the far-field diffraction pattern generated by the interaction of the X-ray beam with the sample is recorded by an area detector and by applying some additional iterative algorithms the phase can be recovered (different phase retrieval algorithms will be explained in sections 1.2.3 and 1.2.4). Since the diffraction contrast is collected without using any X-ray optics, the resolution is not dependent on the optics quality, which is typically the limiting factor^[118]. Therefore, a high spatial resolution down to few nano meter is achievable^[119,120].

In the interaction of X-rays with matter one has to consider the complex refractive index for X-rays n ^[121]:

$$n = 1 - \delta + i\beta \quad \text{Equation 1.3}$$

$$\Phi(x, y) = \frac{2\pi}{\lambda} \int \delta(r) dz \quad \text{Equation 1.4}$$

where δ represents the dispersion term (related to phase contrast) and β is called the absorption term (amplitude) that is related to absorption contrast. The phase shift $\Phi(x, y)$ can be calculated by Equation 1.4 where λ indicates the X-ray wavelength.

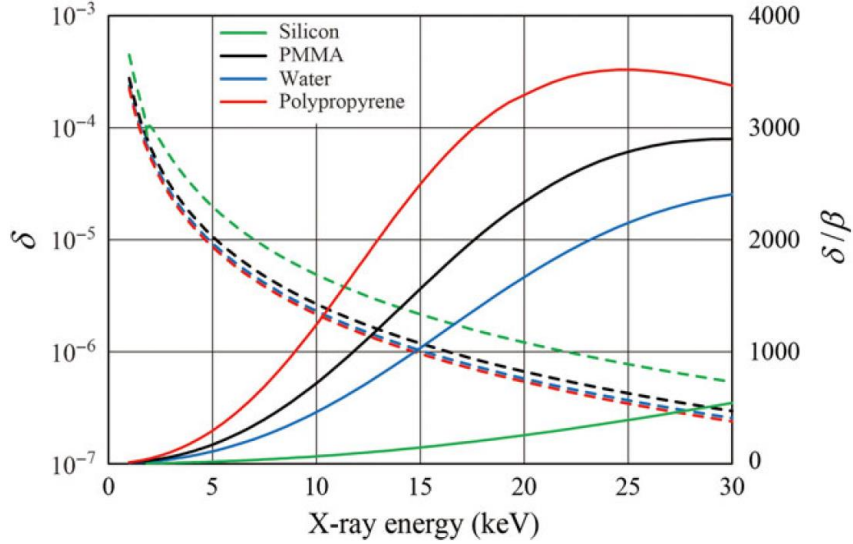


Figure 1.11 Calculated δ and δ/β for different materials. Dashed lines and solid lines show δ and δ/β , respectively. Figure is based on Momose^[122].

The phase contrast, δ , is around three orders of magnitude larger than the absorption contrast, β , at high photon energies particularly for materials consisting predominantly of low Z elements, as seen in Figure 1.11.

Both δ and β can be calculated based on their correlation with the atomic scattering factors, $(f_1 + if_2)$, as written below

$$\delta = \frac{r_e}{2\pi} n_a \lambda^2 f_1 \quad \text{Equation 1.5}$$

$$\beta = \frac{r_e}{2\pi} n_a \lambda^2 f_2 \quad \text{Equation 1.6}$$

where r_e is the classical radius of the electron (2.8×10^{-15} m), n_a is the number density of an atom. In case of neutral atoms, the sum of these modes approaches the atomic number of the element (Z). Also, at high photon energies, f_1 approaches a value close to Z while the absorption term, f_2 , will decrease as λ^2 with respect to f_1 . Different values of f_1 and f_2 are shown for carbon and Gold in Figure 1.12. For instance, it clearly shows that for imaging a low Z element, such as carbon at high photon energies (above 1keV which is the case in Chapters 2, 3, and 4 of this PhD Thesis), there is a large difference between the f_1 and f_2 values, i.e., the phase term, f_1 , is large (larger δ) and the absorption term, f_2 , is very small (smaller β). In these cases, is

therefore highly beneficial to use phase contrast imaging rather than absorption contrast imaging.

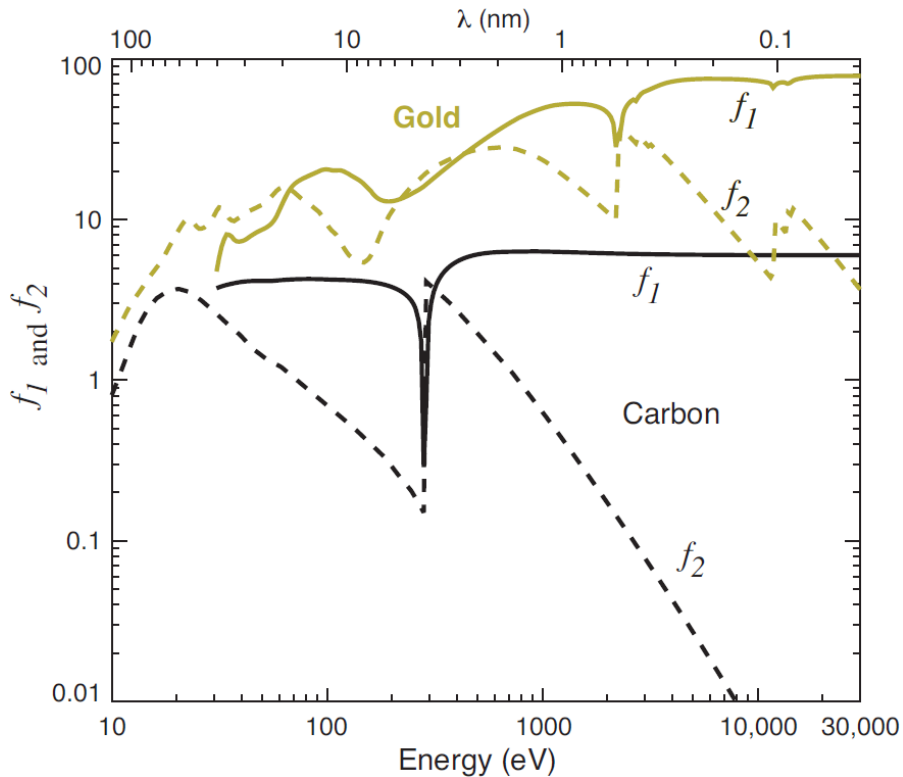


Figure 1.12 Complex number of oscillator modes (f_1+if_2) for Gold and carbon is plotted versus photon energy. At high photon energies, the phase contrast term, f_1 , is few orders of magnitude larger than the absorption term for carbon which implies the better sensitivity of phase contrast imaging for low Z elements. Figure is based on Jacobsen^[111].

Another advantage of the determination of the phase shift is that it is directly related to the electron density of the sample $\rho_e(r)$ as seen in Equation 1.7^[123].

$$\rho_e(r) = \frac{2\pi\delta(r)}{\lambda^2 r_e} \quad \text{Equation 1.7}$$

Using this, the electron density of each pixel can be reconstructed via the calculated phase shift. Eventually, the segmentation of the different phases in the sample based on their electron densities can be done by comparing the calculated electron density values with theoretical electron density values ρ_e which can be calculated using Equation 1.8.

$$\rho_e = \frac{N_A \rho_m Z}{M} \quad \text{Equation 1.8}$$

In this equation, N_A and ρ_m are the Avogadro's constant and the material density, respectively. Z represents the number of electrons and M the molar mass of the reference material.

1.2.3 X-ray Holotomography

The root of the word 'holotomography' lies in the combination of holographic and tomographic reconstruction. It was introduced for the first time in 1999 when holographic reconstruction was developed based on images taken at different distances from the specimen^[124,125]. X-ray holotomography is a powerful full-field phase-contrast imaging technique, which works based on the phase shift induced by the object. Unlike absorption techniques, holotomography is a suitable imaging tool with a variety of applications for the characterization of materials with low atomic number ('soft' materials) such as human brain tissue^[126,127], the carbon binder domain in Li-ion electrodes^[128], polymethacrylate surfaces^[129], and catalysts^[130].

As an example for synchrotron-radiation based X-ray holotomography a schematic of the holotomography experimental setup installed at the P10 beamline of the PETRAIII storage ring at the Deutsches Elektronen-Synchrotron (DESY, Hamburg) can be seen in Figure 1.13^[126]. The X-ray beam passes through an undulator which makes the radiation essentially (transversely) coherent. The monochromator is located around 38.5 m away from the undulator and is used to select the desired wavelength. Afterwards, the X-ray beam is focused by a set of KB mirrors and passes through the wave guide. Next, the whole object, which is placed on the motorized sample stage, is illuminated by the monochromatic cone-shaped beam from the waveguide and the Fresnel diffraction patterns caused by the object are collected by a scintillator-based fiber-coupled scientific (CMOS) detector (pixel size of 6.5 μm ; 2048 \times 2048 pixels; Photonic Science)^[131].

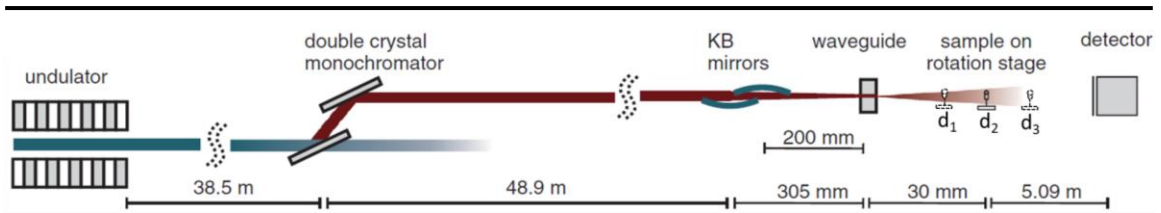


Figure 1.13 Schematic of holotomography setup of the P10 beamline at DESY. Figure is based on Robisch et al.^[126].

The holograms are acquired at multiple distances, that is, magnifications^[124]. Because a cone beam is used, the geometric magnification of projections (M) can be calculated by:

$$M = \frac{Z_{01} + Z_{12}}{Z_{01}} \quad \text{Equation 1.9}$$

where Z_{01} is the distance between waveguide exit and the sample, Z_{12} is the distance between the sample and detector. If the distance between the waveguide and detector is constant, the effective pixel size, p_{size} , is also dependent on the pixel size of the detector, p_{detector} , which can be calculated as follows:

$$p_{\text{size}} = \frac{p_{\text{detector}}}{M} \quad \text{Equation 1.10}$$

Magnified projections can be assumed as holograms from a parallel beam based on the Fresnel theorem^[132]. Then, in this case, the Z_{12} can be replaced by the effective propagation distance which is $Z_{\text{eff}} = Z_{12}/M$.

In a classical holotomography experiment, between 1000 to 2000 projections over 180° or 360° at multiple distances (between 2 to 4) are collected. The acquisition time is normally around 4 h for each sample and depends on the number of distances and the dwell time which is the length of time that a pixel (in scanning techniques) or the whole sample (in full-field techniques) is exposed by the beam; this is dependent on the achieved image contrast (i.e., sample-dependent). In order to correct any non-linearities of the detector^[124] as well as non-homogenous illumination, flat field and dark field images are recorded before and after each tomographic scan for all distances. Flat field images are collected without sample in the beam, while the dark field refers to the image that the detector records without the beam and the

sample. The original intensities, I , can then be corrected using the following equation:

$$I_{corr} = I - \frac{\text{dark}}{\text{flat} - \text{dark}} \quad \text{Equation 1.11}$$

After the acquisition of the holograms, they are rescaled and aligned for the phase retrieval procedure to determine the phase shift from the collected Fresnel diffraction patterns. There are different types of iterative phase retrieval algorithms which can be used in holotomography such as modified hybrid input-output schemes^[133], multiple projections schemes^[134,135], alternating projections^[136] and simultaneous reconstruction of object and probe^[137–139]. After determination of the phase shift for each pixel the electron density for the respective pixel can be calculated as explained in section 1.2.2 and Equation 1.4. This will be followed by a tomographic reconstruction using different algorithms such as filter back projection (FBP) or algebraic reconstruction techniques (ART)^[140] which provide a 3-D reconstruction of the sample's electron density. This allows detailed insights into the structure of the specimen including a quantitative mapping of the electron density and related material composition.

To estimate the achieved 3-D spatial resolution, various approaches in literature have been reported^[130,141,142], although Fourier shell correlation (FSC)^[143] is one of the most commonly used.

1.2.4 Correlative X-ray Ptychography and X-ray Fluorescence Tomography

The word ptychography (pronounced with a silent p) comes from the Greek word 'ptúx' which means "to fold" because information from successive overlapping beam spots is "folded" together^[144]. The idea of ptychography was first used in electron microscopy in 1970, while the limited coherence of the electron beam slowed down the development of the technique^[145–147]. In 1996, Henry Chapman was the first who applied the ptychography approach in a soft X-ray scanning transmission microscope^[148,149]. He tried to determine the complex probe and object functions using a charge coupled device (CCD) detector, which was able to

collect the low noise diffraction pattern^[150]. Later, a significant development was added via use of the Fienup algorithm^[151] that can be used for the reconstruction of the phase information using the partial overlap of diffraction patterns. Also the improvement of other iterative algorithms, detectors and synchrotron instruments in recent years caused ptychography to become a powerful imaging tool for determination of the phase shift (and in turn electron density) and amplitude of the beam after passing through a sample^[152–157].

Ptychographic X-ray computed tomography (PXCT) is a type of lensless CDI. CDI in general requires a so-called finite support constraint, which means the sample has to be isolated and surrounded by a non-diffracting region, while these restrictions are resolved in PXCT. One of the biggest advantages of PXCT, however, is the fact that the resolution is not limited by any focusing optics - it is instead mainly limited by the accuracy of the motor stages that move the sample as well as the largest collected scattering angle. Therefore, the development in synchrotron instruments such as detectors and high precision motor stages as well as improvement of ptychographic reconstruction algorithm has and further will result even in higher achievable spatial resolution and lower measurement times.

PXCT is based on evaluating the recorded diffraction patterns at overlapping beam positions when raster scanning the specimen. This results in a quantitative mapping of the real part of the complex refractive index, which includes the phase information via the dispersion term δ (Equation 1.3). At each projection angle, the coherent, monochromatic and intense X-ray beam is focused both horizontally and vertically by different focusing optics such as KB mirrors, which are capable of reaching a spot size down to 7 nm at 20 keV^[158]. The FOV is raster-scanned by the X-ray beam with a certain step size (normally 100nm to 300nm) and dwell time of few milliseconds. In case of tomography (3-D imaging), the far-field (Fraunhofer) diffraction pattern of each pixel is collected at every projection angles.

The overlapping illuminated regions would normally provide redundant information but here this redundancy is used to iteratively calculate the phase shift and amplitude of the object as well as the complex illumination function

that fully characterizes the beam^[159]. This so-called ptychographic phase-retrieval can be obtained using different iterative algorithms^[154,160–162]. After determination of the phase shift for each pixel, the quantitative electron density can be obtained by Equation 1.7. Then, the same 3-D tomographic reconstruction algorithms explained in the section on holotomography can be applied here to reconstruct the 3-D electron density of the material. The achieved 3-D spatial resolution of the reconstructed tomographic datasets depends, as in all tomographic experiments, on variety of parameters such as the resolution (quality) of the 2-D projection, sample drift, alignment precision and signal to noise ratio of the data. The same methods as mentioned in the holotomography section can be used here to estimate the achieved 3-D spatial resolution.

Unlike holotomography, because of the use of a focused beam, PXCT can simultaneously be performed with XRF tomography, i.e., using the same beam, which enables mapping the distribution of different elements within the sample together with electron density. In addition to collecting the diffraction pattern in each pixel of the 2-D projection, the X-ray fluorescence signal for each pixel will also be recorded by an XRF detector. For instance, Figure 1.14 shows such a correlative PXCT and XRF tomography setup used at the P06 beamline at PETRA III at DESY. The electron density (E.D.) as well as distribution of Cl and Ti was recorded for an individual Ziegler–Natta catalyst particle with $\sim 40 \mu\text{m}$ diameter. The white arrow in the figure indicates a region in which Cl has a high concentration while the Ti signal is low^[163].

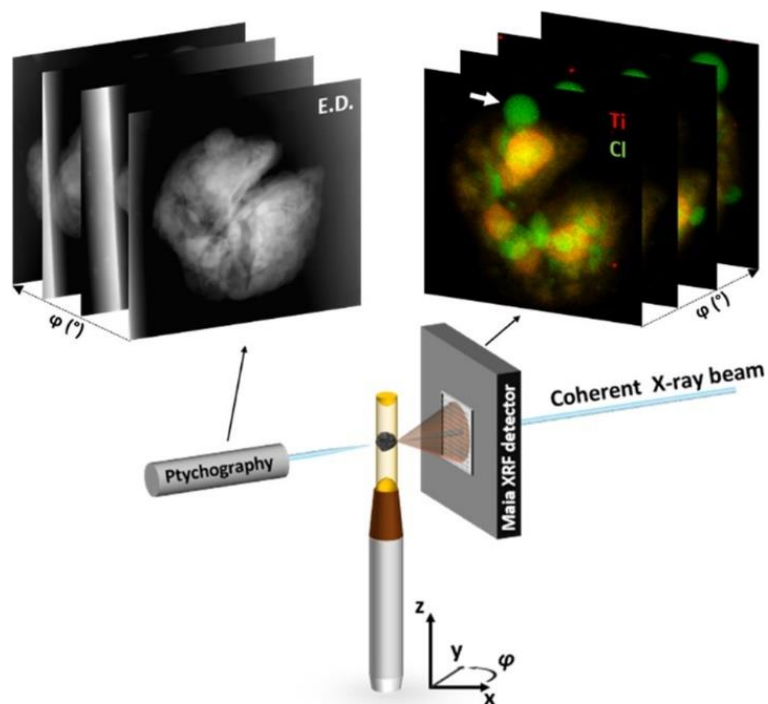


Figure 1.14 Schematic layout of the correlative 3-D X-ray ptychography and fluorescence tomography experimental setup at the P06 beamline at PETRA III. Figure is based on Bossers et al.^[163].

1.2.5 Application of X-ray Microscopy in Catalysis

Characterization of porous catalyst plays a crucial role in determining their performance and in turn their design. Hard X-ray microscopy techniques offer a non-destructive probe with large penetration depth, which can provide 2-D and 3-D images at high spatial resolution, that is, with resolutions down to tens of nanometers^[19,142]. Probing heterogenous catalysts using hard X-ray microscopic techniques gives insight into their structure and catalyst composition. For instance, the zeolite phase in the FCC catalyst, which provides the majority of the catalytic activity is further stabilized by adding rare-earth (RE) metals such as La. These RE metals can be used as a marker to map the zeolite phase within the whole 3-D volume of a catalyst particle. Then the mass transport properties to and from the zeolite phase in that catalyst can be obtained using different modeling approaches. This can inform further development and optimization of catalyst performance^[8].

Hard X-ray nano tomography techniques are capable of revealing a variety of information, such as internal structure^[30,114,164,165], magnetism^[117,166], chemical bonding^[167] and orbital orientation^[168,169]. Also, thanks to the development of improved high-resolution focusing optics as well as the high brilliance of third-generation synchrotron sources, scattering techniques for catalyst characterization at the nanoscale were developed and improved substantially^[170].

For example, Meirer et al.^[171] introduced for the first time the application of differential contrast imaging together with advance analysis such as radial calculation to investigate the 3-D distribution of different metals and their effect on macro-pore structure connectivity and mass transport properties of a single heterogenous catalyst particle. Non-invasive and fast full-field transmission X-ray microscopy (TXM) was used to study the FCC catalyst deactivation by metal poisoning. Mapping the 3-D macro-pore structure provided a better understanding of catalyst pore connectivity and accessibility, while elemental mapping allowed to investigate poisoning metal distribution and their effect on catalyst activity. In this study TXM was used at 4 different X-ray energies, i.e., below and above the Fe and Ni K absorption edges. High-resolution images containing iron and nickel distributions were obtained from the differences between the tomographic data, as shown in Figure 1.15.

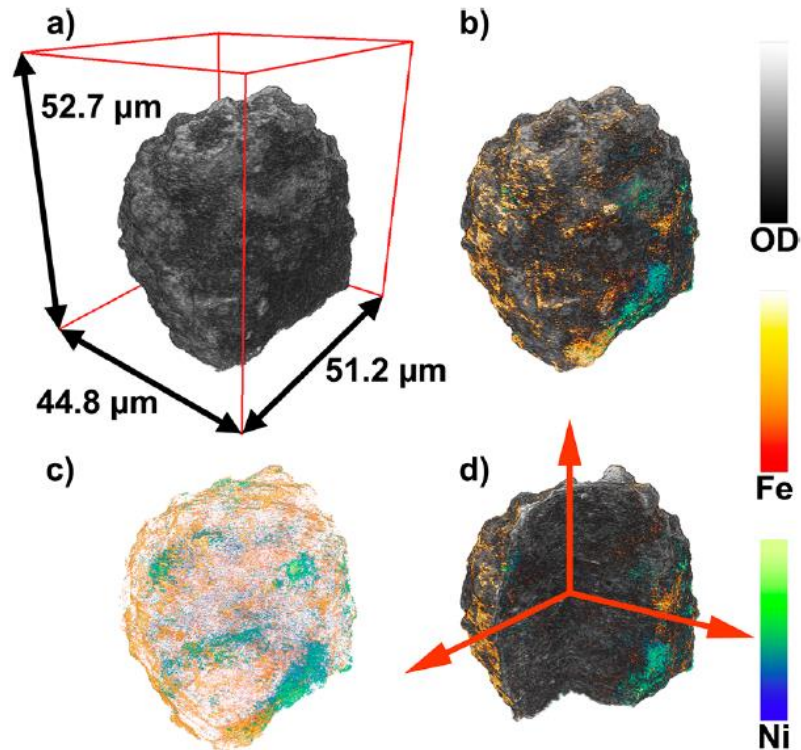


Figure 1.15 Structural and elemental information obtained for an individual of FCC catalyst particle based on TXM mosaic computed tomography. (a) Recorded optical density (OD), (b, c) iron (orange) and nickel (blue) 3-D distribution and (d) a cut-through of the TXM data showing the inner particle structure. This figure is based on Meirer et al.^[171].

Moreover, the radial distribution of Fe and Ni was obtained as a function of distance to the surface. Radial analysis gave insights into metal deposition within the FCC catalyst considering its irregular but still spherical shape. As it is shown in Figure 1.16, despite the fact that both metals generally accumulate mostly near the particle surface, Ni penetrates deeper within the particle when compared to Fe (Figure 1.16a). This shows the higher mobility and penetration depth of Ni compared to Fe.

TXM data also provided information regarding the pore structure of the catalyst particle. The porosity changes due to the presence of metals within the particle as a function of distance to the particle surface are plotted in Figure 1.16. The large porosity change close to the particle surface shown in Figure 1.16b demonstrates that macro-pore blockage occurs mainly at the surface of the particle where the metals have the highest concentration. In summary, it was shown that non-destructive full-field TXM multiple-energy tomography

is a powerful tool to investigate macro-porosity, different metals distribution, their influence on the macro-pore interconnectivity and mass transport capabilities within a whole individual catalyst particle.

Application of X-ray microscopy techniques in catalysis is extensively covered in a recent review article^[8] and also more examples can be found elsewhere^[8,103,118,122,170].

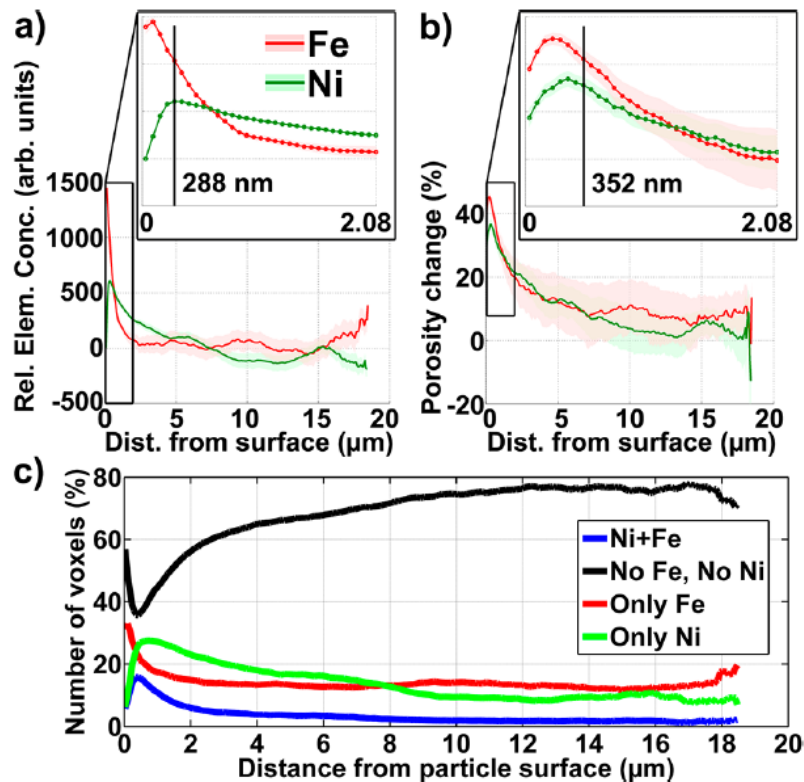


Figure 1.16 (a) Radial analysis of the relative Fe and Ni distributions within a single FCC catalyst particle plotted as a function of distance from the surface of the FCC particle. (a). (b) shows the porosity changes due to the presence of metals and (b) is the insets in both panels which show a zoom of the region close to the surface. The black vertical lines indicated the distances of the 5th and 6th concentric single voxel shells (shells of single voxel thickness) created formed by all voxels with the equal distance to the particle surface are shown with vertical lines. (c) shows the correlation between relative Fe and Ni concentrations. The concentration is the normalized (to percent) number of voxels in each shell containing both Ni and Fe (blue), only Fe (red), only Ni (green), or none of those metals (black). Figure is based on Meirer et al.^[171].

1.3 Pore Network Modeling

It is not always easy to study porous materials and their performance via experiments due to experimental limitations which range from uncertainties in parameters determination to the material complexity to unfeasible process conditions such as temperature and pressure. In this case, modeling approaches can be an alternative tool to better understand different properties of a porous material. Fundamentally, modelling methods can be divided into two categories: i) continuum modeling^[172–176] and ii) pore-scale modeling^[177,178].

In continuum modeling, the assumption is that the porous material is made based on building blocks which are called a representative elementary volume (REV). The size of the REV is chosen in a way that the physical properties of these small REV's are representative of the total porous material^[179]. Despite the fact that continuum modeling is computationally less expensive than pore scale modeling, there are two main disadvantages: i) it is not always easy to define the REV within the porous material due to the anisotropic structure (e.g., FCC catalyst) or limited thickness of the sample (e.g., very thin catalyst layer in PEM fuel cells). ii) determination of bulk-fluid parameters related to the porous material is often obtained experimentally and those experiments are not always straightforward to perform; for example, for very small porous materials (e.g., nano-particle agglomerates). Pore scale modeling, on the other hand, reveals detailed pore-level information even for highly heterogeneous and anisotropic porous materials^[180]. There are six different types of pore-scale models: i) the smoothed particle hydrodynamics (SPH) approach^[181], ii) level-set models^[182], iii) percolation models^[183], iv) direct numerical simulation (DNS)^[184–186], v) Lattice-Boltzmann (LB) models^[187], and vi) pore-network models^[177,188,189]. In this PhD Thesis, the focus will be exclusively on pore network (PN) modeling.

Many models containing pore-level details such as LB or DNS come with high computational costs since all numerical calculations are performed on a mesh which should be large enough for the solver to converge. In comparison to these and other pore-scale models, PN modeling on the other hand is an approach for simulating different phenomena efficiently in terms of

computational costs, because it uses a simplified geometrical structure. The first PN model was introduced by Fatt^[190] who studied the similarities of the flow properties in a random resistance network and porous media. After that, PN models have been expanded to diverse areas of science, particularly for studying transport processes such as adsorption^[191,192], biomass growth^[193–195] and dissolution/precipitation^[196–198].

Fundamentally, PN models are a set of mathematical graphs that represent a specific phase of the material. As shown in Figure 1.17, in this PhD Thesis, PN models always represent the pore space of the porous material, but more generally these graphs can also represent other phases such as a specific solid phase. The graphs consist of so-called nodes, which are the branching points of the graph or network and are connected via so-called segments. Segments are formed by segment points and small cylinders between segment points, both of which are used to represent the detailed geometrical shape/curvature and the volume of the corresponding pore space. This means for a straight pore which does not have a significant change in pore radius, one uses a smaller number of segment points compared to a curvy pore channel with drastic radius changes. PN models are furthermore often simplified into a network consisting only of nodes and segments to further reduce the computational costs for the simulations, which would otherwise be too complex and computationally expensive when taking into account all segment points. In this further simplification, segments are represented by cylinders with a specific length and radius determined from the original pore-space. Specifically, the volume of these cylinders corresponds to the volume of the respective pore space, making it an efficient representation of the actual pore space.

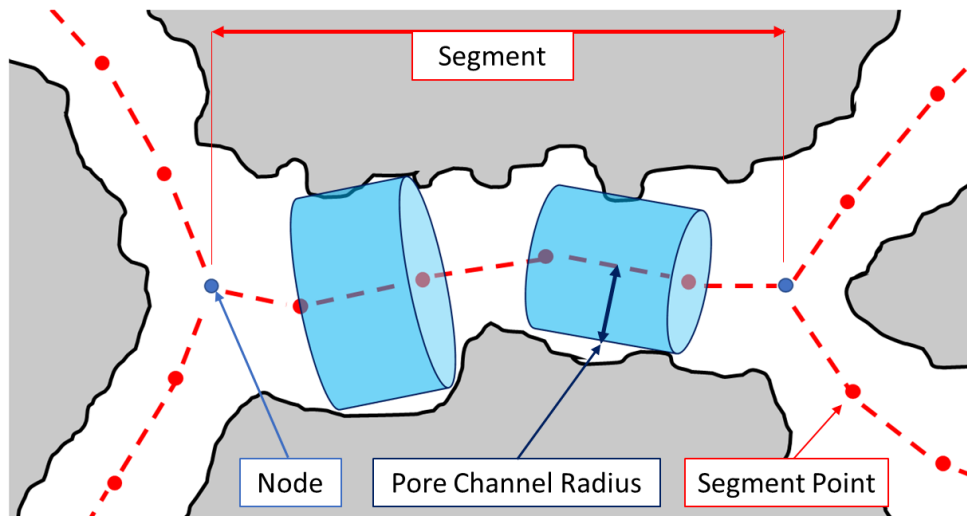


Figure 1.17 Schematics of a pore network model built from of a specific pore structure. Gray and white colors show the solid matter and pore space, respectively. Figure is based on Meirer et al.^[30].

In Chapter 5 of this PhD Thesis a modified version of the PN model, a so-called multi-directional pore network (MDPN)^[199] was used to simulate the diffusion of a reactant within a single FCC catalyst particle. There are two important modifications applied during the generation of MDPN: i) in case that two nodes are connected via multiple segments, those segments are removed and replaced by a single segment which has the average length, sum of the radius, and sum of the volume of those multiple segments and ii) loop connections which connect a node to itself are eliminated from the network as they do not contribute to mass transport but rather act as a dead end pore. To summarize, a PN model of a porous material is a representation of the corresponding pore space volume including detailed topological information.

The reliability of the PN modeling and its result are highly dependent on the extraction method which is used to generate the model. Extraction methods are categorized in three groups: i) statistical reconstruction which is mainly based on the truncated Gaussian random field as well as geometrical properties of the original pore space such as porosity^[200,201]. ii) the grain-based model, which was first developed by Bryant and co-workers^[202–204]. They introduced an algorithm based on random close packing of spheres with equal size to construct networks with coordination numbers less or equal to 4. iii) The direct mapping model, which is able to generate irregular networks based on 4-D images^[205] (3-D+time) of a porous material^[206]. Irregular pore

networks can be constructed with two different algorithms. The first one is called Maximal Ball algorithm. The algorithm finds the largest inscribed sphere centered at each voxel of the pore space in the binarized image (pore space voxel values are '1' and the rest, i.e., solid phase and background voxel values are '0') in a way that spheres just touch the solid phase (boundary). Afterwards, spheres that are included in other big spheres are removed. The remaining spheres are called maximal balls. Then the network that is generated consists of the largest maximal balls (called pores) which are connected by smaller ones (called throats). This method was first used by Silin and co-workers^[207] and was then further developed in other studies^[208,209]. The second method is the Medial axis algorithm, which converts pore space images into a topological skeleton, which can be constructed by thinning^[210,211] or a pore space burning algorithm^[212]. The advantage of the medial axis algorithm is its ability to preserve the topological structure of the original pore space. In this PhD Thesis, a version of the medial axis algorithm is used to construct the skeleton (via so-called skeletonization) and in turn the PN model.

The first step before skeletonization is to obtain images at high-resolution that can resolve the features of interest such as pores at different length scales. After data acquisition, the grayscale images are binarized into pore space and solid phase (segmentation step). In the binarized pore space images, all pore space voxels are assigned a value of 1 and the rest of the voxels (including solid phase and background) have the value 0. The segmentation procedure can be performed using various algorithms, such as watershed segmentation^[213], K-means clustering^[214], and segmentation using Otsu's method^[215]. After segmentation of the pore space, the so-called distance map of the binarized image is calculated. In this step, the distance of each voxel from the closest boundary (voxels with value 0) is determined. Based on the distance map, the thinning algorithm is applied in which the binarized image is converted to one that contains one voxel thick lines, located precisely at the center of each pore; the algorithm works by removing iteratively the pore space voxels (voxels with value 1) based on their distance in the distance map. Finally, different elements of the PN model, i.e., nodes, segments and segment points are obtained by processing the obtained single-voxel lines. Obviously,

PN models may consist of a number of graphs. Each graph is defined as a set of connected nodes, meaning that two graphs in the same PN model are never connected; they each represent a separate interconnected region of the total pore space. In this context, the so-called ‘main graph’ refers to the largest graph in the PNM, i.e., the graph with the largest number of nodes; the other graphs are termed ‘sub-graphs’ in this PhD Thesis.

1.3.1 **Application of X-ray Microscopy in Pore Network Modeling**

Recently, PN modeling has been applied in different areas to explore chemical and biological processes such as biomass growth^[193–195,216,217], CO₂ sequestration^[196–198,218,219], adsorption^[191,220–222] and catalysis. The application of PN modeling in catalysis started by using 2-D^[180,223–230] models. Gheorghiu et al.^[228] studied the influence of the pore network structure and pore size distribution on the yield of first order-reactions with diffusion limitation in heterogenous catalysts. Diffusion simulation based on different transport mechanisms such as molecular, Knudsen, and intermediate regimes were implemented using 2-D PN models with different geometries. It was found that the hierarchical pore network structure, non-uniform distribution of active sites, and broad pore size distribution are the key aspects for the optimization of networks for the majority of geometries. In another study, the effect of particle size, pore size distribution, average pore Damköhler number (a measure of relative strength of reactivity to diffusivity), and macro to nano pore size ratio on the net reaction rate was investigated based on the bi-disperse hierarchical 2-D PN model^[180]. They assumed that the reaction only takes place in nanopores and reactive sites are not present in macro-pores. The reactive transport simulation within the PN model showed that increasing of the macro-porosity does not necessarily lead to a better catalyst activity (net reaction rate) depending on the Damköhler number. For instance, increasing the macro-porosity helps the transport of the diffusive species while it decreases the number of active sites in the pore network at the same time. Therefore, depending on the strength of diffusivity compared to the reactivity (defined by Damköhler number), the activity of the catalyst can change. Moreover, it was shown that PN models with lower pore size ratio (the

average diameter of macro pores to the average diameter of nano pores) display higher kinetical activity.

The effect of the PN model structure on the deactivation of a catalyst by coke deposition during propane dehydrogenation was also studied^[229]. It was shown that catalysts that included large pores with a high degree of interconnectivity and narrow pore size distributions are more prone to the coking deactivation mechanism. All these geometrical optimizations of the pore network and their effects on catalytic reaction performance can lead to maximization of the catalyst yield via an optimized design of these porous catalysts. More recently, due to the more intense use and development of high-resolution imaging techniques such as scanning electron microscopy (SEM)^[231], holotomography^[130], TXM^[232] and focused ion beam scanning electron microscopy (FIB-SEM)^[233] tomography, PN modeling was expanded to generate models and structures based on the imaged, that is, original topology and morphology of the catalyst particle rather than using artificial regular or irregular networks as in previous studies. El-Nafaty et al.^[231] used 2-D SEM images of an FCC catalyst particle to obtain an approximate pore morphology and generate an equivalent 2-D 30×30 pseudo-random PN model to study the coke burn off during the catalytic cracking reaction. The experimental results of burning off coke performed using a micro-scale reaction unit was fairly in line with the simulation results. It was shown that the majority of the coke (more than 90%) was removed in the first half of the reaction time. However, the topology of the pore structure such as pore connectivity and tortuosity in their model did not exactly mimic the original catalyst pore structure properties. Therefore, more recently, advanced XRM techniques were used to image the whole pore space of the sample in 3-D at high spatial resolution and this information was then used to construct 3-D PN models^[31,171,234] which take into account the detailed morphological and topological features of the sample. For instance, El-Zehairy et al.^[234] used a direct mapping model to extracted a 3-D pore network representing the pore space of packed spheres made of uniform spherical glass beads with 50 mm diameter based on X-ray computed tomography (XCT). Also, FIB-SEM tomography was used to characterize the heterogeneity in the 3-D macro-pore

structure of a FCC catalyst particle and its correlation with mass transport properties based on PN modeling^[233].

1.4 Scope of the PhD Thesis

The scope of this PhD Thesis is to combine synchrotron-based X-ray microscopy techniques and pore network (PN) modeling to be able to characterize and explore different properties of a porous catalyst particle ranging from morphological and elemental information to mass transport properties.

In **Chapter 2**, a unique non-destructive characterization methodology, hard X-ray holotomography in differential contrast mode, was developed to study the 3-D distribution of a low Z element within a single catalyst particle. The fluid catalytic cracking (FCC) catalyst particle was used as an archetypical example for a hierarchically complex porous catalyst body. X-ray holotomography in combination with PN modeling enabled to reveal, identify, and assess the effects of carbon deposits within single catalyst bodies at the macro-pore scale. Furthermore, X-ray fluorescence (XRF) tomography data was recorded for the same catalyst particle to reveal spatial correlations between coke deposits and structurally and/or chemically different regions in a commercially used FCC catalyst.

In **Chapter 3**, X-ray holotomography was used this time to study the morphological heterogeneity within silica-supported ethylene polymerization catalysts at five distinct polymerization stages. Advanced analysis provided quantitative insights into porosity changes as well as 3-D distribution of support and polymer phases. Moreover, PN modeling was used to investigate the changes of the particles' interconnectivity, pore size distribution, and tortuosity during the pre-polymerization process. It was concluded that the heterogeneity in fragmentation behavior of particles can be connected to their respective unique pore space and support framework.

In **Chapter 4**, correlative X-ray ptychography and XRF was used to image 434 ethylene polymerized Ziegler-type catalyst particles at high 3-D spatial resolution (estimated as 74 nm). Advanced image processing and data analysis enabled not only to investigate the heterogeneity in fragmentation behavior of

the ensemble at the same stage of polymerization, but also to quantify the degree of fragmentation for each individual particle. This quantification also allowed identifying the dominant fragmentation mechanism that takes place during catalyst pre-polymerization.

In **Chapter 5**, correlative X-ray ptychography and XRF tomography was used to generate a PN model of an aged FCC particle. As in Chapter 2, correlated 3-D XRF data was used to identify regions of highest catalytic activity via the lanthanum distribution that is a marker for rare-earth exchanged ultra-stable Y zeolites in the particle. The PN structure was then used to simulate the diffusion of tracer and reactant molecules into the pore space of the catalyst particle. The reactant molecules react at the zeolite domains to generate products which diffuse out of the particle. A first-of-its-kind analysis of the mass transport properties of a single whole FCC E-cat particle within its real pore-space was used as a methodology to characterize the catalyst pore structure and to quantify the accessibility of the active sites at a single particle basis.

In **Chapter 6**, a summary and concluding remarks of this PhD Thesis was provided. Also, an outlook regarding possible future developments in the application of X-ray microscopy techniques as well as complimentary simulations for better understanding of porous catalyst particle characteristics was explained.

1.5 References

- [1] J. C. Védrine, in *Met. Oxides Heterog. Catal.*, Elsevier, Amsterdam **2018**, pp. 551–569.
- [2] E. T. C. Vogt, B. M. Weckhuysen, *Chem. Soc. Rev.* **2015**, *44*, 7342–7370.
- [3] G. Ertl, H. Knözinger, F. Schüth, and J. Weitkamp (Eds.), *Handbook of Heterogeneous Catalysis (2nd ed.)*, Wiley-VCH, Weinheim, **2008**.
- [4] S. L. Wong, N. Ngadi, T. A. T. Abdullah, I. M. Inuwa, *Renew. Sustain. Energy Rev.* **2015**, *50*, 1167–1180.
- [5] G. Lopez, M. Artetxe, M. Amutio, J. Bilbao, M. Olazar, *Renew. Sustain. Energy Rev.* **2017**, *73*, 346–368.
- [6] Y. Wang, Y. Cao, J. Li, *Renew. Energy* **2018**, *124*, 34–39.
- [7] R. Sadeghbeigi, *Fluid Catalytic Cracking Handbook*, Elsevier, Amsterdam, **2012**.
- [8] F. Meirer, B. M. Weckhuysen, *Nat. Rev. Mater.* **2018**, *3*, 324–340.
- [9] C. Perego, R. Millinib, *Chem. Soc. Rev.* **2013**, *42*, 3956–3976.
- [10] M. Nič, J. Jirát, B. Košata, A. Jenkins, A. McNaught, Eds., *IUPAC Compendium of Chemical Terminology*, IUPAC, Research Triangle Park, **2009**.
- [11] I. Union, O. F. Pure, A. Chemistry, J. Rouquerol, D. Avnir, C. W. Fairbridge, D. H. Everett, J. M. Haynes, N. Pernicone, J. D. F. Ramsay, K. S. W. Sing, K. K. Unger, I. Union, O. F. Pure, A. Chemistry, J. Rouquerol, D. Avnir, C. W. Fairbridge, D. H. Everett, J. M. Haynes, N. Pernicone, J. D. F. Ramsay, K. S. W. Sing, K. K. Unger, *Pure Appl. Chem.* **1994**, *66*, 1739–1758.
- [12] H. S. C. Cerqueira, G. Caeiro, L. Costa, F. Ramõa Ribeiro, *J. Mol. Catal. A Chem.* **2008**, *292*, 1–13.
- [13] C. E. Snape, B. J. McGhee, J. M. Andresen, R. Hughes, C. L. Koon, G. Hutchings, *Appl. Catal. A Gen.* **1995**, *129*, 125–132.
- [14] H. S. Cerqueira, C. Sievers, G. Joly, P. Magnoux, J. A. Lercher, *Ind. Eng. Chem. Res.* **2005**, *44*, 2069–2077.
- [15] A. M. Wise, J. N. Weker, S. Kalirai, M. Farmand, D. A. Shapiro, F. Meirer, B. M. Weckhuysen, *ACS Catal.* **2016**, *6*, 2178–2181.
- [16] J. McMillan, F. Shaffer, B. Gopalan, J. W. Chew, C. Hrenya, R. Hays, S. B. R. Karri, R. Cocco, *Chem. Eng. Sci.* **2013**, *100*, 39–51.
- [17] S. Kalirai, U. Boesenberg, G. Falkenberg, F. Meirer, B. M. Weckhuysen, *ChemCatChem* **2015**, *7*, 3674–3682.
- [18] F. Meirer, S. Kalirai, J. N. Weker, Y. Liu, J. C. Andrews, B. M. Weckhuysen, *Chem. Commun.* **2015**, *51*, 8097–8100.
- [19] J. Ihli, R. R. Jacob, M. Holler, M. Guizar-Sicairos, A. Diaz, J. C. da Silva, D. Ferreira Sanchez, F. Krumeich, D. Grolimund, M. Taddei, W. C. Cheng, Y. Shu, A. Menzel, J. A. van Bokhoven, *Nat. Commun.* **2017**, *8*, 809.
- [20] D. R. R. Rainer, E. Rautiainen, P. Imhof, *Appl. Catal. A Gen.* **2003**, *249*, 69–80.
- [21] A. C. Psarras, E. F. Iliopoulou, L. Nalbandian, A. A. Lappas, C. Pouwels, *Catal. Today* **2007**, *127*, 44–53.
- [22] G. Yaluris, W.-C. Cheng, M. Peters, L. T. McDowell, L. Hunt, in *Stud. Surf. Sci. Catal.*, **2004**, pp. 139–163.
- [23] Z. Yuxia, D. Quansheng, L. Wei, T. Liwen, L. Jun, in *Stud. Surf. Sci. Catal.*, **2007**, pp. 201–212.
- [24] E. Rautiainen, B. Nelissen, *Hydrocarb. Eng.* **2003**, *8*, 41–47.
- [25] J. Scherzer, R. E. Ritter, *Ind. Eng. Chem. Prod. Res. Dev.* **1978**, *17*, 219–223.
- [26] O. Bayraktar, E. L. Kugler, *Catal. Lett.* **2003**, *90*, 155–160.
- [27] W. S. Wieland, D. Chung, *Hydrocarb. Eng.* **2002**, *7*, 55–65.
- [28] Y. Mathieu, A. Corma, M. Echard, M. Bories, *Appl. Catal. A Gen.* **2014**, *469*, 451–465.
- [29] S. Kalirai, P. P. Paalanen, J. Wang, F. Meirer, B. M. Weckhuysen, *Angew. Chem. Int. Ed.* **2016**, *55*, 11134–11138.
- [30] F. Meirer, S. Kalirai, D. Morris, S. Soparawalla, Y. Liu, G. Mesu, J. C. Andrews, B. M. Weckhuysen, *Sci. Adv.* **2015**, *1(3)*, e1400199.
- [31] Y. Liu, F. Meirer, C. M. Krest, S. Webb, B. M. Weckhuysen, *Nat. Commun.* **2016**, *7*, 12634.
- [32] S. R. Bare, M. E. Charochak, S. D. Kelly, B. Lai, J. Wang, Y. C. K. Chen-Wiegart, *ChemCatChem* **2014**, *6*, n/a-n/a.
- [33] J. Ihli, D. Ferreira Sanchez, R. R. Jacob, V. Cuartero, O. Mathon, F. Krumeich, C. Borca, T. Huthwelker, W.-C. Cheng, Y. Shu, S. Pascarelli, D. Grolimund, A. Menzel, J. A. van Bokhoven, *Angew. Chem. Int. Ed.* **2017**, *56*, 14031–14035.
- [34] J. García-Martínez, K. Li, G. Krishnaiah, *Chem. Commun.* **2012**, *48*, 11841–11843.
- [35] J. O. Barth, A. Jentys, J. A. Lercher, *Ind. Eng. Chem. Res.* **2004**, *43*, 3097–3104.
- [36] K. Qian, D. C. ToMczak, E. F. Rakiewicz, R. H. Harding, G. Yaluris, Cheng, X. Zhao, A. W. Peters, *Energy & Fuels* **1997**, *11*, 596–601.
- [37] A. Fonseca, P. Zeuthen, J. B. Nagy, *Fuel* **1995**, *74*, 1267–1276.
- [38] A. Fonseca, P. Zeuthen, J. B. Nagy, *Fuel* **1996**, *75*, 1413–1423.
- [39] A. Fonseca, P. Zeuthen, J. B. Nagy, *Fuel* **1996**, *75*, 1363–1376.
- [40] B. G. Anderson, R. A. Van Santen, L. J. Van Ijzendoorn, *Appl. Catal. A Gen.* **1997**, *160*, 125–138.
- [41] N.-K. Bär, F. Bauer, D. M. Ruthven, B. J. Balcom, *J. Catal.* **2002**, *208*, 224–228.
- [42] M. Guisnet, P. Magnoux, *Appl. Catal.* **1989**, *54*, 1–27.
- [43] P. Gallezot, C. Leclercq, J. Barbier, P. Marecot, *J. Catal.* **1989**, *116*, 164–170.

- [44] H. Shimada, M. Imamura, N. Matsubayashi, T. Saito, T. Tanaka, T. Hayakawa, S. Kure, *Top. Catal.* **2000**, *10*, 265–271.
- [45] M. A. Smith, R. F. Lobo, *Microporous Mesoporous Mater.* **2006**, *92*, 81–93.
- [46] S. M. Davis, Y. Zhou, M. A. Freeman, D. A. Fischer, G. M. Meitzner, J. L. Gland, *J. Catal.* **1993**, *139*, 322–325.
- [47] J. O. Barth, A. Jentys, J. A. Lercher, *Ind. Eng. Chem. Res.* **2004**, *43*, 2368–2375.
- [48] O. Bayraktar, E. L. Kugler, *Appl. Catal. A Gen.* **2002**, *233*, 197–213.
- [49] S. Haitao, D. Zhijian, Z. Yuxia, T. Huiping, *Catal. Commun.* **2011**, *16*, 70–74.
- [50] M. A. den Hollander, M. Makkee, J. A. Moulijn, *Catal. Today* **1998**, *46*, 27–35.
- [51] Y. Schuurman, C. Delattre, I. Pitault, J. P. Reymond, M. Forissier, *Chem. Eng. Sci.* **2005**, *60*, 1007–1017.
- [52] D. A. Jacobs, G. C. Smith, R. D. Vis, A. F. H. Wielers, *J. Catal.* **1998**, *176*, 387–394.
- [53] D. Mance, J. Van der Zwan, M. E. Z. Velthoen, F. Meirer, B. M. Weckhuysen, M. Baldus, E. T. C. Vogt, *Chem. Commun.* **2017**, *53*, 3933–3936.
- [54] J. A. Moulijn, A. E. Van Diepen, F. Kapteijn, *Appl. Catal. A Gen.* **2001**, *212*, 3–16.
- [55] B. R. Mitchell, *Ind. Eng. Chem. Prod. Res. Dev.* **1980**, *19*, 209–213.
- [56] E. L. Kugler, D. P. Leta, *J. Catal.* **1988**, *109*, 387–395.
- [57] J. M. Whitcombe, I. E. Agranovski, R. D. Braddock, *Part. Part. Syst. Charact.* **2006**, *22*, 268–275.
- [58] R. E. Ritter, L. Rheume, W. A. Welsh, J. S. Magee, *July* **1981**, *6*, 103–110.
- [59] S. Järas, *Appl. Catal.* **1982**, *2*, 207–218.
- [60] G. L. Woolery, A. A. Chin, G. W. Kirker, A. Huss, ACS Publications, **1988**, pp. 215–228.
- [61] T. Masudat, M. Ogata, R. Tsurumi, A. Sugimoto, S. Yoshida, Y. Nishimura, *J. Japan Pet. Inst.* **1988**, *31*, 363–367.
- [62] Y. Nishimura, T. Masuda, G. Sato, S. Egashira, *Prepr. Symp.* **1983**, *28*, 707–716.
- [63] U. J. Etim, B. Xu, P. Bai, R. Ullah, F. Subhan, Z. Yan, *J. Energy Chem.* **2016**, *25*, 667–676.
- [64] Z. Liu, Z. Zhang, P. Liu, J. Zhai, C. Yang, *J. Nanotechnol.* **2015**, *2015*, 1–6.
- [65] W. Kaminsky, *Polyolefins: 50 Years after Ziegler and Natta I: Polyethylene and Polypropylene*, Springer, Berlin, **2013**.
- [66] M. Gahleitner, J. R. Severn, *Designing Polymer Properties. In: Tailor-Made Polymers Via Immobilization of Alpha-Olefin Polymerization Catalysts*, Wiley-VCH, Weinheim, **2008**.
- [67] Europe P. Plastic - the Facts 2020, *PlasticEurope* **2020**, *12*.
- [68] A. Gandini, T. M. Lacerda, *Prog. Polym. Sci.* **2015**, *48*, 1–39.
- [69] P. Galli, G. Vecellio, *Polyolefins: The Most Promising Large-Volume Materials for the 21st Century*, **2004**.
- [70] T. J. Pullukat, R. E. Patterson, *Porous Silica in Transition Metal Polymerization Catalysts. In: Handbook of Transition Metal Polymerization Catalysts*, John Wiley & Sons, New York, **2010**.
- [71] J. R. Severn, J. C. Chadwick, *Tailor-Made Polymers*, Wiley, **2008**.
- [72] D. W. Posch, in *Appl. Plast. Eng. Handb. Process. Mater. Appl. Second Ed.*, William Andrew Publishing, Braunau, **2017**, pp. 27–53.
- [73] R. Mülhaupt, *Macromol. Chem. Phys.* **2003**, *204*, 289–327.
- [74] K. Soga, T. Shiono, *Prog. Polym. Sci.* **1997**, *22*, 1503–1546.
- [75] M. A. Ferrero, M. G. Chiovetta, *Polym. Eng. Sci.* **1987**, *27*, 1436–1447.
- [76] L. Noristi, E. Marchetti, G. Baruzzi, P. Sgarzi, *J. Polym. Sci. Part A Polym. Chem.* **1994**, *32*, 3047–3059.
- [77] J. Hermans, P. Henriouille, *Process for the Preparation of a Ziegler-Natta Type Catalyst*, **1973**, US3769233A.
- [78] G. Natta, P. Corradini, G. Allegra, *J. Polym. Sci.* **1961**, *51*, 399–410.
- [79] B. L. Goodall, A. A. van der Nat, W. Sjardijn, *Olefin Polymerization Catalyst Compositions and a Process for the Polymerization of Olefins Employing Such Compositions*, **1983**, US4414132A.
- [80] T. Taniike, M. Terano, **2013**, pp. 81–97.
- [81] M. D’Amore, K. S. Thushara, A. Piovano, M. Causà, S. Bordiga, E. Groppo, *ACS Catal.* **2016**, *6*, 5786–5796.
- [82] G. Giunchi, G. Allegra, *J. Appl. Crystallogr.* **1984**, *17*, 172–178.
- [83] T. F. McKenna, J. B. P. Soares, *Chem. Eng. Sci.* **2001**, *56*, 3931–3949.
- [84] J. A. Fernandes, A.-L. Girard, in *Multimodal Polym. with Support. Catal.*, Springer International Publishing, Cham, **2019**, pp. 55–80.
- [85] J. R. Severn, in *Multimodal Polym. with Support. Catal.*, Springer International Publishing, Cham, **2019**, pp. 1–53.
- [86] E. Berger, J. L. Derroite, *US Pat. Appl. US3 901*, **1975**.
- [87] J. C. J. Bart, W. Roovers, *J. Mater. Sci.* **1995**, *30*, 2809–2820.
- [88] E. Gelus, *Eur. Pat. No. 0,703,246*, **2002**.
- [89] E. S. Gnanakumar, R. R. Gowda, S. Kunjir, T. G. Ajithkumar, P. R. Rajamohanam, D. Chakraborty, C. S. Gopinath, *ACS Catal.* **2013**, *3*, 303–311.
- [90] M. Matsuura, T. Fujita, *US Pat. No. 4,703,026*, **1987**.
- [91] T. J. Pullukat, R. E. Hoff, *Catal. Rev.* **1999**, *41*, 389–428.
- [92] B. Wang, *Coord. Chem. Rev.* **2006**, *250*, 242–258.
- [93] E. O. Fischer, W. Pfab, *Zeitschrift für Naturforsch. B* **1952**, *7*, 377–379.

- [94] G. Wilkinson, J. M. Birmingham, *J. Am. Chem. Soc.* **1954**, *76*, 4281–4284.
- [95] G. G. Hlatky, *Chem. Rev.* **2000**, *100*, 1347–1376.
- [96] W. Kaminsky, *Macromolecules* **2012**, *45*, 3289–3297.
- [97] G. G. Hlatky, *Coord. Chem. Rev.* **1999**, *181*, 243–296.
- [98] M. Gahleitner, L. Resconi, P. Doshev, *MRS Bull.* **2013**, *38*, 229–233.
- [99] J. T. M. Pater, G. Weickert, W. P. M. Van Swaaij, *J. Appl. Polym. Sci.* **2003**, *87*, 1421–1435.
- [100] T. Simonazzi, G. Cecchin, S. Mazzullo, *Prog. Polym. Sci.* **1991**, *16*, 303–329.
- [101] B. Horáčková, Z. Grof, J. Kosek, *Chem. Eng. Sci.* **2007**, *62*, 5264–5270.
- [102] T. F. L. McKenna, A. Di Martino, G. Weickert, J. B. P. Soares, *Macromol. React. Eng.* **2010**, *4*, 40–64.
- [103] R. Falcone, C. Jacobsen, J. Kirz, S. Marchesini, D. Shapiro, J. Spence, *Contemp. Phys.* **2011**, *52*, 293–318.
- [104] A. Bogner, P. H. Jouneau, G. Thollet, D. Basset, C. Gauthier, *Micron* **2007**, *38*, 390–401.
- [105] V. V. Lider, *Physics-Uspeski* **2017**, *60*, 187–203.
- [106] J. Kirz, C. Jacobsen, *J. Phys. Conf. Ser.* **2009**, *186*, 012001.
- [107] P. Kirkpatrick, A. V. Baez, *J. Opt. Soc. Am.* **1948**, *38*, 766.
- [108] H. Mimura, S. Handa, T. Kimura, H. Yumoto, D. Yamakawa, H. Yokoyama, S. Matsuyama, K. Inagaki, K. Yamamura, Y. Sano, K. Tamasaku, Y. Nishino, M. Yabashi, T. Ishikawa, K. Yamauchi, *Nat. Phys.* **2010**, *6*, 122–125.
- [109] C. Bussy, J. Cambedouzou, S. Lanone, E. Leccia, V. Heresanu, M. Pinault, M. Mayne-l’Hermite, N. Brun, C. Mory, M. Cotte, J. Doucet, J. Boczkowski, P. Launois, *Nano Lett.* **2008**, *8*, 2659–2663.
- [110] C. J. Fahmi, *Curr. Opin. Chem. Biol.* **2007**, *11*, 121–127.
- [111] C. Jacobsen, *X-Ray Microscopy*, Cambridge University Press, **2019**.
- [112] E. de Smit, I. Swart, J. F. Creemer, G. H. Hoveling, M. K. Gilles, T. Tyliczszak, P. J. Kooyman, H. W. Zandbergen, C. Morin, B. M. Weckhuysen, F. M. F. de Groot, *Nature* **2008**, *456*, 222–225.
- [113] F. Meirer, J. Cabana, Y. Liu, A. Mehta, J. C. Andrews, P. Pianetta, *J. Synchrotron Radiat.* **2011**, *18*, 773–781.
- [114] Y. Liu, F. Meirer, J. Wang, G. Requena, P. Williams, J. Nelson, A. Mehta, J. C. Andrews, P. Pianetta, *Anal. Bioanal. Chem.* **2012**, *404*, 1297–1301.
- [115] P. Sprenger, T. Sheppard, J.-P. Suuronen, A. Gaur, F. Benzi, J.-D. Grunwaldt, *Catalysts* **2018**, *8*, 356.
- [116] J. C. Andrews, S. Brennan, Y. Liu, P. Pianetta, E. A. C. Almeida, M. C. H. Van Der Meulen, Z. Wu, Z. Mester, L. Ouerdane, J. Gelb, M. Feser, J. Rudati, A. Tkachuk, W. Yun, in *J. Phys. Conf. Ser.*, **2009**, p. 012081.
- [117] H. Ade, H. Stoll, *Nat. Mater.* **2009**, *8*, 281–290.
- [118] J.-D. D. Grunwaldt, C. G. Schroer, *Chem. Soc. Rev.* **2010**, *39*, 4741.
- [119] Y. Takahashi, Y. Nishino, R. Tsutsumi, H. Kubo, H. Furukawa, H. Mimura, S. Matsuyama, N. Zetsu, E. Matsubara, T. Ishikawa, K. Yamauchi, *Phys. Rev. B* **2009**, *80*, 054103.
- [120] C. G. Schroer, P. Boye, J. M. Feldkamp, J. Patommel, A. Schropp, A. Schwab, S. Stephan, M. Burghammer, S. Schöder, C. Riekel, *Phys. Rev. Lett.* **2008**, *101*, 090801.
- [121] J. D. B. O’Sullivan, J. Behnsen, T. Starborg, A. S. MacDonald, A. T. Phythian-Adams, K. J. Else, S. M. Cruickshank, P. J. Withers, *Parasitology* **2018**, *145*, 848–854.
- [122] A. Momose, *J. Electron Microsc. (Tokyo)*. **2017**, *66*, 155–166.
- [123] A. Diaz, P. Trtik, M. Guizar-Sicairos, A. Menzel, P. Thibault, O. Bunk, *Phys. Rev. B* **2012**, *85*, 020104.
- [124] P. Cloetens, W. Ludwig, J. Baruchel, D. Van Dyck, J. Van Landuyt, J. P. Guigay, M. Schlenker, *Appl. Phys. Lett.* **1999**, *75*, 2912–2914.
- [125] D. GABOR, *Nature* **1948**, *161*, 777–778.
- [126] A.-L. Robisch, M. Eckermann, M. Töpperwien, F. van der Meer, C. Stadelmann-Nessler, T. Salditt, *J. Med. Imaging* **2020**, *7*, 1.
- [127] A. Khimchenko, C. Bikis, A. Pacureanu, S. E. Hieber, P. Thalmann, H. Deyhle, G. Schweighauser, J. Hench, S. Frank, M. Müller-Gerbl, G. Schulz, P. Cloetens, B. Müller, *Adv. Sci.* **2018**, *5*, 1700694.
- [128] T.-T. Nguyen, J. Villanova, Z. Su, R. Tucoulou, B. Fleutot, B. Delobel, C. Delacourt, A. Demortière, *Adv. Energy Mater.* **2021**, *11*, 2003529.
- [129] Y. Cheng, H. Suhonen, L. Helfen, J. Li, F. Xu, M. Grunze, P. A. Levkin, T. Baumbach, *Soft Matter* **2014**, *10*, 2982–2990.
- [130] M. Veselý, R. Valadian, L. M. Lohse, M. Toepferwien, K. Spiers, J. Garvoet, E. T. C. Vogt, T. Salditt, B. M. Weckhuysen, F. Meirer, *ChemCatChem* **2021**, *13*, 2494–2507.
- [131] T. Nano-imaging, *Enhancement of the X-Ray Nano-Holography Protocol*, **2017**.
- [132] D. Paganin, *Coherent X-Ray Optics*, Oxford Series On Synchrotron Radiation, Oxford University Press, Newyork, **2006**.
- [133] K. Giewekemeyer, S. P. Krüger, S. Kalbfleisch, M. Bartels, C. Beta, T. Salditt, *Phys. Rev. A* **2011**, *83*, 023804.
- [134] J. Hagemann, A.-L. Robisch, D. R. Luke, C. Homann, T. Hohage, P. Cloetens, H. Suhonen, T. Salditt, *Opt. Express* **2014**, *22*, 11552.
- [135] J. Hagemann, M. Töpperwien, T. Salditt, *Appl. Phys. Lett.* **2018**, *113*, 041109.
- [136] R. W. Gerchberg, W. O. Saxton, *Optic* **1972**, *35*, 237–246.
- [137] J. Hagemann, T. Salditt, *Opt. Express* **2017**, *25*, 20953.
- [138] A.-L. Robisch, K. Kröger, A. Rack, T. Salditt, *New J. Phys.* **2015**, *17*, 073033.

- [139] M. Stockmar, P. Cloetens, I. Zanette, B. Enders, M. Dierolf, F. Pfeiffer, P. Thibault, *Sci. Rep.* **2013**, *3*, 1927.
- [140] R. Gordon, R. Bender, G. T. Herman, *J. Theor. Biol.* **1970**, *29*, 471–481.
- [141] G. Cardone, K. Grünewald, A. C. Steven, *J. Struct. Biol.* **2005**, *151*, 117–129.
- [142] M. Holler, A. Diaz, M. Guizar-Sicairos, P. Karvinen, E. Färm, E. Härkönen, M. Ritala, A. Menzel, J. Raabe, O. Bunk, *Sci. Rep.* **2014**, *4*, 3857.
- [143] M. van Heel, M. Schatz, *J. Struct. Biol.* **2005**, *151*, 250–262.
- [144] R. Hegerl, W. Hoppe, *Berichte der Bunsengesellschaft für Phys. Chemie* **1970**, *74*, 1148–1154.
- [145] W. Hoppe, *Acta Crystallogr. Sect. A* **1969**, *25*, 495–501.
- [146] W. Hoppe, *Acta Crystallogr. Sect. A* **1969**, *25*, 508–514.
- [147] R. H. T. Bates, J. M. Rodenburg, *Ultramicroscopy* **1989**, *31*, 303–307.
- [148] H. N. Chapman, *Ultramicroscopy* **1996**, *66*, 153–172.
- [149] H. N. Chapman, *Scanning Microsc.* **1997**, *11*, 67–80.
- [150] H. N. Chapman, C. Jacobsen, S. Williams, *Rev. Sci. Instrum.* **1995**, *66*, 1332–1334.
- [151] J. R. Fienup, *Opt. Lett.* **1978**, *3*, 27.
- [152] C. Broennimann, E. F. Eikenberry, B. Henrich, R. Horisberger, G. Huelsen, E. Pohl, B. Schmitt, C. Schulze-Briese, M. Suzuki, T. Tomizaki, H. Toyokawa, A. Wagner, *J. Synchrotron Radiat.* **2006**, *13*, 120–130.
- [153] J. M. Rodenburg, A. C. Hurst, A. G. Cullis, B. R. Dobson, F. Pfeiffer, O. Bunk, C. David, K. Jefimovs, I. Johnson, *Phys. Rev. Lett.* **2007**, *98*, 034801.
- [154] P. Thibault, M. Dierolf, O. Bunk, A. Menzel, F. Pfeiffer, *Ultramicroscopy* **2009**, *109*, 338–343.
- [155] A. Schropp, P. Boye, J. M. Feldkamp, R. Hoppe, J. Patommel, D. Samberg, S. Stephan, K. Giewekemeyer, R. N. Wilke, T. Salditt, J. Gulden, A. P. Mancuso, I. A. Vartanyants, E. Weckert, S. Schöder, M. Burghammer, C. G. Schroer, *Appl. Phys. Lett.* **2010**, *96*, 091102.
- [156] C. M. Kewish, P. Thibault, M. Dierolf, O. Bunk, A. Menzel, J. Vila-Comamala, K. Jefimovs, F. Pfeiffer, *Ultramicroscopy* **2010**, *110*, 325–329.
- [157] M. Guizar-Sicairos, A. Diaz, M. Holler, M. S. Lucas, A. Menzel, R. A. Wepf, O. Bunk, *Opt. Express* **2011**, *19*, 21345.
- [158] K. Yamauchi, H. Mimura, T. Kimura, H. Yumoto, S. Handa, S. Matsuyama, K. Arima, Y. Sano, K. Yamamura, K. Inagaki, H. Nakamori, J. Kim, K. Tamasaku, Y. Nishino, M. Yabashi, T. Ishikawa, *J. Phys. Condens. Matter* **2011**, *23*, 394206.
- [159] F. Pfeiffer, *Nat. Photonics* **2018**, *12*, 9–17.
- [160] H. M. L. Faulkner, J. M. Rodenburg, *Phys. Rev. Lett.* **2004**, *93*, 023903.
- [161] J. M. Rodenburg, H. M. L. Faulkner, *Appl. Phys. Lett.* **2004**, *85*, 4795–4797.
- [162] P. Thibault, M. Dierolf, A. Menzel, O. Bunk, C. David, F. Pfeiffer, *Science* **2008**, *321*, 379–382.
- [163] K. W. Bossers, R. Valadian, S. Zanoni, R. Smeets, N. Friederichs, J. Garrevoet, F. Meirer, B. M. Weckhuysen, *J. Am. Chem. Soc.* **2020**, *142*, 3691–3695.
- [164] J. N. Clark, X. Huang, R. Harder, I. K. Robinson, *Nat. Commun.* **2012**, *3*, 993.
- [165] M. Dierolf, A. Menzel, P. Thibault, P. Schneider, C. M. Kewish, R. Wepf, O. Bunk, F. Pfeiffer, *Nature* **2010**, *467*, 436–439.
- [166] M. Kammerer, M. Weigand, M. Curcic, M. Noske, M. Sproll, A. Vansteenkiste, B. Van Waeyenberge, H. Stoll, G. Woltersdorf, C. H. Back, G. Schuetz, *Nat. Commun.* **2011**, *2*, 279.
- [167] S. Huotari, T. Pylkkänen, R. Verbeni, G. Monaco, K. Hämäläinen, *Nat. Mater.* **2011**, *29*.
- [168] B. J. Schultz, C. J. Patridge, V. Lee, C. Jaye, P. S. Lysaght, C. Smith, J. Barnett, D. A. Fischer, D. Prendergast, S. Banerjee, *Nat. Commun.* **2011**, *2*, 372.
- [169] B. A. Collins, J. E. Cochran, H. Yan, E. Gann, C. Hub, R. Fink, C. Wang, T. Schuettfort, C. R. McNeill, M. L. Chabiny, H. Ade, *Nat. Mater.* **2012**, *11*, 536–543.
- [170] M. Holt, R. Harder, R. Winarski, V. Rose, *Annu. Rev. Mater. Res.* **2013**, *43*, 183–211.
- [171] F. Meirer, D. T. Morris, S. Kalirai, Y. Liu, J. C. Andrews, B. M. Weckhuysen, *J. Am. Chem. Soc.* **2015**, *137*, 102–105.
- [172] P. Kočí, F. Štěpánek, M. Kubiček, M. Marek, *Chem. Eng. Sci.* **2007**, *62*, 5380–5385.
- [173] N. Hansen, R. Krishna, J. M. van Baten, A. T. Bell, F. J. Keil, *J. Phys. Chem. C* **2009**, *113*, 235–246.
- [174] H. Li, M. Ye, Z. Liu, *Chem. Eng. Sci.* **2016**, *147*, 1–12.
- [175] V. Novák, P. Kočí, M. Marek, F. Štěpánek, P. Blanco-García, G. Jones, *Catal. Today* **2012**, *188*, 62–69.
- [176] M. Chabanon, B. David, B. Goyeau, *Phys. Rev. E* **2015**, *92*, 023201.
- [177] V. Joekar-Niasar, S. M. Hassanizadeh, *Crit. Rev. Environ. Sci. Technol.* **2012**, *42*, 1895–1976.
- [178] A. A. El-Zehairy, M. W. Lubczynski, J. Gurwin, *Hydrogeol. J.* **2018**, *26*, 109–132.
- [179] R. Hill, *J. Mech. Phys. Solids* **1963**, *11*, 357–372.
- [180] M. A. Sadeghi, M. Aghighi, J. Barralet, J. T. Gostick, *Chem. Eng. J.* **2017**, *330*, 1002–1011.
- [181] U. C. Bandara, A. M. Tartakovsky, M. Oostrom, B. J. Palmer, J. Grate, C. Zhang, *Adv. Water Resour.* **2013**, *62*, 356–369.
- [182] H. A. Akhlaghi Amiri, A. A. Hamouda, *Int. J. Multiph. Flow* **2013**, *52*, 22–34.
- [183] D. Wilkinson, *Phys. Rev. A* **1984**, *30*, 520–531.
- [184] A. Q. Raeini, M. J. Blunt, B. Bijeljic, *J. Comput. Phys.* **2012**, *231*, 5653–5668.

- [185] B. Bijeljic, A. Raeini, P. Mostaghimi, M. J. Blunt, *Phys. Rev. E* **2013**, *87*, 013011.
- [186] R. Aziz, V. Joekar-Niasar, P. Martinez-Ferrer, *Int. J. Multiph. Flow* **2018**, *109*, 51–62.
- [187] Y. Kuwata, K. Suga, *Int. J. Heat Fluid Flow* **2015**, *55*, 143–157.
- [188] B. Bijeljic, A. H. Muggeridge, M. J. Blunt, *Water Resour. Res.* **2004**, *40*, W11501.
- [189] V. Joekar Niasar, S. M. Hassanizadeh, L. J. Pyrak-Nolte, C. Berentsen, *Water Resour. Res.* **2009**, *45*, W02430.
- [190] I. Fatt, *Trans. AIME* **1956**, *207*, 144–181.
- [191] R. C. Acharya, S. E. A. T. M. Van der Zee, A. Leijnse, *Water Resour. Res.* **2005**, *41*, W02020.
- [192] A. Raoof, H. M. Nick, S. M. Hassanizadeh, C. J. Spiers, *Comput. Geosci.* **2013**, *61*, 160–174.
- [193] H. J. Dupin, P. K. Kitanidis, P. L. McCarty, *Water Resour. Res.* **2001**, *37*, 2965–2979.
- [194] M. Gharasoo, F. Centler, P. Regnier, H. Harms, M. Thullner, *Environ. Model. Softw.* **2012**, *30*, 102–114.
- [195] R. Rosenzweig, A. Furman, U. Shavit, *Vadose Zo. J.* **2013**, *12*, vzt2012.0079.
- [196] Q. Kang, P. C. Lichtner, H. S. Viswanathan, A. I. Abdel-Fattah, *Transp. Porous Media* **2010**, *82*, 197–213.
- [197] Y. Mehmani, T. Sun, M. T. Balhoff, P. Eichhubl, S. Bryant, *Transp. Porous Media* **2012**, *95*, 305–326.
- [198] C. Varloteaux, S. Békri, P. M. Adler, *Adv. Water Resour.* **2013**, *53*, 87–100.
- [199] A. Raoof, S. M. Hassanizadeh, *Transp. Porous Media* **2010**, *81*, 391–407.
- [200] H. Okabe, M. J. Blunt, *Phys. Rev. E* **2004**, *70*, 066135.
- [201] P. M. Adler, J.-F. Thovert, *Appl. Mech. Rev.* **1998**, *51*, 537–585.
- [202] S. Bryant, M. Blunt, *Phys. Rev. A* **1992**, *46*, 2004–2011.
- [203] S. L. Bryant, P. R. King, D. W. Mellor, *Transp. Porous Media* **1993**, *11*, 53–70.
- [204] S. L. Bryant, D. W. Mellor, C. A. Cade, *AIChE J.* **1993**, *39*, 387–396.
- [205] K. J. Dobson, S. B. Coban, S. A. McDonald, J. N. Walsh, R. C. Atwood, P. J. Withers, *Solid Earth* **2016**, *7*, 1059–1073.
- [206] M. Piri, M. J. Blunt, *Phys. Rev. E* **2005**, *71*, 026301.
- [207] D. Silin, T. Patzek, *Phys. A Stat. Mech. its Appl.* **2006**, *371*, 336–360.
- [208] A. S. Al-Kharusi, M. J. Blunt, *J. Pet. Sci. Eng.* **2007**, *56*, 219–231.
- [209] H. Dong, M. J. Blunt, *Phys. Rev. E* **2009**, *80*, 036307.
- [210] C. A. Baldwin, A. J. Sederman, M. D. Mantle, P. Alexander, L. F. Gladden, *J. Colloid Interface Sci.* **1996**, *181*, 79–92.
- [211] Z. R. Liang, C. P. Fernandes, F. S. Magnani, P. C. Philippi, *J. Pet. Sci. Eng.* **1998**, *21*, 273–283.
- [212] W. B. Lindquist, S.-M. Lee, D. A. Coker, K. W. Jones, P. Spanne, *J. Geophys. Res. Solid Earth* **1996**, *101*, 8297–8310.
- [213] S. Beucher, F. Meyer, in *Math. Morphol. Image Process.*, CRC Press, **2018**, pp. 433–481.
- [214] A. David, S. Vassilvitskii, D. Arthur, S. Vassilvitskii, in *Proc. Eighteenth Annu. ACM-SIAM Symp. Discret. Algorithms*, Society For Industrial And Applied Mathematics, **2007**, pp. 1027–1035.
- [215] N. Otsu, *IEEE Trans. Syst. Man. Cybern.* **1979**, *9*, 62–66.
- [216] B. J. Suchomel, B. M. Chen, M. B. Allen, *Transp. Porous Media* **1998**, *30*, 1–23.
- [217] D.-S. Kim, H. S. Fogler, *Biotechnol. Bioeng.* **2000**, *69*, 47–56.
- [218] D. Kim, C. A. Peters, W. B. Lindquist, *Water Resour. Res.* **2011**, *47*, W01505.
- [219] A. Raoof, S. M. Hassanizadeh, *Water Resour. Res.* **2012**, *48*, W01514.
- [220] L. Li, C. A. Peters, M. A. Celia, *Adv. Water Resour.* **2006**, *29*, 1351–1370.
- [221] A. Raoof, S. Majid Hassanizadeh, A. Leijnse, in *First Int. Conf. Front. Shallow Subsurf. Technol.*, European Association Of Geoscientists & Engineers, **2010**, cp-150-00026.
- [222] J. M. Köhne, S. Schlüter, H.-J. Vogel, *Vadose Zo. J.* **2011**, *10*, 1082–1096.
- [223] O. H. J. Muhammad, E. K. T. Kam, *Catal. Today* **1997**, *38*, 85–95.
- [224] R. Mann, U. A. El-Nafaty, *Stud. Surf. Sci. Catal.* **1996**, *100*, 355–364.
- [225] R. Mann, P. N. Sharratt, G. Thomson, *Chem. Eng. Sci.* **1986**, *41*, 711–718.
- [226] R. Mann, *Catal. Today* **1993**, *18*, 509–528.
- [227] U. A. El-Nafaty, R. Mann, *Chem. Eng. Sci.* **1999**, *54*, 3475–3484.
- [228] S. Gheorghiu, M.-O. Coppens, *AIChE J.* **2004**, *50*, 812–820.
- [229] G. Ye, H. Wang, X. Duan, Z. Sui, X. Zhou, M.-O. Coppens, W. Yuan, *AIChE J.* **2019**, *65*, 140–150.
- [230] M. P. Hollewand, L. F. Gladden, *Chem. Eng. Sci.* **1992**, *47*, 2757–2762.
- [231] U. A. El-Nafaty, R. Mann, *Chem. Eng. Sci.* **2001**, *56*, 865–872.
- [232] R. Mayorga-González, M. Rivera-Torrente, N. Nikolopoulos, K. W. Bossers, R. Valadian, J. Yus, B. Seoane, B. M. Weckhuysen, F. Meirer, *Chem. Sci.* **2021**, *12*, 8458–8467.
- [233] D. A. Matthijs De Winter, F. Meirer, B. M. Weckhuysen, *ACS Catal.* **2016**, *6*, 3158–3167.
- [234] A. El-Zehairy, M. Nezhad, V. Joekar-Niasar, I. Guymer, N. Kourra, M. A. Williams, *Adv. Water Resour.* **2019**, *131*, 103378.

2. **Characterization of Coke Deposition
within a Single Fluid Catalytic
Cracking Catalyst**

In this Chapter, catalyst deactivation which involves a complex interplay of processes taking place at different length and time scales is studied using X-ray nano tomography. Understanding this phenomenon is one of the grand challenges in solid catalyst characterization. A process contributing to deactivation is carbon deposition (coking), which reduces catalyst activity by limiting diffusion and blocking active sites. However, characterizing coke formation and its effects is challenging as it involves both the organic and inorganic phase of the catalytic process and length scales from the atomic scale to the scale of the catalyst body. This Chapter presents a combination of hard X-ray imaging techniques able to visualize in 3-D the distribution, effect, and nature of carbon deposits in the macro-pore space of an entire industrially used catalyst particle. The findings of this study provide direct evidence for coke promoting effects of metal poisons, pore clogging by coke, and a correlation between carbon nature and its location. These results provide a better understanding of the coking process, its relation to catalyst deactivation and new insights into the efficiency of the industrial scale process of fluid catalytic cracking.

This Chapter is based on: M. Veselý, R. Valadian, L. Merten Lohse, M. Toepperwien, K. Spiers, J. Garrevoet, E. T. C. Vogt, T. Salditt, B. M. Weckhuysen, F. Meirer, *ChemCatChem* **2021**, 13, 2494–2507.

2.1 Introduction

carbon deposits on catalysts are an unwanted side product of any chemical reaction where hydrocarbons react over heterogeneous catalysts. They can play different roles and are commonly reported to deactivate the catalyst by pore clogging or by covering the catalytically active site^[1–5]. These deposits consist of a mix of different hydrocarbon species, are commonly called ‘coke’, and have already been the topic of numerous experimental and theoretical investigations for decades. Various analytical methods have been used in the past to study carbon deposits in solid catalysts providing bulk information on species and origin of the coke accumulated during catalyst operation. Studies on industrial catalysts are less common; coke in industrial reforming, hydrotreating, or cracking catalysts was studied using solid-state carbon magic angle spinning nuclear magnetic resonance (¹³C-MAS-NMR)^[3,6–11], supercritical fluid extraction (SFE)^[3,7], electron paramagnetic resonance (EPR)^[12], near-edge X-ray absorption fine structure (NEXAFS)^[11,13], X-ray photoelectron spectroscopy (XPS)^[7,11], X-ray diffraction (XRD)^[14], matrix-assisted laser/desorption ionization time-of-flight mass spectrometry (MALDI-TOF-MS)^[6], temperature-programmed hydrogenation (TPH) and oxidation (TPO)^[11,15], Raman spectroscopy^[11,14], UV–vis microspectroscopy^[16], proton-induced X-ray emission (PIXE), and nuclear reaction analysis (NRA)^[17]. These techniques often rely on coke-containing samples from which the catalyst was leached (e.g., by dissolution in hydrofluoric acid^[4]) and provide either bulk information or 2-D data at a spatial resolution that is too low to study the relation of catalyst structure and composition on the one hand and coke on the other hand.

In order to reveal the prevailing deactivation mechanism and to quantify the deactivation effect, however, knowledge of the 3-D coke distribution at different length scales is crucial^[18]. At the smallest scale, atom probe tomography (APT) has been successfully used for studying the effect of carbon deposits at the length-scale of the active site^[19]. Electron microscopy (EM) can visualize carbon deposits on length-scales from the single crystal^[20–22] to the single catalyst particle^[23] in two dimensions or carbon-based compounds in three dimensions^[24,25]. Using soft X-ray scanning transmission

X-ray microscopy (STXM) carbon formation can be mapped at sub-micron resolution and in-situ revealing distribution and, if combined with NEXAFS, speciation of carbon deposits on a catalyst^[26]. Finally, confocal fluorescence microscopy (CFM) can visualize coke deposits in single crystals^[27] or industrial-grade catalyst bodies^[16,28] at micrometer resolution.

However, the volume that can be investigated by APT, EM, and soft X-ray STXM tomography is not sufficient to study a complete sub-millimeter catalyst body and CFM still offers limited spatial resolution and certainly limited information depth. Hard X-ray imaging techniques provide a similar spatial resolution as soft X-ray STXM^[29] but the highest information depth of all above mentioned techniques thus enabling 3-D studies of, for example, metal distribution in the macro-pores^[30] (pore sizes > 50 nm) of an entire catalyst body^[31–33] revealing the effect of those deposits on the catalyst's macro-pore space and accessibility. However, while this approach is very sensitive to metal deposits hard X-rays provide much weaker contrast for organic phases than soft X-rays because the energy dependent X-ray absorption is correlated with material density and atomic number (see Section 1.2).

Various coke deposits might cause different deactivation mechanisms and naturally vary in chemical nature. Based on product transient experiments^[34] two mechanisms of FCC catalyst deactivation due to coke deposition have been proposed. In the first mechanism, at low coke contents, the active site of the catalyst is covered by coke, which causes catalyst deactivation by preferential blocking of the strongest acid sites. In the second mechanism at high coke contents, pore-clogging causes reduced diffusion in micro-pores^[35] (pore sizes < 2 nm^[30]) hindering mass transport of products and feedstock, in turn reducing catalyst efficiency.

In tackling the challenge of visualizing weakly absorbing organic phases by hard X-rays, in this Chapter we used a unique characterization methodology to reveal, identify, and assess the effects of carbon deposits within single catalyst bodies at the macro-pore scale by using non-destructive, hard X-ray holotomography in differential contrast mode. We further combined this method with X-ray fluorescence (XRF) tomography data

recorded for the same catalyst particle to reveal spatial correlations between coke deposits and structurally and/or chemically different regions in a commercially used FCC catalyst particle that was used as an archetypical example for a hierarchically complex porous catalyst body.

The developed characterization methodology is summarized in Figure 2.1, which illustrates the complex workflow that integrates two synchrotron-radiation (SR) based X-ray holotomography experiments and one X-ray fluorescence (XRF) tomography performed at two different beamlines on the same sample. The imaged sample was a coked, used equilibrium catalyst (E-cat) catalyst particle of 60 μm in average diameter harvested from a batch taken from an industrial FCC unit. The sample was selected for its high coke content; by nature of the FCC process there is, on a single catalyst particle level, always inhomogeneity in the catalyst age, and thus the coke loading of individual catalyst particles. To ensure that the individual catalyst particle selected for this study was indeed a coked catalyst material, a particle was selected that appeared black in the optical microscope (Figure 2.1a, Section 2.4.1). This single coked catalyst particle was then imaged by X-ray holotomography using a 64 nm pixel size resulting in a 3-D representation of the sample's electron density that was segmented into pore space and solid matter (Section 2.4.3). After imaging the coked catalyst material, the particle was placed in an in-house developed chamber for calcination of individual catalyst particles (Section 2.4.2) and calcined in air for 4 h at 600 °C using a 5 °C/min ramp to ensure removal of all carbon deposits in the catalyst without damaging the internal structure or causing any phase changes in the catalyst. This was confirmed by complementary lab-based powder XRD measurements of the same catalyst batch before and after calcination (Section 2.4.12) and by conducting an additional experiment: an E-cat catalyst batch (the same batch from which the individual catalyst particle was retrieved) was calcined during a SR-based in-situ small- and wide-angle scattering measurement that was combined with a differential scanning calorimetry measurement (SAXS/WAXS/DSC) (see Section 2.4.13 for further details).

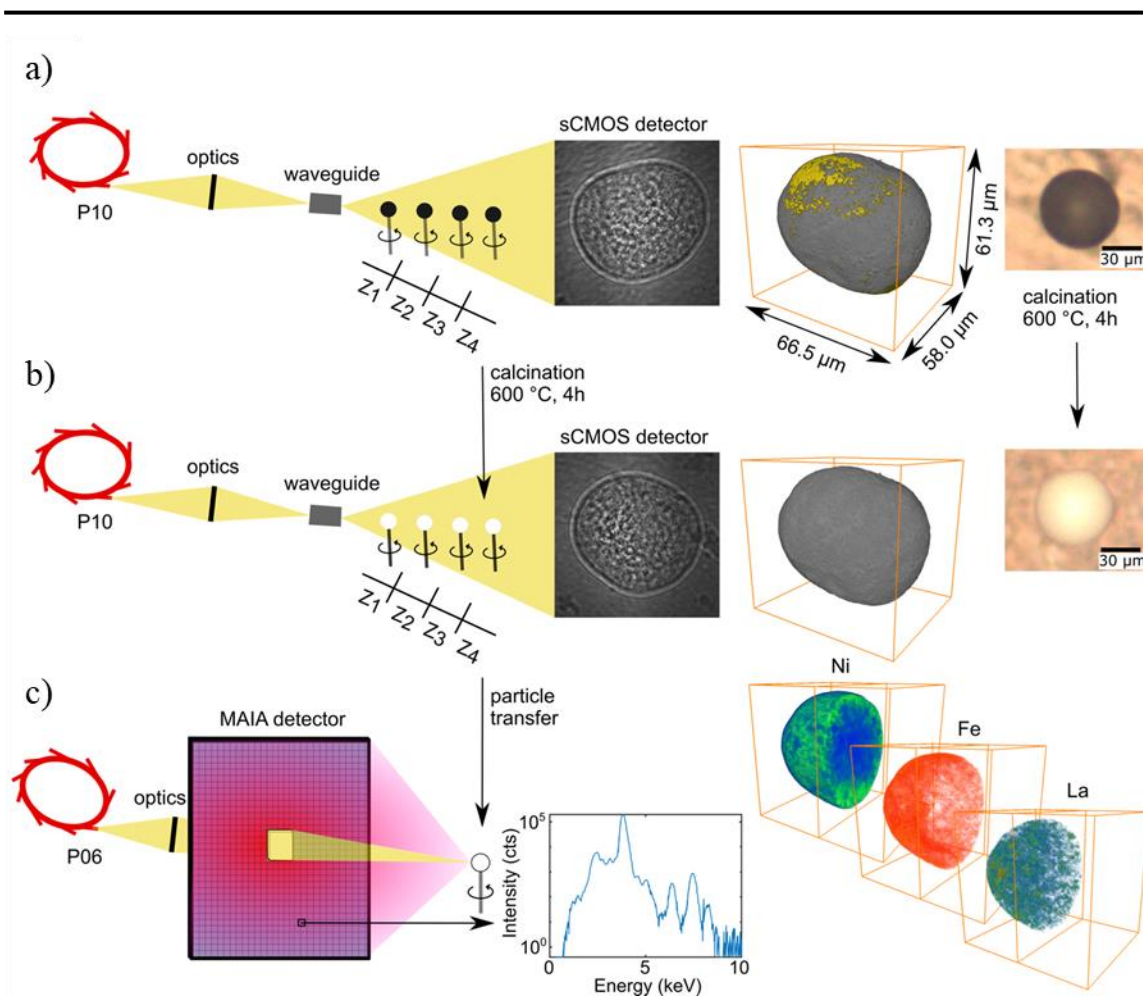


Figure 2.1 Experimental workflow and detection schemes. (a) In X-ray holotomography performed at beamline P10 of the PETRA III synchrotron, Kirkpatrick-Baez (KB) mirrors focus the X-ray beam generated by the synchrotron storage ring into a waveguide that creates a virtual point source with smoother illumination and smaller focus size, which is then used to image the FCC catalyst particle mounted on a carbon tip. Tomography was performed at four different distances between sample and a scintillator-based fiber-coupled sCMOS detector. (b) After the first measurement, the particle was calcined to burn off coke deposits. During this step, the particle color changed from black to white evidencing the removal of the carbon deposits on the surface, while no other morphological changes took place. The particle was then re-mounted and measured again at beamline P10. (c) After this second X-ray holotomography the catalyst was also imaged by X-ray fluorescence (XRF) tomography at the PETRA III beamline P06. The emitted XRF was detected by means of a MAIA detector and XRF spectra were fitted to quantify the relative concentrations of the detected elements in every single pixel and at each projection angle. In the final step the 3-D representations of the sample's electron density as well as the 3-D distribution of coke deposits (displayed as yellow surface deposits in (a)) had been reconstructed from X-ray holotomography, and the 3-D distribution of specific elements of interest was reconstructed from XRF tomography.

The results of this experiment confirmed stable crystallinity, pore broadening, and heat evolution during the calcination of the E-cat (Section 2.4.13). After a cooling phase (5 °C/min ramp) the calcined particle was

remounted and imaged again and the difference between the two X-ray holotomographies was used to obtain the 3-D coke distribution (Figure 2.2, Sections 2.4.5, 2.4.8, 2.4.9, 2.4.11).

Finally, these results were combined with data from XRF tomography ($200 \times 200 \times 200 \text{ nm}^3$ voxel size) recorded for the same calcined particle to investigate any spatial correlation between coke and specific metals present in the catalyst particle. Lanthanum stabilizes zeolite Y and is, in the brand of FCC catalyst particle used here, only present in the zeolite phase of the catalyst. It can therefore be used as a spectroscopic marker for this most active component, while iron and nickel are typical examples of poisoning metals, of which Ni is suspected to promote coke formation^[5].

Figure 2.2 shows all the above-mentioned data processing steps including differential contrast holotomography and its correlation with XRF tomography. It also emphasizes the nature of the differential contrast data, which is independent of the local phase of the catalyst. This means the carbon deposits in all solid phases (zeolite, aluminosilicate matrix, clay, iron, nickel) and pores contribute to the difference in image contrast.

Solid-state ^{13}C NMR^[3,12] methods previously distinguished two different carbon species, i.e., aromatic and aliphatic species, to be present in the E-cat FCC catalyst particle. This was confirmed by studying the effect of coke deposition during gas oil cracking (i.e., using a feedstock without carbon residue) and residue feedstock cracking (where the feedstock contained 4.3 wt.% of carbon residue)^[36]. While the coked catalyst that was used in gas oil cracking contained mainly aliphatic carbon, both aliphatic and aromatic carbon were found in the other case. The authors therefore suggested that catalytic cracking generates aliphatic carbon, while the main source of aromatic species is residual coke from the feedstock stream. However, these studies neither identified the spatial distribution of the carbon deposits within the catalyst particle (and therefore could not draw conclusions on their effect on e.g., the catalyst's pore space) nor considered the effect of poisoning metals. It is known that both nickel and vanadium are active in hydrogenation-dehydrogenation reactions^[5] and have therefore been suspected to increase coke selectivity^[37].

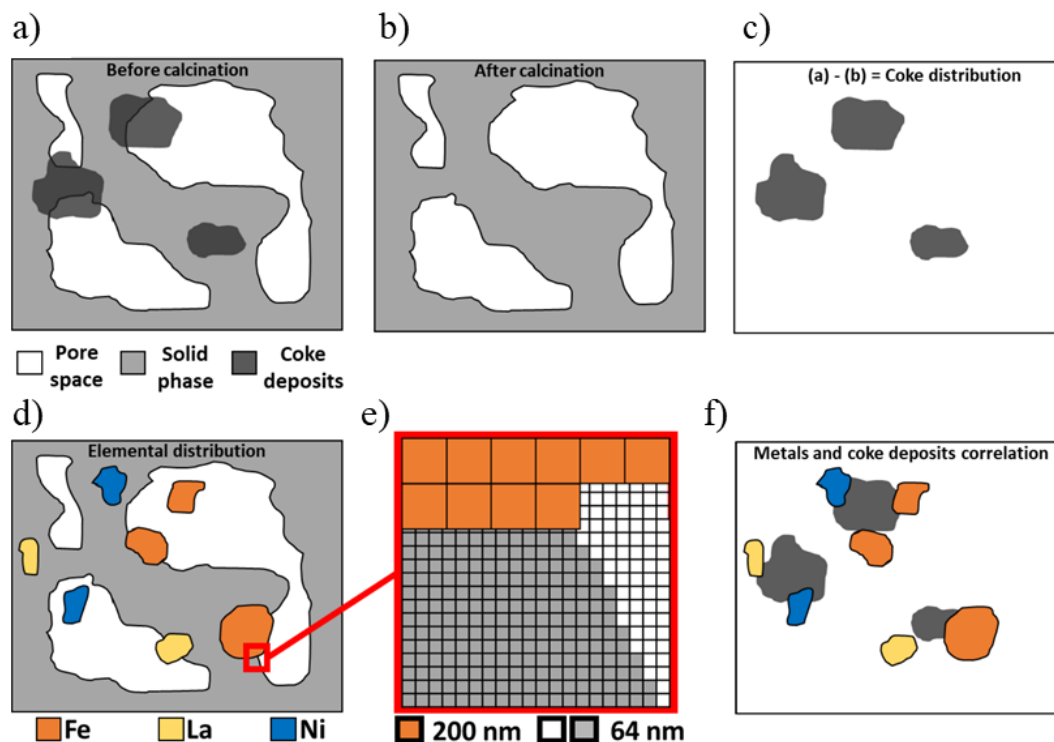


Figure 2.2 Schematic representation of the workflow of differential contrast X-ray holotomography combined with X-ray fluorescence (XRF) tomography. (a) Holotomography data before the calcination step. Here the coke deposits only contribute very little to the spatially resolved X-ray absorption resulting in very little contrast to resolve them (the contrast is artificially enhanced in the schematic for clarity). (b) X-ray holotomography data after the calcination step. These data are almost identical to (a) and show again the microstructure, but without the small absorption contribution of the carbon deposits. In (c), which is the difference image of the images (a) and (b) after registration, the spatial distribution of the carbon deposits is revealed. This method reveals carbon deposits in all solid phases of the catalyst as well as the pore space, that is, independent of their nature or location in the catalyst. Panel (d) displays a schematic overlay of holotomography data after the calcination step (b) and the corresponding metal distribution determined by XRF tomography. A zoom-in in (e) schematically depicts how these two data sets that have different voxel sizes ($200 \times 200 \times 200 \text{ nm}^3$ voxel size for XRF data and $64 \times 64 \times 64 \text{ nm}^3$ voxel size for holotomography data) have been registered. The difference in voxel size results in a smoother surface for carbon deposits and a rougher ('pixelated') surface for metals in the digital representation of the catalyst's microstructure. Panel (f) depicts how it was possible to study the spatial correlation between metals (from XRF tomography data) and carbon deposits (from X-ray holotomography data) in the FCC catalyst particle based on the complex registration of three independent 3-D tomography measurements of the same whole FCC catalyst particle.

The author is only aware of one spatially resolved coke study that identified carbon deposits in FCC catalysts not only on the particle surface used NRA line scans across particle cross-sections with a spatial resolution of several micrometers – that study revealed uniformly distributed carbon^[17]. In

a more recent study using NMR and EPR^[12], the authors determined an approximate location of aromatic and aliphatic carbon deposits in FCC catalyst particles. Aliphatic coke was deposited within the particle, while aromatic coke was found predominantly in the outer part of the particle close to a paramagnetic species, such as iron. However, NMR and EPR methods are not able to determine the 3-D spatial distribution of carbon deposits and their effect on the pore space inside a whole individual FCC catalyst particle, while the 3-D distribution of metal deposits has been studied previously at tens of nanometers precision^[38].

2.2 Results and Discussion

2.2.1 Accessibility and Interconnectivity of the Catalyst's Pore Network

The 3-D representation of the catalyst material obtained by X-ray holotomography was used to characterize the studied FCC catalyst particle using single particle metrics established previously^[31,39] (Figure 2.3, Section 2.4.16, Table 2.3, Table 2.4). The good agreement with earlier work^[31,38,39] confirms that a typical, i.e., representative, aged FCC catalyst particle was investigated and, in agreement with bulk XRD data and SR-based in-situ SAXS/WAXS/DSC measurements, the comparison of values before and after calcination confirms that no morphological changes other than coke removal took place (see Sections 2.4.12 and 2.4.13 for further details).

The removal of coke deposits is evident in the histograms of electron density recorded before and after calcination (Section 2.4.8). A small shift towards lower values of electron density is seen after calcination, which can only be caused by the removal of matter containing electrons. This is the basis for differential contrast holotomography that is, mapping the 3-D coke distribution as the difference between the two datasets. This also allowed segmenting the 3-D coke distribution into a set of voxels containing carbon deposits (Section 2.4.9). Next, the total amount of coke in the catalyst particle was estimated to 2.37 vol.% (1.68 wt.% assuming the density of graphite), a value that was very close to typically reported amounts (0.7 – 1.5 wt.%)^[5] for commercially used E-cat, and in excellent agreement with the 1.75 wt.%

previously reported for E-cat with high carbon content^[12], confirming the validity of our segmentation approach. This result was double checked and confirmed by performing simultaneous thermogravimetric and differential thermal analysis combined with mass spectrometry to determine the amount of coke in the catalyst batch the single particle was taken from (Section 2.4.15). The results showed that the total weight loss caused by carbon deposits was 1.38 wt.%. This confirms that the individual particle selected from this batch was one with a high coke content.

Having both a 3-D representation of macro-pore space and coke distribution (Figure 2.3a,b) allowed investigating the effect of carbon deposits on the macro-pore network of the catalyst as previously done for metal deposits^[31,40]. Two pore network models were constructed, one each for the non-calcined and calcined particle (see Sections 2.4.17 and 1.3 for further details). The majority of nodes (almost 90%) of both networks were found interconnected, that is, in one graph (the ‘main graph’), while other graphs (‘sub-graphs’) contained only few nodes covering just a small percentage of the particle’s pore network. The observation that the main graph covers almost the entire pore network of an FCC catalyst particle is in line with previous work^[31,41] and highlights the high degree of macro-pore interconnectivity. This interconnectivity is smaller before coke removal, as evidenced by the larger number of sub-graphs in the network of the coked particle (Figure 2.3c).

In order to assess the accessibility of the macro-pores depending on their location in the particle the percentage of accessible nodes as function of their Euclidean distance from the particle surface was determined (Figure 2.3d). The fraction of accessible nodes was higher for the calcined particle because the pore system became more interconnected and accessible.

The node accessibility in the network of the non-calcined particle further continuously decreased towards the particle center indicating that coke deposits throughout the catalyst incessantly blocked macro-pores and caused lower pore connectivity. A comparison of the bulk properties of both pore networks is reported in Figure 2.3e and Table 2.5.

Here an important advantage of our analytical approach and related data analysis should be emphasized: the small difference in the mean pore diameter (7.4 nm) is statistically significant, independent of a much larger isotropic voxel size of 64 nm – this fact is thoroughly discussed in other papers^[31,38]. Also, the values reported in Figure 2.3e, Table 2.3, and Table 2.5 are based on a statistical evaluation of the networks and they are not dependent on the isotropic voxel size. Thus the 3-D data allows pinpointing and visualizing the suggested pore clogging and path shortening for any specific macro-pore of the catalyst. As an example, Figure 2.4 reports the shortest paths between two arbitrarily chosen nodes (indicated by green and yellow circles) in both the calcined and non-calcined particle macro-pore networks highlighting the pore-clogging effect of coke.

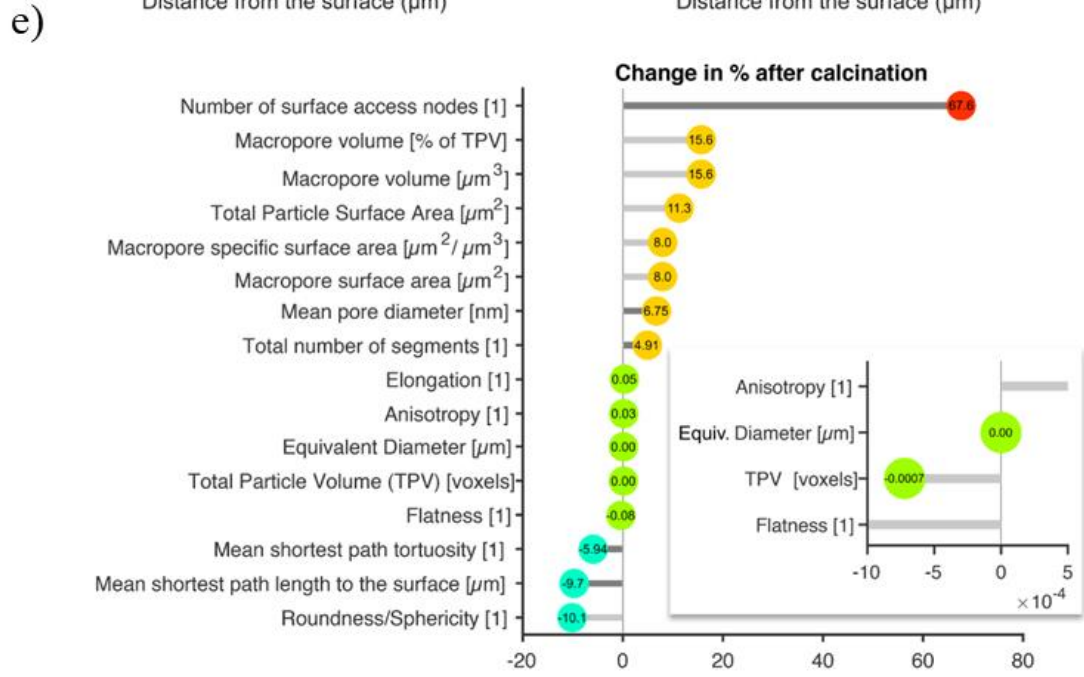
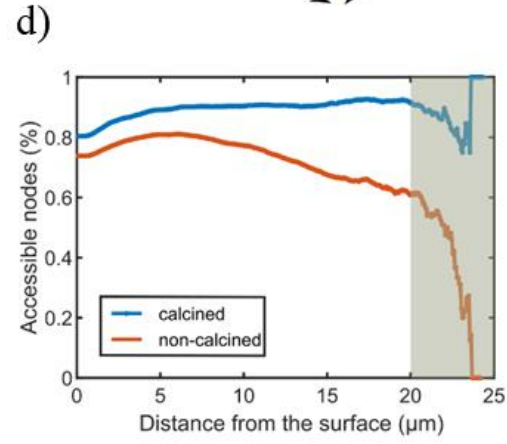
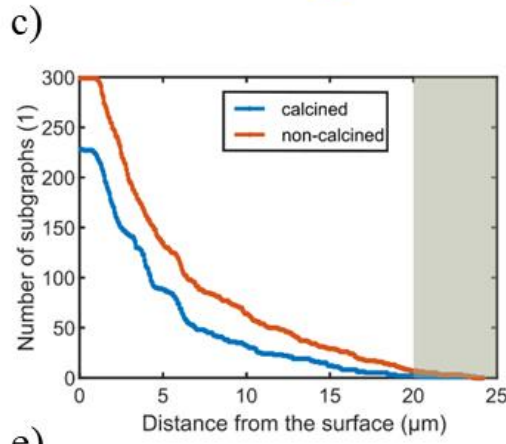
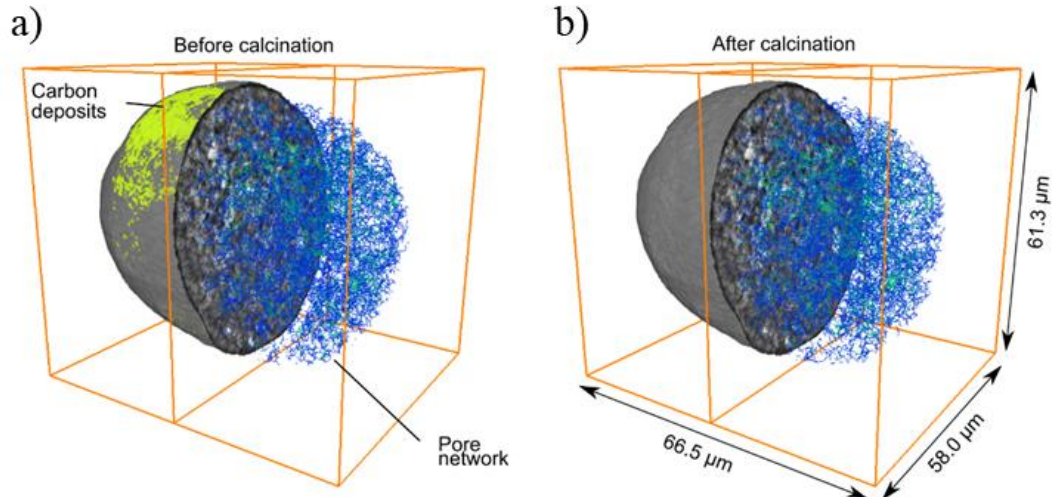


Figure 2.3 Effects of carbon deposits at the single catalyst particle level. (a,b) A virtual cut through the E-cat FCC particle before and after calcination as imaged by X-ray holotomography. The coke distribution is displayed in yellow-green. (c) The number of sub-graphs (isolated pore networks) of the pore network versus their distance from the particle surface shows that the largest number of sub-graphs was found within 2 μm from the surface, i.e., in the denser surface layer of FCC particles that contains more isolated cavities, especially in aged catalysts. Their number decreases towards the particle center, where porosity and pore connectivity increase, and the pore space is mainly represented by one large, interconnected network. The number of sub-graphs decreased after calcination of the particle, evidencing that coke deposits indeed block macro-pores and isolate small pore volumes. The grey region indicates the statistically insignificant region which is related to the small number of voxels these shells have that are close to the center of the particle. (d) The corresponding analysis of the accessibility of the nodes of the pore network as a function of their distance to the particle surface. (e) A comparison of single particle metrics (Section 2.4.16, Table 2.3) before and after calcination confirms that no morphological changes other than a clear increase in accessible pore volume and a very small reduction (2655 voxels or 0.0072 %) in the total particle volume took place indicating coke removal from the particle surface. Dark grey bars indicate values based on changes in the single particle pore network. Colors of circles indicate the changes of parameters after calcination, i.e., red shows a big increase, yellow shows a small increase, green shows no significant change, and cyan indicates a small decrease. All changes indicate how coke filled dips in the catalyst's surface, reduces accessibility via surface pore blockage and clogs macro-pores inside the particle. All reported values were established from the tomographic reconstruction of the single particle studied.

We also evaluated the limited mass transport ability caused by carbon deposits by determining the effective permeability of the sub-volume displayed in Figure 2.4 (for further details see also Section 2.4.19). Further details regarding the permeability simulation can be found elsewhere^[40].

The sub-volume's effective permeability increased from 132 nm^2 for the non-calcined particle to 162 nm^2 for the calcined catalyst particle, that is, the carbon deposits caused a 15.4% drop in the effective permeability. Moreover, the flow was found completely blocked along one axis. To visualize the effect of restricted mass transport in this sub-volume, the flow in the pore space along one principal axis is shown in Figure 2.4e (i.e., the non-calcined particle) and Figure 2.4f (i.e., the calcined particle). The shape and total number of streamlines demonstrate less restricted flow in the macro-pores of the calcined particle. The shape and total number of streamlines highlight a less restricted flow in the macro-pores of the calcined particle.

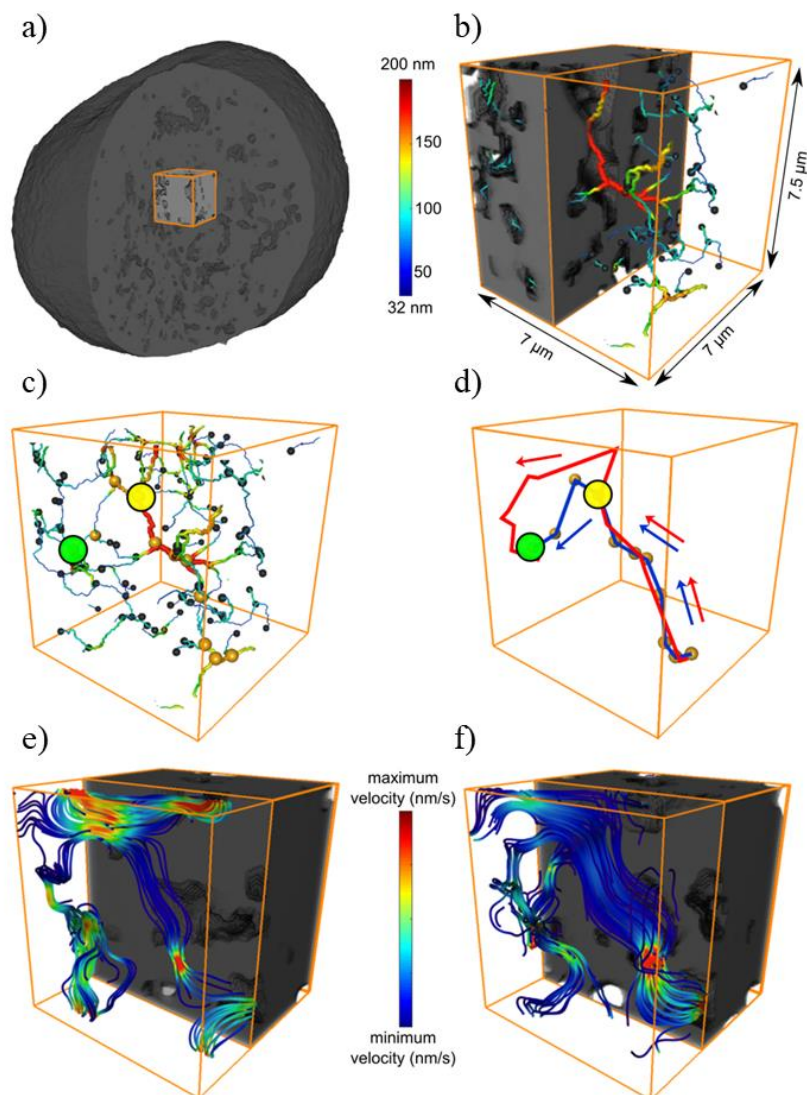


Figure 2.4 Pore blockage by carbon deposits within a catalyst particle. Specific example for pore narrowing and blockage inside the catalyst particle caused by the presence of carbon deposits. (a) Position of the sub-volume within the catalyst particle. (b) Zoom of the sub-volume displaying how the macro-pore volume is used to generate the pore network model with nodes (black spheres) and connecting segments. The color and thickness of the segments indicate the variation of the pore diameter in every point of the pore network (not drawn to scale). In (c) the gold spheres indicate a specific path through the network that starts in the lower right part of the displayed volume and connects the nodes indicated by the yellow and green circles. This path indicates the shortest path between these two nodes in the calcined particle. This shortest connection is again highlighted in (d) by the blue path, which is shorter than the shortest path between these two nodes in the non-calcined particle (red path). This exemplifies how a path between two nodes of the pore network can be blocked by carbon deposits but is freed up after calcination (blue path). Panels (e) and (f) visualize this effect of pore blockage via the simulated mass flux based on a permeability calculation for the sub-volume along the (vertical) x-axis. The number, distribution, and color of the streamlines (indicating normalized mass flow velocity) illustrate how mass flux is less restricted after coke removal in (f).

2.2.2 Correlation Between Electron Densities of Coke Deposits and Their Location

The example in Figure 2.4 shows that it was possible to identify individual coke deposits in a whole catalyst particle. The analysis of separable and localized deposits or ‘coke clusters’ (Section 2.4.11) showed that the largest clusters are mainly located on the surface of the catalyst particle with the exception of one big cluster that was found close to the center of the catalyst particle, while smaller clusters (below volumes of $3 \mu\text{m}^3$ or 10000 voxels) are distributed more homogeneously throughout the catalyst particle (Figure 2.15). Figure 2.5 shows a virtual cut through the particle indicating the individual carbon clusters located inside the catalyst particle (non-surface clusters shown in magenta) and at the surface (surface clusters shown in cyan). The separation also allowed inspecting the electron density values of surface and non-surface coke deposits reported as probability density functions for both types of coke (Figure 2.16). A clear increase of electron density in surface clusters shows the denser coke deposits at the surface of the particle. This observation of electron-denser carbon species being closer to the surface becomes obvious when plotting the mean electron density of the coke clusters as a function of distance to the particle surface (Figure 2.5c), which shows three distinct regions. The same plot including the standard deviation at each distance from the particle surface is reported in Figure 2.17 and shows a significantly larger variation of electron density closer to the surface. This larger variation clearly shows that ‘surface coke’ is more heterogeneous in terms of a different chemical nature (most probably represented by large polyaromatic species and aliphatic type species) and/or coke porosity than ‘core coke’, which is on average of lower electron density. The transient region between ‘surface coke’ and ‘core coke’ exhibits a linear decrease connecting high (‘surface coke’) and low coke electron density (‘core coke’) regions, which is also reflected in the corresponding probability density functions of electron density (Figure 2.5d). In agreement with literature^[3,12], this shift in electron density between ‘surface coke’ and ‘core coke’ can be

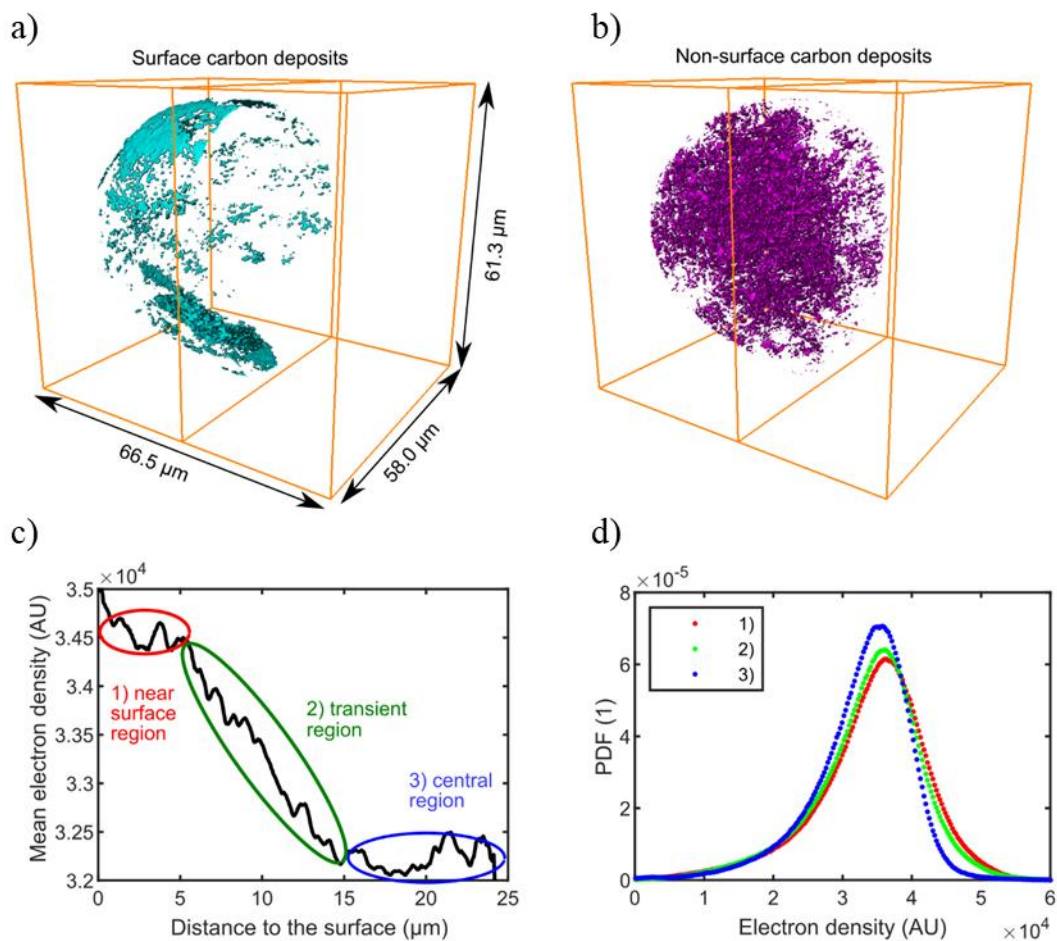


Figure 2.5 3-D speciation of carbon deposits within a catalyst particle via electron density. (a) Virtual cut through the 3-D distribution of surface (cyan) and (b) non-surface (magenta) carbon deposits. Surface coke clusters are defined as clusters that contain at least one voxel that is located within 2 voxels from the particle's surface. In (c), the mean electron density value of all coke voxels (independent of whether they are classified as members of a surface or non-surface cluster) as a function of distance to the surface reveals three distinct regions: a near surface region, a transient region, and a central region. The corresponding probability density functions of these regions' electron density values are reported in (d) clearly showing the decreased electron density of coke deposits located in the center of the catalyst particle. The probability density functions (i.e., the histograms of the electron density values normalized by setting their integral to unity) were used to directly compare these histograms because the total number of voxels in near surface, transient, and central region is very different.

assigned to the presence of large polyaromatic species and aliphatic type species, respectively. However, the 3-D packing of the same carbon species (coke porosity) within the catalyst particle can have the same effect and cause such a shift of the electron density. We can indeed imagine that the 3-D packing of carbon deposits could be denser at the outer surface of the catalyst particle (i.e., less porous coke is present), as the packing is not limited by

space restrictions. These results show that the developed differential contrast imaging is clearly sensitive enough for a tentative identification of small changes in electron density making the developed method more generally applicable to a wide range of catalytic reactions and systems.

2.2.3 Origin of Coke Deposits

Figure 2.6 reports the radial distribution (see Section 2.4.10 for further details) of coke, poisoning metals, and lanthanum, showing a much higher coke amount close to the particle surface, related to the patchy surface deposits of large polyaromatic coke species or denser coke packing. Both iron and nickel concentration profiles show the typical radial deposition profiles of poisoning metals in E-cat particles^[31,32,38,40–42]. Their concentration is relatively higher close to the surface. Nevertheless, Ni can diffuse deeper into the particle due to its higher mobility compared to Fe. Therefore, iron ‘hotspots’ (regions with highest Fe concentration) appear closer to the surface than Ni hotspots. This co-location of the highest concentrations of coke, Ni, and Fe is in line with the reported promotional effect of metals for coke formation^[5] and/or the effect that metal transporting porphyrin-like species from the feedstock are co-deposited with the metals they carry. However, to quantify this effect we determined the total amounts of both surface and non-surface coke in the iron-, nickel-, and lanthanum-rich areas (Table 2.1).

To assess the domains’ intrinsic average activity for non-surface coke formation the determined non-surface coke amount per domain was divided by the volume of the respective domain and expressed as percent of total activity. Note that activity here includes both accessibility and reactivity because the amount of non-surface coke formed per unit volume depends on both. Clearly, the La and Ni domains show significantly higher activity for the formation of non-surface coke than the Fe and metal-free areas. This is in line with the reported higher dehydrogenation activity of nickel^[5,37] and the high density of active acid sites in the La-exchanged zeolites that are the most active domains in the FCC catalyst particle for both cracking and coke formation^[43], which in turn confirms that non-surface coke is dominated by less dense aliphatic coke. Interestingly, only 28.8% of all individual La domains were found to contain coke. This also shows how the limited

accessibility of the deactivated E-cat leads to the participation of less than a third of the zeolite domains in the cracking reaction.

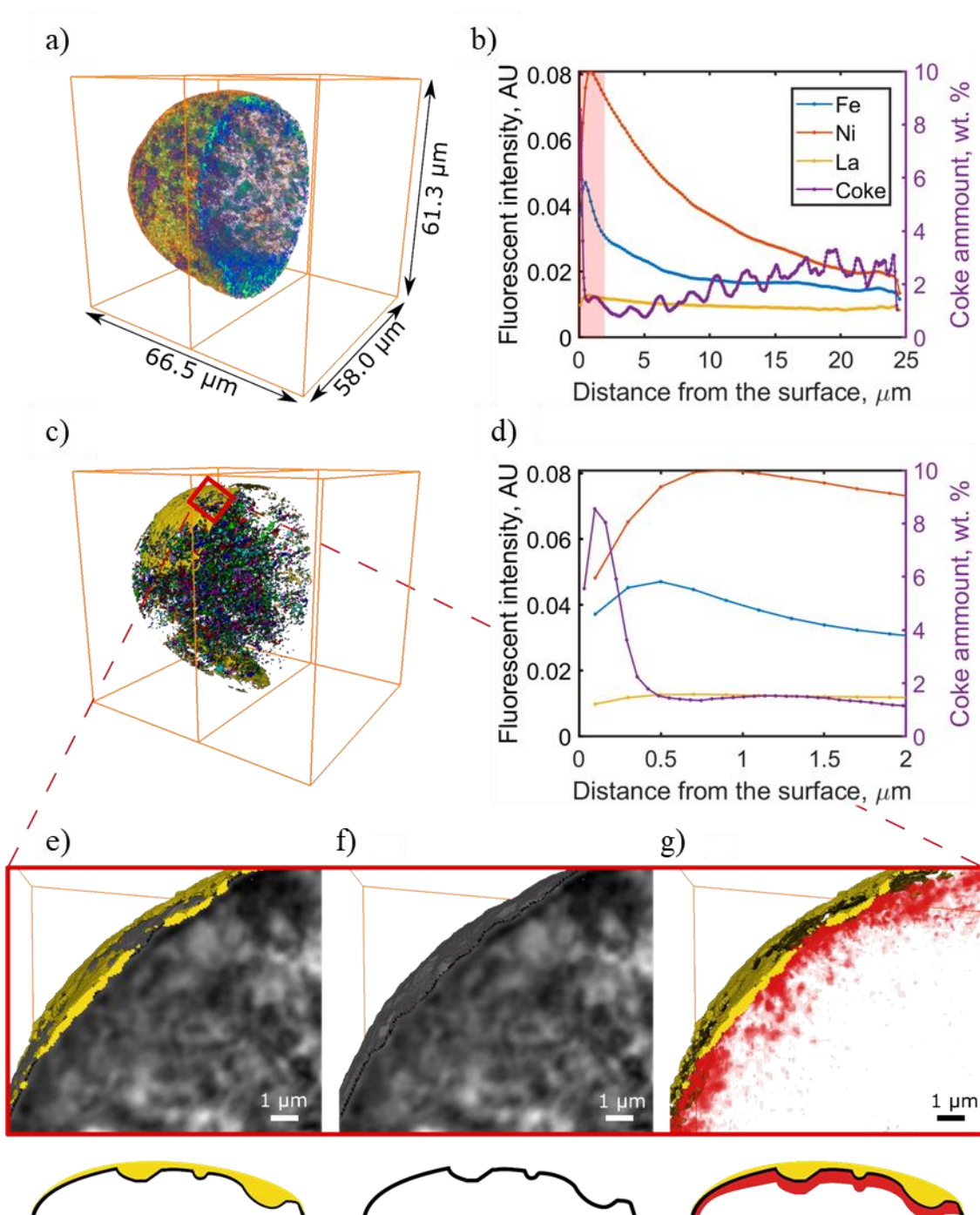


Figure 2.6 Correlated 3-D distributions of carbon deposits and metals within a single catalyst particle. (a) Virtual cut through the 3-D distribution of iron (yellow-red), nickel (blue-green), and lanthanum (magenta) as imaged by XRF tomography. The radial profiles (see Section 2.4.10) in (b) report relative concentrations of iron, nickel, lanthanum (from XRF), and carbon deposits (from

X-ray holotomography); the red region indicates the typical 1-2 μm thick surface region of decreased porosity. (c) 3-D distribution of individual carbon deposit clusters (individual clusters are plotted in different colors) identified by differential contrast holotomography. In (d) a zoom into the near surface region of the radial plot is displayed revealing the large amount of carbon deposited on the catalyst particle's surface. In (e) a zoom into the near-surface region of the catalyst particle is shown displaying the particle (X-ray holotomography, grey) and one of the large surface carbon deposit clusters (yellow). The comparison with panel (f) reveals how these patchy surface clusters smoothen the nodulated surface of the particle by filling dips and dents (the sketch below panels e-f). Panel (g) displays the 3-D Fe concentration distribution together with the surface cluster in the same sub-volume, showing that surface coke is in close vicinity to the highest Fe concentrations found close to the surface of the catalyst particle. Note that, as this is a 3-D perspective image, the scale bar indicates the length correctly only in the plane of the virtual cut. This observation confirms a previous NMR study that suggested aromatic coke to be mainly in the near surface regions of the catalyst particle and close to a paramagnetic species, such as iron^[12].

Domain	Total amount of surface coke (Vol.%)	Total amount of non-surface coke (Vol.%)	Normalized activity for non-surface coke formation (%)
Fe	6.11	3.56	17.9
Ni	4.86	8.81	21.2
La	6.62	11.19	46.4
Metal-free	85.16	78.86	14.5

Table 2.1 Absolute amounts of the two types of coke detected in metal-free as well as iron-, nickel-, and lanthanum-rich domains of the single catalyst particle. Metal-rich areas were defined via thresholding of the XRF data (see Section 2.4.14 for technical details). The last column reports the normalized activity of those domains for non-surface coke formation. As expected, based on its proposed origin and location, surface coke (dominated by large polyaromatic species mainly transferred from the feed) was not found to be preferentially present in metal-rich regions of the catalyst particle: 85.16% of this coke was localized in metal-free domains. Non-surface, i.e., mainly aliphatic coke generated by cracking or hydrogenation reactions, showed a higher spatial correlation with metal-rich areas, but also in this case the majority, namely 78.86%, of this type of coke was localized in metal-free domains, that is, in the pores of the catalyst particle.

2.3 Conclusions

In this work a carbon surface layer with a thickness of less than 1 μm has been identified filling dips and dents in the nodulated surface of an aged FCC catalyst particle (Figure 2.6). This is in line with suggestions from recent literature^[12], however, the analytical approach presented here not only provides clear evidence for this phenomenon but further allowed for a detailed analysis of the effect of coke deposits in E-cat catalyst particles as well as a correlation between its nature and 3-D location. It was shown that the (electron) dense surface coke blocks a significant fraction of the macro-pores in the surface of the catalyst body hence severely limiting accessibility of the catalyst. A completely new observation from this study is that most (less electron dense) non-surface coke was found in the macro-pore space of the catalyst, and it is interesting to note that the radial analysis of the coke

distribution showed that higher amounts of coke are present in the core of the catalyst particle than in a region within $\sim 1\text{-}10\ \mu\text{m}$ from the surface. This suggests that coke accumulates during multiple FCC cycles due to incomplete coke removal during regeneration caused by a limited average residence time in the regenerator unit (which is typically at the order of minutes)^[44]. During the time spent in this unit only coke in the regions close to the surface seems to be released – a process that is also influenced by the reduced mass transport ability of an aged FCC catalyst. This shows how the previously reported irreversible reduction in catalyst accessibility caused by metal poisoning has even more severe effects than previously assumed when investigating completely calcined FCC catalyst particles^[31,32,38,40,41,45], because incomplete coke removal leads to additionally reduced catalyst accessibility. We further show that Fe and metal-free areas show significantly lower activity for the formation of non-surface coke than the La (zeolite) and Ni domains, providing proof for the suggested higher dehydrogenation activity of nickel^[5,37].

These new insights lead to a further revision of our understanding of FCC catalyst ageing: while metal poisoning generally causes reduced porosity in the near surface regions of the catalyst, deposited Ni specifically increases coke formation. Incomplete coke removal during regeneration of the catalyst leads to accumulation of coke in the core of the particle blocking pores there. From the above it becomes clear that with the presented approach we have added a tool to the catalyst characterization toolbox that paves new ways for a more complete investigation of heterogeneous catalysts in its ability to visualize in 3-D both organic and inorganic phases in catalyst bodies of tens of microns at sub-200 nm 3-D resolution. In other words, the reported findings are not limited to FCC catalyst particles but can be used in a wide variety of catalytic reactions and systems.

2.4 Experimental Section

2.4.1 Optical Microscopy of Spent Fluid Catalytic Cracking Catalyst Particles

The spent catalyst batch contained particles with different coke loadings indicated by different degrees of blackening observed in the optical

micrographs, as displayed in Figure 2.7. This was expected and is normal for a batch of E-cat FCC catalyst particles, which always, by nature of the process, have an age (and therefore coke loading) distribution^[44]. To assess whether coke was present throughout the particles several of them were crushed revealing that the material's color is indeed the same also inside the particles. This is especially visible in the completely black particle in the bottom right of the region indicated by a red line: after crushing the particle split into three fragments revealing the inside of the particle, which shows that it is indeed black (i.e., coked) everywhere.

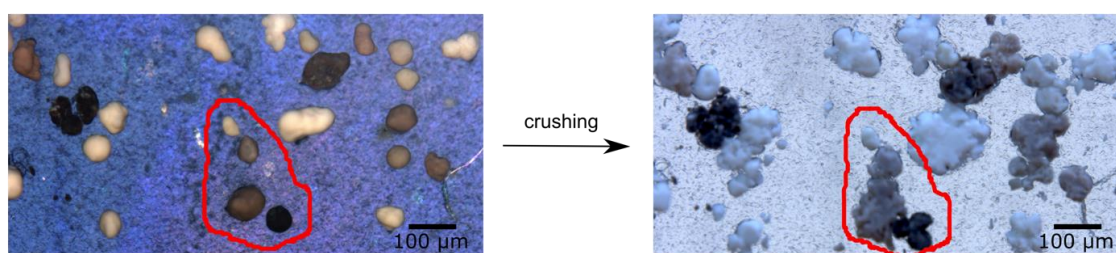


Figure 2.7 Optical image of the E-cat FCC particles before and after crushing. Highlighted in red is an area with a black particle that split into three fragments revealing the inside of the particle. Note that the characteristic color of each particle remains the same before and after the crushing step indicating that coke is indeed everywhere in the particles.

2.4.2 Setup for Individual Catalyst Particle Calcination

To allow calcination of a single catalyst particle after X-ray holotomography, we developed a quartz chamber (Figure 2.8) enabling a re-mounting of the same catalyst particle on a new graphite pin after calcination. A laboratory chamber furnace was used, model LM-112, Linn High Term, Germany, to burn off the coke deposits in the catalyst particle during the calcination, which we did in two steps. First, a 2 °C/min ramp was used to reach a temperature of 120 °C, then the sample stayed at 120 °C for 1 h to release the particle from the graphite pin. Finally, the particle was heated up to 600 °C (5 °C/min) for 4 h to remove all coke inside the particle, indicated by the color change from black to white.

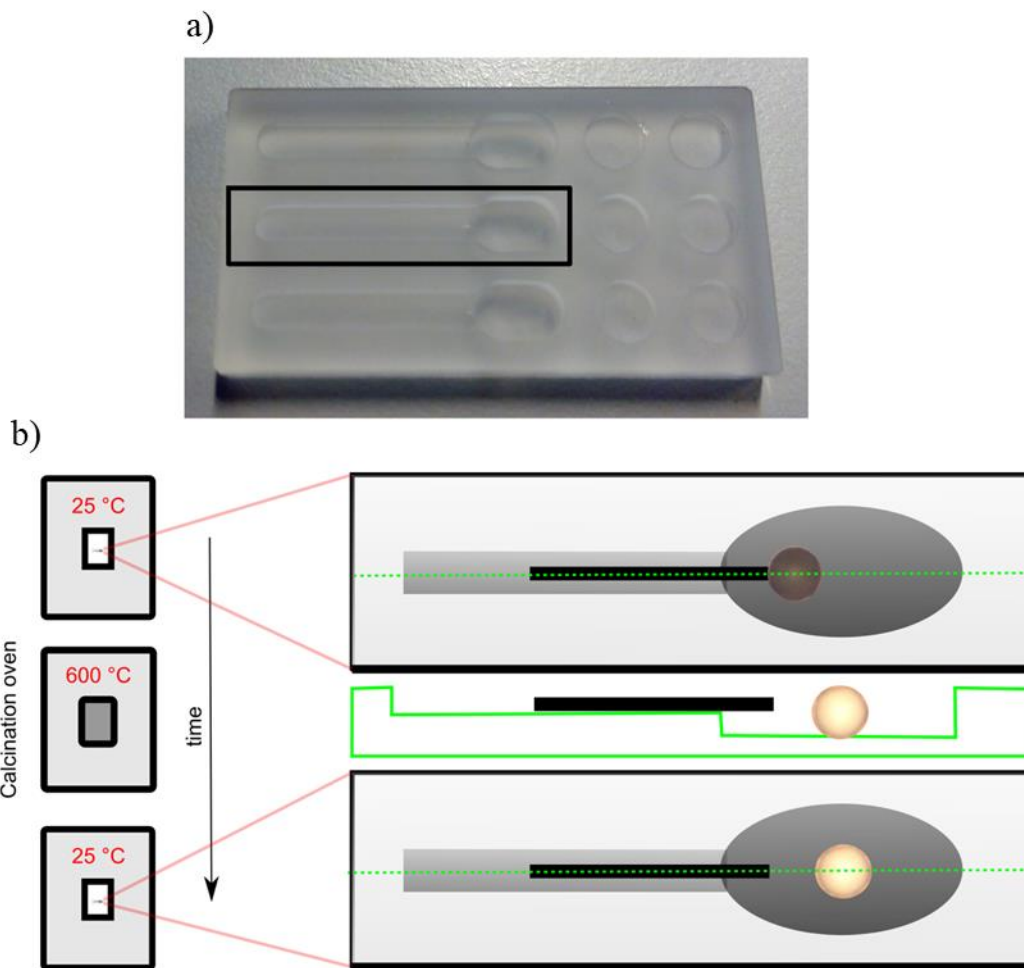


Figure 2.8 (a) Photograph of the bottom part of the quartz calcination chamber designed for calcination of a single catalyst particle. The top part, a lid, consists of flat quartz plate. (b) Corresponding sketch of the chamber with particle positions during the calcination. At the beginning of the calcination, the coked particle is mounted on the graphite pin using wax. During the calcination, both the wax and carbon deposits are burned off and the calcined particle drops into the dedicated dip in the calcination chamber. A side view of the chamber is displayed in green.

2.4.3 X-ray Holotomography

The individual catalyst particle was examined using the X-ray holotomography setup GINIX (Göttingen Instrument for Nano-Imaging with X-Rays) installed at the P10 beamline at the PETRA III storage ring, DESY, Hamburg, Germany^[46]. Projections were acquired at four different source-to-sample distances^[47,48] (see Section 1.2.3 for further details). The total time needed for sample mounting and holotomography was approximately 4 h. The sample was roughly positioned in the X-ray beam using an optical microscope

with a comparably large field of view, which was aligned with respect to the beam path. Fine adjustments of the sample position with respect to the center of rotation and the ultimate field of view were performed using the X-ray microscope. The experiments were carried out at an X-ray energy of 13.8 keV, which was achieved using a channel-cut monochromator. The X-ray beam was focused by a set of Kirkpatrick-Baez (KB) mirrors, leading to a focus size of approximately $300 \times 300 \text{ nm}^2$. In order to reduce high-frequency artifacts caused by inhomogeneities on the mirror surface, as well as increase the coherence of the X-ray beam and reduce the focal spot size, a waveguide was placed in the focal plane of the KB mirrors^[46]. The waveguide was formed by two crossed planar Mo/C/Mo thin films lamellae, each with 80 nm guiding layer. Approximately 5 m behind the sample, a scintillator-based fiber-coupled sCMOS detector with Gadox as scintillation material and a pixel size of $6.5 \text{ }\mu\text{m}$ was placed (Photonic Science). Due to the divergent beam geometry, the setup comprises a large geometric magnification, leading to an effective pixel size of 64 nm in the sample plane. The individual coked catalyst particle was mounted on top of a graphite pin. The sample was placed at the four different source-to-sample distances and 1000 projection angles covering an angular range of 180° were recorded. Prior to phase retrieval with a CTF-based approach^[49], all projections were scaled to the same pixel size and aligned to each other in Fourier space^[50]. Tomographic reconstruction was carried out with the MATLAB implementation of the filtered back projection using a standard Ram-Lak filter. The resulting 3-D representation of the sample's electron density distribution was converted to 16-bit integer format and further processed by applying an anisotropic diffusion filter^[51] and watershed segmentation^[52] to determine pore and solid space. For image presentation, we used inverted grayscale colormap, i.e., the low electron density values appear as white pixels (voxels) and the high electron density values appear as black pixels (voxels).

2.4.4 X-ray Holotomography Spatial Resolution Estimation

Firstly, the 3-D resolution of every data set was estimated using the Fourier ring correlation^[53] (FRC) method. The FRC estimated resolution was calculated by separating the aligned original 2-D projections in odd and even

angles and performing a FBP reconstruction on each half dataset. These two reconstructed half datasets should theoretically contain the same spatial information. Using the Fourier transform of both 3-D reconstructed volumes, their statistical correlation is calculated for each shell of constant spatial frequency with varying magnitude. A FRC curve plots this correlation going from low spatial frequency to high spatial frequency (1/voxel size) and the spatial resolution is then estimated as the cross-section of the correlation plot versus a chosen threshold value.

The FRC analysis was performed on the 200 most centrally located reconstructed virtual slice pairs, and the calculated FRC values were averaged over these slices. The resolution was determined as the intersection point of the FRC curve with the corresponding 2- σ criterion (Figure 2.9), estimating the achieved 3-D resolution to 179 nm. Secondly, as a supplementary method, the X-ray holotomography resolution was estimated from 27 line profiles over characteristic features in 2-D virtual cuts to be 221 ± 38 nm using the 10%-90% criteria^[54]. The workflow from Holler^[54] was used, containing identification of the characteristic feature in the virtual 2-D slice (Figure 2.10a), selection of the line cut (Figure 2.10b), and the intensity plot along the line cut (Figure 2.10c). The intensity plot shows the 10%-90% criteria (horizontal dotted lines) and the distance determining the edge resolution (vertical dashed lines).

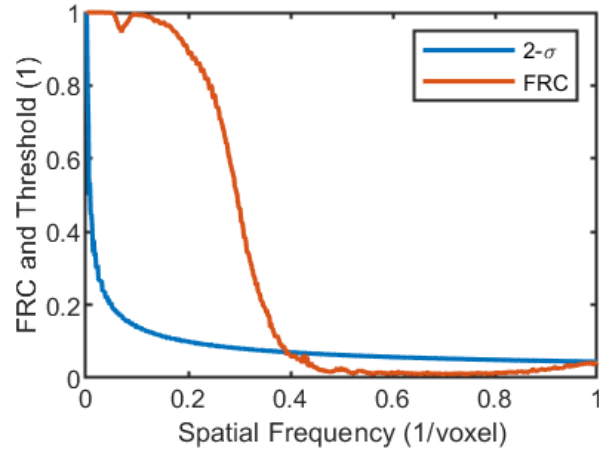


Figure 2.9 FRC resolution estimation for the X-ray holotomography data recorded for the FCC particle before calcination. The resolution is determined by the intersection of the FRC curve calculated from 200 reconstructed virtual slices and the corresponding $2\text{-}\sigma$ criterion. The intersection point at 0.3560 reciprocal voxels results in a 3-D resolution of 179 nm.

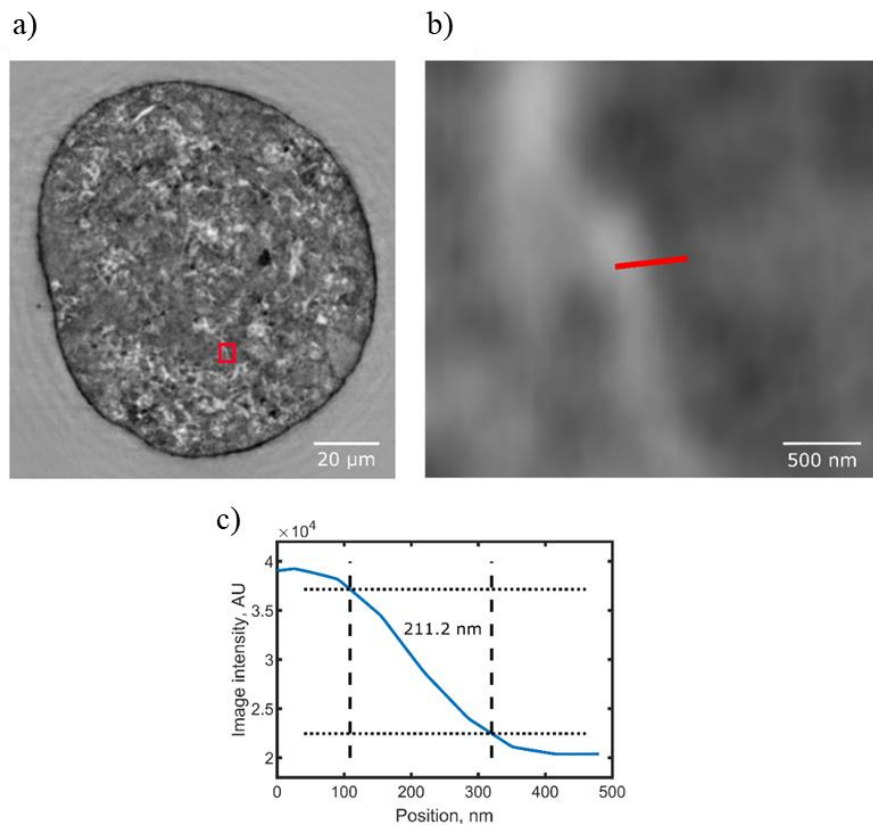


Figure 2.10 Example of a line scan used for the edge scan resolution estimation method for the X-ray holotomography data recorded for the FCC particle before calcination. (a) Virtual cut through the FCC particle. (b) Zoomed-in region indicated by the red rectangle in (a). The red line denotes the line profile used in (c). (c) Line profile across the edge indicated in (b) showing an effective resolution of 211.2 nm using the 10%-90% criterion^[54].

2.4.5 Differential Contrast Holotomography

The subtraction of the electron density values of each voxel of the data set (the smallest volume unit in a 3-D data set) recorded before and after calcination shows regions where the electron density changed, i.e., the locations, where carbon was located before the calcination. Differential contrast holotomography is sensitive to any misalignment of the two subtracted data sets and also to differences in the achieved 3-D resolution. To ensure that the detected change in electron density was not due to artifacts caused by these effects the effective 3-D resolution of both data sets was estimated using Fourier ring correlation^[53] (Section 2.4.4) and found to be 179 nm and 189 nm for the non-calcined and calcined particle, respectively. Because the difference in the achieved 3-D resolution (10 nm) was found to be more than six times smaller than the used voxel size (64 nm) it can be concluded that any effect of differences in 3-D resolution is negligible. These values furthermore confirm the high reproducibility of the X-ray holotomography method. The second possible effect preventing a precise localization of coke deposits is a misalignment of the two data sets before subtraction. In order to achieve the best possible alignment of the two data sets a post-measurement image registration was performed, which was also necessary because the catalyst particle had to be mounted again on the pin manually in a light microscope after calcination and it is impossible to mount it in the exact same position as for the first measurement (before calcination). A careful two-step data alignment procedure was developed where in the first step a rough registration was performed using the total particle volumes (TPVs) of the two data sets. During the second step a fine alignment was carried out using the grayscale volume images of the recorded electron density refining the initial registration. More details about the registration procedure can be found in the Section 2.4.6. Since the result of volume subtraction is extremely sensitive to the registration procedure, the precision of the registration was checked using a scale-invariant feature transform^[55] (SIFT) procedure (Section 2.4.7). The histogram of the mean square displacement values is reported in Figure 2.12a, which shows that almost all displacement values are smaller or equal than 3.45 voxels - taking this as a very conservative estimate for registration and feature determination uncertainty we obtain

220.8 nm, implying almost perfect registration with an uncertainty close (i.e., within one voxel) to the limit set by the spatial resolution of the data set (189 nm or 2.95 voxels).

As discussed in previous work^[31] the subtraction of the registered volume images leads to a volume image containing both positive and negative values. The negative values contain a contribution of noise and can be used to assess the noise level. The positive values contain contributions from noise and carbon deposits. To distinguish the carbon contribution from noise, a statistical treatment was applied supposing a Gaussian signal for noise that allowed determining an electron density threshold to identify carbon deposits (Section 2.4.9). The identified amounts of carbon deposits in the catalyst particle were expressed in weight percentage using the known mean density of FCC particles^[31], 2.957 g/cm³, and graphite, 2.100 g/cm³. The total amount of coke, 2.37 vol.% (1.68 wt.% assuming the density of graphite), was close to the value 1.75 wt.% previously reported for a commercial E-cat catalyst with high carbon content^[12], confirming the validity of the developed thresholding approach.

2.4.6 Registration of Two Datasets

The volume images from the holotomography measurements (before/after calcination) were aligned using the registration tool available in the Avizo software package. The non-calcined volume image was set as a reference microstructure and the data volume recorded for the calcined particle was allowed to translate, rotate, shear, and scale. To achieve optimal results, the registration was processed in two steps. In the first step a coarse registration was performed using the corresponding binary total particle volume (TPV) of each particle, which is defined as the volume of the particle including the pore space (see below for a more detailed definition). In the second step a fine alignment was performed using the grayscale volume images that resulted from the coarse registration as a starting point. The registration algorithm used here is based on the least squares minimization between two pixels with the same coordinates. The Quasi-Newton optimizer was used for minimization of the whole 3-D images. Although all possible transformations were allowed to find the best fit, the final scaling factor was very close to one (0.99947), which

highlights the very stable measurement setup and the robustness of the alignment procedure. This is important to stress as an artificial ‘shrinking’ of the particle due to errors in measurement or data processing could lead to an artificial surface layer of coke around the catalyst particle when subtracting aligned data sets. However, expressed in voxels, the obtained scaling factor corresponds to a size change of 0.6 voxels for an object of ~1000 voxels in diameter. Such an artificial shrinking would further result in a continuous layer of removed material from the surface while our analysis shows that coke was present in patches on the surface of the FCC catalyst particle.

The result of registration is depicted in Figure 2.11 displaying the same virtual slice through the particle before and after the calcination step. The regions encircled in red highlight areas in the particle where apparent changes in electron density happened, i.e., regions where coke was removed.

The registration of holotomography and XRF data was performed in a single step using the XRF TPV that was calculated from the sum XRF spectrum, that is, considering the contribution of all detected elements in the catalyst particle.

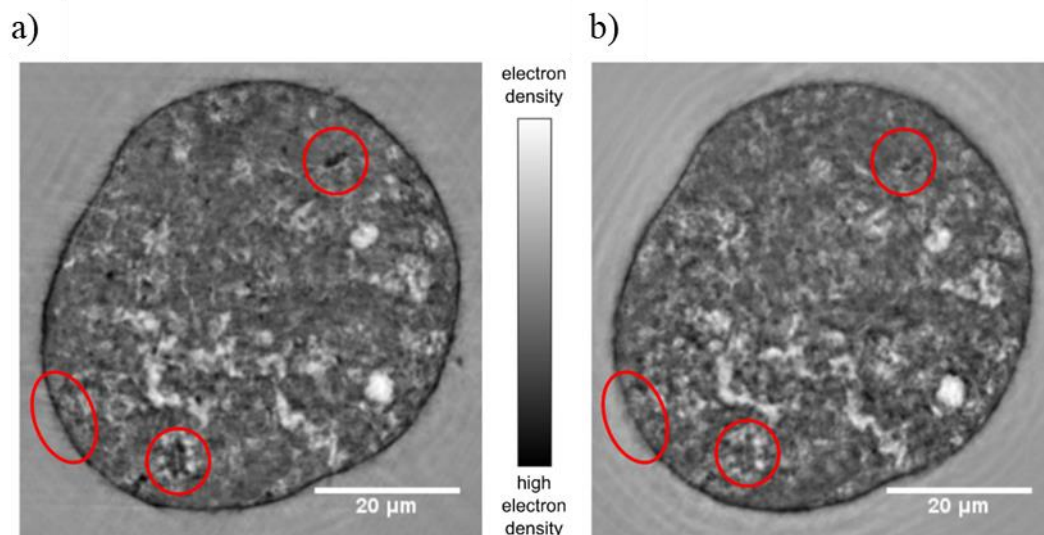


Figure 2.11 The same virtual slice through the registered volume images of (a) non-calcined and (b) calcined FCC catalyst particle. The dark pixels denote places with high electron density and vice versa. Note, that pores (white pixels) contain air, which is less electron dense than the wax, in which the particle was embedded. The regions highlighted in red show areas where significant changes in electron density are visible. While we predominantly see ‘electron loss’ in most areas (change from dark gray to lighter gray), very few regions show the opposite effect (i.e., a darkening after calcination; see, for example, the large pore (white) in the lower right region of the virtual slice displayed). We assume that the following two effects can lead to these observations: 1) these effects indicate imaging artifacts due to insufficient resolution, that is, a noise effect. This noise effect causing an apparent higher electron density after calcination is also visible in the histogram of the differential contrast data where negative values exist (Figure 2.14) We expect that coke removal is not complete during calcination and some coke is actually not fully removed from the catalyst particle but just detached from its original location and then re-deposited, forming new coke deposits at different locations in the particle.

2.4.7 Alignment Precision Assessment Using Scale-Invariant Feature Transform

The Scale-invariant feature transform^[55] (SIFT) procedure finds identical local features in two 2-D images that are invariant against transformations. In order to assess the precision of the applied alignment procedure described above nine pairs of virtual slices were analyzed in the planes x-y, x-z and y-z, where x, y and z denote the principal axis of the volume images. For every plane, 3 virtual slices were analyzed, one taken from the first third (S1) of the whole stack of planes representing the total data volume, one from the second, central third (S2) of the stack, and one from the last third (S3) of the stack. In total, i.e., for all 9 pairs of slices, SIFT detected 352 feature pairs and calculated the mean square displacement for each pair. The resulting

displacement values, determined as the square root of the mean square displacement values, were found with a distribution as displayed in Figure 2.12a, with an average value of 1.33 voxels and with a standard deviation value 0.83 voxels. To demonstrate the SIFT evaluation, Figure 2.12b reports as an example the central slice in the x-y plane with the feature positions indicated by red dots and the corresponding feature displacement values in Figure 2.12c. The histogram of the displacement values displayed in Figure 2.12d shows that the distribution is close to uniform with values between zero and 2.6 voxels. No significant differences were detected in the mean of the displacement values (Table 2.2) or their distribution between the 3 planes x-y, x-z, and y-z confirming isotropy of the processed and aligned data, which is an important prerequisite for 3-D real space processing.

Slice plane	Spline position		
	S1	S2	S3
x-y	1.3468	1.3209	1.3417
x-z	1.3416	1.3293	1.3354
y-z	1.3399	1.3228	1.3423

Table 2.2 Mean displacement values for all three principal planes (x-y, x-z, y-z) and slices S1-3.

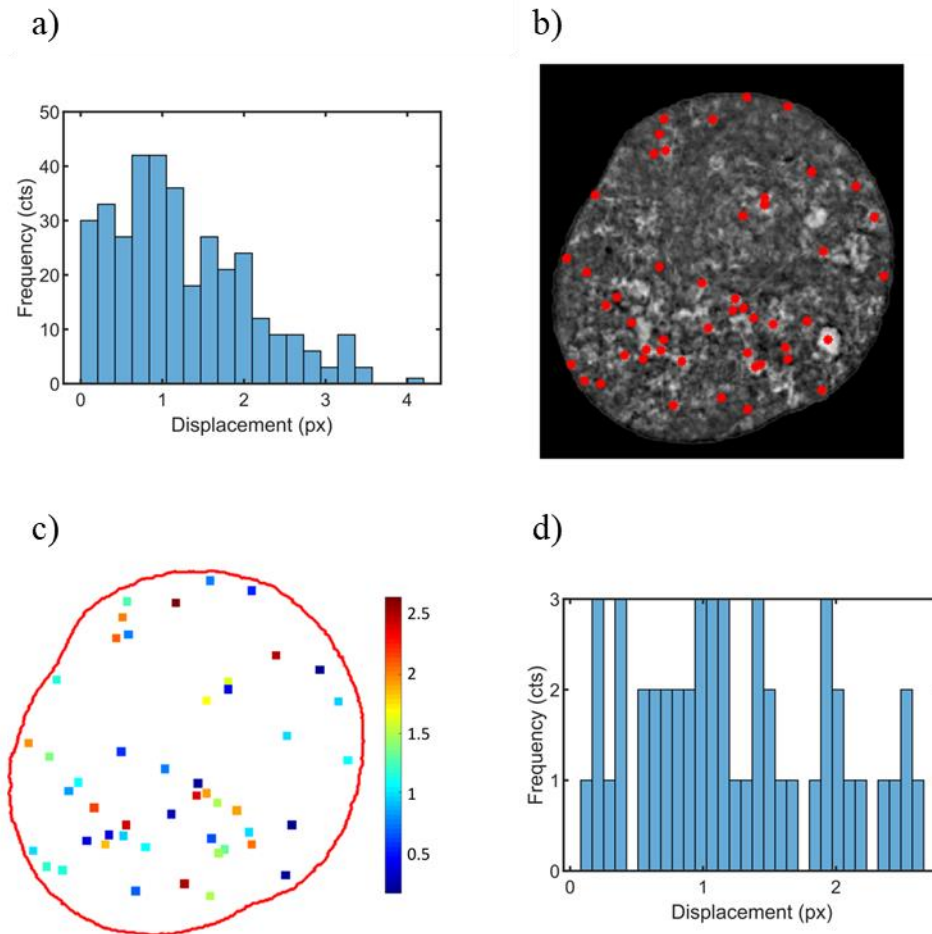


Figure 2.12 SIFT analysis of the data alignment precision. (a) Distribution of the mean square displacement of the features over nine 2-D virtual slices in the 3 planes x-y, x-z, y-z. (b) Central virtual slice in the x-y plane with SIFT features marked as red dots, showing their homogenous distribution over the slice. (c) Map of the same features as shown in (b) with their color indicating the displacement of each feature; no correlation between location and degree of displacement is observed, suggesting that the displacement is exclusively due to the noise in the data. (d) The displacement histogram for the features of the virtual slice shown in (b) and (c).

2.4.8 Histograms of the Electron Density Before and After Calcination

The holotomography data acquisition before and after the calcination step was always carried out with the same setup and experimental settings. Therefore, the local changes in electron density are caused only by removing matter containing electrons – here the carbon deposits. Summation of the local changes provides the total change in electron density, which is evident in the

corresponding histograms (Figure 2.13). The histograms clearly show lower electron density for the calcined particle.

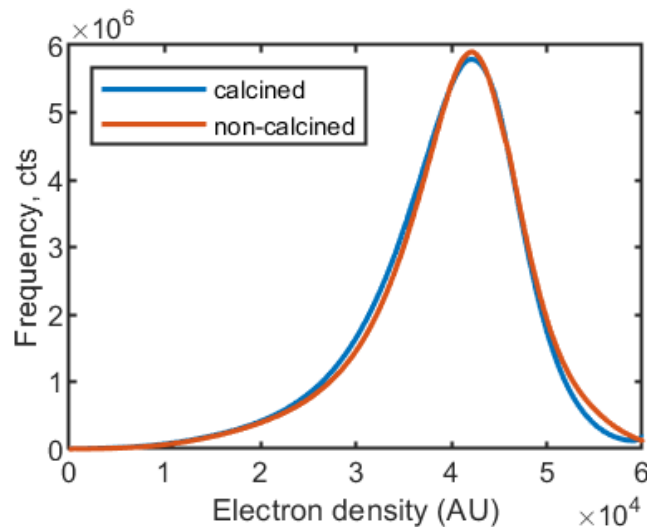


Figure 2.13 Histograms of the 3-D volume images obtained by X-ray holotomography before and after calcination. The histogram is shifted towards lower electron density values after the calcination, which is caused by the removal of the coke deposits.

2.4.9 Thresholding of Differential X-ray Holotomography Data to Determine the 3-D Coke Distribution

The direct subtraction of the X-ray holotomography data sets leads to a volume image containing both positive and negative values (Figure 2.14a); the latter originate from the noise in the raw holotomography data and are therefore randomly distributed over the sample volume. Therefore, the histogram of electron density difference values (Figure 2.14, red line), which were calculated from values displayed in Figure 2.13, was fit using a Gaussian function optimizing the fit to the negative part of the histogram. Both histogram and fit clearly show that many voxels exist with positive values that are above this noise level. From the fit to the negative side of the histogram the threshold was (conservatively) determined to 11500 (green vertical line), i.e., where the histogram clearly deviates from the Gaussian distribution as shown in Figure 2.14b, which reports a zoom to the region around this value. This threshold was then used to segment the data into voxels containing no coke (all voxels with difference values below 11500 and those containing coke (voxel with values ≥ 11500). This resulted in the coke distribution

shown e.g., in Figure 2.5a,b with a reasonable coke cluster size distribution (Section 2.4.11) and a total amount of coke in the catalyst particle to be 2.37 vol.% (1.68 wt.% assuming the density of graphite for conversion) that was found in line with literature (1.75 wt%)^[3].

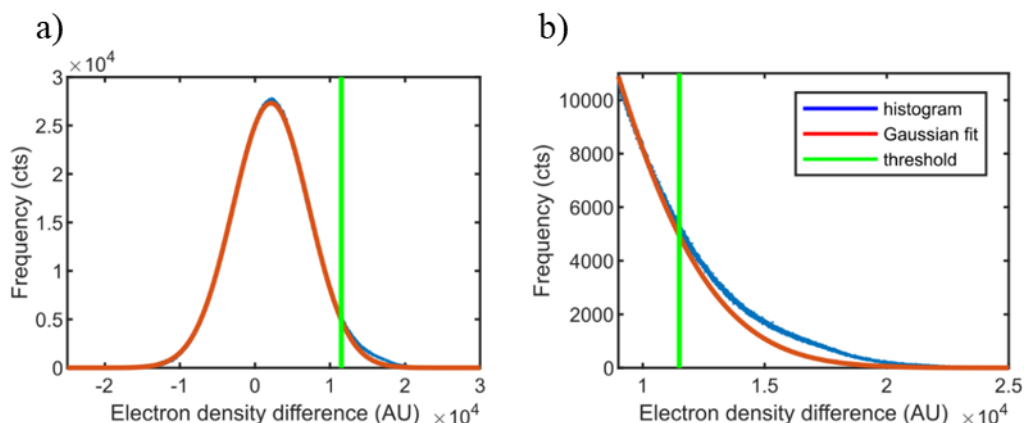


Figure 2.14 Histogram of electron density difference values obtained from the difference X-ray holotomography data set (difference of data set collected before and after calcination). The histogram was fitted with a Gaussian function, optimizing the fit to the negative part of the histogram. The right panel shows the deviation of the histogram from the noise distribution around the threshold value 11500 that was used to segment the data into empty (with values < 11500) and coke containing voxels.

2.4.10 Radial Analysis

The radial distribution of different elements, such as phase A, within the structure of the porous catalyst was calculated as follows in a first workflow processing loop (usually implemented in computer code):

1. Generate total particle volume (TPV). TPV is the binarized image in which the background voxels have the value of 0 and voxels belonging to the particle's volume have a value of 1.
2. Create a distance map in 3-D to find the central voxel of the TPV. What this does is that the Euclidean distance of any non-zero voxel towards the closest zero (background) voxel is calculated. Effectively, the center voxel therefore will have the largest value since it should be the one furthest away from any background voxels.

3. This distance transformation in step 2 also reveals the voxels belonging to the surface of the binarized object (shortest or lowest calculated Euclidean distance values).

In a second loop within the first loop the following sequence is started:

4. Calculate for all surface voxels the fraction of voxels assigned to phase A.
5. Erode the TPV by 1 voxel. This removes a shell of one voxel thickness from the outer surface at each iteration using the calculated distance map from step 2.
6. Repeat step 4 and 5 until the center of the particle is reached.

The data of step 4 to 6 is then saved in a matrix as a function of voxel shells removed from the original binarized volume and can then easily be converted into a volume fraction of phase A as a function of the distance from the particle's surface. Since shells of one voxel thickness close or at the center of each particle typically only contain a few voxels, the volume fraction of phase A in those shells is not statistically significant.

2.4.11 Coke Cluster Analysis

The cluster analysis of the carbon deposits revealed a correlation between the size of the carbon clusters and their characteristic distance to the surface (Figure 2.15). To statistically evaluate coke deposits for the whole catalyst particle we have identified coke clusters in 3-D defined as a set of connected voxels containing coke and using a 6-connected neighborhood rule. In this step statistically insignificant clusters consisting of only 30 voxels or less have been treated as noise and removed. These small clusters contained only 0.27% of all voxels identified as coke. Then the correlation between the size of the coke clusters and their Euclidian distance to the particle surface was analyzed (Figure 2.15), which was calculated as the average value of all Euclidian distances of all voxels in the cluster. Note that we do not detect a continuous large coke layer covering the whole surface of the particle as might be expected from the optical microscopy image showing a completely black

particle before calcination (Figure 2.7). The reason is that a layer that is significantly thinner than the resolution of the method used here cannot be detected.

The results show that large clusters are located on or close to the surface of the particle. We also found one large cluster closer to the center of the particle, in agreement with the higher coke content found there. Most clusters were found to be significantly smaller (below $3 \mu\text{m}^3$ or 10000 voxels) and distributed homogeneously in the catalyst particle. Further, the electron density values for surface and non-surface coke clusters were studied. We defined all clusters containing at least one voxel located within 2 voxels from the particle's surface as surface coke cluster. Figure 2.16a shows a virtual cut through the particle indicating the individual carbon clusters within and distinguishing non-surface clusters (magenta) and surface clusters (cyan), as also presented separately in Figure 2.5a,b. This separation allowed inspecting the electron density values of surface and non-surface coke reported as probability density functions for both types of coke (Figure 2.16b), which show a clear electron density shift towards more electron dense surface clusters, i.e., more electrons participate in chemical bonds in carbon deposits on the surface of the particle. Again, this is in excellent agreement with literature suggesting that this higher electron density is caused by large polyaromatic species that dominate the composition of surface coke, while non-surface species are mainly aliphatic in nature^[3,12]. Figure 2.16c shows that our definition of surface coke clusters can generate clusters that extend deeper into the particle, but never create a cluster extending through the whole particle volume.

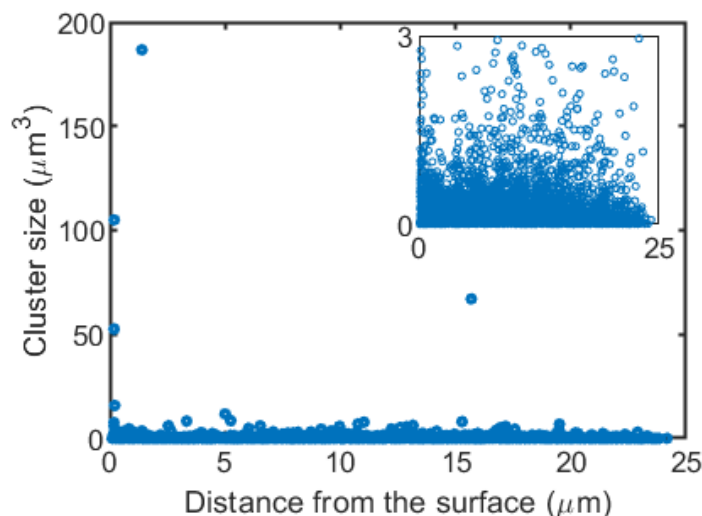


Figure 2.15 Correlation plot of mean cluster distance to the surface versus cluster size. The inset displays a zoom to the region of clusters below $3 \mu\text{m}^3$.

The electron density values of surface and non-surface coke that are reported as probability density functions for both types of coke in Figure 2.16b show a clear shift towards surface clusters with higher electron density, i.e., carbon deposits on the surface of the particle have higher electron density. We conclude that the shift is caused by the different nature of carbon deposits in FCC catalysts: aliphatic and aromatic coke^[12]. As discussed above it was suggested that during the FCC process aliphatic coke, which is created by the cracking reaction, is mainly deposited in the inner part of the catalyst particle, while aromatic coke, which has more electrons constituting the aromatic character and mainly originates from the feedstock stream, is preferentially deposited on the outer surface of the catalyst particle. The aromatic-aliphatic distribution we observe here therefore fully supports these previous findings^[12]. These results further evidence the high sensitivity of the X-ray holotomography approach to assess subtle differences in electron density of carbonaceous species, which is in this case crucial to distinguish these two different types of carbon deposits. Here it is important to point out that the probability density functions of the electron density displayed in Figure 2.5d show significantly overlapping values, indicating that both surface and non-surface coke consist of a mix of more and less dense coke, and does not imply the identification of specific molecular structures of hydrocarbon deposits. The histograms are further artificially broadened as an effect of the limited

resolution of the technique: voxels that are not completely filled with coke, but only with a layer of coke that is thinner than the voxel size will appear as a voxel of lower coke electron density. However, because all coke clusters, including those on the surface, are generally thicker than one voxel (small insignificant coke clusters have been removed), the spatial probability distribution of not completely filled voxels is independent of their position in the inspected volume, i.e., we do not expect more or less not completely filled voxels in the surface or in the non-surface clusters. This is confirmed by the fact that the two probability density functions of the electron density have a very similar width: the effect of not completely filled voxels only broadens the probability density functions but does not affect their shift, i.e., the shift between the average electron density values of surface and non-surface coke species.

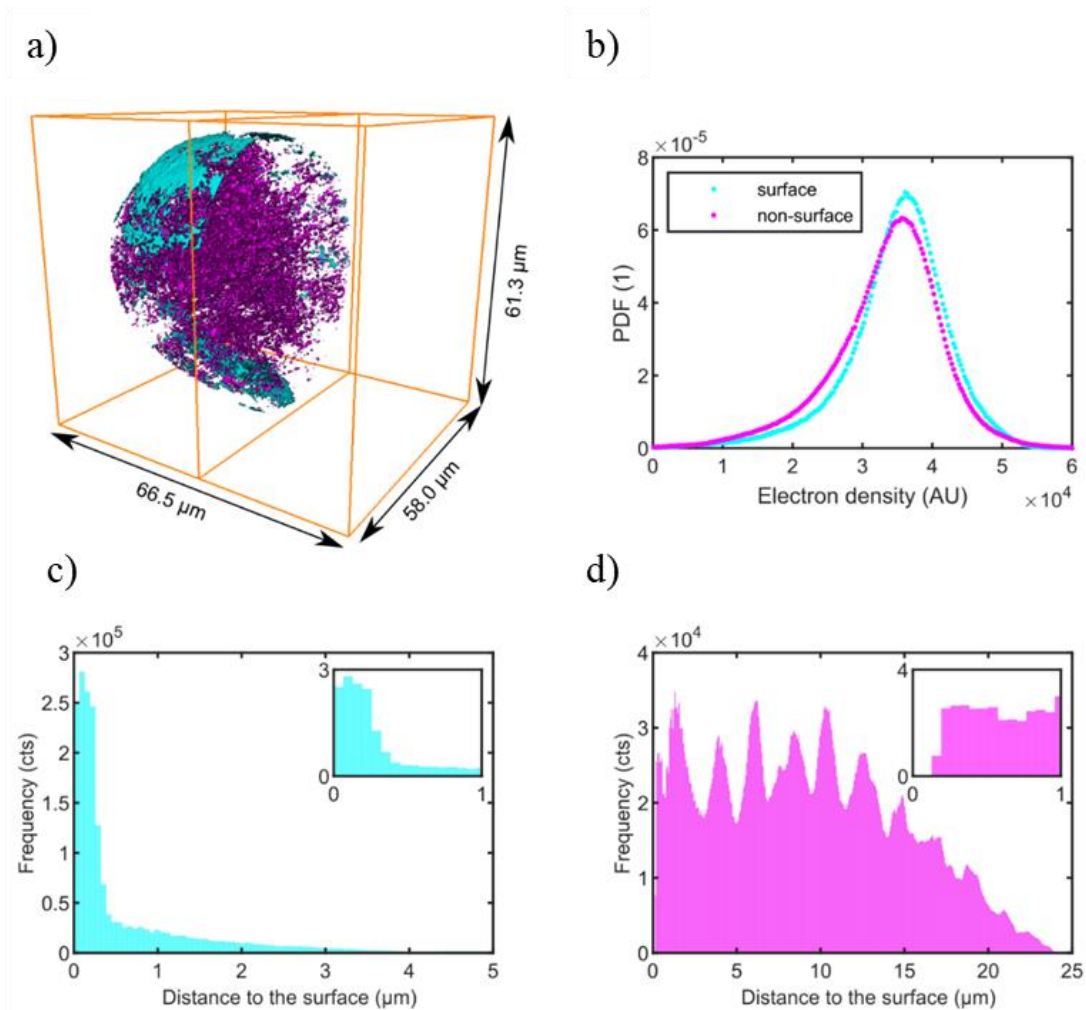


Figure 2.16 (a) Virtual cut through the 3-D distribution of surface (cyan) and non-surface (magenta) carbon deposits. Surface coke clusters are defined as clusters that contain at least one voxel that is located within 2 voxels from the particle's surface. In (b) the corresponding probability density functions of the electron density values of the images of both surface and non-surface coke are plotted. The probability density functions (i.e., the histograms of the electron density values normalized by setting their integral to unity) were used to directly compare these histograms because the total number of voxels of surface and non-surface coke is very different. The electron density of the surface coke is clearly shifted towards higher electron density values, which means that more electrons participate in bonds within the surface coke. The number of coke voxels in surface (c) and non-surface (d) coke clusters in dependence of distance to the surface confirm the presence of surface and non-surface coke clusters in the first 5 μm from the particle surface. This is a result of the fact that coke clusters are irregularly shaped and can e.g., extend from the surface into deeper parts of the particle causing some overlap of clusters that are classified as one type or the other. The insets in (c) and (d) displaying the first 1 μm further show the effect of the 2-voxel criterion used to determine surface clusters.

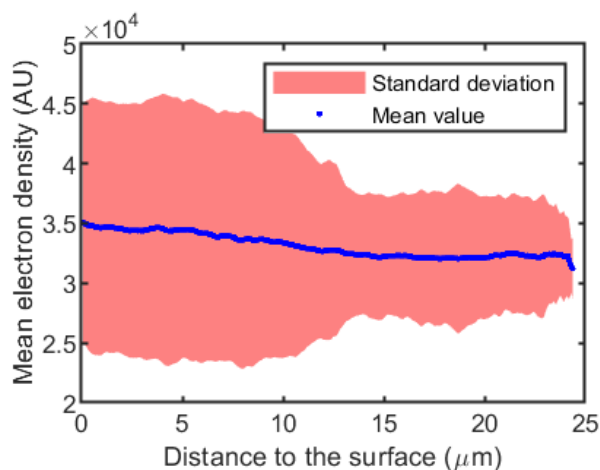


Figure 2.17 The mean electron density value of all coke voxels (independent of whether they are classified as members of a surface or non-surface cluster) plotted together with the corresponding standard deviation in measured electron density as a function of distance to the surface. The variation in the standard deviation highlights a distance related change in the ratio between the carbon deposits with higher and lower electron density. The surface area contains contribution from coke with both higher and lower electron density. This means that the surface coke is more heterogeneous in terms of a different chemical nature (large polyaromatic species and aliphatic type species) and/or coke porosity.

2.4.12 Powder X-ray Diffraction of a Spent Catalyst Particle Batch Before and After Calcination

Powder X-ray Diffraction (XRD) was used to confirm the microstructure stability of the same catalyst batch before and after the calcination. Note, that we applied the same calcination procedure for individual catalyst particle calcination in the calcination chamber. Diffraction patterns were collected using a Bruker D2 Phaser (2nd Gen) instrument using a cobalt radiation source, $\text{Co } \alpha = 1.789 \text{ \AA}$, and the samples were rotated at 15 revolutions/min. The diffraction patterns (Figure 2.18) were not normalized since we supposed no significant weight-change of the crystalline part in the catalyst batch (the 1.5-2% of coke that are removed changes the electron density slightly, but not significantly as shown in Figure 2.13). The diffraction pattern does not differ in the crystallinity or phase of the catalyst components. Therefore, we assumed that the calcination removed only the carbon deposits and did not damage the structural integrity of the particle.

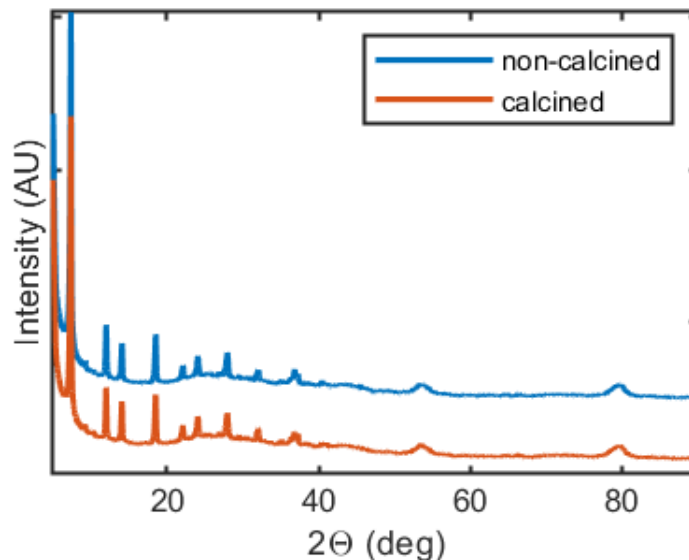


Figure 2.18 The XRD pattern of a batch of the E-cat particles before and after calcination confirm the stability of the microstructure, i.e., no loss of crystallinity or phase change was detected. The sample was taken from the same batch as the individual catalyst particle used in holotomography. The calcination was performed using the same parameters as for the individual particle.

2.4.13 In-situ Small- and Wide-angle Scattering Combined with Differential Scanning Calorimetry

Calcining the catalyst particle for 4 h was significantly longer than the typical cycle time in an industrial regenerator, which is 10 – 15 min^[44,56]. Therefore, we had to verify that the calcination removed only the carbon deposits and did not damage the structural integrity of the catalyst particle. For this purpose, bulk in-situ small- and wide-angle scattering (SAXS/WAXS) and differential scanning calorimetry (DSC) was used with a batch of coked particles to double check the heat evolution related to burning the coke and to confirm that no change took place in the crystallinity or phase of the catalyst components (Figure 2.19). Moreover, SAXS was used to investigate the effect of coke formation at the length-scale of the micropores in the zeolite domains of the FCC catalyst particles.

The SAXS/WAXS/DSC measurement was performed at the DUBBLE beamline at the ESRF, Grenoble, France using a monochromatic X-ray beam of 8.5 keV. The FCC particles were placed in an aluminum pan, which was placed in the heating stage of the DSC600 instrument (Linkam Scientific, Germany) integrated in the beamline. During heating SAXS patterns were

recorded using a Pilatus 1M detector and WAXS patterns were recorded using a 300K-W linear Pilatus detector. The patterns were recorded during the calcination process involving heating to 600 °C with a ramp of 5 °C/min, holding at 600 °C for 120 min, and finally cooling down to 30 °C with a ramp of 10 °C/min. We have used 25 s counting time for each SAXS/WAXS pattern and waited for 5 s between subsequent pattern acquisitions. All acquired data were corrected for varying beam intensity measured in by a pin-diode integrated in the beamstop.

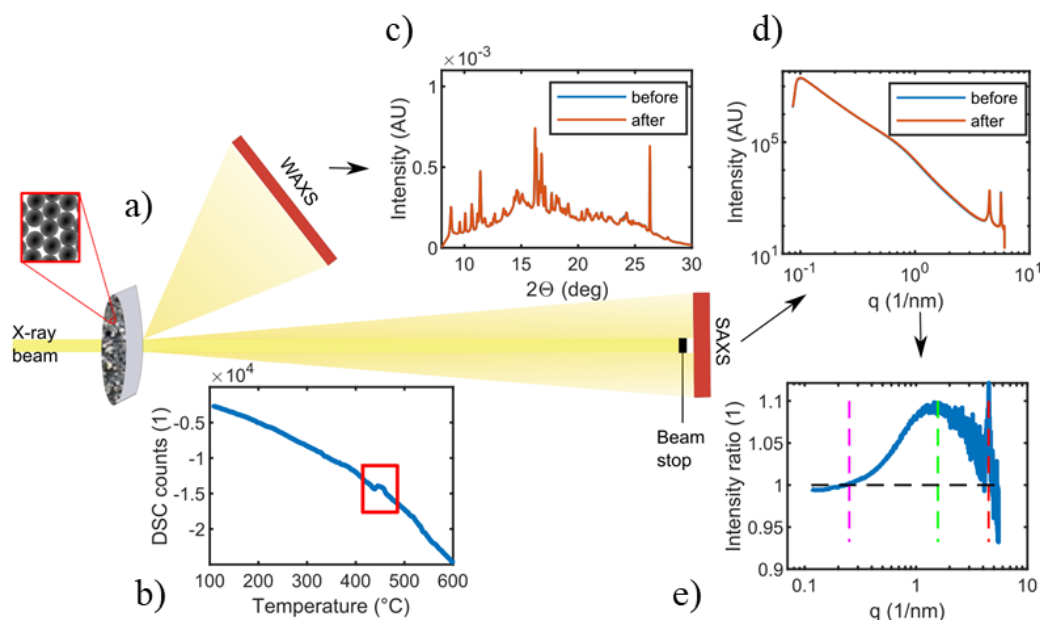


Figure 2.19 Differential scanning calorimetry (DSC), small-angle X-ray scattering (SAXS), and wide-angle X-ray scattering (WAXS) measurements of E-cat FCC particles. (a) Calorimeter with the FCC particles in the X-ray beam and (b) corresponding DSC counts during the calcination procedure. The red square indicates the temperature region of exothermic coke removal. (c) WAXS pattern of the system before and after the calcination confirming the stability of the microstructure, i.e., no loss of crystallinity or any phase change was detected. (d) Radially integrated SAXS patterns before and after the calcination exhibit peaks corresponding to periodic sizes present in the zeolite Y phase of the FCC catalyst. (e) A small but appreciable difference in the pattern can be emphasized by plotting the ratio of the radially integrated SAXS pattern before and after calcination. The ratio unraveled a sharp peak corresponding to the structure periodicity of the zeolite Y d-spacing parameter ($1.40 \text{ nm} = 4.5 \text{ nm}^{-1}$, red dash line), which means that coke has been removed from the micropores of the zeolite phase. The broad peak indicates that larger agglomerates, or clusters, of coke have also been removed that fill some mesopores present in the catalyst. The maximum of the broad peak ($4 \text{ nm} = 1.6 \text{ nm}^{-1}$, green dash line) for example corresponds to a cluster size of three structure periods in zeolite Y. However, also larger coke clusters up to a size of $\sim 21 \text{ nm}$ (magenta dash line) have been removed during calcination freeing up clogged mesopores within the mesoporous phases of the FCC catalyst.

The DSC curve (Figure 2.19b) indicates the heat loss caused by the heat exchange of the calorimeter with the surroundings, which results in the displayed characteristic curve given by the thermal conductivity of aluminum. Even though this background contribution is significant, we clearly see a region around 450 °C, highlighted in the red box, where some additional heat was released from the investigated system. This extra heat loss denotes a change in the investigated system and can only be caused by two phenomena. The first possibility is an exothermic phase change of a component in the catalyst. The second possibility is that the carbon deposits burned out. To rule out the first possibility, we compared the WAXS pattern before and after calcination (Figure 2.19c) to check for any phase change or a loss of crystallinity. The identical WAXS pattern before and after calcination confirm unambiguously that the long-term calcination only removed carbon deposits.

The simultaneously recorded SAXS pattern further allowed investigating micropore broadening during the calcination (Figure 2.19d). To avoid any misinterpretation stemming from a temperature-dependent signal intensity in the SAXS pattern, we compared both non-calcined and calcined pattern at 50 °C. Not surprisingly, the small amount of coke present in the micro- and mesopores of the catalyst causes an almost negligible change in the SAXS pattern during calcination. However, the ratio plot (Figure 2.19e) of the SAXS pattern recorded before and after calcination emphasizes characteristic sizes, i.e., where the catalyst particles scatter more after calcination (ratio values larger than one). The ratio plot reveals a sharp ($1.40 \text{ nm} = 4.5 \text{ nm}^{-1}$, red dashed line) and a broad peak corresponding to increased scattering. The sharp peak denotes to d-spacing parameter of the zeolite Y and shows increased regularity in the zeolite Y periodic structure after coke removing, which clearly indicates that coke was removed from the micropores. The broad peak of increased scattering shows that coke tends to cluster and does not only fill single cavities or pores in the mesoporous phases of the catalyst. The maximum of the broad peak ($4 \text{ nm} = 1.3 \text{ nm}^{-1}$, green dashed line) indicates the size of the most frequent coke clusters that have been removed. Together with the maximum cluster size ($21 \text{ nm} = 0.3 \text{ nm}^{-1}$, magenta dashed line), this increase in scattering after calcination confirmed that coke was present in the zeolite crystallites^[5,57] and other mesoporous phases of the spent catalyst,

which reduced the effective pore diameter and therefore hinders diffusion^[58,59].

2.4.14 X-ray Fluorescence Tomography

To determine correlative 3-D distributions of the poisonous metals, such as iron and nickel, as well as lanthanum, which acts as a marker for the embedded rare-earth exchanged ultra-stable Y zeolites (RE-USY)^[44], the catalyst particle was mapped using X-ray fluorescence (XRF) tomography. X-ray fluorescence tomography was performed at the P06 beamline, PETRA III using a primary photon energy of 15 keV and was focused to a 200 nm × 200 nm beam size by means of KB mirrors. A 200 nm × 200 nm raster scan step size was used resulting in a corresponding pixel size of 200 nm × 200 nm for each projection image. The sample was placed in the focal spot and raster scanned generating a point-by-point image. The X-ray fluorescence signal was detected using a 384-element Maia detector array^[60]. We have used the same sample analyzed by X-ray holotomography placed on the same graphite pin. XRF tomography was accomplished by applying 120 projection angles covering 360°. This imaging strategy was successfully tested previously by our group^[31] to minimize possible self-absorption effect in the E-cat FCC particle. The total time needed for sample mounting and tomography was 16 h. The collected XRF signal was processed using the GeoPIXE^[61] software to fit the summed spectra and then to de-convolute each single pixel XRF spectrum in order to evaluate the relative concentration of the individual metals in 3-D. The resulting individual element specific XRF projection images were aligned and reconstructed using the iterative Algebraic Reconstruction Technique (i-ART) available within the TXM-Wizard software package^[62]. The XRF resolution of 540 ± 180 nm was estimated based on edge line profiles described in Section 2.4.4. Finally, the Avizo Fire software was used for image registration (alignment) of the reconstructed X-ray holotomography and XRF volume data, and 3-D image visualization. Note that although the XRF tomography and Holotomography resolution differ, we still can perform a proper spatial correlation as it was thoroughly discussed by Liu & Meirer et al. ^[38]. To identify and segment metal-rich domains within the catalyst particle the 3-D concentration distribution of Fe and Ni were

thresholded by a value determined from the respective histograms of Fe and Ni single voxel concentrations. For La domain segmentation a different approach was used as La is only present in the zeolite domains and also because their average 2-D size is known from previous work on FCC catalyst particle cross-sections^[63]. Therefore a 3-step segmentation was performed: (i) first a histogram-based thresholding was performed as before for Fe and Ni; next (ii) the local maxima of the La concentration were used as initial markers for separation of individual zeolite domains using (iii) a marker-based watershed segmentation utilizing the distance map calculated from the thresholded data in step (i). Then the parameters used in steps (i-iii) were tuned to achieve the best agreement with literature reporting 2-D sizes between $0.52 \mu\text{m}^2$ and $0.55 \mu\text{m}^2$ for two different equilibrium catalyst (E-cat) particle cross-sections. In this way the final optimal domain size used for segmentation was found as $0.4938 \mu\text{m}^2$.

2.4.15 **Simultaneous Thermogravimetric and Differential Thermal Analysis Combined with Mass Spectrometry**

Simultaneous thermogravimetric and differential thermal analysis combined with mass spectrometry (TG-DTA-MS) was used to estimate the amount of coke in the catalyst batch. We used the combination of a TG-DTA thermal analyzer (Setaram Setsys Evolution, France) with an OmniStarTM quadrupole-type mass spectrometer (Pfeiffer Vacuum, Germany). To distinguish between the weight-loss given by water desorption and the weight loss caused by carbon deposits removal, the sample was first heated in nitrogen atmosphere. The heating started at room temperature and finished at $300 \text{ }^\circ\text{C}$, where the temperature was kept constant for 30 min (Figure 2.20a) to remove all the water from the catalyst batch. The drying period is characterized by a MS peak of water, whilst the CO_2 counts show no change (Figure 2.20a). Water desorption, being an endothermic process, is further confirmed by DTA (Figure 2.20b). After this drying phase, the atmosphere was changed to air (that is and oxygen containing atmosphere), which burned out the carbon deposits. The burning product, CO_2 , was again detected by MS showing a maximum CO_2 evolution at about $520 \text{ }^\circ\text{C}$. The total weight-loss caused by carbon deposits was 1.38 wt.%, which corresponds to a typical

carbon content in commercial equilibrium FCC catalyst^[5,12]. The burning is an exothermic process causing a positive peak in DTA (Figure 2.20c) with a maximum at 480 °C, indicating the temperature at which the major part of the carbon deposits was burned out. The difference between the maximum temperatures found by TGA and CO₂ MS can be attributed to an incomplete burning of carbon deposits at temperatures below 500 °C, which produces heat, CO, and CO₂.

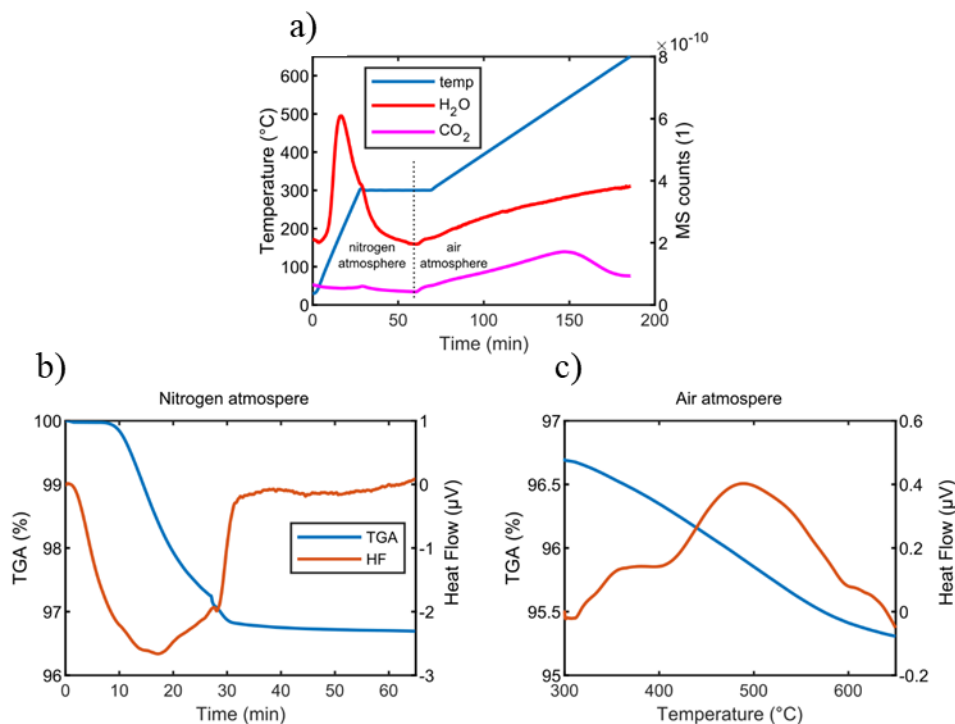


Figure 2.20 Simultaneous thermogravimetric and differential thermal analysis combined with mass spectrometry on coked FCC particles. (a) The temperature program for the drying period in nitrogen atmosphere and for the oxidation period in air atmosphere. The corresponding mass-spectrometry signals for H₂O and CO₂, which distinguish between the two atmospheric regimes is shown. (b) TGA-DTA for the drying period shows the amount of adsorbed water in the FCC catalyst batch. The negative DTA peak corresponds to water desorption, which is an endothermic process. (c) TGA-DTA for the oxidation period shows the weight-loss caused by burning off the carbon deposits. This is an exothermic process confirmed by the positive DTA peak with a maximum at ~480 °C, which is the temperature at which the majority of deposits were burned off.

2.4.16 Single Particle Metrics and Porosity Profiles

Single catalyst particle studies have to rely on the fact that the sample under study is a representative example of the catalyst. We therefore determined a set of single particle metrics to establish a typical aged FCC

catalyst particle that was studied. The single particle metrics (Table 2.3) were calculated based on the segmented data and corresponding total particle volume (TPV), which is a binary representation of the total particle volume including all pores, cavities, and holes in the catalyst body, i.e., the volume of the particle with zero porosity. A detailed description of the individual quantities used and introduced in previous work^[31,39] is provided in the following:

The (degree of) anisotropy of a particle is a measure of its 3-D symmetry and an indicator for structural alignment along a specific direction. It was determined as 1 minus the ratio of the minimum over the maximum eigenvalue of the data cloud obtained by mean intercept length analysis. Mean intercept length analysis is performed with the binarized particle volume and determines the number of (filled) voxels that intersect with a set of oriented rays sent through the volume at different angles. The mean number of intersecting voxels as a function of angle forms the data cloud then used in eigenvalue analysis. Closer equality between the minimum and maximum eigenvalues leads to higher isotropy (i.e., the degree of anisotropy becomes zero), which means that there is no privileged structural direction (e.g., for an isotropic sphere), while the degree of anisotropy becomes 1 for total anisotropy.

The elongation of each particle was determined as the ratio of the medium and the largest eigenvalue of the covariance matrix, causing elongated objects to have values close to zero (a perfect sphere has an elongation of one).

The flatness of each particle was determined as the ratio of the smallest and the medium eigenvalue of the covariance matrix, which means that flat objects have values close to zero (a perfect sphere has a flatness of one).

The roundness/sphericity value is another measure describing how spherical an object is. The roundness/sphericity value is one for a perfect sphere because it is determined as $(\pi^{1/3} (6V)^{2/3})/A$, where V indicates the total particle volume and A the corresponding surface area of the total particle volume.

The equivalent diameter defined as the diameter of a sphere of identical (total particle) volume V and was determined as $(6V/\pi)^{1/3}$.

The total particle surface area is defined as the outer surface of the corresponding TPV.

The macro-pore volume and the corresponding macro-pore surface area were calculated for the pore space of the particle. The calculated values were also normalized to the TPV, which gave values of macro-porosity and macro-pore specific surface area.

To ensure that the individual particle used in the analysis is a statistically representative example for an E-cat particle the above mentioned metrics were compared to previous values reported in literature and were found in good agreement^[31,39]. Furthermore, to confirm the trends of the very small morphological changes reported for the particle, we measured a second FCC catalyst particle of the same batch. The results are reported in Table 2.4 and confirm the statistical significance of the observed trends.

Metric	Non-calcined	Calcined
Anisotropy ^[44]	0.33347	0.33356
Elongation ^[44]	0.7549	0.7553
Flatness ^[44]	0.8829	0.8822
Roundness/Sphericity ^[44]	0.9594	0.8622
Equivalent Diameter (μm)	57.782	57.782
Total Particle Volume (TPV) (μm^3)	101,013.8	101,013.8
Total Particle Volume (TPV) (voxels)	367,824,409	367,821,754
Total Particle Surface Area (μm^2)	10,932.1	12,164.6
Macro-pore volume (μm^3)	15,256	17,636
Macro-pore volume (% of TPV)	15.10	17.46
Macro-pore surface area (μm^2)	61,209	66,101
Macro-pore specific surface area ($\mu\text{m}^2/\mu\text{m}^3$)	0.6059	0.6544

Table 2.3 Single particle metrics based on total particle volume (TPV) and based on segmented data (grey rows).

Metric	Particle 1		Particle 2	
	Non-calcined	Calcined	Non-calcined	Calcined
Anisotropy ^[44]	0.33347	0.33356	0.460906	0.460588
Elongation ^[44]	0.7549	0.7553	0.79583	0.814386
Flatness ^[44]	0.8829	0.8822	0.677398	0.662354
Roundness/Sphericity ^[44]	0.9594	0.8622	0.6652	0.6259
Equivalent Diameter (μm)	57.782	57.782	101.410	101.226
Total Particle Volume (TPV) (μm^3)	101,013.8	101,013.8	547,670	543,100
Total Particle Surface Area (μm^2)	10,932.1	12,164.6	34,602	36,979

Table 2.4 Single particle metrics based on total particle volume (TPV) for both measured FCC catalyst particles.

A comparison of these morphological parameters determined from the data recorded before and after calcination further confirms that almost no morphological changes other than changes in the accessible pore volume took place during calcination. The only change observed was that the total particle volume (TPV), which is defined as the volume of the particle including the pore space, decreased by a very small amount (2655 voxels or 0.0072 %) after calcination. The TPV includes the pore space and is therefore not sensitive to changes in pore space, hence this change was expected as it indicates that matter that absorbed X-rays before calcination was removed from the surface of the particle during coke removal. The fact that this change is so small indicates that only very little coke is actually deposited on the surface of the catalyst. When inspecting the 3-D distribution of coke deposits it further becomes clear that this effect is not likely caused by the noise level in the data, because the removed voxels are not randomly distributed over the whole particle surface (as one would expect if the removal was due to noise in the data) but clustered in patches filling dips and dents in the catalyst particle surface. This observation is confirmed by the significant increase of total particle surface area (defined as the surface of the particle not considering the pores) indicating a rougher surface after calcination, which is further supported by the roundness and sphericity parameters. The latter is a metric characterizing the particle's similarity to a perfect sphere (for which the roundness and sphericity parameters become one). The value before calcination confirms a smooth particle surface, which becomes rough after calcination – this again suggests that (patches of) coke deposits on the surface fill dips and dents in the catalyst's surface, which is in excellent agreement

with earlier observations of a nodulated surface of aged (calcined) FCC catalyst particles^[31,32,39–41,45].

With respect to the observed porosity changes taking place due to calcination we investigated a significant increase in macro-porosity and macro-pore surface area after the calcination step (Figure 2.3 and Table 2.3), which indicates that matter was removed also from the pores of the catalyst particle. Note that the measured porosity here inherently considered the previously reported metals contribution to pore space reduction^[32,38,40,41] since the primary beam energy was above the metal's absorption edge. The mean pore diameter indicates narrower pores in the non-calcined particle, while the total number of segments designates a larger network, implying better interconnectivity of the pore space for the calcined particle. These changes support the idea that carbon deposits actually narrow (and also close) macro-pores. The parameters 'mean shortest path length' and 'mean shortest path tortuosity' are calculated as the average length and average tortuosity of the shortest path connecting every node of the pore network with the surface of the particle. This is a measure for a changing accessibility before and after calcination as it assesses a shortening or prolongation of the shortest diffusion path (i.e., a change in its tortuosity) from the surface to a node and vice-versa. Related to this but focused on pore clogging at the surface is the number of surface access nodes that clearly shows how surface coke deposits significantly reduce the number of open macro-pores in the surface that provide access to the internal pore space of the catalyst.

2.4.17 Pore Network Model Generation

Pore networks were generated from X-ray holotomography data for both the calcined and non-calcined sample (see Section 1.3 for further details). The pore network model represents the catalyst particle's pore structures as a 3-D network of interconnected pores connected via narrow segments preserving not only important properties such as pore diameter and length but also abstracting the complexity of pore space connectivity to a model that is more effective and feasible in terms of computational costs for studying such a very large and complex 3-D pore structure. In FCC catalyst, the majority of the nodes (almost 90%) exist in a main-graph (largest sub-graph in the network)

which plays a crucial role in the accessibility of nodes within the pore network. To prevent the fragmentation of the topology into too many branches, the parameter ‘end of length’ is introduced. This value indicates the minimum length of the branches during skeletonization. Here we used end of length equal to 5 voxels.

To construct the pore network model, we used the binary registered 3-D images from the X-ray holotomography of the non-calcined and the calcined particle. The binary images (1 indicates matter, 0 represents empty space) were thinned to produce a so-called skeleton of the pore space characterizing the topological properties of the pore network. This thinned skeleton is formed by a set of lines with a thickness of 1 voxel that are located precisely in the center of each pore, i.e., with an equidistant distance to the pore boundaries. This pore space skeleton was then converted into a geometrical spatial graph containing nodes (branching points of the network) and segment points (the set of points connecting the nodes) (Figure 1.17). A graph is a set of connected nodes (or segment points), while two graphs, although in the same network, can never be connected. Because the segment points comprise the line located in the center of each pore every segment point is associated a pore radius via its distance to the pore walls. This pore radius can be understood as the radius of a cylinder, which fits best to the pore space it represents.

2.4.18 Effect of Pore Clogging by Means of Pore Network Analysis

To compare the two pore networks before and after the calcination step, we have used the registered datasets and identical parameters for pore network generation. Each pore network consisted of some isolated sub-graphs with nodes that were not connected to the main graph that spanned almost the whole particle. These small sub-graphs represented isolated pores or cavities in the pore space of the analyzed catalyst particle. Note that the majority of all nodes (almost 90%) were found in the main graph, which indicates the high interconnectivity and also accessibility of nodes within the pore network of the catalyst. The number of sub-graphs is therefore a good indicator for the interconnectivity or fragmentation of the catalyst’s pore space into smaller isolated pockets of pore space. When comparing the pore-network before and

after calcination the decrease in the number of sub-graphs reported in Figure 2.3c shows that macro-pore interconnectivity increased in the calcined particle. For both the calcined and non-calcined particle the majority of the small sub-graphs are located close to the surface, again in agreement with earlier work and in line with the observation of a lower macro-porosity in the surface of the particle, which causes lower pore interconnectivity there^[31,32,38].

Because such a pore network model was obtained for both data sets, i.e., before and after calcination, the registered data set allowed a direct comparison of both pore networks and to track any changes of the pore space cause by coke removal as shown in Table 2.5.

Pore network parameters	Non-calcined	Calcined
Mean pore diameter (nm)	94.72	101.12
Total number of segments	24,499	25,702
Mean shortest path length to the surface (μm)	27.34	24.68
Mean shortest path tortuosity	2.3046	2.1678
Number of surface access nodes	247	414

Table 2.5 Effective properties of the pore networks

Here one may be concerned about the pore structure features with the size of one or two voxels (i.e. features below the estimated spatial resolution), which can be characterized as "hot" voxels. However, it is important to mention that all pore size evaluation results are based on the pore network model extracted from the volume images. That is why even a single voxel includes real information. Indeed, this situation is valid only when the voxel is the neighbor of other voxel(s) within an interconnected topology. Because this is an important topic, the influence of spatial 3-D resolution on image and pore network analyses is extensively reviewed in Appendix A.

2.4.19 Permeability Simulation

The absolute permeability expresses the ability of pore space to transport fluids and is independent of the properties of the fluid. Therefore, the absolute permeability values calculated for the same sub-volume in non-calcined and calcined particle evaluate the narrowing and blocking effect of the carbon deposits on mass transport within the pore structure of the sub-volume. To calculate the absolute permeability, we used the Avizo XLabSuite Extension

implemented in the Avizo Software package, which applies the Stokes equation for an incompressible Newtonian fluid in a steady-state flow:

$$\mu \nabla^2 V(\mathbf{x}) = \nabla P(\mathbf{x}) \quad \text{Equation 2.1}$$

$$\nabla \cdot V(\mathbf{x}) = 0 \quad \text{Equation 2.2}$$

where μ is the dynamic viscosity of the fluid, $V(\mathbf{x})$ is the local velocity field, and $P(\mathbf{x})$ is the pressure field) together with Darcy's law

$$Q = \frac{\beta S \Delta P}{\mu L} \quad \text{Equation 2.3}$$

where Q is the total volume flow rate, β is the permeability, S is the cross-section through which the fluid flows, and L is the length of the sample volume. The boundary conditions assumed zero velocity at the fluid-pore interface and a constant pressure difference at the opposite sites of the rectangular sub-volume. We calculated the elements of the permeability tensor from the values of the absolute permeability along all three principal axes of the sub-volume. The main diagonal elements of the absolute permeability tensor, which denote the absolute permeability along the principal axes, are reported in Table 2.6. The effective permeability value for the selected sub-volume was eventually calculated as the average value of the elements on the main diagonal of the permeability tensor. As expected, the effective permeability value increased after removal of carbon deposits. However, a detailed view on the permeability tensors shows two different effects of the carbon deposits: 1) The permeability along the y-axis increased by a factor of 1.34 after calcination. This change is caused by removal of the carbon deposits narrowing and opening the pores (Figure 2.4). The permeability along the z-axis increased by a factor of 231, which correlates to blocked pores by carbon deposits (no flow) along the z-axis before calcination. 3) The negligible change in permeability along the x-axis suggest a very similar (or almost identical) macro-pore structure both in the non-calcined and calcined sub-volume. This similarity highlights the overall precision of the performed imaging, image registration, and image segmentation. Note that the absolute permeability values are in perfect agreement with a previous permeability calculation performed on 31 uniform

sub-volumes of an aged FCC catalyst^[40], where permeability values were found in the range from $6.65 \times 10^{-6} \mu\text{m}^2$ to $4.74 \times 10^{-3} \mu\text{m}^2$.

Absolute permeability tensor–elements on main diagonal	Particle	
	Non-calcined	Calcined
$\beta_{xx} (\mu\text{m}^2)$	1.87×10^{-4}	1.83×10^{-4}
$\beta_{yy} (\mu\text{m}^2)$	2.09×10^{-4}	2.80×10^{-4}
$\beta_{zz} (\mu\text{m}^2)$	0.11×10^{-6}	2.54×10^{-5}
$\beta_{\text{eff}} (\mu\text{m}^2)$	1.32×10^{-4}	1.62×10^{-4}

Table 2.6 Main diagonal elements of the effective permeability tensor determined for the sub-volume reported in Figure 2.4.

2.5 References

- [1] G. Ertl, H. Knözinger, F. Schüth, and J. Weitkamp (Eds.), *Handbook of Heterogeneous Catalysis (2nd ed.)*, Wiley-VCH, Weinheim, **2008**.
- [2] J. Hagen, *Industrial Catalysis, A Practical Approach*, Wiley-VCH, Weinheim, **2008**.
- [3] C. E. Snape, B. J. McGhee, J. M. Andresen, R. Hughes, C. L. Koon, G. Hutchings, *Appl. Catal. A Gen.* **1995**, *129*, 125–132.
- [4] M. Guisnet, P. Magnoux, *Appl. Catal.* **1989**, *54*, 1–27.
- [5] H. S. S. Cerqueira, G. Caeiro, L. Costa, F. Ramôa Ribeiro, *J. Mol. Catal. A Chem.* **2008**, *292*, 1–13.
- [6] J. O. Barth, A. Jentys, J. A. Lercher, *Ind. Eng. Chem. Res.* **2004**, *43*, 2368–2375.
- [7] K. Qian, D. C. Tomczak, E. F. Rakiewicz, R. H. Harding, G. Yaluris, Cheng, X. Zhao, A. W. Peters, *Energy & Fuels* **1997**, *11*, 596–601.
- [8] A. Fonseca, P. Zeuthen, J. B. Nagy, *Fuel* **1995**, *74*, 1267–1276.
- [9] A. Fonseca, P. Zeuthen, J. B. Nagy, *Fuel* **1996**, *75*, 1413–1423.
- [10] A. Fonseca, P. Zeuthen, J. B. Nagy, *Fuel* **1996**, *75*, 1363–1376.
- [11] S. R. Bare, F. D. Vila, M. E. Charochak, S. Prabhakar, W. J. Bradley, C. Jaye, D. A. Fischer, S. T. Hayashi, S. A. Bradley, J. J. Rehr, *ACS Catal.* **2017**, *7*, 1452–1461.
- [12] D. Mance, J. Van der Zwan, M. E. Z. Velthoen, F. Meirer, B. M. Weckhuysen, M. Baldus, E. T. C. Vogt, *Chem. Commun.* **2017**, *53*, 3933–3936.
- [13] H. Shimada, M. Imamura, N. Matsubayashi, T. Saito, T. Tanaka, T. Hayakawa, S. Kure, *Top. Catal.* **2000**, *10*, 265–271.
- [14] D. Espinat, H. Dexpert, E. Freund, G. Martino, M. Couzi, P. Lespade, F. Cruege, *Appl. Catal.* **1985**, *16*, 343–354.
- [15] J. O. Barth, A. Jentys, J. A. Lercher, *Ind. Eng. Chem. Res.* **2004**, *43*, 3097–3104.
- [16] J. Ruiz-Martínez, I. L. C. Buurmans, W. V. Knowles, D. van der Beek, J. A. Bergwerff, E. T. C. Vogt, B. M. Weckhuysen, *Appl. Catal. A Gen.* **2012**, *419–420*, 84–94.
- [17] D. A. Jacobs, G. C. Smith, R. D. Vis, A. F. H. Wielers, *J. Catal.* **1998**, *176*, 387–394.
- [18] S. Mitchell, N.-L. Michels, K. Kunze, J. Pérez-Ramírez, *Nat. Chem.* **2012**, *4*, 825–831.
- [19] J. E. Schmidt, J. D. Poplawsky, B. Mazumder, Ö. Attila, D. Fu, D. A. M. de Winter, F. Meirer, S. R. Bare, B. M. Weckhuysen, *Angew. Chem. Int. Ed.* **2016**, *55*, 11173–11177.
- [20] J. E. Zuliani, T. Miyata, T. Mizoguchi, J. Feng, D. W. Kirk, C. Q. Jia, *Fuel* **2016**, *178*, 124–128.
- [21] E. Tracz, R. Scholz, T. Borowiecki, *Appl. Catal.* **1990**, *66*, 133–147.
- [22] J. R. Rostrup-Nielsen, **1984**, pp. 1–117.
- [23] M. Zbuzek, A. Vráblík, V. Tukač, M. Veselý, A. Prokešová, R. Černý, *Catal. Today* **2015**, *256*, 261–268.
- [24] O. Orhan, E. Haffner-Staton, A. La Rocca, M. Fay, *Tribol. Int.* **2016**, *104*, 272–284.
- [25] O. Ersen, J. Werckmann, M. Houllé, M.-J. Ledoux, C. Pham-Huu, *Nano Lett.* **2007**, *7*, 1898–1907.
- [26] I. K. van Ravenhorst, C. Vogt, H. Oosterbeek, K. W. Bossers, J. G. Moya-Cancino, A. P. van Bavel, A. M. J. van der Eerden, D. Vine, F. M. F. de Groot, F. Meirer, B. M. Weckhuysen, *Angew. Chem. Int. Ed.* **2018**, *57*, 11957–11962.
- [27] Q. Qian, J. Ruiz-Martínez, M. Mokhtar, A. M. Asiri, S. A. Al-Thabaiti, S. N. Basahel, B. M. Weckhuysen, *Catal. Today* **2014**, *226*, 14–24.
- [28] G. T. Whiting, N. Nikolopoulos, I. Nikolopoulos, A. D. Chowdhury, B. M. Weckhuysen, *Nat. Chem.* **2019**, *11*, 23–31.

- [29] F. Meirer, B. M. Weckhuysen, *Nat. Rev. Mater.* **2018**, *3*, 324–340.
- [30] I. Union, O. F. Pure, A. Chemistry, J. Rouquerol, D. Avnir, C. W. Fairbridge, D. H. Everett, J. M. Haynes, N. Pernicone, J. D. F. Ramsay, K. S. W. Sing, K. K. Unger, I. Union, O. F. Pure, A. Chemistry, J. Rouquerol, D. Avnir, C. W. Fairbridge, D. H. Everett, J. M. Haynes, N. Pernicone, J. D. F. Ramsay, K. S. W. Sing, K. K. Unger, *Pure Appl. Chem.* **1994**, *66*, 1739–1758.
- [31] F. Meirer, S. Kalirai, D. Morris, S. Soparawalla, Y. Liu, G. Mesu, J. C. Andrews, B. M. Weckhuysen, *Sci. Adv.* **2015**, *1*(3), e1400199.
- [32] J. Ihli, R. R. Jacob, M. Holler, M. Guizar-Sicairos, A. Diaz, J. C. da Silva, D. Ferreira Sanchez, F. Krumeich, D. Grolimund, M. Taddei, W. C. Cheng, Y. Shu, A. Menzel, J. A. van Bokhoven, *Nat. Commun.* **2017**, *8*, 809.
- [33] P. Sprenger, T. Sheppard, J.-P. Suuronen, A. Gaur, F. Benzi, J.-D. Grunwaldt, *Catalysts* **2018**, *8*, 356.
- [34] Y. Schuurman, C. Delattre, I. Pitault, J. P. Reymond, M. Forissier, *Chem. Eng. Sci.* **2005**, *60*, 1007–1017.
- [35] Y. S. Zhang, X. Lu, R. E. Owen, G. Manos, R. Xu, F. R. Wang, W. C. Maskell, P. R. Shearing, D. J. L. L. Brett, *Appl. Catal. B Environ.* **2020**, *263*, 118329.
- [36] S. Haitao, D. Zhijian, Z. Yuxia, T. Huiping, *Catal. Commun.* **2011**, *16*, 70–74.
- [37] C. A. Trujillo, U. N. Uribe, P.-P. Knops-Gerrits, L. A. Oviedo A, P. A. Jacobs, *J. Catal.* **1997**, *168*, 1–15.
- [38] Y. Liu, F. Meirer, C. M. Krest, S. Webb, B. M. Weckhuysen, *Nat. Commun.* **2016**, *7*, 12634.
- [39] S. R. Bare, M. E. Charochak, S. D. Kelly, B. Lai, J. Wang, Y. C. K. Chen-Wiegart, *CheCatChem* **2014**, *6*, n/a-n/a.
- [40] F. Meirer, D. T. Morris, S. Kalirai, Y. Liu, J. C. Andrews, B. M. Weckhuysen, *J. Am. Chem. Soc.* **2015**, *137*, 102–105.
- [41] F. Meirer, S. Kalirai, J. N. Weker, Y. Liu, J. C. Andrews, B. M. Weckhuysen, *Chem. Commun.* **2015**, *51*, 8097–8100.
- [42] S. Kalirai, U. Boesenberg, G. Falkenberg, F. Meirer, B. M. Weckhuysen, *ChemCatChem* **2015**, *7*, 3674–3682.
- [43] M. Guisnet, P. Magnoux, D. Martin, *Studies in Surface Science and Catalysis*, **1997**, *111*, 1–19.
- [44] E. T. C. C. Vogt, B. M. Weckhuysen, *Chem. Soc. Rev.* **2015**, *44*, 7342–7370.
- [45] F. Krumeich, J. Ihli, Y. Shu, W.-C. Cheng, J. A. van Bokhoven, *ACS Catal.* **2018**, *8*, 4591–4599.
- [46] T. Salditt, M. Osterhoff, M. Krenkel, R. N. Wilke, M. Priebe, M. Bartels, S. Kalbfleisch, M. Sprung, *J. Synchrotron Radiat.* **2015**, *22*, 867–878.
- [47] P. Cloetens, W. Ludwig, J. Baruchel, D. Van Dyck, J. Van Landuyt, J. P. Guigay, M. Schlenker, *Appl. Phys. Lett.* **1999**, *75*, 2912–2914.
- [48] S. Zabler, P. Cloetens, J.-P. Guigay, J. Baruchel, M. Schlenker, *Rev. Sci. Instrum.* **2005**, *76*, 073705.
- [49] L. D. Turner, B. B. Dhal, J. P. Hayes, A. P. Mancuso, K. A. Nugent, D. Paterson, R. E. Scholten, C. Q. Tran, A. G. Peele, *Opt. Express* **2004**, *12*, 2960.
- [50] M. Guizar-Sicairos, S. T. Thurman, J. R. Fienup, *Opt. Lett.* **2008**, *33*, 156.
- [51] P. Perona, J. Malik, *IEEE Trans. Pattern Anal. Mach. Intell.* **1990**, *12*, 629–639.
- [52] F. Meyer, *Signal Processing* **1994**, *38*, 113–125.
- [53] M. van Heel, M. Schatz, *J. Struct. Biol.* **2005**, *151*, 250–262.
- [54] M. Holler, A. Diaz, M. Guizar-Sicairos, P. Karvinen, E. Färm, E. Härkönen, M. Ritala, A. Menzel, J. Raabe, O. Bunk, *Sci. Rep.* **2014**, *4*, 3857.
- [55] D. G. Lowe, in *Proc. Seventh IEEE Int. Conf. Comput. Vis.*, IEEE, **1999**, *2*, 1150–1157.
- [56] R. Sadeghbeigi, *Fluid Catalytic Cracking Handbook*, Elsevier, Amsterdam, **2012**.
- [57] G. Caeiro, J. Lopes, P. Magnoux, P. Ayrault, F. Ramoaribeiro, *J. Catal.* **2007**, *249*, 234–243.
- [58] P. D. Hopkins, J. T. Miller, B. L. Meyers, G. J. Ray, R. T. Roginski, M. A. Kuehne, H. H. Kung, *Appl. Catal. A Gen.* **1996**, *136*, 29–48.
- [59] B. A. Williams, S. M. Babitz, J. T. Miller, R. Q. Snurr, H. H. Kung, *Appl. Catal. A Gen.* **1999**, *177*, 161–175.
- [60] U. Boesenberg, C. G. Ryan, R. Kirkham, D. P. Siddons, M. Alfeld, J. Garrevoet, T. Núñez, T. Claussen, T. Kracht, G. Falkenberg, *J. Synchrotron Radiat.* **2016**, *23*, 1550–1560.
- [61] C. G. Ryan, D. R. Cousens, S. H. Sie, W. L. Griffin, *Nucl. Inst. Methods Phys. Res. B* **1990**, *49*, 271–276.
- [62] Y. Liu, F. Meirer, P. A. Williams, J. Wang, J. C. Andrews, P. Pianetta, *J. Synchrotron Radiat.* **2012**, *19*, 281–287.
- [63] S. Kalirai, P. P. Paalanen, J. Wang, F. Meirer, B. M. Weckhuysen, *Angew. Chem. Ed.* **2016**, *55*, 11134–11138.

**3. Morphological Heterogeneity in
Metallocene-Type Ethylene
Polymerization Catalysts**

In this Chapter, the morphological heterogeneity of a silica-supported ethylene polymerization catalyst at different stages of polymerization will be discussed. During olefin polymerization on supported catalysts, the controlled morphological evolution of the catalyst is vital for ensuring optimal product properties and high catalyst activity. Non-destructive hard X-ray holotomography was employed to determine the morphology of multiple silica-supported hafnocene-based catalyst particles during the early-stages of gas-phase ethylene polymerization. Image processing and pore network modeling revealed clear variations in the dimensions and interconnectivity of the pristine particles' macro-pore networks. Furthermore, marked differences in fragmentation behavior were observed in pre-polymerized particles, suggesting that the reactivity of individual particles is largely dictated by their unique support and pore space architectures. Under mild experimental conditions, layer-by-layer fragmentation was observed both at the particle surface and, to a significant degree, in the particle interior. This implies that appropriate pre-polymerization conditions and catalyst kinetics can guarantee sufficient accessibility of a particle's inner volume for incoming ethylene monomer, thereby promoting a more homogeneous fragmentation of the catalyst support.

This Chapter is based on: Maximilian J. Werny, Roozbeh Valadian, Leon M. Lohse, Anna-Lena Robisch, Silvia Zanoni, Coen Hendriksen, Bert M. Weckhuysen, and Florian Meirer, *Chem Catalysis*, 2021, doi: <https://doi.org/10.1016/j.checat.2021.10.008>. This Chapter will also be part of the PhD Thesis of Maximilian Werny.

3.1 Introduction

In supported olefin polymerization catalysts, polymer formation at the active sites leads to the disintegration of the porous catalyst support, thereby yielding a complex composite material that is constituted by the obtained polymer and fragments of the support. With early-stage support fragmentation known to play a vital role in maintaining catalytic activity as well as determining the final polymer particle morphology and properties^[1-7], significant research efforts have been directed towards visualizing the morphology of olefin polymerization catalyst particles. From a mechanistic point of view, experimentally observed support fragmentation depends both on the catalyst properties (i.e., active sites, support properties and kinetics), the applied reaction conditions (i.e., pressure, temperature and process type) as well as the properties of the formed polymer (i.e., crystallinity and viscoelasticity). In order to obtain novel insights into this complex process, well-defined morphological studies, focused on the variation of a limited number of parameters during the initial stages of olefin polymerization, are required. While the morphology of olefin polymerization catalysts is usually assessed in 2-D by means of microtoming and scanning electron microscopy (SEM)^[2,8-13], high-resolution 3-D imaging techniques can contribute decisively by delivering quantitative information on the fragmentation of entire catalyst particles.^[7,14,15]

Over the years, X-ray microscopy has become an invaluable tool for the characterization of catalyst particles due to its non-invasive and non-destructive nature, its capacity to enable full 3-D imaging due to the high penetration power of hard X-rays, as well as its steadily increasing spatial resolution.^[16-20] While several investigations have been performed on the 3-D distribution of metals within catalyst particles^[14,21-27], mapping the 3-D distribution of low atomic number (Z) materials with hard X-ray tomography remains challenging^[28]. In the field of olefin polymerization catalysis, synchrotron- and lab-based hard X-ray computed tomography (CT) techniques have been successfully used in the past to determine the morphology of both low Z polymer and the support in individual catalyst particles^[29-37]. Despite the technique's capacity to deliver sub-100 nm

resolutions^[15,38,39], it is limited by its long measurement times (e.g., 22 h for a $120 \times 120 \times 20 \mu\text{m}^3$ in reference 15, $\approx 220 \mu\text{m}^3/\text{min}$). This can complicate the characterization of more extensive sample sets, especially when multiple (larger) particles from different batches or reaction stages are subject to investigation.

In this Chapter, the morphological evolution of a silica-supported hafnocene-based catalyst during the initial stages of gas-phase ethylene polymerization using full-field hard X-ray holotomography was studied. Inline holograms, collected at different angles and sample-detector distances, were used to reconstruct 3-D representations of individual catalyst particles, with grayscale values that are proportional to the particles' relative electron density distributions^[40]. Holotomography relies on propagation-based phase-contrast and is thus suitable for visualizing low Z materials at sub-micron spatial resolution^[26,28,40–45]. Moreover, its superior acquisition speed (2.5 h for $90 \times 90 \times 81 \mu\text{m}^3$, 4 distances, $\approx 4400 \mu\text{m}^3/\text{min}$) enables high sample throughput. Thus, multiple catalyst particles from five different reaction stages *ex situ* (pristine, 1 min, 10 min, 30 min and 60 min) were analyzed. In contrast to the mesoporous MgCl_2 support of the previously discussed Ziegler-type catalyst^[15], the silica support of the here examined catalyst is significantly larger (pristine: $D_{50} = 25.0 \mu\text{m}$) and less friable. These properties, together with the support's extensive macro-pore networks (Figure 3.1), are assumed to have a direct impact on the process of support fragmentation. To assess this, the porosity, composition, and phase distribution of the individual catalyst particles were determined based on the mapped relative electron density differences between the constituent phases. Furthermore, the dimensions and connectivity of the particles' respective macro-pore networks were evaluated by means of pore network modeling.^[21–23] This in-depth analysis not only provided valuable insights into the morphological heterogeneity amongst pristine catalyst particles, but also revealed notable differences in reaction progress and morphology amongst pre-polymerized particles of the same batch. The divergent behavior amongst individual catalyst particles implies correlations between the particles' reactivities and their initial support morphologies, which, in turn, can severely affect mass and heat transfer during ethylene polymerization. Fragmentation

was generally observed to occur in large portions of the catalyst particles, thus implying a sufficient accessibility of the particle interior for ethylene gas under the given experimental conditions.

3.2 Results and Discussion

The hafnocene-based catalyst material was pre-polymerized with ethylene under mild conditions for different amounts of time to obtain low polymer yield samples that were suitable for our investigations on the early-stage fragmentation of the catalyst (1 min/10 min/30 min/60 min, 1.6 bar ethylene, room temperature, yielding 0.7–6.4 g_{PE}/g_{cat}, PE = polyethylene; Table 3.2, Section 3.4.2). Holotomographic scans (Figure 3.1a) were performed on randomly selected pristine and pre-polymerized catalyst particles (Figure 3.1b) at the GINIX end station of the PETRA III storage ring, DESY, Hamburg (Section 3.4.4). The particles were either embedded in epoxy glue (denoted as ‘E’, Figure 3.1c) or mounted in Kapton capillaries (denoted as ‘K’, Figure 3.1c) and scanned at a low photon energy of 8 keV at multiple distances (Z_1 – Z_4) to the detector. The combination of these two preparation techniques allowed us to identify optimal measurement conditions for the low Z PE/silica composite materials. A total of 12 pristine and pre-polymerized particles, labelled as **E₀**, **K₀**, **E₁**, **K₁**, **E₁₀**, **K₁₀**, **K₃₀₋₁**, **K₃₀₋₂**, **E₆₀₋₁**, **E₆₀₋₂**, **K₆₀₋₁** and **K₆₀₋₂** in accordance with their respective reaction stages, were measured and reconstructed (Figure 3.1c; Sections 3.4.4 and 3.4.5). Prior to image segmentation post-processing, the data sets were binned by a factor of 2 to reduce their size. The particles’ corresponding grayscale volumes were subsequently segmented into pore space and solid phase to study the particles’ microstructure in 3-D as well as their respective macro-pore networks (Section 3.4.5).

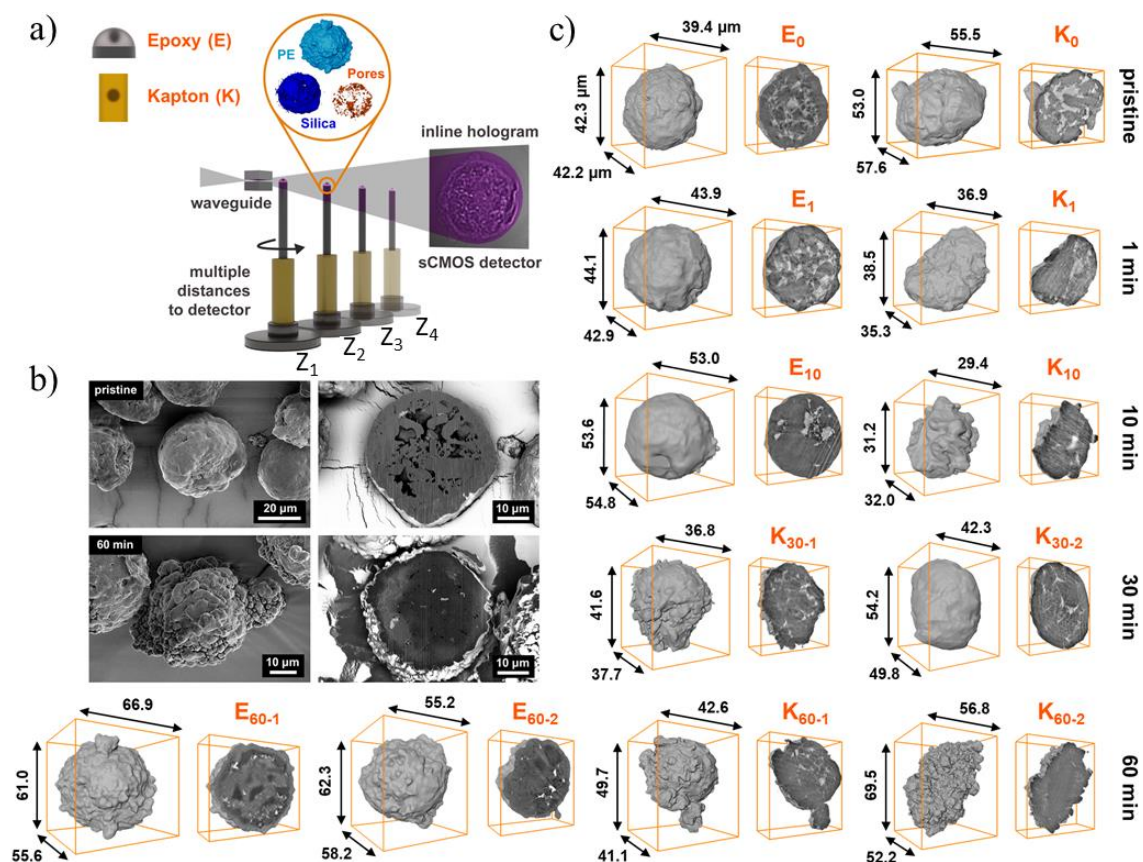


Figure 3.1 a) Schematic of the propagation-based phase contrast imaging set-up (GINIX) at the P10 beamline of the PETRA III storage ring, DESY. Monochromatic X-rays are focused by Kirkpatrick-Baez (KB) mirrors (not shown here) onto a waveguide. The polymerization catalyst particle, which is either embedded in epoxy glue or mounted inside a Kapton capillary, is illuminated by a cone beam from this coherent point source and rotated for tomographic measurements. A sCMOS camera, placed approximately 5 m behind the sample, is used for detection. Scans are performed at multiple distances to the detector (max. 4). A phase-retrieval procedure is applied to the collected holograms to obtain the corresponding 2-D phase shift images (related to the relative electron density distribution), which are then used to reconstruct the scanned specimen via a filtered back-projection algorithm. b) Scanning electron microscopy (SEM) images of a pristine and 60 min pre-polymerized hafnocene-based catalyst particle (gas-phase, 1.6 bar, room temperature) (light gray: silica support, dark gray: PE). c) Reconstructed volumes of the pristine (E_0 , K_0), 1 min (E_1 , K_1), 10 min (E_{10} , K_{10}), 30 min (K_{30-1} , K_{30-2}) and 60 min pre-polymerized (E_{60-1} , E_{60-2} , K_{60-1} , K_{60-2}) hafnocene-based catalyst particles as well as their corresponding virtual particle cross-sections (white/light gray: low relative electron density, macro-pores; gray: intermediate relative electron density, PE-dominant phase; dark gray: high relative electron density, silica-dominant phase).

As can be seen in Figure 3.1b, all catalyst particles possess a well-defined external and internal morphology. In fact, the pristine and 60 min pre-polymerized catalyst particles are comparable to the scanning electron microscopy (SEM) images recorded of catalyst particles from the same batch

shown in Figure 3.6. While the pristine (**E**₀, **K**₀) and 1 min pre-polymerized (**E**₁, **K**₁; 0.7 g_{PE}/g_{cat}) catalyst particles possess smooth external surfaces, the 60 min pre-polymerized particles (**E**₆₀₋₁, **E**₆₀₋₂, **K**₆₀₋₁, **K**₆₀₋₂; 6.4 g_{PE}/g_{cat}) feature a cauliflower-like morphology, indicating a significant build-up of PE at the surface. The surface morphologies of particles **E**₁₀₋₁, **K**₁₀₋₁, **K**₃₀₋₁, and **K**₃₀₋₂ vary and may be indicative of their respective polymerization degrees.

In general, the obtained phase contrast and, thus, the ability to differentiate between phases in the particle interior, were found to depend on the type of sample preparation. In the case of the pre-polymerized particles mounted in Kapton capillaries, the PE and silica phases could not be differentiated at 8 keV. This is presumably related to a large difference in refractive index between the particle and the surrounding air. Significantly higher contrast was, however, achieved by embedding the catalyst particles in epoxy glue. As is evident from the reconstructed cross-sections of the 60 min pre-polymerized catalyst particles **E**₆₀₋₁ and **E**₆₀₋₂ (Figure 3.1c), macro-pores (low relative electron density (ED), white/light gray), a PE-dominant phase (intermediate relative ED, gray) and a silica-dominant phase (high relative ED, dark gray), featuring pristine and fragmented support granulates, are distinguishable at more advanced reaction stages. The classification into PE- and silica-dominant phases was adopted to account for the resolution limitations of the technique (Table 3.3; Section 3.4.6) as well as the high degree of intermixing of the PE and silica phases (Figure 3.1b, Figure 3.6), which together effectively inhibit the differentiation of the two phases at length scales below the achieved spatial resolutions.

In order to segment these three phases, a k-means clustering algorithm ($k = 3$), was applied to the corresponding data sets. This ensured comparability of the extracted data between the measured catalyst particles. Silica fragments, polymer domains and pores smaller than the determined spatial resolutions (246–546 nm, Table 3.3; Section 3.4.6) were excluded from the analysis of the segmented images. It must be noted that polymer could not be detected in the remaining epoxy-embedded particles **E**₁ and **E**₁₀, presumably due to the low amounts of PE that were formed and/or resolution limitations.

Based on the segmented grayscale images, the porosity and macro-pore volume (V_{mp}) of each particle were determined (Table 3.1, Section 3.4.5). As expected, a gradual decline in porosity is generally observed with increasing polymerization degree. While the pristine particles \mathbf{E}_0 and \mathbf{K}_0 and the 1 min pre-polymerized particle \mathbf{E}_1 ($0.7 \text{ g}_{PE}/\text{g}_{cat}$) feature comparatively high porosities in the range of 12–13%, the porosities of the 60 min pre-polymerized particles \mathbf{E}_{60-1} , \mathbf{E}_{60-2} , and \mathbf{K}_{60-2} ($6.4 \text{ g}_{PE}/\text{g}_{cat}$) fall in the range of 1–3%. In order to obtain a more thorough understanding for the spatial distribution of the macro-pores, radial analysis^[21,22,46] was applied to all particles as shown Figure 3.2. Here, the porosity of each concentric single pixel shell of the catalyst particles was plotted as a function of the normalized Euclidean distance to the particle surfaces (d_s) ($d_{s,surface} = 0$, $d_{s,central \text{ voxel}} = 1$). All catalyst particles display low porosity in close vicinity to their respective surfaces ($d_s \leq 0.1$) and a subsequent increase in porosity when moving towards to the particle center. The observed fluctuations can be attributed to structural heterogeneity within the individual catalyst particles. The previously discussed decrease in porosity, as a function of reaction progress, is easily discernible from the two radial analysis plots shown in Figure 3.2.

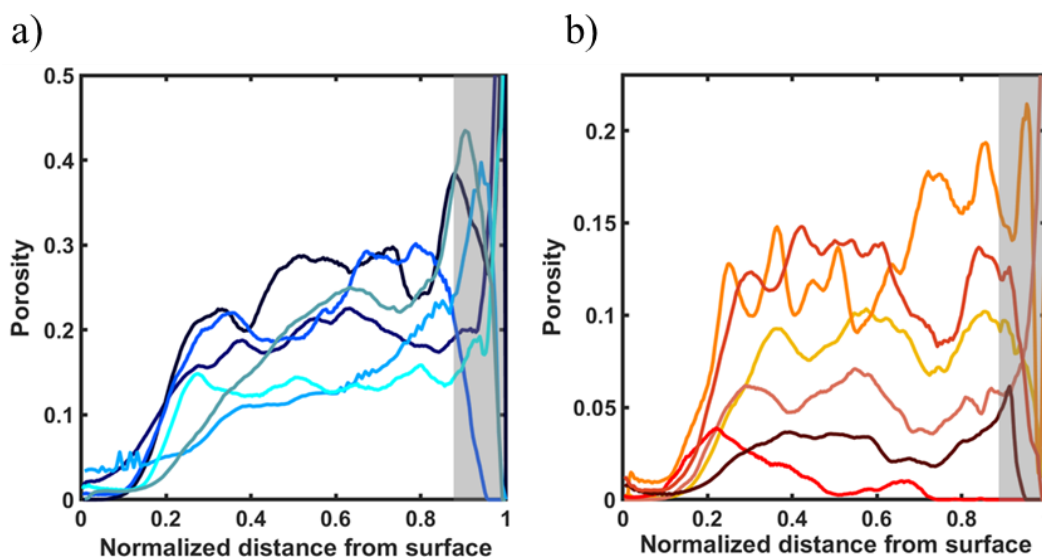


Figure 3.2 a) and b) show the radial analysis of the reconstructed catalyst particles' porosity. The porosity of each concentric single voxel shell was plotted as a function of the normalized distance from the particle surface (d_s ; center: $d_s = 1$, surface: $d_s = 0$). The final 5–10% of the radial analysis (light gray) are typically ignored due to the limited number of voxels per shell at low remaining particle volumes (statistically insignificant regime).

To further assess the properties of the catalyst particles' respective macro-pore networks, pore network models (PNMs), representing the macro-pore volume of the measured catalyst particles, were generated based on the binarized (segmented) pore space images (images for PNMs binned by a total factor of 4; Section 3.4.7, Section 1.3). By performing a binning simulation explained in Appendix A, a limited effect of the binning procedure on the results of the pore network model and grayscale image analysis was determined. Using the sub-graphs, the connectivity and tortuosity of the catalyst particles' macro-pore networks were determined (Table 3.1; Section 3.4.7). Note that pores smaller than the obtained spatial resolutions were not assessed. To determine the average connectivity of all nodes in the respective PNMs, the nodes connectivity ratio (NCR) was calculated for each network. This corresponds to the ratio of connected nodes to the total number of nodes in all sub-graphs of a pore network (Appendix A). While a large NCR value denotes a high connectivity of a PNM's nodes, a small value indicates a lower connectivity of the pore space. The tortuosity of the pore networks was also deduced from the averaged ratio of the mean real distance between connected nodes (i.e., the distance along open pores) to the corresponding mean Euclidean distance between nodes.

	Equivalent spherical diameter (ESD) [μm]	Porosity	Macro-pore volume (V_{mp}) [μm^3]	Number of sub-graphs	Graph nodes connectivity ratio (NCR)	Mean dist. between connected nodes [μm]	Mean Euclidean dist. between connected nodes [μm]	Mean tortuosity
E₀	38.3	0.13	3819	106	0.93	197.5	105.2	1.91
K₀	40.2	0.12	4069	350	0.74	329.6	144.2	2.31
E₁	35.2	0.12	2750	149	0.89	240.8	115.2	2.16
K₁	23.7	0.08	561	206	0.72	163.0	79.3	2.09
E₁₀	43.1	0.08	3352	288	0.79	296.7	130.5	2.27
K₁₀	18.6	0.08	268	130	0.37	138.8	54.1	2.58
K₃₀₋₁	29.3	0.04	529	418	0.25	169.3	70.4	2.49
K₃₀₋₂	34.9	0.07	1563	1890	0.76	363.9	134.1	2.76
E₆₀₋₁	60.4	0.01	1155	361	0.03	51.8	28.7	1.73
E₆₀₋₂	52.6	0.03	2291	202	0.09	142.9	60.9	2.29
K₆₀₋₁	35.1	0.06	1359	517	0.60	268.9	94.0	2.95
K₆₀₋₂	49.4	0.02	1259	586	0.04	75.6	39.3	1.89

Table 3.1 Metrics for the pristine (E₀, K₀), 1 min (E₁, K₁), 10 min (E₁₀, K₁₀), 30 min (K₃₀₋₁, K₃₀₋₂) and 60 min pre-polymerized (E₆₀₋₁, E₆₀₋₂, K₆₀₋₁, K₆₀₋₂) hafnocene-based catalyst particle reconstructions, as derived via image segmentation, pore network modeling (PNM) and analysis.

The high NCRs (≥ 0.74) and porosities ($\geq 12\%$) (Table 3.1) that were obtained for the pristine catalyst particles **E₀** and **K₀** and the pre-polymerized catalyst particle **E₁** imply that the particles feature accessible and interconnected macro-pore networks at reaction onset. These allow ethylene to diffuse to large portions of the catalyst body. In contrast to this, the pre-polymerized catalyst particles **E₆₀₋₁**, **E₆₀₋₂** and **K₆₀₋₂** were evaluated to have relatively low NCR values (≤ 0.09) and porosities ($\leq 3\%$) (Table 3.1). This considerable reduction in macro-pore connectivity and porosity at low PE yields is assumed to impede mass transport throughout the catalyst particles at a relatively early reaction stage. No clear trend in tortuosity was observed as a function of reaction time.

In general, the strong divergence of the above-mentioned metrics (i.e., porosity, NCR, tortuosity; Table 3.1) amongst catalyst particles from the same batch clearly indicates morphological heterogeneity, both in pristine and pre-polymerized particles. For the latter, such variations can be attributed to differences in reactivity. For example, the 10 min pre-polymerized catalyst particle **K₁₀**, in contrast to particle **E₁₀**, possesses a comparatively low NCR value (0.37). This, together with its uneven surface morphology (polymer-rich, Figure 3.1c), suggests that the particle is more polymerized. A possible explanation is given by its rather small dimensions (ESD = 18.6 μm), which may have facilitated a relatively fast diffusion of ethylene throughout the particle. Another notable deviation was observed in catalyst particle **K₆₀₋₁**, which, considering its reaction stage, features a comparatively high porosity (0.06) and NCR (0.60). This could be related to its initial support morphology. A similar observation also applies to catalyst particle **K₃₀₋₂**, which possesses a high NCR (0.76) and intermediate porosity (0.07). All in all, these outliers suggest that the reactivity of individual catalyst particles is related to their initial support and pore space architectures, which, in turn, govern mass and heat transport within the particles.

Because polymerization and concurrent fragmentation are both expected to be correlated to the spatial arrangement of macro-pores, we visualized the 3-D distribution of pore space sub-volumina (i.e., connected pore space voxels) and their relative distances to the catalyst particles' centroids (i.e., geometric center) in so-called dispersion plots as shown in Figure 3.3 (more

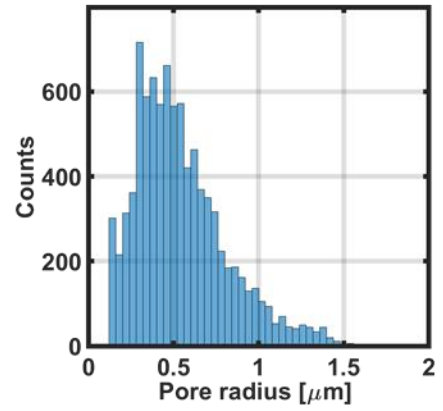
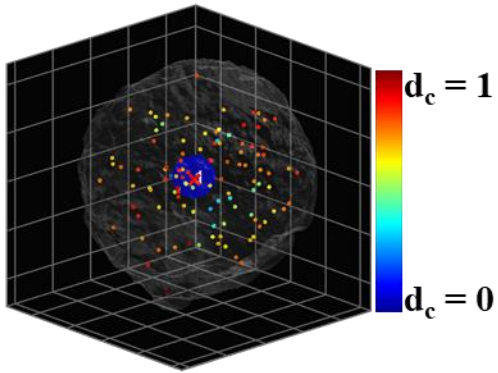
details on dispersion plots are provided in Section 3.4.8). Here, all pore space sub-volumina of the catalyst particles are visualized as small spheres, with the color of a sphere indicating the sub-volume's distance to the catalyst particle's centroid, denoted with a red cross in the respective figures. Each sphere is positioned at the centroid of the corresponding sub-volume and scales directly with the sub-volume's dimensions. The sphere representing the largest sub-volume therefore has the largest diameter and is labelled as '1' while sub-volumina smaller than 1% of the largest sub-volume ($V_{\text{threshold}} = 0.01 \times V_{\text{max}}$) are visualized as spheres with a fixed diameter. As is apparent from Figure 3.3, the pristine catalyst particles \mathbf{E}_0 and \mathbf{K}_0 are dominated by a single, extensive pore space sub-volume. In addition to this, smaller sub-volumina that are disconnected from the largest sub-volume are visible throughout the two particles. While particle \mathbf{E}_0 features a low number of disconnected sub-volumina, particle \mathbf{K}_0 features a significantly higher concentration of disconnected sub-volumina. This is also reflected by the larger number of sub-graphs in the PNM of particle \mathbf{K}_0 (350) relative to particle \mathbf{E}_0 (106) (Table 3.1). Both metrics indicate a lower degree of connectivity in catalyst particle \mathbf{K}_0 , where approximately 6% of the macro-pore volume is disconnected from the central macro-pore system ($(V_{\text{mp}} - V_{\text{max}})/V_{\text{mp}}$), versus 0.5% in catalyst particle \mathbf{E}_0 . Similar conclusions, in terms of connectivity, were also drawn from the calculated NCRs (lower NCR for \mathbf{K}_0 relative to \mathbf{E}_0). These variations in pore space connectivity can lead to differences in reactivity during the initial reaction stages.

Finally, the established PNMs were used to approximate the catalyst particles' respective (macro)pore size distributions (PSDs) (Figure 3.3). As can be seen in Figure 3.3, both pristine catalyst particles feature pores with diameters of 0.2 μm –3.4 μm , with a majority of the pore diameters falling in the range of 0.6–1.6 μm . The data stands in agreement with the pore size distribution of a comparable silica-supported metallocene, which was assessed via mercury porosimetry (Figure 3.8). More pronounced differences in the PSDs are observed in the pre-polymerized catalyst particles. The PSDs, together with the previously discussed radial analysis, NCRs, and dispersion plots clearly illustrate the variations in dimensions, interconnectivity, and spatial distribution of the macro-pores in both pristine and pre-polymerized

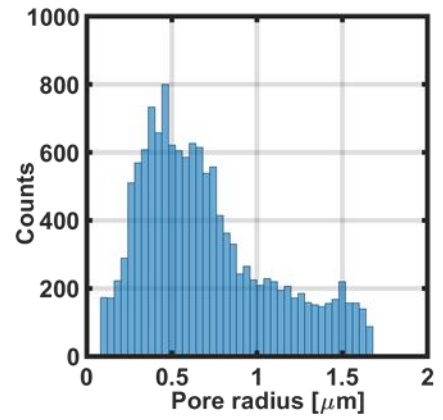
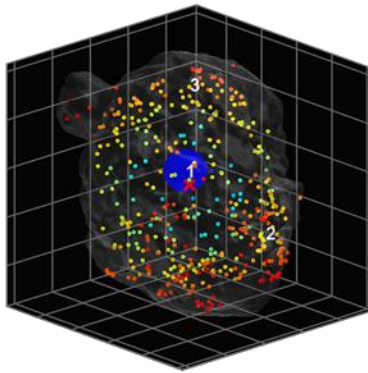
catalyst particles. This has considerable implications for both mass transport and reaction kinetics at the single particle level and can explain the morphological heterogeneity in pre-polymerized catalyst samples.

As mentioned above, the 3-D distribution of PE- and silica-dominant phases as well as macro-pores was determined for the pre-polymerized catalyst particles **E₆₀₋₁** and **E₆₀₋₂** (6.4 g_{PE}/g_{cat}), based on the reconstructed and segmented X-ray holotomography data (Figure 3.4a-d; Section 3.4.5). This yielded quantitative information on the particles' composition as well as phase distribution. While the two catalyst particles feature very similar percentages of pore space (1% vs 3%), particle **E₆₀₋₁** consists of a higher percentage of PE-dominant phase (67%) than particle **E₆₀₋₂** (59%). Radial phase distribution analysis revealed a high concentration of PE-dominant phase at the external surface of the catalyst particles (Figure 3.4e,f). In fact, both catalyst particles are enveloped by a thick layer of polymer-dominant phase. As can be deduced from the corresponding radial analysis plots, the polyethylene-rich shell occupies 15–20% in diameter of particle **E₆₀₋₂**, while the value is slightly lower for particle **E₆₀₋₁**. In both particles, diffusion limitations are likely to arise due to this pronounced surface build-up of polymer and consequent pore blocking.

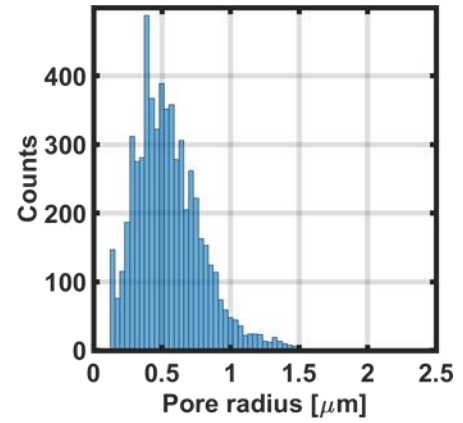
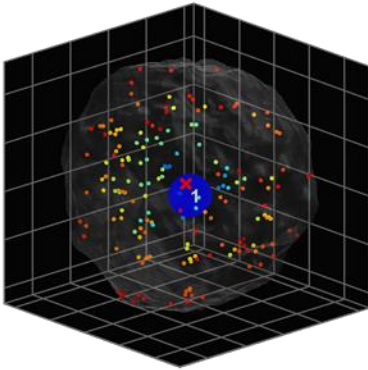
E_0



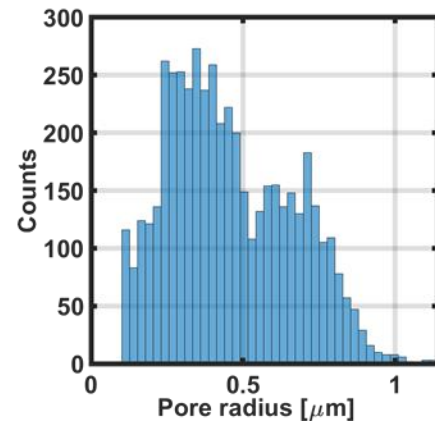
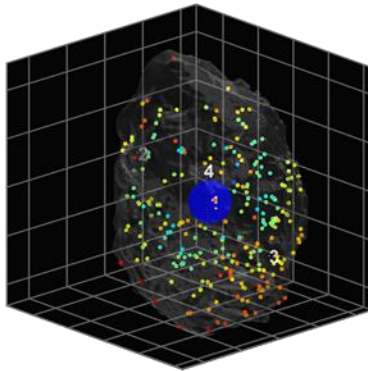
K_0

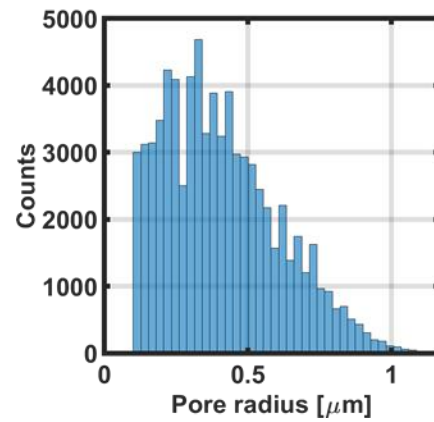
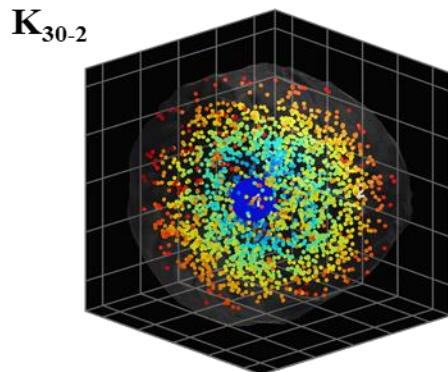
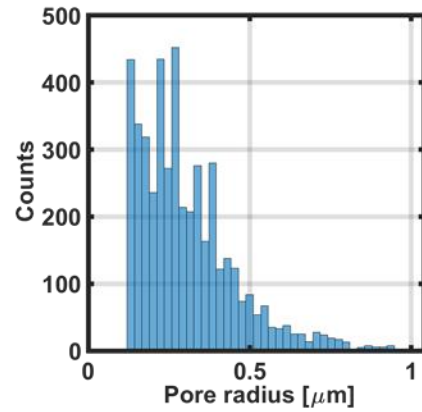
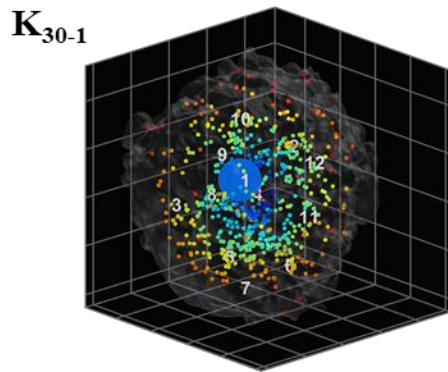
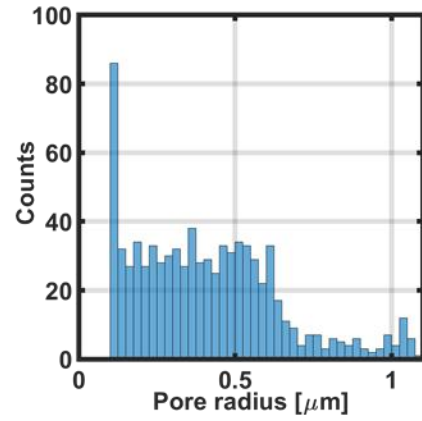
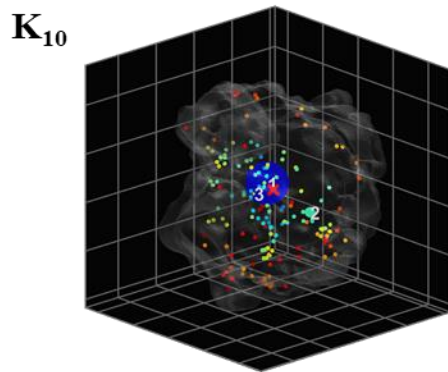
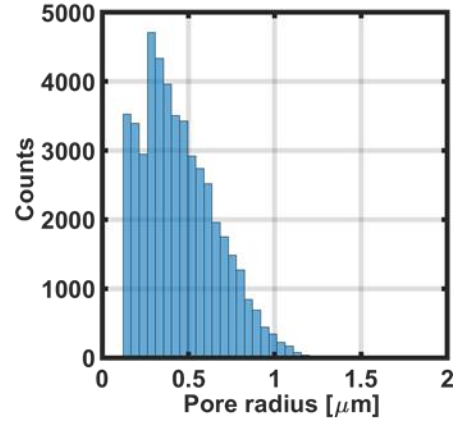
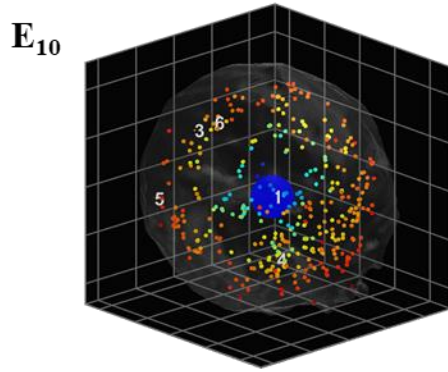


E_1

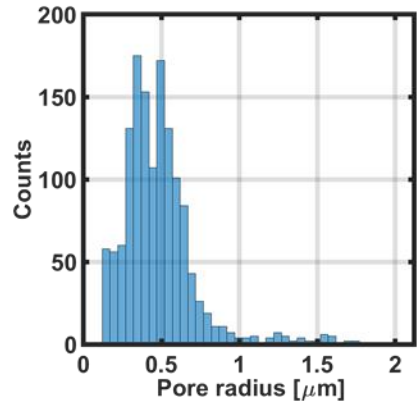
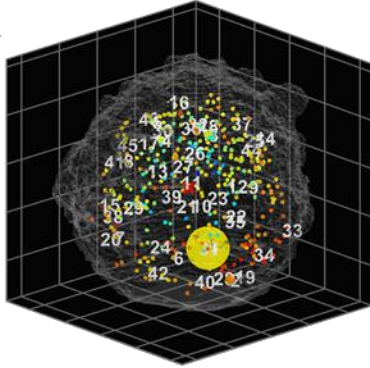


K_1

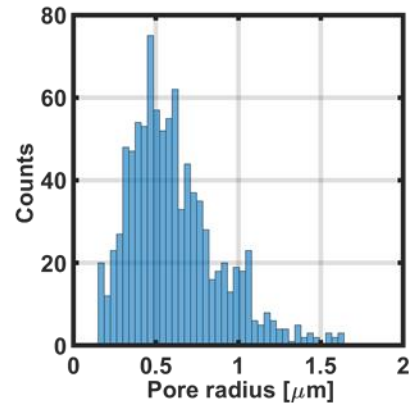
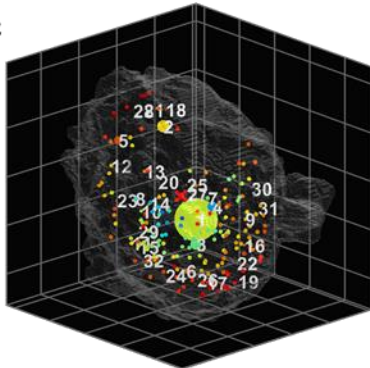




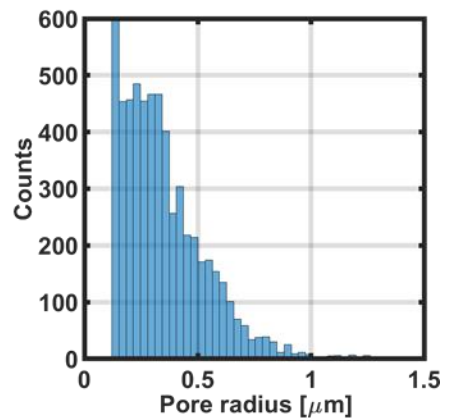
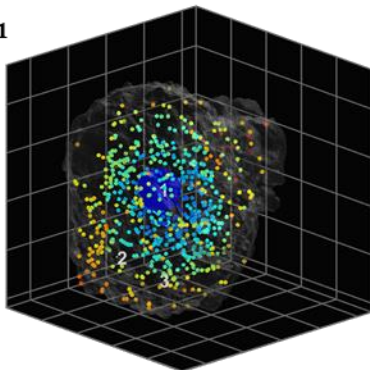
E₆₀₋₁



E₆₀₋₂



K₆₀₋₁



K₆₀₋₂

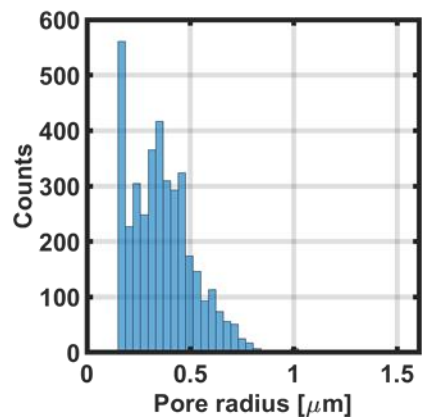
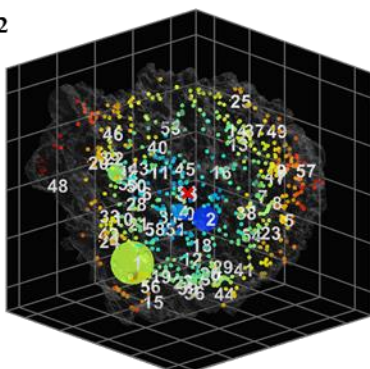


Figure 3.3 Dispersion plot and pore size distribution for the macro-pore space sub-volumina of all particles. d_c denotes the distance of a pore space sub-volume to the particle's centroid. The maximum pore space volume and the threshold of all particles used in dispersion plots are as follows: E_0 ($V_{\max} = 3800 \mu\text{m}^3$, $V_{\text{threshold}} = 38 \mu\text{m}^3$), K_0 ($V_{\max} = 3816 \mu\text{m}^3$, $V_{\text{threshold}} = 38 \mu\text{m}^3$), E_1 ($V_{\max} = 2636 \mu\text{m}^3$, $V_{\text{threshold}} = 26 \mu\text{m}^3$), K_1 ($V_{\max} = 498 \mu\text{m}^3$, $V_{\text{threshold}} = 5.0 \mu\text{m}^3$), E_{10} ($V_{\max} = 2843 \mu\text{m}^3$, $V_{\text{threshold}} = 28 \mu\text{m}^3$), K_{10} ($V_{\max} = 187 \mu\text{m}^3$, $V_{\text{threshold}} = 1.9 \mu\text{m}^3$), K_{30-1} ($V_{\max} = 303 \mu\text{m}^3$, $V_{\text{threshold}} = 3.0 \mu\text{m}^3$), K_{30-2} ($V_{\max} = 1237 \mu\text{m}^3$, $V_{\text{threshold}} = 12 \mu\text{m}^3$), E_{60-1} ($V_{\max} = 658 \mu\text{m}^3$, $V_{\text{threshold}} = 6.6 \mu\text{m}^3$), E_{60-2} ($V_{\max} = 447 \mu\text{m}^3$, $V_{\text{threshold}} = 4.5 \mu\text{m}^3$), K_{60-1} ($V_{\max} = 1215 \mu\text{m}^3$, $V_{\text{threshold}} = 12 \mu\text{m}^3$) and K_{60-2} ($V_{\max} = 183 \mu\text{m}^3$, $V_{\text{threshold}} = 1.8 \mu\text{m}^3$).

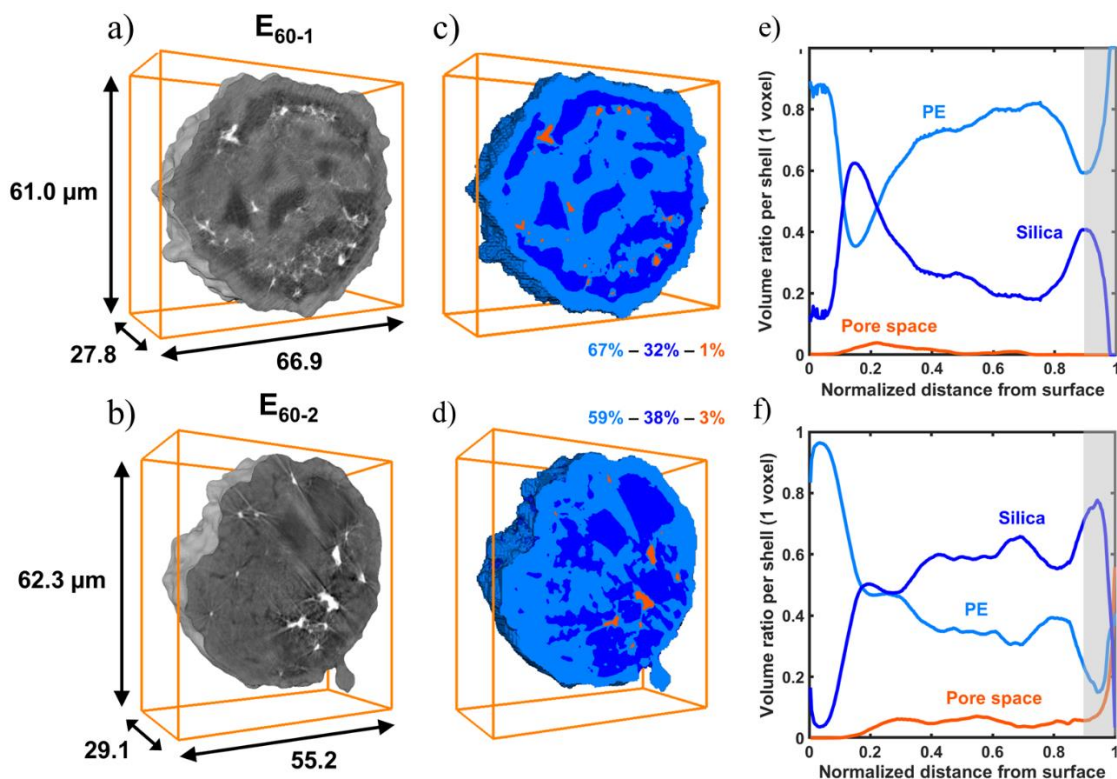


Figure 3.4 (a) and (b) show reconstructed volumes and cross-sections of particles E_{60-1} and E_{60-2} (grayscale). (c) and (d) Segmented volumes and cross-sections of particles E_{60-1} and E_{60-2} (light blue: polymer-dominant phase, dark blue: silica-dominant phase, orange: macro-pores). (e) and (f) show the radial analysis of the particle composition for E_{60-1} and E_{60-2} (d_s ; central voxel: $d_s = 1$, surface: $d_s = 0$). The final 5–10% of the radial analysis (light gray) are typically ignored due to the limited number of voxels per shell at low remaining particle volumes (statistically insignificant regime).

Further notable differences, in terms of composition and phase distribution, become apparent when inspecting the catalyst particles' respective interiors. Particle E_{60-1} exhibits a higher concentration of residual silica-dominant phase close to its surface, directly below the layer of PE. The particle interior is, however, primarily constituted by PE-dominant phase. Similar phase distributions were also observed for other catalyst particles that

were assessed qualitatively in 2-D with FIB-SEM (Figure 3.1b and Figure 3.6). The presence of substantial amounts of polymer-dominant phase in the particle interior as well as larger residual support-dominant phase in its outer sphere both indicate a strong involvement of the catalyst particle interior's accessible active sites in the polymerization process. Similar conclusions can also be drawn from reports by Conner *et al.*^[29,31] and Ruddick and Badyal^[47], who detected residual support fragments at the surface of other silica-supported catalyst systems at comparatively higher PE yields.

The internal morphology of particle **E₆₀₋₂** differs strongly in comparison to that of particle **E₆₀₋₁**. In fact, its inner volume is constituted by more than 50% silica-dominant phase, thus indicating a less advanced degree of fragmentation. The surface build-up of polymer, in combination with potentially unfavorable dimensions and connectivity of the catalyst particle's macro-pore network, may have induced diffusion limitations, which consequently lead to a lower accessibility of the particle interior for gaseous ethylene monomer. A similar catalyst particle morphology was indeed also reported by Zanoni *et al.* for a gas-phase pre-polymerized zirconocene-based catalyst.^[48] Hence, even under mild experimental conditions and at low polymer yields, diffusion limitations are highly likely to influence the polymerization rate and fragmentation of individual catalyst particles during gas-phase ethylene polymerization.

To further investigate the non-uniform fragmentation behavior of the two catalyst particles of interest, the number and average volume of silica-dominant and PE-dominant sub-volumina was determined as a function of their distance to the particles' respective centroids (d_c) (Figure 3.5). The analysis was performed using the segmented grayscale images. In both catalyst particles, the largest support- and polymer-dominant sub-volumina are located close to the particle centroids. This is also apparent from their corresponding dispersion plots (support-dominant sub-volumina: Figure 3.5b,f, polymer-dominant sub-volumina: Figure 3.5d,h). Featuring average volumes in the order of 10^4 – 10^5 μm^3 , these extensive silica- or PE-dominant sub-volumina occupy large portions of the catalyst particles' volumes. It is important to note, however, that the sub-volumina are irregular in shape and size.

When considering the remaining smaller sub-volumina, notable differences can be observed between particle **E₆₀₋₁** and particle **E₆₀₋₂**. As is evident from the corresponding histograms, the interior of catalyst particle **E₆₀₋₁** ($d_c < 0.8$) mainly features a limited number of low and intermediate volume silica-dominant sub-volumina ($10^{-3} \mu\text{m}^3 < V_{\text{avg, support}} < 10^1 \mu\text{m}^3$) while its periphery ($d_c > 0.8$) is constituted by a comparatively high number of low volume silica-dominant sub-volumina ($10^{-3} \mu\text{m}^3 < V_{\text{avg, support}} < 10^0 \mu\text{m}^3$) (Figure 3.5a,b). PE-dominant sub-volumina, mostly low in volume ($10^{-3} \mu\text{m}^3 < V_{\text{avg, polymer}} < 10^0 \mu\text{m}^3$), are predominantly found in the outer sphere of the particle ($d_c > 0.8$) (Figure 3.5c,d). Catalyst particle **E₆₀₋₂**, on the other hand, possesses a substantially higher number of low volume silica-dominant sub-volumina ($10^{-3} \mu\text{m}^3 < V_{\text{avg, support}} < 10^0 \mu\text{m}^3$) that are dispersed throughout the particle (Figure 3.5e,f). In contrast to particle **E₆₀₋₁**, the PE-dominant sub-volumina of particle **E₆₀₋₂** are mostly located in the particle interior ($d_c < 0.8$) and have a limited volume ($10^{-3} \mu\text{m}^3 < V_{\text{avg, polymer}} < 10^0 \mu\text{m}^3$) (Figure 3.5g,h). The higher total number (denoted as Σ) and dispersion of detectable silica-dominant sub-volumina in particle **E₆₀₋₂**, compared to particle **E₆₀₋₁**, further support the assumption that the particle is in a less advanced reaction stage. As previously observed in the radial analysis, both catalyst particles feature higher concentrations of residual support fragments close to the particle surface (represented by red and orange spheres in corresponding dispersion plots, Figure 3.5b,f) where layer-by-layer fragmentation is assumed to be dominant.^[2] The same can be seen in FIB-SEM images shown in Figure 3.6 as well.

With the collected tomography data clearly indicating strong morphological heterogeneity amongst pristine catalyst particles, the differences in fragmentation and reactivity between particles **E₆₀₋₁** and **E₆₀₋₂** was ascribed mainly to the specific arrangement and connectivity of their pristine silica support granulates. Mass transport and reaction kinetics at the single particle level are governed by the resulting non-ordered macro-pore networks and their corresponding accessibilities. This can be referred to findings by Abboud et al.^[49] and Machado et al.^[50], who observed non-uniform fragmentation behavior for silica-supported Ziegler-Natta and metallocene-based catalysts, respectively. While a catalyst's support structure

is key to its morphological evolution, heterogeneous fragmentation pathways may also be partially introduced by the higher local accessibility of a certain particle domain or surface for incoming monomer gas at the onset of the reaction. These differences in accessibility may arise from particles' contact with other catalyst particles (agglomeration) or even the walls of the reactor. Consideration must also be given to the distribution of the metallocene complex, which may not be homogeneous at the sub-micron scale and will thus affect the local activity and fragmentation phenomena.

The absence of significant ruptures, propagating through the entire volume of the respective catalyst particles, can lead to a pronounced sectioning pathway rarely occurs at particle level^[14,35,51] under the given experimental conditions (1.6 bar, room temperature, gas-phase). Instead, a strong involvement of a layer-by-layer fragmentation mechanism^[2,35,51] is postulated, both at the particle and individual silica domain level,^[48] due to the high accessibility of the particles' interior volume for ethylene gas (Figure 3.1b,c). While the interior of catalyst particle **E₆₀₋₁** is assumed to have polymerized to a significant degree following this mechanism, the fragmentation of the interior of catalyst particle **E₆₀₋₂** was presumably impeded by diffusion limitations. In this case, the onset of more pronounced mass transfer limitations may lead to a larger involvement of the sectioning mechanism, which would otherwise remain more subdued under mild experimental conditions.

Based on the obtained data, a high degree of homogeneous support fragmentation may be achieved by means of i) controlled pre-polymerization under carefully selected operating conditions (i.e., low temperature and pressure) and ii) by using a catalyst with appropriate kinetics. Alternatively, a pre-polymerization with a less reactive monomer (e.g., propylene) can be performed, which is expected to yield similar results. In addition to the already discussed support configuration, both the applied experimental conditions and catalyst kinetics are instrumental in determining the accessibility of the silica granulates during the initial stages of the reaction.

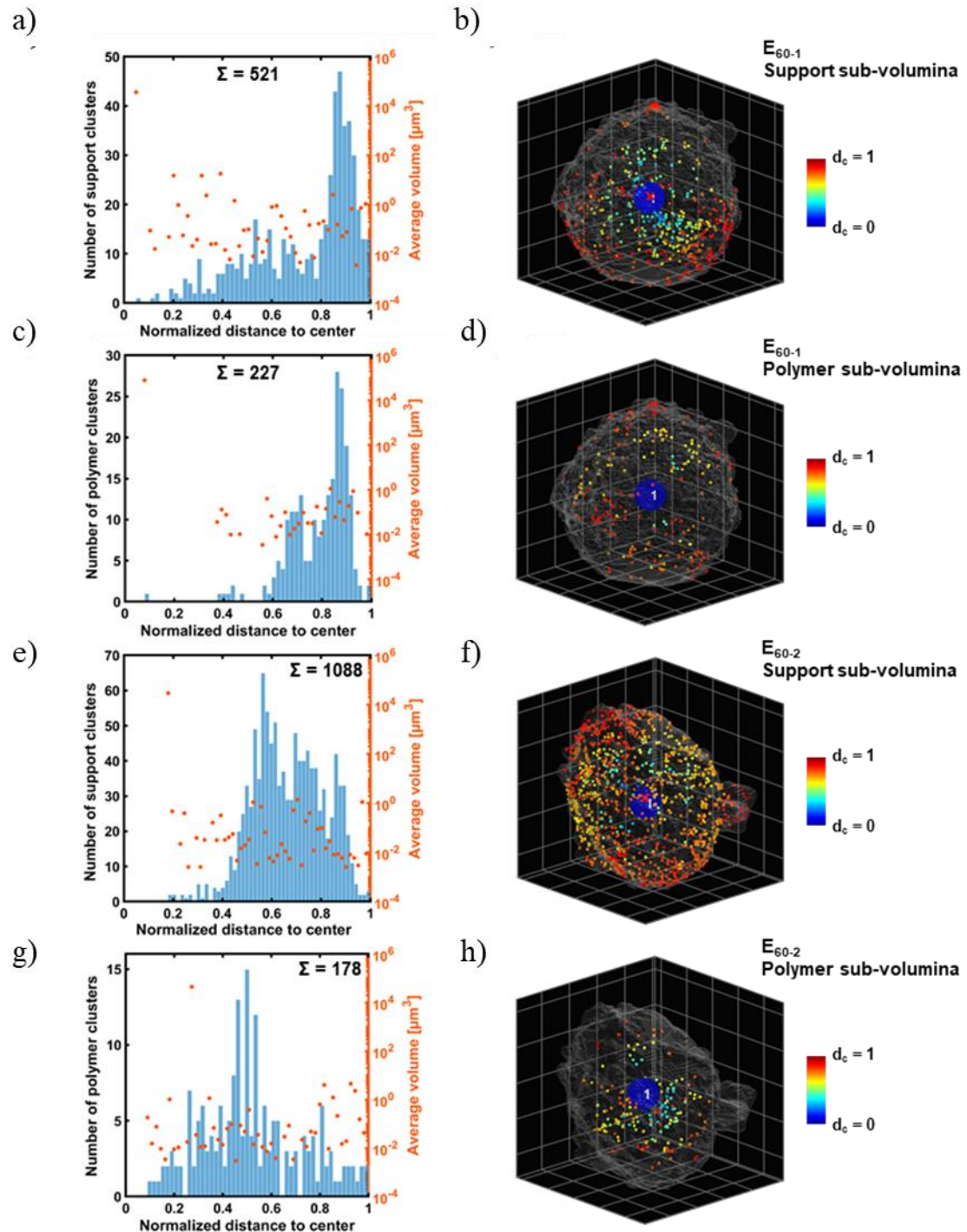


Figure 3.5 a) Number and average volume (V_{avg}) of silica-dominant sub-volumina (per bin) as a function of the normalized distance to the particle centroid (d_c) for particle E₆₀₋₁ (center: $d_c = 0$, surface: $d_c = 1$). The total number of sub-volumina per particle is denoted as Σ . b) Dispersion plot for the silica-dominant sub-volumina of particle E₆₀₋₁ ($V_{\text{max}} = 36371 \mu\text{m}^3$, $V_{\text{threshold}} = 364 \mu\text{m}^3$). c) Number and average volume (V_{avg}) of PE-dominant sub-volumina for particle E₆₀₋₁. d) Dispersion plot for the PE-dominant sub-volumina of particle E₆₀₋₁ ($V_{\text{max}} = 77089 \mu\text{m}^3$, $V_{\text{threshold}} = 771 \mu\text{m}^3$). e) Number and average volume (V_{avg}) of silica-dominant sub-volumina for particle E₆₀₋₂. f)

Dispersion plot for the silica-dominant sub-volumina of particle E₆₀₋₂ ($V_{\max} = 29152 \mu\text{m}^3$, $V_{\text{threshold}} = 292 \mu\text{m}^3$). g) Number and average volume (V_{avg}) of PE-dominant sub-volumina for particle E₆₀₋₂. h) Dispersion plot for the PE-dominant sub-volumina of particle E₆₀₋₂ ($V_{\max} = 44726 \mu\text{m}^3$, $V_{\text{threshold}} = 447 \mu\text{m}^3$).

3.3 Conclusions

Owing to its high spatial resolution (down to 246 nm), relatively low measurement times and good sensitivity for low Z elements, full-field hard X-ray holotomography has been shown to be highly suitable for obtaining quantitative information on the morphological evolution of supported olefin polymerization catalysts. The high acquisition speed of the technique facilitated the characterization of multiple hafnocene-based catalyst particles at five different stages of polymerization. Image processing and analysis delivered quantitative insights into the particles' composition, porosity as well as the 3-D distribution of support- and polymer-dominant sub-volumina within. This was further refined with a radial analysis of the support, polymer, and macro-pore space distribution. Differences in pore space interconnectivity, tortuosity and pore size distribution were revealed by means of pore network modeling amongst both pristine and pre-polymerized catalyst particles. Furthermore, deviations in catalyst support fragmentation were evident at more advanced reaction stages. Based on the above-mentioned analysis and results, the notable interparticle heterogeneity, observed both in terms of fragmentation degree and pathway, can be attributed to the unique configuration of the particles' respective supports and pore space networks. The general decrease in porosity and macro-pore space connectivity that was observed with increasing polymer yields underlines the importance of controlled catalyst support fragmentation in overcoming potential mass transfer limitations. A high degree of homogeneous support fragmentation, mainly manifested in form of a layer-by-layer mechanism, was achieved by means of (pre-)polymerization under mild conditions. On the whole, holotomography is not only suitable for obtaining highly resolved morphological and chemical information on polymerization catalysts at high sample throughput, but also, on any other catalyst system, potentially, under reaction conditions.

3.4 Experimental Section

3.4.1 Catalyst Synthesis

The hafnocene-based catalyst was synthesized and provided by Saudi Basic Industries Corporation (SABIC). In a first step, ES757 silica (PQ Corporation, $D_{50} = 25.0 \mu\text{m}$, $S_{\text{BET}} = 295 \text{ m}^2/\text{g}$, $V_{\text{Pore}} = 1.6 \text{ mL/g}$) was calcined for 4 h at 600 °C. The silica was then impregnated with a solution of a 2,2'-biphenylene-bis-2-indenyl HfCl_2 complex and methylaluminoxane (MAO, co-catalyst, 30 wt%, Chemtura; Al/Hf molar ratio = 150) in dried toluene (Braun solvent purification system). A free-flowing powder was finally obtained after removing the solvent by a stream of N_2 at room temperature for 20 h. A weight loading of ~0.59 wt% Hf was determined for the catalyst via X-ray fluorescence (XRF) analysis.

3.4.2 Catalyst Pre-polymerization

All pre-polymerization experiments were conducted at room temperature in a nitrogen-filled glovebox under inert conditions. Approximately 6.7 mg of the hafnocene-based catalyst were placed in a dedicated glass-reactor (~100 mL) and subjected to constant ethylene pressure (1.6 bar) for the designated time periods (Table 3.2). The ethylene gas was fed to the reactor via a gas line installed inside the glovebox. In order to reduce agglomeration and the degree of overheating during the exothermic polymerization reaction, the catalyst powder was well dispersed inside the reactor. All experiments were conducted under static conditions (no fluidization or stirring). The pre-polymerized catalyst samples were weighed outside of the glovebox to determine their respective polyethylene yields.

Time [min]	1	10	30	60
Catalyst yield [$\text{g}_{\text{PE}}/\text{g}_{\text{cat}}$]	0.7	1.4	2.6	6.7

Table 3.2 Polyethylene (PE) yields in $\text{g}_{\text{PE}}/\text{g}_{\text{cat}}$ as obtained during the gas-phase polymerization of ethylene over the hafnocene-based catalyst in a dedicated glass-reactor set-up (1.6 bar C_2H_4 , room temperature).

3.4.3 Focused Ion Beam - Scanning Electron Microscopy

A FEI Helios NanoLab G3 UC scanning electron microscope was employed for the focused ion beam - scanning electron microscopy (FIB-SEM) experiments following a procedure from literature.^[52]

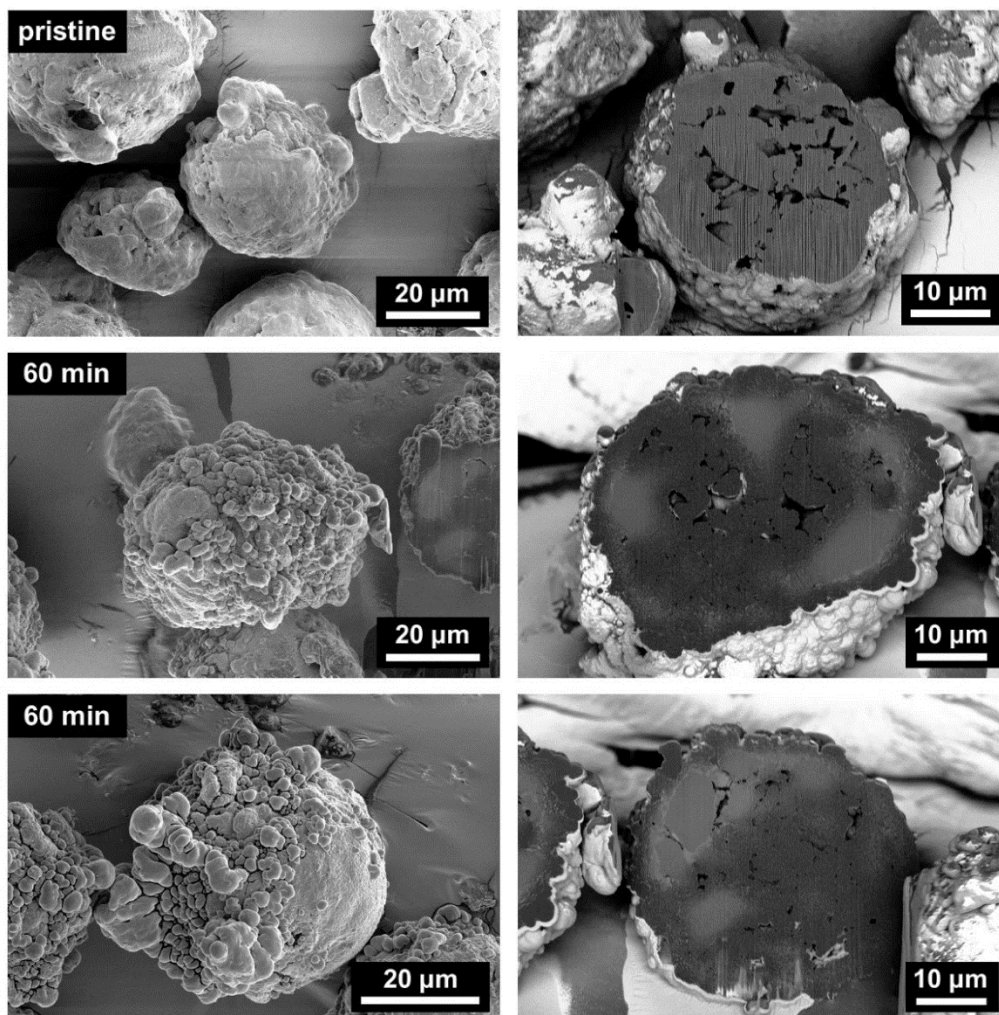


Figure 3.6 Scanning electron microscopy (SEM) images of pristine and 60 min pre-polymerized hafnocene-based catalyst particles (gas-phase, 1.6 bar, room temperature) and their corresponding cross-sections (left: recorded in SE mode, right: recorded in BSE mode). The full particle and cross-sectional images were acquired at different stage tilt and rotation angles. The vertical stripes in the cross-sectional images are artifacts from FIB cutting.

The samples were dispersed over a double-sided adhesive, conductive carbon tape, which was then mounted on an Aluminum SEM stub. A Cressington 208HR sputter coater was utilized to apply a Pt coating of ~ 6 nm.

Slices were milled horizontally to the surface using a 45° angled SEM stub. SEM images were recorded at 2 kV and 0.1 nA, either in secondary electron (SE) mode using an Everhart-Thornley detector, or in backscattered electron (BSE) mode using a Through the Lens Detector (TLD) in combination with an immersion lens (Figure 3.6).

3.4.4 Hard X-ray Holotomography

X-ray holotomography was performed on multiple pristine and pre-polymerized hafnocene-based catalyst particles using the Göttingen Instrument for Nano-Imaging with X-Rays (GINIX) set-up at the P10 beamline, located at the PETRA III storage ring, Deutsches Elektronen Synchrotron (DESY), Hamburg, Germany.^[53] The set-up is highly suitable for near-field phase-contrast imaging at high magnification and resolution. All measurements were performed at a photon energy of 8 keV using a Si (111) channel-cut monochromator. The X-ray beam was focused by Kirkpatrick-Baez (KB) mirrors to a size of approximately 300 x 300 nm². A 1 mm long silicon waveguide with a sub-100 nm guiding layer, fabricated by e-beam lithography (Eulitha, Switzerland) and capped by wafer bonding, was placed in the focal plane of the KB mirror to reduce high-frequency artifacts arising from inhomogeneities on the mirror surface, improve the focal spot size and increase the coherence of the X-ray beam.^[53] A Zyla 5.5 sCMOS detector (Andor) with a pixel size of 6.5 μm was employed approximately 5 m after the sample. In general, holograms were acquired at a minimum of one and at a maximum of four different source-to-sample distances, leading to slightly different effective propagation distances. The acquisition of holograms was performed at multiple distances (see Section 1.2.3 and references^[40,54] for further details). Depending on the source-to-sample distance, an effective pixel size between 53.5 nm and 79.0 nm was obtained. Approximately 2–4 h were required per sample for mounting, alignment and holotomography. At every source-to-sample distance, 1000 projections were acquired over an angular range of 180°.

In terms of sample preparation, the individual polymerization catalyst particles were either embedded in X-ray transparent epoxy glue (Araldite® Rapid epoxy) and mounted on top of a graphite pin, or loaded inside a

polyimide (Kapton, $d = 360 \mu\text{m}$) capillary. While it is difficult to assess the intrusion of the epoxy into the particles directly at the particle surface, this can be excluded in the particle interior. Here, regions with low relative electron density (i.e., regions appear white or light gray) that represent the empty macropore network of the catalyst particle (e.g., refer to the 2-D virtual slice of catalyst particle **E₆₀₋₁** in Figure 3.7) was observed. The assignment is based on the comparison of the obtained 2-D virtual slices and SEM data acquired of pristine catalyst particles. The viscosity of the epoxy after 2–3 minutes of curing is high enough to avoid it entering the macropores. This was also demonstrated in Chapter 2 which holotomography was used to characterize an epoxy-embedded FCC catalyst particle.

3.4.5 Phase Retrieval, Image Reconstruction and Segmentation

As mentioned above, holotomography requires the acquisition of multiple holograms at different propagation distances. Phase retrieval performed on these holograms yields two-dimensional (2-D) images of the projected phase shift of the sample, which form the basis for the tomographic reconstruction of the three-dimensional (3-D) relative electron density distribution of the sample (obtained phase shift is approximately proportional to the relative electron density).^[40] Due to the large size of the files, the projections were binned by a factor of 2 prior to phase retrieval. All projections were also scaled to the same pixel size and aligned to each other in Fourier space. Phase retrieval was performed from dark and empty beam corrected holograms, using a non-linear adaptation of the contrast transfer function (CTF) method based on Tikhonov regularization (NL-CTF).^[55,56] The code package HoloTomoToolbox was employed for this.^[56] A filtered back-projection (FBP) algorithm with standard Ram-Lak filter was utilized for the tomographic reconstruction of the retrieved phase images. The reconstructed 32-bit images (2-D virtual slices) were converted to 16-bit integer format. In general, the images are visualized with a grayscale colormap, in which white and black pixels (voxels) correspond to low and high electron density values, respectively.

The Avizo™ software package by Thermo Fisher Scientific Inc. was employed for post-processing of the reconstructed images. After determining the total particle volume (TPV, i.e., binary representation of a particle's volume including pore space) for every particle, the 16-bit integer images were masked with the TPV. In the case of ring and/or streak artifacts, a non-local means filter was applied to make the TPV generation easier. The masked images were then segmented into their corresponding pore space and solid phase using k-means clustering^[57] (MATLAB). In the case of artifacts and/or incorrect segmentation of the pore space, manual thresholding was applied.

For the two epoxy-embedded catalyst particles **E₆₀₋₁** and **E₆₀₋₂**, a MATLAB-based k-means clustering approach (see Section 4.4.10), was adopted to distinguish between phases based on their relative electron densities (ED). Three clusters ($k = 3$) were used to segment the masked grayscale images into a silica-dominant phase (high relative ED), a polymer-dominant phase (intermediate relative ED) and macro-pore space (low relative ED). Due to the resolution limitations of the technique and the high degree of intermixing of silica and polymer, the silica-dominant phase is overestimated. Both polymer and support features that are smaller than the determined resolutions go undetected or are excluded after segmentation. Polyethylene in the micro- and meso-pores as well as a portion of the macro-pores of the denser silica granulates can thus not be accounted for.

The binarized TPV and segmented pore space of each particle were used to determine its equivalent spherical diameter (ESD) [$ESD = (6V/\pi)^{1/3}$, V is equivalent to TPV], assuming spherical geometry, as well as its porosity and macro-pore volume (V_{mp}) in MATLAB.

3.4.6 Estimation of Spatial Resolution

The spatial resolution was estimated per catalyst particle based on 12 line profiles fitted over well-defined features in the 2-D virtual slices using a 10%–90% criterion (Table 3.3). Following a method described by Holler et al.^[58] (this method is also used in Chapter 2, Section 2.4.4), the edge resolution was determined from the horizontal distance between the vertical lines that pass through the line profile at 10% and 90%, respectively (Figure 3.7).

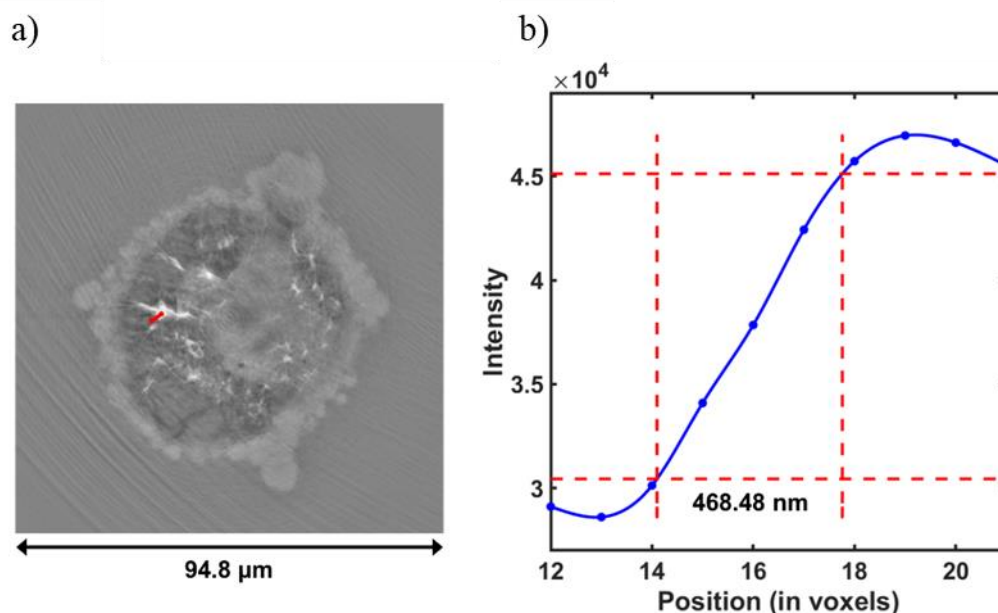


Figure 3.7 Line scan analysis performed on a 2-D virtual slice of catalyst particle E_{60-1} following the 10%–90% criterion. (a) shows a 2-D projection taken from the E_{60-1} dataset and (b) is the corresponding intensity profile of the red line shown in (a). A resolution of 468.48 nm was determined from the corresponding edge profile.

The achieved 3-D spatial resolution ranges between approximately 285 nm and 546 nm (average resolution: 393 nm). This variance is mostly due to motion artifacts during the measurements as well as artifacts arising from the inclusion of air bubbles in the epoxy and/or interference from the sample holder.

Particle	E_0	K_0	E_1	K_1	E_{10}	K_{10}	K_{30-1}	K_{30-2}	E_{60-1}	E_{60-2}	K_{60-1}	K_{60-2}
Resolution [nm]	491	365	315	246	290	465	285	387	491	417	422	546

Table 3.3 Spatial resolutions of the hafnocene-based catalyst particles as determined via the 10%–90% criterion.

3.4.7 Pore Network Model

Pore network models (PNMs) were generated from the binarized (segmented) pore space images of the reconstructed catalyst particles (see Section 1.3 for further details). Due to their large size, the images were binned two times (binning factor = 4) before pore network analysis.

Based on the radii of the segments within a pore network model, an approximate pore size distribution (PSD) was determined. Due to the resolution limitations of holotomography (Section 3.4.6), however, the PSDs only account for the macro-pores of the respective catalyst particles. As can be seen in Figure 3.3, the macropore diameters of the pristine and pre-polymerized particles fall in a range of approximately 0.1–3.4 μm (maxima in the range of 0.6–1.2 μm). This stands in agreement with mercury porosimetry data collected on a comparable ES757-supported zirconocene catalyst, which features macropores in a similar range (Figure 3.8). By using the pore diameters from the pore network model as input values, the average volume of the pristine catalyst’s detectable macropores (i.e., macropores that were successfully resolved with holotomography) was derived from the mercury porosimetry data. A total pore volume of ~ 0.2 mL/g was determined for all macropores in the range of 0.2–3.4 μm , which corresponds to a porosity of approximately 24%. Considering the porosities of particles \mathbf{E}_0 and \mathbf{K}_0 ($\leq 13\%$, Table 1 in main text), the detection and quantification of the macropore space can be also affected by resolution limitations and the high degree of intermixing of support, polymer and macropores.

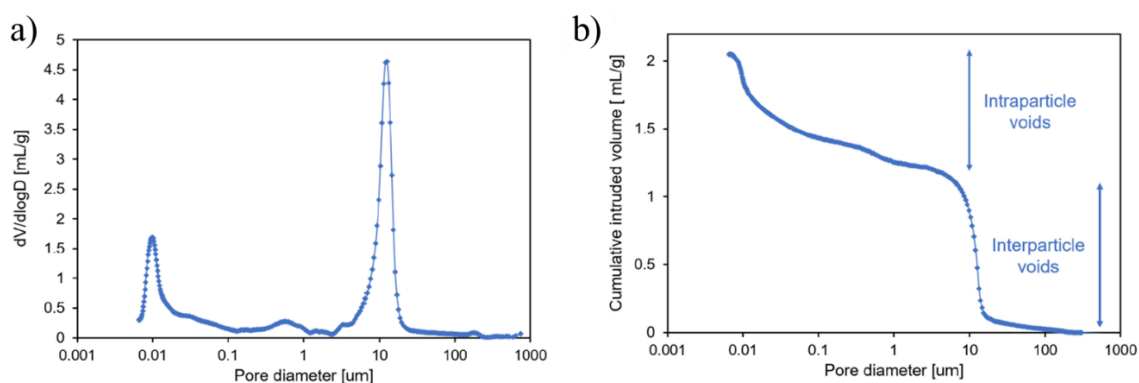


Figure 3.8 Mercury porosimetry data of a comparable ES757-supported zirconocene catalyst (Al/Zr molar ratio = 150 eq., 0.3 wt% Zr): a) Pore size distribution of the catalyst, b) Cumulative intrusion volume as a function of pore diameter.

3.4.8 Dispersion Plots

The 3-D distribution of the catalyst particles’ constituent phases (silica-dominant, polymer-dominant phases or pore space) was visualized in MATLAB in so-called dispersion plots. Here, the corresponding sub-

volumina of a particular phase (i.e., connected voxels) are visualized as small spheres, with the color of a sphere indicating the sub-volume's distance to the particle centroid, which is visualized as red cross in the figures. The center of each sphere is positioned at the centroid of the corresponding sub-volume and scales directly with the sub-volume's dimensions. The sphere representing the largest sub-volume therefore has the largest diameter and is labelled as '1' while sub-volumina smaller than 1% of the largest sub-volume ($V_{\text{threshold}} = 0.01 \times V_{\text{max}}$) are visualized as spheres with a fixed diameter.

3.5 References

- [1] G. Weickert, G. B. Meier, J. T. M. Pater, K. R. Westerterp, *Chem. Eng. Sci.* **1999**, *54*, 3291–3296.
- [2] G. Fink, B. Steinmetz, J. Zechlin, C. Przybyla, B. Tesche, *Chem. Rev.* **2000**, *100*, 1377–1390.
- [3] T. F. McKenna, J. B. P. Soares, *Chem. Eng. Sci.* **2001**, *56*, 3931–3949.
- [4] L. L. Böhm, *Angew. Chem. Int. Ed.* **2003**, *42*, 5010–5030.
- [5] J. R. Severn, J. C. Chadwick, R. Duchateau, N. Friederichs, *Chem. Rev.* **2005**, *105*, 4073–4147.
- [6] Z. Grof, J. Kosek, M. Marek, *AIChE J.* **2005**, *51*, 2048–2067.
- [7] T. F. L. McKenna, A. Di Martino, G. Weickert, J. B. P. Soares, *Macromol. React. Eng.* **2010**, *4*, 40–64.
- [8] J. T. Pater, G. Weickert, J. Loos, W. P. van Swaaij, *Chem. Eng. Sci.* **2001**, *56*, 4107–4120.
- [9] S. Knoke, F. Korber, G. Fink, B. Tesche, *Macromol. Chem. Phys.* **2003**, *204*, 607–617.
- [10] J. M. Zhou, N. H. Li, N. Y. Bu, D. T. Lynch, S. E. Wanke, *J. Appl. Polym. Sci.* **2003**, *90*, 1319–1330.
- [11] H. Hammawa, S. E. Wanke, *Polym. Int.* **2006**, *55*, 426–434.
- [12] H.-L. Rönkkö, T. Korpela, H. Knuutila, T. T. Pakkanen, P. Denifl, T. Leinonen, M. Kemell, M. Leskelä, *J. Mol. Catal. A Chem.* **2009**, *309*, 40–49.
- [13] T. Taniike, V. Q. Thang, N. T. Binh, Y. Hiraoka, T. Uozumi, M. Terano, *Macromol. Chem. Phys.* **2011**, *212*, 723–729.
- [14] K. W. Bossers, R. Valadian, S. Zanoni, R. Smeets, N. Friederichs, J. Garrevoet, F. Meirer, B. M. Weckhuysen, *J. Am. Chem. Soc.* **2020**, *142*, 3691–3695.
- [15] K. W. Bossers, R. Valadian, J. Garrevoet, S. van Malderen, R. Chan, N. Friederichs, J. Severn, A. Wilbers, S. Zanoni, M. K. Jongkind, B. M. Weckhuysen, F. Meirer, *JACS Au* **2021**, *1*, 852–864.
- [16] J.-D. Grunwaldt, C. G. Schroer, *Chem. Soc. Rev.* **2010**, *39*, 4741.
- [17] F. Meirer, B. M. Weckhuysen, *Nat. Rev. Mater.* **2018**, *3*, 324–340.
- [18] I. D. Gonzalez-Jimenez, K. Cats, T. Davidian, M. Ruitenbeek, F. Meirer, Y. Liu, J. Nelson, J. C. Andrews, P. Pianetta, F. M. F. de Groot, B. M. Weckhuysen, *Angew. Chem. Int. Ed.*, **2012**, *124*, 12152–12156.
- [19] S. R. Bare, M. E. Charochak, S. D. Kelly, B. Lai, J. Wang, Y. C. K. Chen-Wiegart, *ChemCatChem* **2014**, *6*, n/a-n/a.
- [20] Y. S. Zhang, X. Lu, R. E. Owen, G. Manos, R. Xu, F. R. Wang, W. C. Maskell, P. R. Shearing, D. J. L. L. Brett, *Appl. Catal. B Environ.* **2020**, *263*, 118329.
- [21] F. Meirer, S. Kalirai, D. Morris, S. Soparawalla, Y. Liu, G. Mesu, J. C. Andrews, B. M. Weckhuysen, *Sci. Adv.* **2015**, *1*, e1400199.
- [22] F. Meirer, D. T. Morris, S. Kalirai, Y. Liu, J. C. Andrews, B. M. Weckhuysen, *J. Am. Chem. Soc.* **2015**, *137*, 102–105.
- [23] Y. Liu, F. Meirer, C. M. Krest, S. Webb, B. M. Weckhuysen, *Nat. Commun.* **2016**, *7*, 12634.
- [24] J. Ihli, R. R. Jacob, M. Holler, M. Guizar-Sicairos, A. Diaz, J. C. da Silva, D. Ferreira Sanchez, F. Krumeich, D. Grolimund, M. Taddei, W. C. Cheng, Y. Shu, A. Menzel, J. A. van Bokhoven, *Nat. Commun.* **2017**, *8*, 809.
- [25] J. Ihli, D. Ferreira Sanchez, R. R. Jacob, V. Cuartero, O. Mathon, F. Krumeich, C. Borca, T. Huthwelker, W.-C. Cheng, Y. Shu, S. Pascarelli, D. Grolimund, A. Menzel, J. A. van Bokhoven, *Angew. Chem. Int. Ed.* **2017**, *56*, 14031–14035.
- [26] P. Sprenger, T. Sheppard, J.-P. Suuronen, A. Gaur, F. Benzi, J.-D. Grunwaldt, *Catalysts* **2018**, *8*, 356.
- [27] M. Gambino, M. Vesely, M. Filez, R. Oord, D. Ferreira Sanchez, D. Grolimund, N. Nesterenko, D. Minoux, M. Maquet, F. Meirer, B. M. Weckhuysen, *Angew. Chem. Int. Ed.* **2020**, *59*, 3922–3927.
- [28] M. Vesely, R. Valadian, L. M. Lohse, M. Toepperwien, K. Spiers, J. Garrevoet, E. T. C. Vogt, T. Salditt, B. M. Weckhuysen, F. Meirer, *ChemCatChem* **2021**, *13*, 2494–2507.
- [29] W. Curtis Conner, S. W. Webb, P. Spanne, K. W. Jones, W. C. Conner, S. W. Webb, P. Spanne, K. W. Jones, *Macromolecules* **1990**, *23*, 4742–4747.

-
- [30] K. W. Jones, P. Spanne, S. W. Webb, W. C. Conner, R. A. Beyerlein, W. J. Reagan, F. M. Dautzenberg, *Nucl. Inst. Methods Phys. Res. B* **1991**, 56–57, 427–432.
- [31] K. W. Jones, P. Spanne, W. B. Lindquist, W. C. Conner, M. Ferrero, *Nucl. Instruments Methods Phys. Res. Sect. B Beam Interact. with Mater. Atoms* **1992**, 68, 105–110.
- [32] M. A. Ferrero, R. Sommer, P. Spanne, K. W. Jones, W. C. Conner, *J. Polym. Sci. Part A Polym. Chem.* **1993**, 31, 2507–2512.
- [33] S. Boden, M. Bieberle, G. Weickert, U. Hampel, *Powder Technol.* **2008**, 188, 81–88.
- [34] L. Seda, A. Zubov, M. Bobak, J. Kosek, A. Kantzas, *Macromol. React. Eng.* **2008**, 2, 495–512.
- [35] J. B. P. Soares, T. F. L. McKenna, *Polyolefin Reaction Engineering*, Wiley-VCH, Weinheim, **2012**.
- [36] L. Meisterová, A. Zubov, K. Smolná, F. Štěpánek, J. Kosek, *Macromol. React. Eng.* **2013**, 7, 277–288.
- [37] A. Alizadeh, T. F. L. McKenna, *Macromol. React. Eng.* **2018**, 12, 1700027.
- [38] A. Diaz, P. Trtik, M. Guizar-Sicairos, A. Menzel, P. Thibault, O. Bunk, *Phys. Rev. B* **2012**, 85, 020104.
- [39] F. Pfeiffer, *Nat. Photonics* **2018**, 12, 9–17.
- [40] P. Cloetens, W. Ludwig, J. Baruchel, D. Van Dyck, J. Van Landuyt, J. P. Guigay, M. Schlenker, *Appl. Phys. Lett.* **1999**, 75, 2912–2914.
- [41] O. Coindreau, G. Vignoles, P. Cloetens, *Nucl. Instruments Methods Phys. Res. Sect. B Beam Interact. with Mater. Atoms* **2003**, 200, 308–314.
- [42] T. F. Morgener, H. Proudhon, P. Cloetens, W. Ludwig, Q. Roirand, L. Laiarinandrasana, E. Maire, *Polymer (Guildf)*. **2014**, 55, 6439–6443.
- [43] A. Khimchenko, C. Bikis, A. Pacureanu, S. E. Hieber, P. Thalmann, H. Deyhle, G. Schweighauser, J. Hench, S. Frank, M. Müller-Gerbl, G. Schulz, P. Cloetens, B. Müller, *Adv. Sci.* **2018**, 5, 1700694.
- [44] M. Töpperwien, F. van der Meer, C. Stadelmann, T. Salditt, *Proc. Natl. Acad. Sci. U. S. A.* **2018**, 115, 6940–6945.
- [45] A.-L. Robisch, M. Eckermann, M. Töpperwien, F. van der Meer, C. Stadelmann-Nessler, T. Salditt, *J. Med. Imaging* **2020**, 7, 1.
- [46] F. Meirer, S. Kalirai, J. N. Weker, Y. Liu, J. C. Andrews, B. M. Weckhuysen, *Chem. Commun.* **2015**, 51, 8097–8100.
- [47] V. J. Ruddick, J. P. S. Badyal, *J. Phys. Chem. B* **1997**, 101, 1791–1793.
- [48] S. Zaroni, N. Nikolopoulos, A. Welle, A. Vantomme, B. M. Weckhuysen, *Catal. Sci. Technol.* **2021**, 11, 5335–5348.
- [49] M. Abboud, P. Denifl, K.-H. Reichert, *Macromol. Mater. Eng.* **2005**, 290, 558–564.
- [50] F. Machado, E. L. Lima, J. C. Pinto, T. F. McKenna, *Polym. Eng. Sci.* **2010**, 51, 302–310.
- [51] B. Horáčková, Z. Grof, J. Kosek, *Chem. Eng. Sci.* **2007**, 62, 5264–5270.
- [52] D. A. Matthijs De Winter, F. Meirer, B. M. Weckhuysen, *ACS Catal.* **2016**, 6, 3158–3167.
- [53] T. Salditt, M. Osterhoff, M. Krenkel, R. N. Wilke, M. Priebe, M. Bartels, S. Kalbfleisch, M. Sprung, *J. Synchrotron Radiat.* **2015**, 22, 867–878.
- [54] S. Zabler, P. Cloetens, J.-P. Guigay, J. Baruchel, M. Schlenker, *Rev. Sci. Instrum.* **2005**, 76, 073705.
- [55] V. Davidoiu, B. Sixou, M. Langer, F. Peyrin, *Proc. - Int. Symp. Biomed. Imaging* **2012**, 19, 106–109.
- [56] L. M. Lohse, A. L. Robisch, M. Töpperwien, S. Maretzke, M. Krenkel, J. Hagemann, T. Salditt, *J. Synchrotron Radiat.* **2020**, 27, 852–859.
- [57] A. David, S. Vassilvitskii, D. Arthur, S. Vassilvitskii, in *Proc. Eighteenth Annu. ACM-SIAM Symp. Discret. Algorithms*, Society For Industrial And Applied Mathematics, **2007**, pp. 1027–1035.
- [58] M. Holler, A. Diaz, M. Guizar-Sicairos, P. Karvinen, E. Färm, E. Härkönen, M. Ritala, A. Menzel, J. Raabe, O. Bunk, *Sci. Rep.* **2014**, 4, 3857.

4. **Heterogeneity in the Fragmentation of
Ziegler-Type Ethylene Polymerization
Catalysts**

In this Chapter, the heterogeneity in the fragmentation of an ensemble of catalyst particles at the same stage of ethylene polymerization using X-ray nano tomography will be discussed. Ziegler-type catalysts are the grand old workhorse of the poly-olefin industry, yet their hierarchically complex nature complicates polymerization activity-catalyst structure relationships. In this work, the degree of catalyst framework fragmentation of a high-density polyethylene (HDPE) Ziegler-type catalyst was studied using ptychography X-ray computed nano-tomography (PXCT) in the early stages of ethylene polymerization. An ensemble consisting of 434 fully reconstructed ethylene pre-polymerized Ziegler-type catalyst particles prepared at a polymer yield of 3.4 g HDPE/g catalyst was imaged. This enabled a statistical route to study the heterogeneity in the degree of particle fragmentation and therefore local polymerization activity at an achieved 3-D spatial resolution of 74 nm without requiring invasive imaging tools. To study the degree of catalyst fragmentation within the ensemble, a fragmentation parameter was constructed based on a k-means clustering algorithm, that relates the quantity of polyethylene formed to the average size of the spatially resolved catalyst fragments. With this classification method, we have identified particles that exhibit weak, moderate, and strong degrees of catalyst fragmentation, showing that there is a strong heterogeneity in the overall catalyst particle fragmentation and thus polymerization activity within the entire ensemble. This hints towards local mass transfer limitations or other deactivation phenomena. The methodology used here can be applied to all polyolefin catalysts including metallocene-type and the Phillips-type catalysts to gain statistically relevant fundamental insights in the fragmentation behavior of an ensemble of catalyst particles.

This Chapter is based on: Bossers, K.W., Valadian, R., Garrevoet, J., van Malderen, S., Chan, R., Friederichs, N., Severn, J., Wilbers, A., Zanoni, S., Jongkind, M.K. Weckhuysen, B.M., and Meirer, F., Heterogeneity in the Fragmentation of Ziegler Catalyst Particles during Ethylene Polymerization Quantified by X-ray Nanotomography, *JACS Au*, **2021**, 1, 852-864. This Chapter is also part of the PhD Thesis of Koen Bossers.

4.1 Introduction

After the discovery of a free radical polymerization route of ethylene into a highly branched low-density polyethylene at extreme reaction conditions in the early 1930's by Reginald Gibson and Eric Fawcett, two different catalyst systems, based on respectively Chromium and Titanium active sites, were developed in the 1950's operating at considerably milder reaction conditions and giving a more linear and dense polyethylene product^[1-3]. One of these systems was developed by Karl Ziegler based on combining a TiCl_4 pre-catalyst with a dialkylchloroaluminium co-catalyst to form a Ti^{3+} active site. This discovery would ultimately result in awarding the 1963 Nobel prize to both Karl Ziegler and Giulio Natta, who discovered that the $\alpha\text{-TiCl}_3$ form could also be used for the synthesis of stereoregular polyolefins such as isotactic polypropylene^[4,5]. Today, three different catalyst systems, namely the Ziegler-type catalyst, the Phillips-type catalyst, and molecular, single-center catalyst in homogeneous and immobilized form as well as the non-catalytic process developed by Reginald Gibson and Eric Fawcett are used to synthesize a wide variety of different polyethylene grades ranging from highly branched low-density (LDPE), linear low-density (LLDPE), medium-density (MDPE) to high-density (HDPE) polyethylene^[6]. These different polyethylene (PE) grades possess distinct mechanical and physicochemical properties, such as impact strength, stiffness, friction and wear resistance, melting point, and processability, leading to wide-spread applications ranging from insulating layers for electricity cables, high durability pipes for the transport of gasses and liquids, to medical appliances and protective equipment^[7]. Finally, polyolefins can also be synthesized from biomass- and municipal waste-derived feedstock, such as ethylene derived from bioethanol and pyrolysis-cracking of plastic waste, and they can be implemented in a circular economy through either mechanical or chemical recycling, such as remolding and thermal decomposition to the raw feedstock^[8-10].

The α -olefin polymerization process, including the growth of the polyolefin particles, starts with the fragmentation of the catalyst particle at the nanometer to micrometer scale^[11-17]. Typically, this is referred to as the early stage of olefin polymerization. The fragmentation is a necessary phenomenon

as it leads to the exposure of new active sites and prevents mass transfer limitations through the densely formed polyolefin layer that would otherwise inhibit catalyst activity^[18,19]. However, a controlled fragmentation process is preferable to prevent the formation of fines that can lead to fouling in the reactor or downstream equipment as well as to maintain good control over the evolution of particle morphology and particle size distribution (PSD) to facilitate easier polymer powder processing^[11,20,21]. A common approach at industrial plants is to implement a pre-polymerization step at mild reactions conditions, e.g., 0.1 MPa and close to room temperature, to facilitate a smooth fragmentation process followed by the actual polymerization conditions of 1-10 MPa and around 364 K^[3,22-25].

From a fundamental aspect, there are two limiting modes of catalyst particle fragmentation, namely the layer-by-layer or shrinking core mode and the continuous bisection mode^[17]. Which fragmentation mode dominates the overall fragmentation behavior is determined by the type of α -olefin monomer and catalyst properties, such as pore size and pore size distribution, crystalline nature of the formed polymer, friability of the framework, distribution, nature and activation procedure of the active sites as well as heat transfer and mass transfer properties, which are influenced strongly by the operating conditions, such as gas-phase versus slurry-phase^[26-30].

The fragmentation behavior of polyolefin catalyst particles has been studied in the past decades mainly with the use of electron microscopy techniques^[31-34]. Zheng and Loos used cross-sectional scanning electron microscopy (SEM) on both Ziegler-Natta and immobilized metallocene-type catalysts operating under different reaction conditions^[35-37]. For a propylene polymerized Ziegler-Natta catalyst they observed that as a function of the pore size, either the shrinking core or continuous bisection mode was dominating^[36]. These findings signify the crucial role that catalyst pore size and mass transfer resistance play in the fragmentation behavior. Interestingly, an immobilized metallocene-type catalyst showed a dominating shrinking core fragmentation behavior under ethylene polymerization conditions and the continuous bisection fragmentation behavior under propylene polymerization conditions^[35]. The McKenna group showed in a series of articles the development of stopped-flow reactors and a rapid quenched-flow

device that allowed the investigation of the early stages of ethylene polymerization under industrially relevant conditions both in the gas-phase and slurry-phase conditions^[38–42]. These unique polymerization reactors achieved reaction times as low as 40 ms at industrially relevant reaction conditions, such as 0.8 MPa ethylene. On the contrary, Pater et al. developed a reactor setup that allowed the pre-polymerization of a Ziegler-Natta catalyst with propylene under extremely low reaction rates to obtain well-defined polymerization conditions, which allowed studying the intra- and interparticle morphologies with cross-sectional SEM^[24]. Unfortunately, these electron microscopy-based studies require either invasive and destructive cutting techniques to observe a 2-D representation of the interior of the particle or are limited to information regarding exclusively the catalyst particle's exterior.

Fortunately, state-of-the-art X-ray microscopes both at synchrotron-based and lab-based facilities are able to image the interior and exterior of objects, such as catalyst and polymer particles ranging from several tens of microns to even millimeters in size with 3-D achieved spatial resolution ranging from sub-100 nm to several microns without requiring invasive preparation methods^[42]. Additionally, the high beam brilliance and tuneability of the photon energy at synchrotrons has enabled chemical, elemental, and diffractive tomographic imaging, even under operando catalytical conditions^[43–50]. For example, the Beale group demonstrated the advances made in operando X-ray tomographic imaging for both the oxidative coupling and reforming of methane^[51,52]. Due to the state-of-the-art photon detector and advanced on-line data-analysis the collection of each X-ray diffraction computed tomography (XRD-CT) dataset only took 117 s with a pixel size close to 3 microns^[51]. They further demonstrated the use of a multi-modal μ -X-ray fluorescence/absorption/XRD CT toolbox^[52]. An-other exciting development, performed by the Grunwaldt group, has shown the strengths of correlative multimodal spectroscopy and 3-D imaging techniques bridging the fields of electron, ion, and X-ray tomography^[53–55]. Furthermore, they recently reported on the fabrication of two nanoreactors for in-situ electron and X-ray tomographic studies allowing pressures and temperatures of up to 100 kPa and 1573 K with a tilting angle of +/- 35° for a fully mounted cell^[56]. The van Bokhoven group recently reported on a 3-D estimated spatial resolution

between 30-40 nm for the sub-volume of several fluid catalytic cracking (FCC) catalyst particles using ptychographic X-ray computed tomography (PXCT)^[57-60]. They found that zeolite amorphization and structural changes are the underlying driving forces for the FCC catalyst deactivation process^[59]. X-ray nano-tomography performed for studying FCC catalysts^[61-69], demonstrated how the generation of a 3-D pore network for FCC catalyst particles allowed for advanced mass transport simulation studies as well as correlated localization of active sites, metal poison species, and coke species. Pioneering work on the use of computed X-ray microscopy tomography for the field of polyolefin catalysis was performed in the early 1990's at Brookhaven National Laboratory and subsequently in the late 2000's^[17,70-74] with achieved spatial resolution of several microns allowing the study of porosity of full polyolefin particles and to calculate monomer diffusion and degassing properties^[19].

A powerful correlated 3-D X-ray ptychography and fluorescence microscopy toolbox was introduced to directly observe in 3-D the Ti distribution, comprising the active sites, within the isotactic polypropylene phase of an individual Ziegler-Natta catalyst particle in the early stages of propylene polymerization^[75]. Also, it was shown that for the slurry-phase propylene polymerized catalyst particle, both fragmentation models were present within the same particle but furthermore that the continuous bisection model was dominating the overall fragmentation behavior. In this Chapter, the focus will be mainly on the ptychographic X-ray computed tomography (PXCT) dataset, which allowed us to study the heterogeneity in catalyst fragmentation and obtain geometrical parameters of many individual ethylene polymerized Ziegler-type catalyst particles from an ensemble of 434 particles within the measured field of view.

4.2 Results and Discussion

In Figure 4.1 a schematic overview of the experimental approach is given, starting from the setup of the synchrotron-based correlated X-ray ptychography and fluorescence (XRF) tomography setup to the 3-D reconstruction of the ptychographic dataset and marker-based watershed segmentation resulting in 434 individual Ziegler-type ethylene

polymerization catalyst particles used for the statistical analysis of the fragmentation behavior. The catalyst was sealed inside a Kapton capillary to prevent hydration of the highly sensitive MgCl_2 framework, which would otherwise result in morphological changes and prohibit a study on the fragmentation behavior^[75].

By optimizing the drying procedure post slurry-phase reaction, minimal beam induced morphological changes were observed during the collection of 360 2-D projections with a total acquisition time of 22 h (Figure 4.9). This resulted in an estimated Fourier shell correlation (FSC) 3-D spatial resolution of 74 nm for the PXCT dataset (Figure 4.13) for a large field of view (FOV) of $120 \times 120 \times 20 \mu\text{m}^3$. The XRF dataset was used to support the segmentation of the PXCT data (confirming the presence of Ti in all particles) however, the low signal to noise ratio of the XRF data did not allow for a detailed analysis of the Ti distribution within individual particles. Here, a new strategy has been devised based on the achieved high spatial resolution of the PXCT data and using a k-means clustering method to study and quantify the degree of fragmentation of each individual particle within the entire ensemble using a classification based on a designed fragmentation parameter. A relationship between the degree of catalyst fragmentation and therefore local polymerization activity and the observed fragmentation behavior within an ethylene polymerized catalyst particle was found and is represented schematically in Figure 4.1f.

The Ziegler-type catalyst used for this experiment is an industrially relevant $\text{MgCl}_2/\text{TiCl}_4$ based system that was chosen specifically for its small D_{50} value of $3.64 \mu\text{m}$ and narrow particle size distribution (span of 1.04). Ethylene polymerization was carried out under mild conditions at 2.6 bar ethylene and room temperature with triethylaluminium as co-catalyst in the slurry-phase at short polymerization times to give a yield of 3.4 g HPDE /g catalyst. This gives a theoretical D_{50} of $5.9 \mu\text{m}$ for the HDPE-catalyst composite particles based on Equation 4.1.

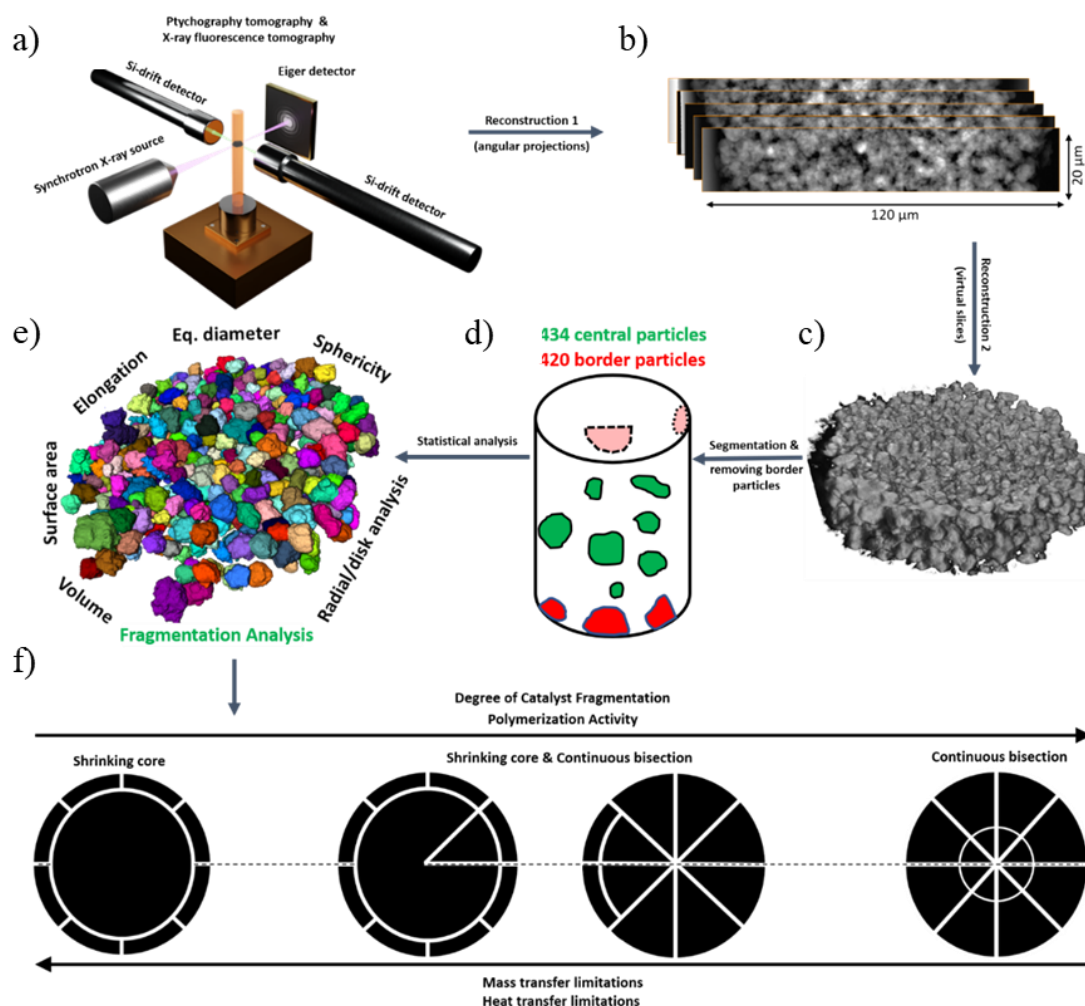


Figure 4.1 X-ray ptychography and fluorescence nano-tomography on an ensemble of ethylene pre-polymerized Ziegler-type catalysts. (a) Schematic representation of the correlated X-ray ptychography and fluorescence tomography set-up used at the P06 beamline at DESY. The beam was focused onto the sample by KB mirror optics and the X-Ray fluorescence signal was detected using 2 side-looking silicon drift detectors (SDDs). An Eiger X 4M detector behind the sample was used to record the diffraction data for Ptychographic X-ray Computed Tomography (PXCT). (b) Reconstructed 2-D X-ray ptychography projections at different angles. (c) 3-D reconstructed volume of the real part of the refractive index represented as grayscale intensity. (d) After a watershed segmentation procedure, composite polymer-catalyst particles that were cut-off from the field-of-view were classified as ‘border particles’ and not included in the subsequent statistical analysis. (e) The remaining 434 segmented particles were then analyzed with respect to their geometrical properties and fragmentation behavior. (f) Schematic representation of the relationship between the dominating or highly mixed limiting modes of fragmentation behavior observed namely, the shrinking core and continuous bisection, versus the catalyst particle’s polymerization activity and degree of catalyst fragmentation, which hints towards strong local mass and heat transfer limitations.

In Figure 4.11 a flowchart is given, starting with the acquisition of the raw data from both X-ray ptychography (far-field diffraction patterns) and fluorescence tomography to the ptychographic reconstruction of the real part of the refractive index of the sample components, which is related to the local electron density and therefore local mass density according to Equation 1.7. After alignment of the 2-D projections with respect to the center of rotation and to correct for sample drift and motor inaccuracies, the 3-D PXCT volume was reconstructed using filtered back projection with a $45.4 \times 45.4 \times 45.4 \text{ nm}^3$ voxel size followed by removing noise in 3-D using a non-local means filter algorithm. The XRF dataset was reconstructed with an iterative algorithm (iART) with $200 \times 200 \times 200 \text{ nm}^3$ voxel size. An in-depth methodology description of the reconstruction of both PXCT and XRF datasets is given in Section 4.4.5. At this point, the reconstructed PXCT volume, as shown in Figure 4.1c, contains many highly connected composite particles. Therefore, due to this high particle connectivity a standard labelling procedure on the polymerized catalyst particle ensemble of either the ptychographic or XRF reconstructed volumes would result in a single label being assigned to all particles. In Figure 4.6 and Figure 4.8, scanning electron microscopy (SEM) images of the pristine and pre-polymerized catalyst particles are shown. Indeed, one can observe here that the pre-polymerized catalyst particles are highly aggregated and polymer fibers are acting as an interparticle glue. Various explanations can be found, such as: i) a high catalyst concentration in the lab-based model reactor (5 g cat/L diluent) meaning that the odds of two or more catalyst particles to be in close vicinity is increased, or ii) a relatively high ethylene polymerization versus crystallization rate at the catalyst surface and iii) absence of a chain terminating agent, such as H_2 , causing the formation of long polymer fibers that can lead to interparticle entanglements and hence agglomeration. It should be noted that this is not the same as reactor fouling, as it was observed that with increased polymerization time and therefore an increase of the size of each composite polymer-catalyst particle at a certain point the hydrodynamic forces from the stirring are able to cause a deagglomeration and finally individual and spherical polymer particles are obtained.

To overcome this problem of highly connected particles a marker-based watershed algorithm using manually generated markers was employed for the segmentation into separated particles^[76,77]. The strategy to manually draw the markers in 3-D provided a supervised control over the segmentation process. Finally, 434 completely reconstructed particles were identified and used for subsequent analysis. The result of the manual marker-based watershed segmentation in separating and classifying the particles is shown in Figure 4.2. In Figure 4.2b, indicated by the red arrow, the advantage of using manual markers can be seen in the successful segmentation of the cyan, light-green, light-pink, and red colored particles. In Figure 4.2c-d, respectively, the overlay of the grayscale and k-means segmented electron density on the particle labels is visualized.

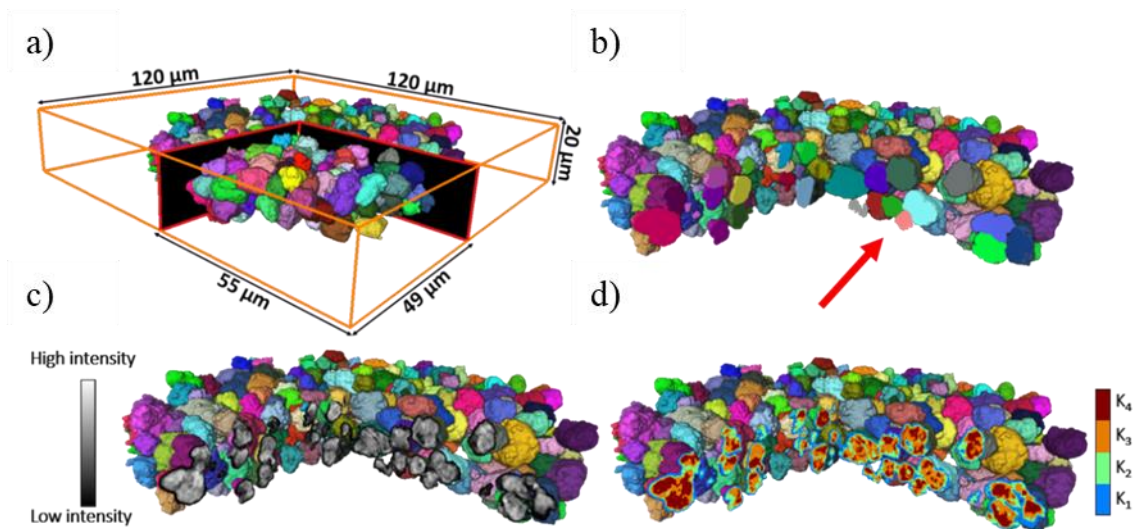


Figure 4.2 (a) 3-D volume rendering ($45.4 \times 45.4 \times 45.4 \text{ nm}^3$ voxel size) of the tomography data after manual marker-based watershed segmentation resulting in 434 individually labelled particles. The black planes with red outline depict the position for the visualization of the cross-sections in b-d. (b-d) Cut-out volumes showing respectively, (b) the complete particle labels, (c) the overlay of the Ptychographic X-ray Computed Tomography (PXCT) grayscale intensity values within these labels and (d) the k-means clustering results using 4 clusters (K_1 to K_4) to segment the PXCT grayscale intensity values.

With the successful segmentation of the highly agglomerated particle ensemble into 434 individual particles, geometrical parameters, such as the particle's volume, area, equivalent spherical diameter (ESD), PSD, sphericity, elongation, and flat-ness could be analyzed. The calculation of these particle metrics is described in Section 4.4.9. The mean and standard deviation values

of these particle metrics are provided in Table 4.1. The geometrical parameters concerning the particle shape such as sphericity, elongation and flatness show a quite narrow distribution, especially for the sphericity with a standard deviation of 4%. This shows that the overall particle morphology within the entire ensemble is relatively homogeneous. In the case of a smooth catalyst fragmentation process, the morphology of the catalyst particle has been observed experimentally to be replicated in the final polymer particle, called the replication phenomenon^[12,33]. The mean elongation of 0.60 (value = 1 for a perfect sphere) for the composite polymer-catalyst particles confirms the presence of the morphological replication phenomena as the pristine catalyst based on SEM observations given in Figure 4.6, is also slightly elongated. In Figure 4.3a both the degree and orientation of the elongation of each particle are visualized in 3-D. Additionally, in Figure 4.3b the correlation is plotted between the ψ (yaw) and ϕ (pitch) Euler angles of the major principal axis of each particle, which represent the direction of the elongation (Section 4.4.9). Finally, the histograms showing the elongation and sphericity values within the entire ensemble are given in respectively Figure 4.3c,d. Based on this plot no clear preferred orientation is observed for the elongation axis within the ensemble. Therefore, although the composite particles themselves are elongated and highly agglomerated, the non-ordered orientation of the elongation direction of the particles of the ensemble shows that there is no preferred expansion direction of the agglomeration as a whole (spheroidal). Furthermore, having measured a relatively large ensemble of particles allowed to calculate the PSD, which can then be compared to both the theoretically expected D_{50} based on the polymer yield or bulk particle size measurement techniques such as static laser scattering (SLS). In Table 4.1, the ESD and PSD ($D_{10,50,90}$ and span) of the composite particles is given. The calculated D_{50} of 5.61 μm of the center particles is only 5.8% smaller than that of the calculated D_{50} of 5.96 μm based on Equation 4.1 (at a yield of 3.4 g HDPE per g catalyst).

V (μm^3)	SA (μm^2)	ESD (μm)	D ₁₀ (μm)	D ₅₀ (μm)	D ₉₀ (μm)	Span	Sphericity	Elongation	Flatness
109.5± 79.2	144.2 ± 67.0	5.69 ± 1.17	4.40	5.61	6.87	0.44	0.74 ± 0.04	0.60 ± 0.16	0.67 ± 0.13

Table 4.1 Overview of the mean and standard deviation values of the volume (V), surface area (SA) and equivalent spherical diameter (ESD), the 10,50,90 percentile fraction of particle size (D_x) and their span, sphericity, elongation and flatness values for the 434 completely reconstructed ethylene polymerized catalyst particles.

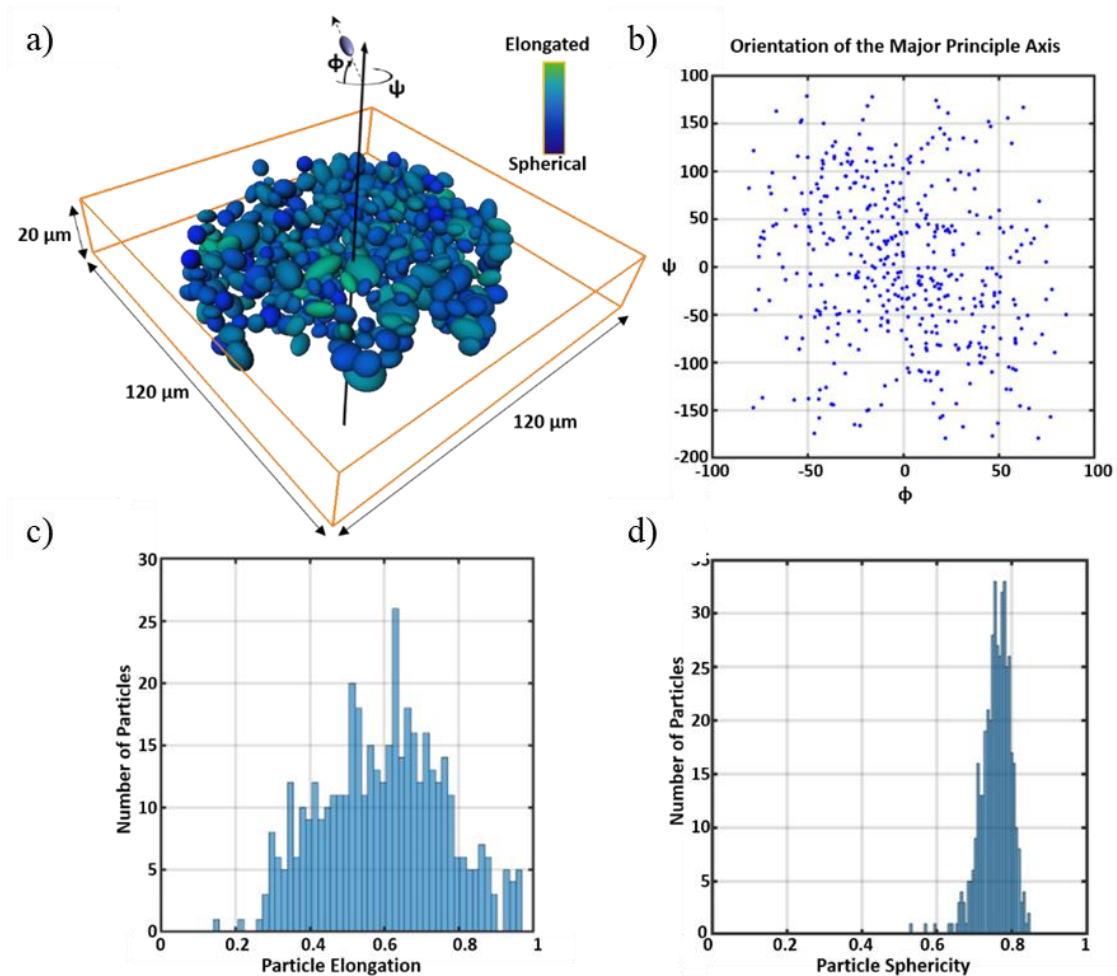


Figure 4.3 (a) 3-D volume rendering of the orientation and degree of elongation of the 434 ethylene polymerized catalyst particles. A dark blue color represents a high degree of sphericity whereas a light green color represents a high degree of elongation. (b) A plot between the ψ (yaw) and ϕ (pitch) Euler angles that shows the orientation of the major principle axis, the elongation direction, of a particle. (c) A histogram of the elongation values of all particles where a value of 0 means highly elongated and value of 1 highly spherical. (d) A histogram of the sphericity values of all particles where a value of 1 means a perfect sphere.

However, with respect to the span calculated for the pristine catalyst of 1.04 based on SLS results, the span and thus a measure of the width of the particle size distribution found here with PXCT of 0.44 is considerably smaller. This can be explained by the intrinsic differences between the two techniques, such as better bulk statistics with SLS, the method used to interpret the ESD values from the SLS raw data, and that SLS measures the ESD of the scattering objects in the path length of the laser-source, meaning that agglomerated objects are considered as a single particle in SLS and can thus increase and broaden the PSD determined. This last argument was indeed observed experimentally here for the agglomerated composite polymer-catalyst particles, where the SLS results gave D_{50} values going from 350 μm down to 160 μm during the collection of multiple measurements where increased stirring time was observed to cause partial deagglomeration.

The MgCl_2 framework consisting of MgCl_2 platelets as small as 5 nm bound through ionic interactions has a higher friability compared to the covalently bound SiO_2 framework used for other polyolefin catalyst types, such as the metallocene-type and Philips-type catalysts (although $\text{SiO}_2/\text{MgCl}_2/\text{TiCl}_4$ Ziegler-type catalysts are also in use)^[12,17,78–83]. This typically facilitates a faster degree of framework disintegration for MgCl_2 based catalysts. Filling of the pore network of the Ziegler-type catalyst (main pore size distribution = 20-50 nm of the catalyst studied here) due to the local polymerization of ethylene and subsequent fragmentation caused by the stress on the framework is therefore expected to lead to a high mixing of the polymer and catalyst phases below the achieved PXCT 3-D spatial resolution of 74 nm. This intimate mixing of the polymer and catalyst phases leads to a strong broadening of the histogram of the electron density intensity values (Figure 4.16). However, since the polymer and catalyst phases have different ρ_m values of, respectively, $\sim 0.95 \text{ g/cm}^3$ for HDPE and $\sim 2.32 \text{ g/cm}^3$ for the catalyst (assuming bulk anhydrous MgCl_2) their mixing will provide a range of weighted electron density values that portray their relative concentrations as shown in Equation 1.8. This means that a sub-volume dominant in a catalyst phase will have a higher average electron density than that of an equally mixed sub-volume of HDPE and catalyst, which in turn will be higher than that of a sub-volume dominant in HDPE. A k-means clustering algorithm was used to

separate the PXCT grayscale intensity values in four mixed chemical phases (Section 4.4.10). The conventional Otsu's method is expected to give the same result for this multilevel thresholding but is computationally more exhaustive as it searches for a global optimal threshold with respect to the local optimal threshold search by the k-means algorithm^[84]. These four k-means clusters are sorted here in terms of increasing average electron density as follows: (K_1) a HDPE-dominant phase, (K_2 and K_3) two highly mixed HDPE-catalyst phases where in K_2 and K_3 respectively the HDPE or catalyst has a higher concentration in that voxel's volume and finally (K_4) a catalyst-dominant phase. The k-means partitioned grayscale intensity histogram along with the mean grayscale intensity of each k-means cluster is given in Figure 4.16.

Therefore, in this Chapter, to study the degree of catalyst fragmentation within each composite particle a unitless fragmentation parameter (FP), referred to as V_r , has been designed and calculated that considers both the spatially resolved catalyst fragments (identified via K_4) and the quantity of the formed HDPE phase (via clusters K_{1-3}) directly using the k-means clusters. A brief description of this parameter is given below - a more detailed explanation can be found in the Section 4.4.11.

V_r provides a relationship between the formed HDPE phase and the fragmented catalyst phase. This is achieved by taking the ratio of the total volume of the first three k-means clusters of each particle, $K_{1,2,3}$, which constitutes both the polymer and the spatially non-resolved catalyst fragments, over the mean volume of the spatially resolved catalyst fragments in the fourth k-means cluster, K_4 . These spatially resolved catalyst fragments in the K_4 cluster are referred to as the non-connected components (NCCs).

In the Section 4.4.11, two different fragmentation parameters that only take the catalyst fragmentation into account (that is to say it doesn't include polymer formation) are compared to the parameter V_r . Whereas these other parameters fundamentally speaking should be sufficient to study the catalyst fragmentation degree, the spatial resolution limits their usefulness since catalyst fragments smaller than 74 nm are most likely to either disappear to the $K_{1,2,3}$ clusters or appear as part of a larger fragment in K_4 .

In Table 4.2 the mean, median, minimum, and maximum values as well as the standard deviation of the parameter V_r for the 434 imaged composite particles in the ensemble are reported. While the unitless values themselves have no physical meaning, the large spread of V_r , as evidenced by the standard deviation being larger than the mean, nonetheless shows that there is significant heterogeneity in the degree of catalyst fragmentation within the ensemble. To visualize this heterogeneity the central slice along the XY plane of each of the 434 composite particles is displayed in Figure 4.4. The distribution of the k-means clusters was visualized to provide a clear overview of the HPDE-rich, highly mixed, and catalyst-rich phases. It should be noted that only one central slice is visualized here for simplicity and therefore doesn't provide the 3-D overview of each particle in terms of the degree of fragmentation and fragmentation behavior (type of fragmentation model dominating). The particle at the top left has the lowest V_r value and exhibits the weakest degree of catalyst fragmentation. It therefore exhibited the lowest local ethylene polymerization activity whereas the particle on the bottom left showed the largest V_r value and thus the strongest degree of catalyst fragmentation and in turn the highest local polymerization activity. The heterogeneity in the degree of fragmentation of each particle and therefore the local polymerization activity observed are most likely the result of mass transfer limitations induced by the particle agglomeration. The particle agglomeration in turn could be caused by the high concentration of the catalyst used in the model reactor (5 g cat/ L diluent) that leads to a higher probability of catalyst particles undergoing ethylene polymerization to stick together. These agglomerations would then limit the diffusion of ethylene to all the otherwise available Ti active sites within each individual particle. Other deactivation phenomena such as the presence of poisons and heat transfer limitations seem less likely due to the presence of excess triethylaluminium co-catalyst, which also acts as a scavenger for poisons and the slurry-phase operation under mild reaction conditions (2 bar ethylene, room temperature) to facilitate better heat transfer.

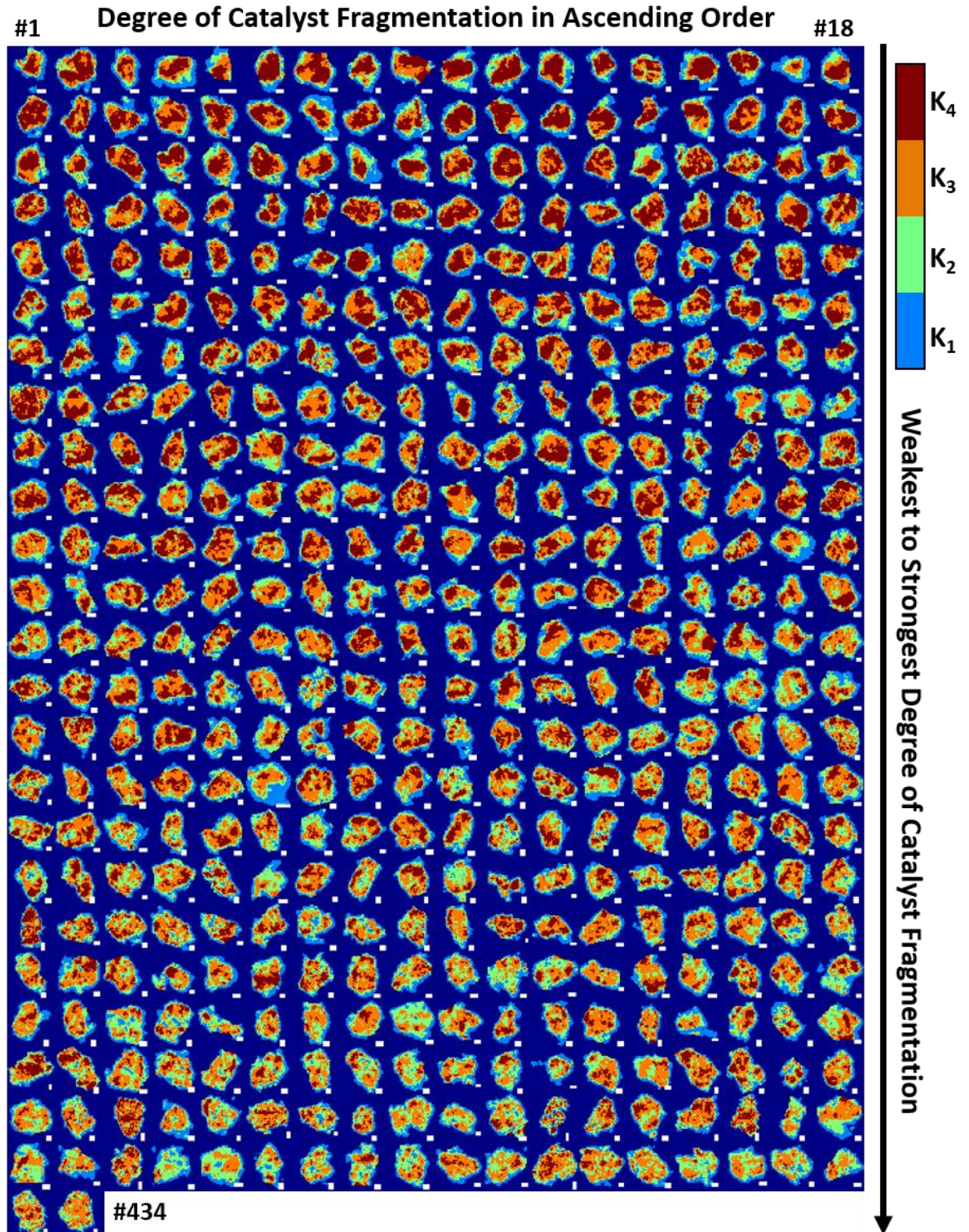


Figure 4.4 ‘Family album’ of virtual cross-sections through all evaluated catalyst particles. The figure shows the results of the k-means cluster analysis of the PXCT grayscale values of the central slice of each particle. Particles have been sorted by their degree of catalyst fragmentation from

weakest, at the top left, to strongest, at the bottom left, fragmentation degree within the entire ensemble of 434 particles based on the unitless V_r fragmentation parameter. The white scale bar at the bottom right of each central image depicts a size of 1 micron.

Fragmentation Parameter	Mean Value	Median Value	Minimum Value	Maximum Value	Standard Deviation
V_r	436	268	13	7180	549

Table 4.2 Overview of the mean, median, minimum, and maximum values and the standard deviation of the V_r fragmentation parameter as calculated for the 434 composite particles in the imaged ensemble to study the degree of catalyst fragmentation.

After all particles had been sorted according to their respective degree of fragmentation within the entire ensemble using the V_r fragmentation parameter, it became possible to look more in-depth into the fragmentation behavior of particles that exhibited either a weak, moderate, or strong degree of catalyst fragmentation. In Figure 4.5, three particles have been selected that fall in one of these three groups. The volume renderings report the 3-D distribution of the 4 k-means clusters and show how each particle is enveloped in a shell of the HDPE-dominant K_1 (blue) cluster. However, from the surface towards the core of each particle we observe a mix of K_2 (in green), K_3 (orange) and even K_4 (red), depending on the particle's fragmentation degree. To complement this visualization, the radial distribution of the volume ratio of each cluster is reported in Figure 4.5b. This radial analysis gives the volume ratio of each k-means cluster at a single voxel shell, which is normalized by the total voxel count in that shell, at a certain distance from the surface. At the core of a particle and hence the largest distances from the surface, the volume ratio can therefore show an abrupt behavior since that shell consists only of a few (central) voxels (Section 4.4.12). For the first particle it was observed that at the surface, the HDPE-dominant K_1 cluster has the largest volume ratio and as it goes towards the core the highly mixed HDPE-catalyst K_2 and K_3 clusters sequentially dominate the volume ratio in a shell followed finally by the catalyst-dominant K_4 cluster and again a rise in the volume ratio of K_3 close to the center. In fact, this type of alternating sequence strongly fits to the shrinking-core fragmentation model where the main catalyst polymerization activity is occurring at the particle's external surface and leads to the peeling of typically small catalyst fragments of the original catalysts external surface that will become partitioned to the $K_{1,2,3}$ clusters depending on the volume

ratio of HDPE to catalyst in a voxel. Additionally, the increase of K_3 at the core could point towards the formation of polyethylene also inside the core of this particle, which the visual cross-section in Figure 4.5a confirms. The formation of polyethylene at the core could there indicate that also the continuous bisection model is occurring for this weakly fragmented particle, albeit with a seemingly lower contribution to the overall fragmentation behavior than the shrinking core.

The external surfaces of the other two more fragmented particles are still composed of first the K_1 cluster followed by an increase of the K_2 cluster, which shows that the shrinking core model is still occurring for these more active particles. However, whereas the first particle shows a clear sequential profile between all four clusters going from the surface to the core, a change in this behavior is observed for the other two particles. For instance, the moderately fragmented particle has a second local maximum of the K_2 cluster close to the center of the particle. Furthermore, the $K_{3,4}$ clusters are more homogeneously distributed throughout this particle, with a constant higher concentration of K_3 over K_4 at each distance from the surface. This means that for this moderately fragmented particle, considerable amounts of polyethylene have now also been formed at the core of the particle in addition to the polymer layer at the surface ($K_{1,2}$), which has stayed almost constant in terms of volume ratio width (number of voxel shells). Here the formation of polyethylene at the core of the particle has led to sufficient local fragmentation to push spatially resolved catalyst fragments (K_4) towards the surface of the particle. The dispersion of large K_4 fragments towards the surface of the particle and presence of the $K_{2,3}$ clusters at the core of the particle is also observed in the visualization of the cross-section of this moderately fragmented particle in Figure 4.5a. This shows that now besides the shrinking core fragmentation model, the continuous bisection fragmentation model is also playing a significant role in the overall fragmentation behavior of this moderately fragmented particle. Finally, for the strongest fragmented particle the most homogeneous distribution of $K_{2,3,4}$ is observed by going from the surface towards the core of the particle. This would be expected in the scenario where the original catalyst particle keeps breaking up internally due to the formation of polyethylene within the core of the particle, which will push the

smaller and smaller catalyst fragments towards the external surface. Indeed, a maximum of the K_4 volume ratio is now observed closer to the external surface than for the least and moderately fragmented particles. Additionally, the thickness of the $K_{1,2}$ cluster layers at the external surface has stayed nearly constant throughout the three particles. This means that for this strongest fragmented particle a shift towards a larger contribution of the continuous bisection fragmentation model in the fragmentation behavior is found.

Together with the central slices of all the particles given in Figure 4.4, it therefore was observed that the least fragmented particles mainly consist of a dense catalyst core of the K_4 cluster followed by sequential shells of the $K_{3,2,1}$ clusters. Alternatively, the moderately and strongly fragmented particles show the presence of many K_4 fragments dispersed throughout the composite particle's volume. The combination of these findings, which is shown schematically in Figure 4.1f, shows that for particles exhibiting a weak degree of catalyst fragmentation, the shrinking core fragmentation model is dominating whereas for the moderately fragmented catalyst particles a more equal contribution of both shrinking core and continuous bisection fragmentation models is observed and for the strongly fragmented catalyst particles the continuous bisection fragmentation model is dominating the overall fragmentation behavior. The formation of polyethylene mainly at the particle's external surface as observed for the weakly fragmented particles can be explained by both internal and external mass transfer limitations or alternatively a higher concentration of active sites at the surface than the core, which can happen when the co-catalyst has not come in contact with the internally located Ti^{4+} pre-active sites upon addition of the α -olefin^[27].

The disk analysis plots in Figure 4.5c report the mean grayscale intensity values per slice along the XY plane, which represents the mean electron density in a slice. The first particle shows a gradual increase of the mean electron density until a peak is reached close to the central slice along the XY plane and confirms what was observed with the radial analysis of the k-means clusters' volume ratios. That is to say that also with the disk analysis on the pure grayscale intensity values (so without a k-means clustering approach) a gradual change is observed from a low mean electron density phase to that of a high electron density phase. That means that there is a smooth change from

a HDPE phase at the surface of the particle towards a catalyst phase at the core of the particle. The ~ 10 slices offset of the maximum grayscale intensity value (around slice 50) from the central slice (roughly at slice 40) also confirms why the K_3 cluster shows a volume ratio of 1 at this first particle's center voxels. Going towards the moderately and strongly fragmented particles we see that instead of a peak a plateau is reached that maintains a rather constant mean intensity value for more than 50 slices for the moderately fragmented particle and almost 200 slices for the strongly fragmented particle. Furthermore, instead of a smooth gradient from low to high intensity as observed for the weakly fragmented particle a sharp transition is experienced especially for the strongly fragmented particle. This shows that especially for the strongly fragmented particle the catalyst phase is already highly dispersed through-out the formed HDPE phase, where local maxima can be observed even close to the edges with regards to the XY plane and is additional proof for the continuous bisection fragmentation model playing a significant role in the fragmentation behavior of these two particles.

In the Section 4.4.13, a rough estimation is provided on the distribution of how many particles are classified as showing either a weak, moderate, or strong degree of catalyst fragmentation. Based on this rough estimation, respectively 274, 123 and 37 particles belong to the weak, moderate, and strong classifications of degree of catalyst fragmentation.

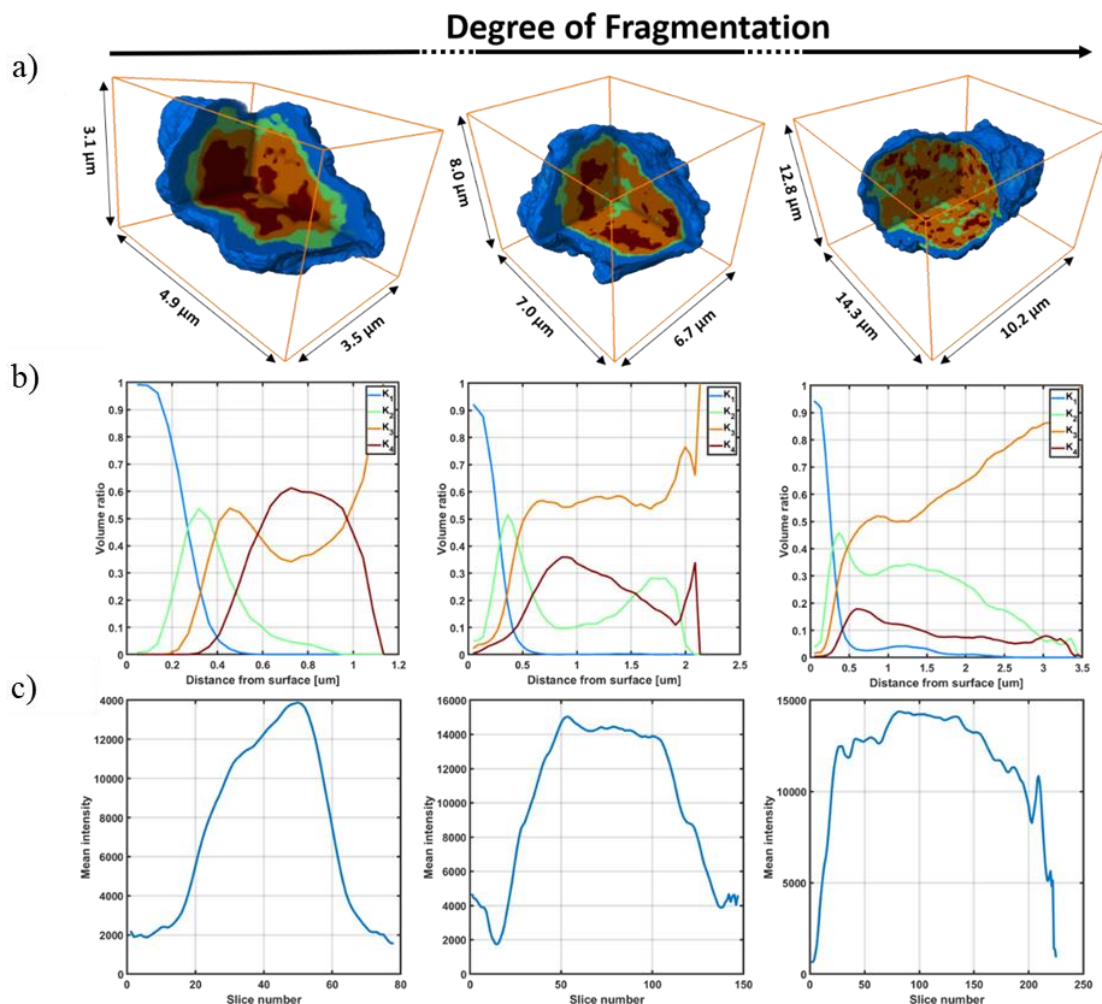


Figure 4.5 (a) Cross-sectional volume rendering of the k-means clustering of the grayscale intensities from three composite particles representing from left to right respectively the weakest, moderate, and strongest degrees of catalyst fragmentation as based on their sorting by the parameter V_r . (b) Radial analysis of the volume ratio of each k-means cluster going from the surface of the respective particle towards the core. (c) Disk analysis along the XY plane giving the mean grayscale intensity value of each slice going from one edge of the particle to the other.

4.3 Conclusions

Using the strength of ptychography X-ray computed nano-tomography (PXCT) to visualize the local mean electron density with an achieved 3-D spatial resolution of 74 nm over a large, scanned field of view of $120 \times 120 \times 20 \mu\text{m}^3$, the heterogeneity in the degree of fragmentation of 434 ethylene polymerized Ziegler-catalyst particles was analyzed and visualized in the early stages of ethylene polymerization under mild reaction conditions and with a high catalyst loading. The highly connected composite particles were

successfully segmented in the reconstructed volume using a supervised marker-based watershed algorithm. This segmentation allowed for the analysis of geometrical parameters for each individual particle such as the volume, surface area, equivalent spherical diameter, sphericity, and elongation. The elongation degree of the particle ensemble showed that the composite particles followed the replication phenomena of the slightly elongated pristine Ziegler catalyst particles.

Due to the high degree of mixing between the HDPE and catalyst phases below the achieved 3-D spatial resolution a k-means clustering algorithm on the PXCT grayscale intensity values was used to identify a HDPE-rich phase, two highly mixed HDPE-catalyst phases and one catalyst-rich phase. Using these clusters, a fragmentation parameter V_r was designed to study the heterogeneity in the degree of fragmentation and therefore local polymerization activity. This fragmentation parameter is based on the ratio of the summed volumes of the HDPE-rich and highly mixed HDPE-catalyst phases over that of the mean volume of the spatially resolved catalyst fragments. The advantage of this parameter is that it takes into account: i) the catalyst activity in terms of HDPE formation, ii) the loss of any catalyst fragments that have become too small to spatially resolve them from the HDPE phase, and iii) the change in the size of the catalyst fragments as a function of polymerization activity. Using this fragmentation parameter, a strong heterogeneity was found within the entire ensemble of 434 composite particles with respect to the degree of catalyst fragmentation. Three representative particles that were categorized with respect to showing either a weak, moderate, or strong degree of catalyst fragmentation at this specific yield of 3.4 g HDPE /g catalyst were analyzed in depth. The weakly fragmented composite particle showed mainly a dominating shrinking core fragmentation model with hints to the presence of the continuous bisection fragmentation model. For the moderately and strongly fragmented composite particles the shrinking core fragmentation mode was still observed to occur, but the continuous bisection fragmentation mode had become the dominating pathway for fragmentation, which shows that monomer diffusion towards the interior of the catalyst particle was not limited with respect to the weakly fragmented composite particle; this in turn explains the higher local

polymerization activity of these particles. A rough estimation was then performed on how many particles are classified as portraying either a weak, moderate, or strong degree of catalyst fragmentation to give values of respectively, 274, 123 and 37 particles.

4.4 Experimental Section

4.4.1 Synthesis of the Ziegler-Type Catalyst

A Ziegler catalyst, industrially relevant for the production of high molecular weight and high-density polyethylene without the addition of co-monomers was synthesized in accordance with the description in patent WO2009112254^[85]. The as-synthesized catalyst formulation resembles that of a typical $\text{MgCl}_2/\text{TiCl}_4$ Ziegler-type catalyst with a Ti weight loading of 4% obtained from Inductively Coupled Plasma- Atom Emission Spectroscopy (ICP-AES). The median particle size (D_{50}) and particle size distribution (span, defined as $(D_{90}-D_{10})/D_{50}$) using Static Laser Scattering (SLS) were obtained using a Mastersizer 3000 laser diffraction particle size analyzer instrument. The $D_{10,50,90}$ values of the pristine catalyst are respectively 2.23, 3.64 and 6.01 μm giving a span of 1.04. Scanning electron microscopy (SEM) images of the pristine catalyst, transferred under inert conditions using a transfer module from Kammrath & Weiss, to a ThermoFisher FEI Versa 3-D FEG SEM were obtained at a 2 kV accelerating voltage and are shown in Figure 4.6. Based on SEM, the pristine catalyst particles are observed to be elongated. N_2 physisorption on a typical batch of this Ziegler-type catalyst shows a BET surface area of 6.3 m^2/g and a pore volume of 0.026 cm^3/g . Only mesoporosity is observed for the catalyst with a pore size distribution mainly between 20 to 50 nm.

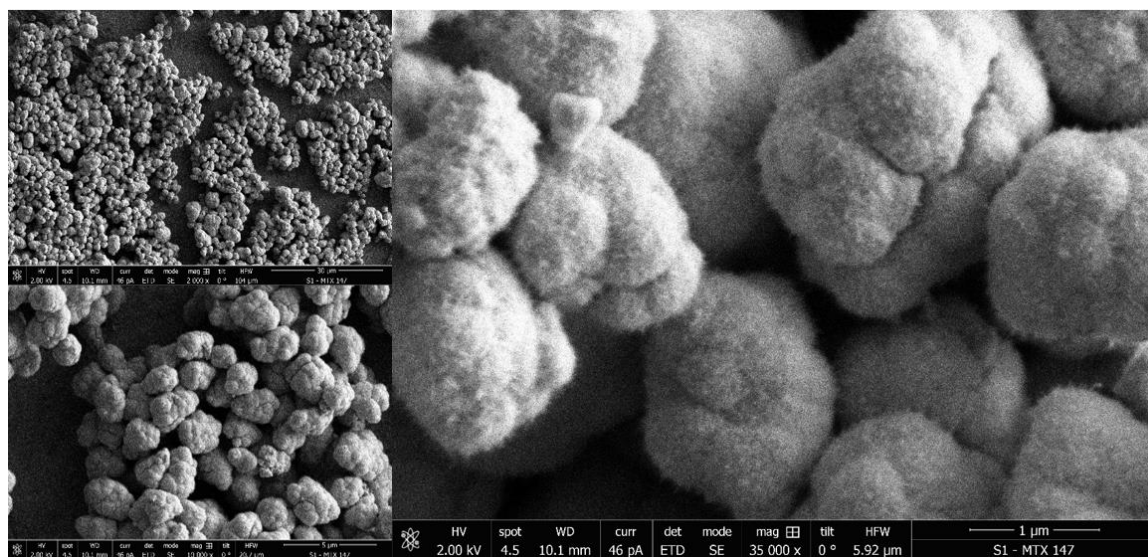


Figure 4.6 Scanning electron microscopy (SEM) images of the Ziegler catalyst used. The catalyst particles are observed to have a cauliflower type of shape with a rough surface and cracks can be observed on the external surface, likely due to the agglomeration of smaller sub-units. A majority of the catalyst particles seems to be slightly elongated.

4.4.2 Slurry-phase Ethylene Polymerization

Due to the high sensitivity of the as-synthesized Ziegler-type catalyst to moisture and oxygen all further procedures were performed inside a glovebox operating under inert conditions of N_2 with <0.3 ppm H_2O and <1 ppm O_2 . A low-pressure, room-temperature polymerization set-up was designed to run from inside the glovebox, with a schematic drawing given in Figure 4.7. A cylindrical glass reactor of circa 100 mL internal volume with a single inlet can be either set under vacuo to remove the gas atmosphere inside the reactor or be filled with ethylene at a set pressure of 1.2 barg. A typical polymerization reaction was performed as follows. First, 10 mL of anhydrous (99.9% purity, dried and stored over 3\AA molecular sieves, Across Organics) heptane was introduced in the open glass reactor equipped with a magnetic stirring bar. A 500 μL solution of triethylaluminium co-catalyst (1M in heptane, Sigma-Aldrich) was then added whilst stirring at 400 rpm with a ratio with regards to the catalyst of $[Al]/[Ti]=72$. The co-catalyst serves two purposes here, to further purify the diluent as well as the monomer gas-feed and to activate the Ziegler pre-catalyst. Meanwhile the catalyst that was kept in a hexane slurry was dried at room temperature inside the glovebox after which 50 mg was added to the diluent mixture in the reactor whilst stirring at

400 rpm. The reactor chamber was then closed, and the evacuation/feed tubing attached. The reactor was first evacuated slowly to several tens of mbar pressure to remove the N₂ atmosphere after which the ethylene (3.5N purity, Linde) was fed to the reactor. During the entire duration of the polymerization reaction the gas-feed was kept open as to ensure a constant pressure of ethylene. After five minutes of polymerization, the ethylene feed was quickly removed by switching the reactor to the vacuum pump followed by introducing N₂. The slurry was then filter dried inside the glovebox using the same vacuum pump set-up and washed successively three times with heptane and three times with pentane. Afterwards, the powder was dried for 60 minutes at room temperature followed by drying at 80 °C overnight on a hotplate inside the glovebox. The next day, the resulting dried polymer powder was weighed and gave a yield of 3.4 g HDPE / g catalyst after which it was stored until further use in a glass vial in the glovebox. The reactor set-up was designed for its simplicity in use inside a glovebox, however it should be noted that a model reactor for low polymer yields such as designed by the group of McKenna et al., would allow industrially relevant polymerization conditions whilst having high control over the polymer yield^[38–41].

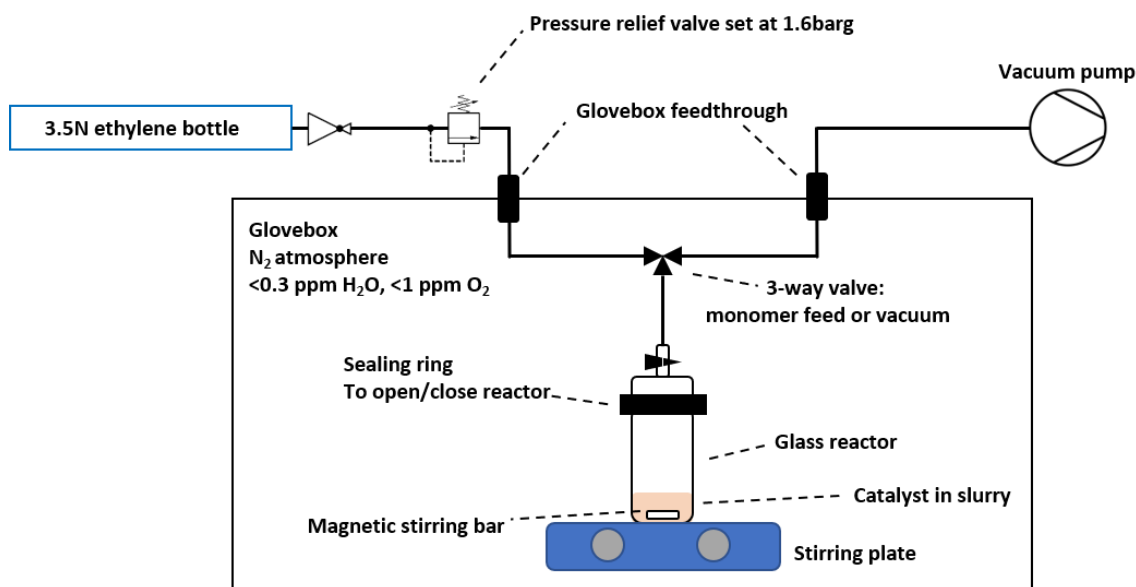


Figure 4.7 Schematic representation of the lab-based model reactor for ethylene polymerization under mild conditions (pressure up to 1.6 barg and room temperature).

The polymer yield can also be estimated based on the median of the particle size distribution, D_{50} , as shown in Equation 4.1:

$$D_{50\text{-polymer}} = D_{50\text{-catalyst}} \cdot R_f \cdot \sqrt[3]{PY + 1} \quad \text{Equation 4.1}$$

Here $D_{50\text{-polymer}}$ and $D_{50\text{-catalyst}}$ are the D_{50} values of respectively the obtained polymer particles and the pristine catalyst used. R_f is a constant, which is assumed to be 1, and relates to the physical nature of the polymer and catalyst particles and that one catalyst particle is converted into one polymer particle. The polymer yield, PY, gives the yield of polymer in terms of g polymer/ g catalyst and can be deduced from Equation 4.1 if one knows the D_{50} values of polymer and catalyst^[86].

The particle size distribution ($D_{10,50,90}$ and span) of the product was measured with SLS. The SLS results on these composite polymer-catalyst particles gave a D_{50} value starting at 371 μm that would decrease to 172 μm during 20 consecutive runs. The decrease in D_{50} based on the run-time is due to the constant mechanical stirring inside the SLS machine, which therefore indicates that the HDPE-Ziegler catalyst composite particles are highly agglomerated and break up due to the induced mechanical forces. SLS is able to measure such agglomerations since the working principle of SLS is based on the scattering of the laser light induced by any objects through its path towards the detector.

To confirm this agglomeration, SEM analysis was also performed of the polymerized catalyst sample and is shown below in Figure 4.8. Clearly HDPE fibers can be observed bridging multiple particles together in the right side of Figure 4.8. Whereas this catalyst yielded agglomerations at low yields, at industrially relevant yields on the order of several kg HDPE / g catalyst spherical and isolated HDPE particles are obtained. This indicates that at some point during the polymerization process, the mechanical forces induced by the stirring in addition to the ever-increasing diameter of the particles seem to overcome the strength of the fibers bridging two or more particles together and cause a deagglomeration process.

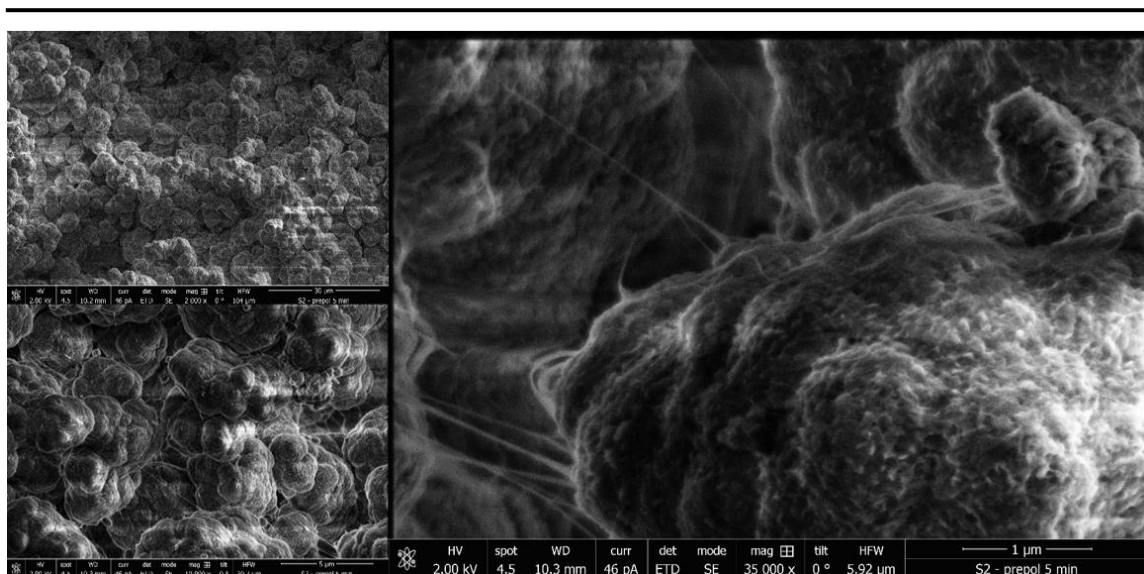


Figure 4.8 Scanning electron microscopy (SEM) images of the ethylene polymerized Ziegler-type catalyst. The agglomeration of the composite polymer-catalyst particles is evident in the top left and bottom left images. Furthermore, the zoom-in SEM image in the right shows the presence of polymer fibrils below 100 nm thickness bridging particles together and is likely the reason of the agglomeration of the composite particles. Furthermore, the zoom-in shows the roughness of the particle surface is maintained.

Since, the D_{50} of the composite polymer-catalyst particles from SLS are unreliable due to the strong agglomeration, the theoretical D_{50} value was calculated based on Equation 4.1. Here the polymer yield of 3.4 g HDPE / g cat was used, which was found simply by weighing the final polymer product and correcting for the amount of catalyst injected in the reactor. With the D_{50} -catalyst value of 3.6 μm , that was found reliably with SLS for the pristine catalyst, the D_{50} -polymer value is estimated to be 5.9 μm .

4.4.3 Loading of Sample in Polyimide Capillary

The sample loading inside a polyimide capillary was similar to that performed in our previous work and all actions were performed inside a N_2 -filled glovebox operating at <0.3 ppm H_2O and <1 ppm O_2 unless otherwise stated^[75]. Polyimide capillaries obtained from MicroLumen with an inside diameter of 120 μm and wall thickness of 10 μm were used. To load the agglomerated powder, which looks like small flakes, the capillary was gently inserted into a flake and turned up-side down so that the composite powder is now at the top of the capillary. The capillary is then mildly agitated by tapping it gently from the outside with a tweezer so that the agglomerated particles

drop towards the center of the capillary. Care was taken not to squeeze the center of the capillary or hit the agglomerated particles directly with the tweezer as this could cause any unwanted morphological changes to the sample unrelated to the actual polymerization process. Finally, a two-component, low-outgassing and near-hermetic sealing epoxy from Epotek®, product label H74, was used to seal the two ends of the capillary. The epoxy had to be cured at 80 °C for 30 min to ensure the desired sealing effect. This was performed by placing the capillaries on a hotplate. To make sure the capillaries don't get stuck on a hotplate, small aluminum foil pieces were attached to the ends of each tubing where the epoxy was applied. Transport from the glovebox environment to the synchrotron beamline was performed by placing the loaded capillaries inside glass vials sealed with Teflon tape and placing them in steel vacuum tubes fitted with Viton O-rings and a closing ring.

4.4.4 Synchrotron Correlated X-ray Ptychography and Fluorescence Microscopy Set-up

The correlated ptychography X-ray computed tomography (PXCT) and X-ray fluorescence (XRF) tomography experiment was performed at the Hard X-ray Micro/Nano-Probe beamline, P06, at the PETRA III synchrotron facility, DESY. The PXCT raw data was collected using an Eiger X 4M hybrid pixel detector (Dectris Ltd.). Two SII Vortex EM Si-drift detectors (internally collimated to a 50 mm² area) were used to collect the Ti XRF dataset. The field-of-view (FOV) of 120 × 20 μm² (H × V) was raster-scanned with a coherent and monochromatic X-ray beam focused down to 170 × 160 nm² (H × V) at 12 keV using KB mirrors with a step size of 200 nm and a dwell time of 2 ms. A total of 360 projections were obtained from 0-360°, thus a 1° interval, with a half degree off-set after 180° as to correct for any self-absorption events that might happen with XRF without duplicating collection angles. The acquisition time (including motor movement and initialization) for a single projection was 220 s and the total acquisition time of all projections was 22 h. The Ti XRF raw data was fitted according to Solé et al., using PyMCA^[87]. The raw data collected with PXCT consists of a far-field Fraunhofer diffraction pattern collected at each scanning point. Using an in-

house developed iterative reconstruction algorithm, the real part of the refractive index, $\delta(r)$, is then reconstructed for the object measured^[88]. Due to the absence of a stable reference in this work with a known refractive index (air) in the FOV, the normalization was performed using the beam intensity without any rescaling of the real and imaginary part of the refractive index. This means that the real part of the refractive index, $\delta(r)$, measured here and therefore the local electron density, ρ_e , is in this case not quantitative.

In Figure 4.9 a comparison is given of the first and 362nd PXCT projections, which are taken 22 hours of continuous scanning and therefore exposure to the X-ray beam apart. No significant beam-damage was observed here, whereas Bossers et al.^[75] observed significant beam-damage most likely due to residual solvent molecules within the polyolefin phase. It should be noted here that there is a 0.5° degree off-set between the two projections ($0-180^\circ$ and $180.5-360.5^\circ$).

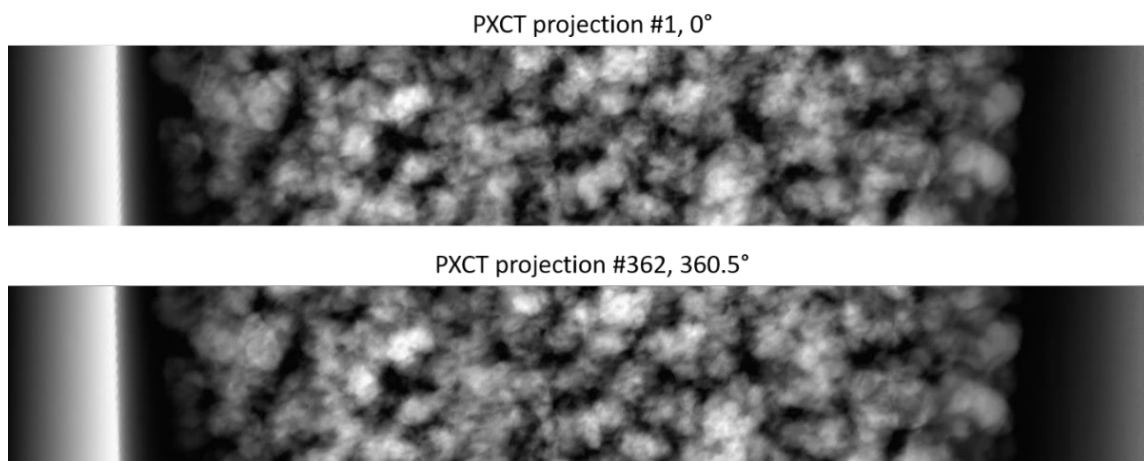


Figure 4.9 Comparison of the first and 362nd horizontally aligned PXCT projections taken respectively at the collection angles of 0° and 360.5° (constant increment of 1° with a 0.5° offset after 180°). No significant beam-damage is observed during the 22 h total scanning time.

4.4.5 Tomography Reconstruction of the Ptychography X-ray Computed Tomography and X-ray Fluorescence Datasets

All subsequent analytical and reconstruction procedures were performed on a workstation equipped with an Intel® Xeon® Gold 6242 CPU running at

2.80 GHz with 16 cores, 256 GB of DDR4 RAM memory running at 2933 MHz and a Nvidia® Quadra GV100 GPU. Typically, around 20-50 GB of memory was occupied due to the size of the non-binned PXCT dataset and any subsequent 3-D operations. Tomographic reconstruction of the 3-D volume of the X-ray Ptychography and XRF 2-D projections was performed inside the TXM-Wizard software package^[89]. After the collection of the first 180 projections a slight drift of the capillary was noticed due to mounting the capillary on the sample holder using clay and could be optimized further by switching to an epoxy glue instead. To obtain a high-resolution 3-D reconstruction of the obtained datasets, this drift together with any motor position inaccuracies must be corrected for. Normally, in the ideal case of measuring an isolated spherical object with ample of empty space measured at all sides of the object, correcting for any movement is relatively simple. Strategies involve manually tracking the same feature(s) at each subsequent 2-D projection and using this as the center of rotation as well as the use of a registration algorithm to automatically find any displacement in both horizontal and vertical (or even tilting angle corrections) directions of the region of interest. A combination of both where at first a feature is tracked manually for a rough alignment followed by a registration algorithm for sub-pixel accuracy can be highly effective^[90,91]. In this particular situation, the manual tracking isn't feasible due to the difficulty of tracking the same feature(s) over the large FOV scanned consisting of many particles.

Instead, the following combination was used for the alignment of the ROI to the rotation axis (horizontal alignment) of both the PXCT and XRF datasets. No significant drift was observed in the vertical direction. Steps B to E are visualized in Figure 4.10 and a generalized flowchart is given in Figure 4.11:

- A. The first step is to flip the 180.5 to 359.5° 2-D projections horizontally. This effectively makes the second half of the dataset go from 0.5 ° to 179.5° with a 1° increment. This step proved to be crucial for good results in the final alignment used in step D. The reason to collect the angles from 0-360° was to mitigate any possible self-absorption effects while collecting the Ti XRF data (see Section 1.2 for further details).

- B. Inside the AvizoTM software package (due to its ease in visualization), the raw 2-D projections of both PXCT and XRF datasets were binarized at a threshold at 10% of the grayscale values. This means that if the histogram of pixel intensities has a theoretical range from 0-100 then all values below 10 are set equal to 0 and all values above 10 are set equal to 1. This removes low-intensity noise from the first rough alignment performed in step C. Furthermore, in the case of PXCT the capillary wall is removed from each 2-D projection manually. It should be noted here that for the Ti XRF datasets the capillary walls are not observed.
- C. A first rough alignment to bring all ROI's towards the center of image is performed as follows. For each horizontal line within the binarized image, the index of the center of the filled voxels (voxel value is 1) is found using an in-house developed MATLAB code. This is achieved by finding the index of the first and last value equal to 1 at each horizontal line and taking the average of these indexes as the center of the respective horizontal line. The average of index of all horizontal lines is then taken to be the horizontal center of that respective 2-D projection. This is then repeated in a loop for all 2-D projections. These values give the difference of the center of the horizontal dimension of a 2-D projection with regards to the center of the ROI inside this 2-D projection. To illustrate this: for a typical PXCT 2-D projection the horizontal center of the image is at a pixel value 1250 (total size is 2500 pixels in width) and if the center of the ROI is found to be at 1240 then a horizontal translation of $1250 - 1240$ pixels = +10 pixels within MATLAB. The translation values necessary for each 2-D projections are then both applied to the thresholded and masked 2-D projections for the subsequent fine alignment in step D as well as saved in a text-file to perform later on the original and non-thresholded 2-D projections.
- D. A registration algorithm between each thresholded and masked 2-D projection with the previous projection is then used for the fine alignment of the horizontal displacement. The Astra toolbox compatible with MATLAB was used for this purpose^[90,91]. The

translation values of the fine alignment were also saved in a text-file similar to step C.

- E. The rough and fine alignment steps gave two text files of translation values. These were applied sequentially to the original 2-D projections after which the original 2-D projections were aligned successfully with respect to each other and still contain the full range of data.
- F. During a typical filtered back projection (FBP) reconstruction with a Shepp-Logan filter of the central slice of each dataset, we noticed that the rotation center was still slightly off for the PXCT dataset. Using a horizontal off-set value of -20 pixels within the TXM-Wizard software package, the sharpest reconstructed central slice was obtained. This offset value is similar to step C in the sense that it performs a horizontal translation but, in this case, the offset value is equal for all 2-D projections.
- G. Finally, all slices of the PXCT dataset were then reconstructed using the Shepp-Logan filter with a FBP reconstruction algorithm. Due to the low signal-to-noise ratio of the Ti XRF dataset, an iterative algebraic reconstruction algorithm (iART) was used in the TXM-Wizard software package.

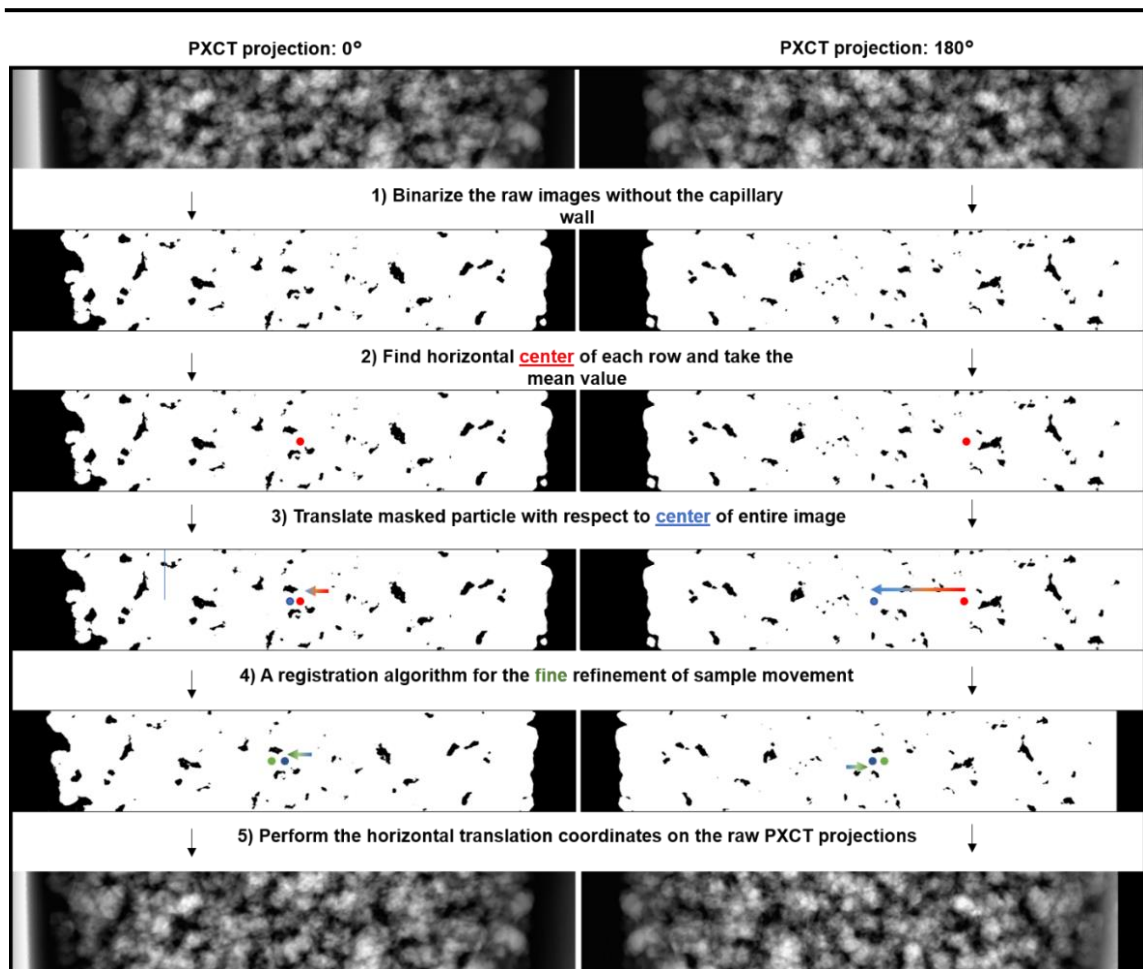


Figure 4.10 Methodology used to align and correct for any horizontal drift of the sample. The 0° and 180° PXCT projections are shown for illustration. In step 1 the raw 2-D PXCT projections are binarized with a 10% threshold and the capillary wall is removed manually. In the second step, for each horizontal line the center position is found based on the mean value of the first and last 1-valued pixels in that horizontal line (background has a value of 0 for each pixel in a binarized image). Then the mean horizontal center position is calculated for the entire 2-D projection. In step 3 this mean value is used to perform a first rough translation on the masked images. These translation values are meanwhile also saved in a text file. In step 4 a registration algorithm is applied as a fine refinement step, which aligns a 2-D projection to its previous 2-D projection and these translation values are again saved in a separate text-file. In step 5, the rough and fine alignment translations are applied to the original non-masked PXCT projections sequentially to finally obtain the PXCT projections aligned with respect to each other. In a final step not shown here, corrections for the off-set of the center of rotation are optimized within the TXM-Wizard software to yield the best reconstructed 3-D volume.

The voxel size of the reconstructed PXCT dataset is $45.4 \times 45.4 \times 45.4$ nm³ and that of the XRF dataset is $200 \times 200 \times 200$ nm³. All subsequent volume rendering was performed in either the Avizo™ software package or within MATLAB. To remove noise from the reconstruction a 3-D non-local

means (NLM) filter implemented within Avizo was used. One of the main advantages of this filter is that it assumes the noise to be white-noise and preserves the sharpness of strong edges. An example of the central slice in the XY plane before and after the 3-D NLM filter is shown below in Figure 4.12. An image registration algorithm within Avizo was used to align the XRF dataset to that of the PXCT. The reconstructed PXCT dataset is originally in a 32-bit float format, which allows for storing the raw quantitative electron density data if obtained. However, since here the electron density isn't quantitative, most of the subsequent data analysis was performed on a 16-bit unsigned converted dataset. This linearly scales all values into a format that can easily be exported from Avizo as 2-D tiffs to be opened in MATLAB when using in-house developed codes, without losing information on the relative position of each chemical phase.

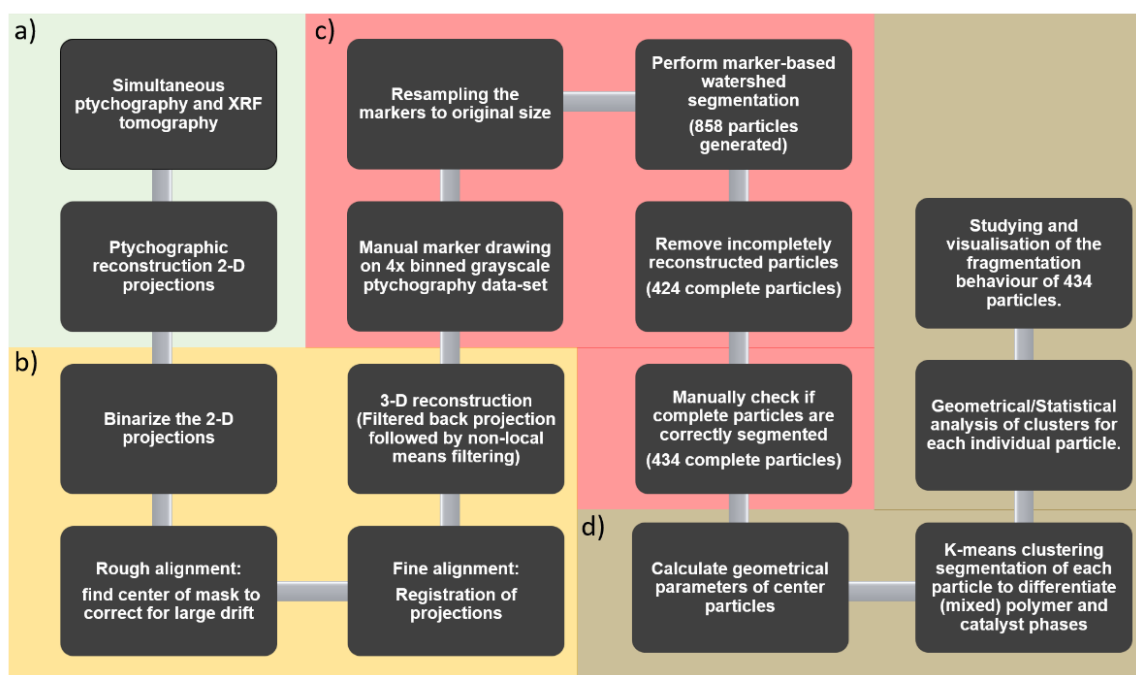


Figure 4.11 (a) Acquisition and reconstruction of the 2-D X-ray ptychographic and fluorescence projections. (b) Alignment procedure of the 2-D projections followed by a 3-D filtered back projection (FBP) reconstruction and subsequent 3-D non-local means filtering to remove white-noise. (c) Manual marker drawing procedure followed by a marker-based watershed segmentation to isolate the particles not touching any borders. (d) Statistical analysis on the isolated particles as a whole to generate geometrical parameters (e.g., sphericity, equivalent spherical diameter, elongation) as well as intra-particle segmentation based on k-means clustering algorithm to separate the highly mixed polymer and catalyst phases to study the fragmentation behavior.

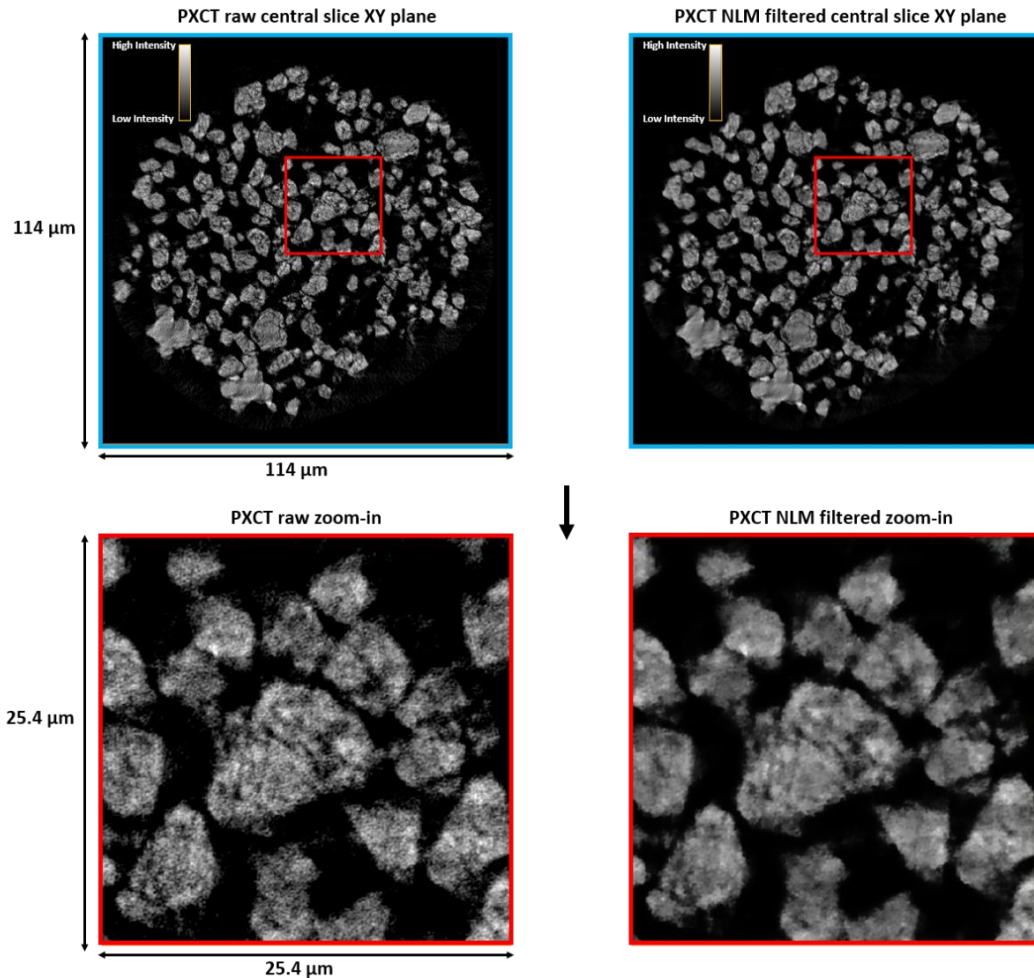


Figure 4.12 (a) In blue contour, the central slices in the XY plane are given for the PXCT dataset before (left) and after (right) applying a non-local means (NLM) filter in 3-D to eliminate white-noise. (b) In red contour, the zoom-ins are given for a detailed comparison between the raw and NLM filtered datasets.

4.4.6 Fourier Shell Correlation Estimation of the Achieved 3-D Spatial Resolution

To estimate the achieved 3-D spatial resolution of the PXCT and XRF datasets, the Fourier Shell Correlation (FSC) technique was used^[92,93] (see Section 2.4.4 for further details). Here the half-bit criterion is chosen as the value above which point the collected information can be reliably used to interpret the 3-D reconstructed volume (also both the 1-bit (full-bit) and ½-bit (half-bit) criterion are given in Figure 4.13).

In Figure 4.13 the FSC curves are given for the PXCT and XRF datasets before any noise-reduction steps (raw reconstructions) using a MATLAB code from the Astra toolbox^[90,91]. For the PXCT dataset the achieved 3-D spatial resolution is 74 nm whereas for the Ti XRF dataset this is 217 nm.

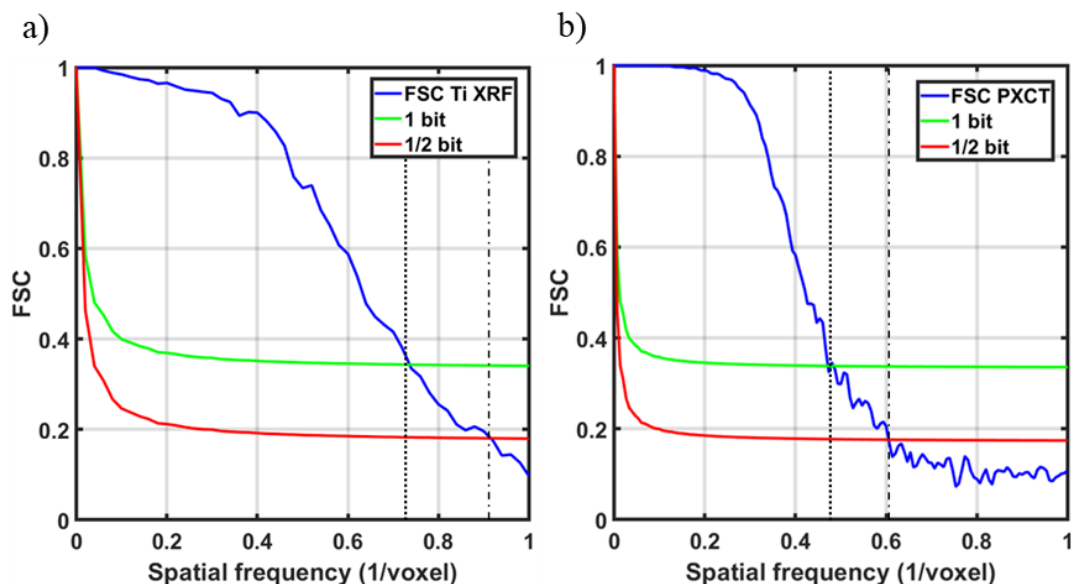


Figure 4.13 Fourier Shell Correlation (FSC) plots of (a) Ti XRF with 1/voxel size intersections of 0.74 for 1-bit and 0.92 for 1/2-bit giving estimated 3-D resolution values of respectively 270 and 217 nm and (b) PXCT with 1/voxel size intersections intersection of 0.47 for 1-bit and 0.61 for 1/2-bit giving estimated 3-D resolution values of respectively 97 and 74 nm.

4.4.7 Limited Information from the Ti X-ray Fluorescence Dataset

Despite the FSC estimated 3-D spatial resolution of 217 nm for the Ti XRF dataset assessment of the state of fragmentation within each catalyst particle didn't work as done in our previous work where the system investigated was at a higher polymerization yield and therefore exhibited more pronounced and stronger catalyst support fragmentation^[75]. In Figure 4.14 a comparison of the central slice of the Ti XRF and PXCT datasets is given as well as a zoom-in for one randomly selected particle. It becomes clear that whereas PXCT shows clear regions of different intensity values with high-resolution, which are the cracks of the catalyst framework most likely due to the polymerization, these features are not clearly visible within the Ti XRF dataset. This could simply be due to the fact that the 3-D spatial

resolution of the Ti XRF dataset, albeit close to the 2-D pixel value, is about 3 times larger than the PXCT dataset. In addition to the spatial resolution gap, the Si drift XRF detectors used in this experiment causes less counts in the FOV compared to the MAIA XRF detector^[75]. Nonetheless, high quality Ti and even Cl and Mg XRF datasets could be collected with improvements in the solid collection angles of the XRF detectors, smaller X-ray beam-and-step-size and switching to a He-filled (or vacuum) measuring chamber. This would change the attenuation length of Ti and Cl K_{α} photons at respectively ~ 4.5 and ~ 2.6 keV from several centimeters and millimeters in air towards several tens of meters in He.

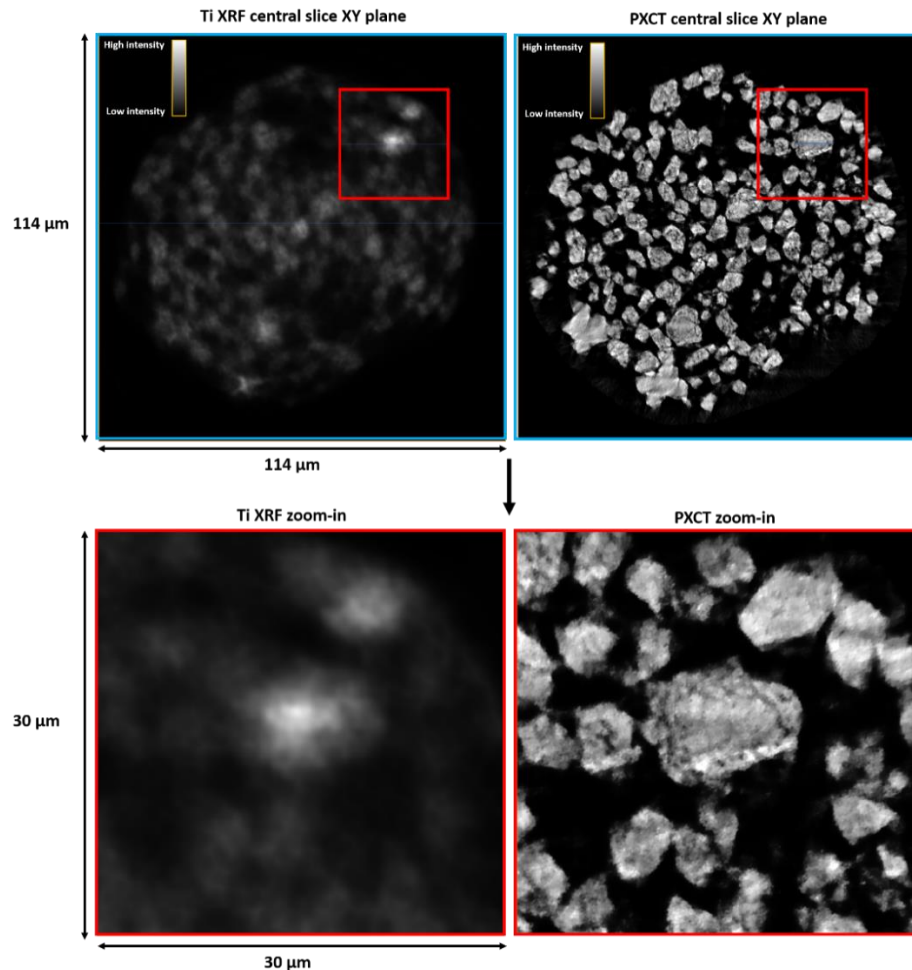


Figure 4.14 Visualizations of the reconstructed central slices in the XY plane of the Ti XRF dataset on the top-left with $200 \times 200 \times 200 \text{ nm}^3$ voxel size and the PXCT dataset on the top-right with $45.4 \times 45.4 \times 45.4 \text{ nm}^3$ voxel size. A zoom-in of the same $30 \times 30 \text{ μm}^2$ area for both datasets is given in the bottom row, which shows the clear difference in quality between the Ti XRF and PXCT datasets.

4.4.8 Marker-based Watershed Segmentation

From the central slices in Figure 4.14, it becomes clear that many particles are present in the scanned FOV, which opens the route to a statistical analysis of the state of fragmentation of each individual particle. A common approach would be to first binarize the 3-D volume based on a certain threshold and then use a labelling procedure to assign each particle a unique identity. However, a labelling procedure performed directly on a PXCT binarized 3-D volume results in a severe underestimation of the number of composite particles imaged. The reason for this is the high connectivity between the composite particles as evidenced also by the agglomeration of the composite particles with SEM images in Figure 4.6. Morphological operations such as erosion or selective closing (dilation followed by erosion) could be used in an attempt to remove the connectivity between adjacent particles, but this didn't give satisfactory results for this PXCT dataset.

A different approach is to segment the 3-D reconstructed agglomeration into individual particles. A common approach is the so-called watershed segmentation algorithm^[76]. This algorithm is based on finding the watershed ridge lines that separate catchment basins from each other. In this case, the catchment basin can be seen as the center of each particle and the watershed ridge lines would be defined at regions where the transition of low intensity voxels (background) to high intensity voxels (particle) is largest. The watershed segmentation process works best when providing some a priori knowledge about the position and number of particles expected through feeding the algorithm with markers. A common strategy to create these markers automatically is as follows:

- A. Transform the grayscale volume into a binarized volume.
- B. Calculate the distance map of the binarized volume, which gives the Euclidian distance between each voxel and the first non-zero voxel neighbors.
- C. Use the inverted distance map to calculate the H-minima (ergo the position of each catchment basin), where H is a chosen value of the depth of this catchment basin from the watershed ridge lines where

markers falling below this H-criterion are merged together to prevent over-segmentation.

However, despite the use of this H-criterion the non-supervised watershed segmentation algorithm is often plagued by either under- or over-segmentation. Therefore, in this case a more time-consuming approach by manually drawing the markers was chosen to have a strong control over the amount of particles are generated and to prevent both under- and over-segmentation that could otherwise occur with different H-values for the H-minima marker generation. To make a compromise between the time-consumption of drawing markers and its accuracy the following strategy was chosen (all steps performed in Avizo unless mentioned otherwise):

- A. Resample the original dataset of $2500 \times 2500 \times 440$ voxels to $625 \times 625 \times 110$ voxels.
- B. Draw the markers manually in the XY plane (110 instead of 440 slices due to the resampling step) on the resampled grayscale PXCT dataset whilst having cross-sectional views of the XZ and YZ planes open to confirm correct marker drawing. During this step it is highly important that different markers should not overlap in the 3-D volume or during the subsequent labelling procedure they will be assigned the same identity.
- C. Resample the manually drawn markers back to the original size of $2500 \times 2500 \times 440$ voxels.
- D. Label the upscaled markers.
- E. Binarize the original PXCT reconstructed volume using a manually found 10% threshold on the grayscale intensities. Using the near-full intensity histogram for the watershed segmentation would add too much background and noise signal to the labels and create unrealistically large particles.
- F. However, the 10% thresholded binarized images underestimates the volume of each particle as we remove not only voxels belonging to the background but also part of each particle. To counter-act this,

the binarized images are dilated in a ball-expansion mode (isotropic expansion). In Figure 4.15, the mean intensity of each single voxel shell added on the PXCT NLM filtered grayscale images during dilation is shown to find the dilation factor threshold that should be used. Based on these values a turnover point was observed around a dilation factor of 5, which was therefore used as the threshold for dilation. The dilation of the binarized PXCT volume was performed using in-house developed code within MATLAB on a 16-bit unsigned conversion of the original 32-bit float dataset.

- G. The use of this dilation factor of 5 can potentially still add voxels to the binarized volume with a mean grayscale intensity value low enough that it should be assigned to a background voxel. In Figure 4.15, this background mean grayscale intensity value was obtained by looking at the plateau achieved at very large dilation factors. In this case, a plateau of a mean grayscale intensity value of 315 was found after 15 voxel dilation. All voxels from the PXCT grayscale dataset with a value equal or lower than 315 were then removed from the 5x dilated binarized volume to correct for background voxels added during dilation.
- H. Create the distance map in 3-D from the corrected binarized PXCT volume in step G.
- I. Invert this generated distance map.
- J. Perform a marker-based watershed algorithm on the inverted distance map from step I using the upscaled labelled markers from step D. The chosen output of this algorithm is the catchment basins (meaning the separated particles).
- K. The created catchment basins are automatically labelled but are still separated from each other through the calculated watershed ridge lines. The labels are therefore expanded isotropically to fill the full volume.

- L. Finally, these labels are then masked by the corrected binarized volume from step G to give the separated composite polymer-catalyst particles with the entire background successfully removed.

These separated composite particles, each with its own unique label identity, can then be used for further analysis. However, from the 858 generated particles, 434 particles were partially cut-off by the lower and upper borders in the XY plane (as found by calculating the number of particles that have voxels interfacing any border). This means that these 434 particles, referred to as border particles, were not reconstructed completely due to the chosen FOV (as shown in Figure 4.1d schematically). After removal of these 434 incomplete particles, 424 completely imaged particles were obtained. These 424 separated particles were then saved as 16-bit unsigned 2-D tiff images to be opened in MATLAB. Then in MATLAB each of these 424 particles was visualized in 3-D using the maximum intensity projection volume rendering from the visualization toolbox. All particles were then inspected in terms of proper segmentation and several particles were found to instead consist of multiple particles. After manually correcting these faulty markers and redoing steps H-K, the final PXCT dataset was found to contain 434 separated and completely imaged particles.

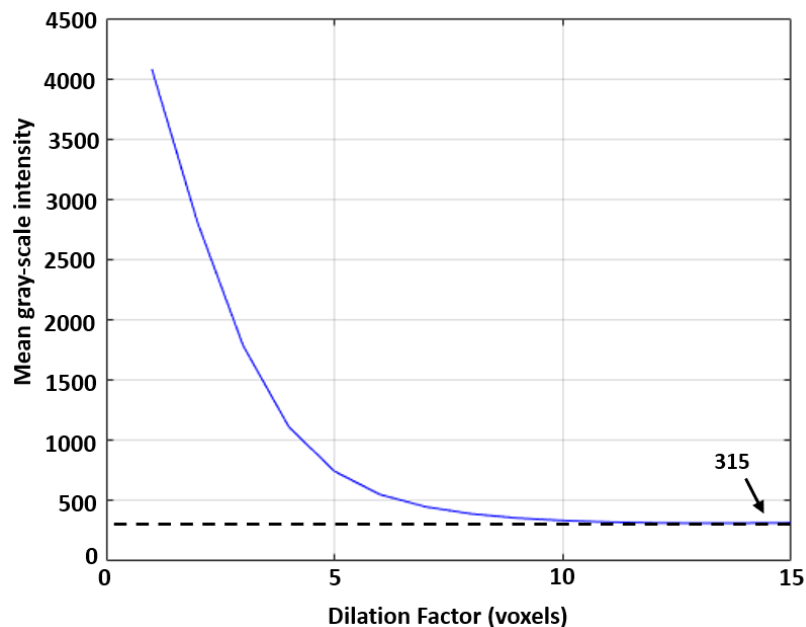


Figure 4.15 A plot of the PXCT mean grayscale intensity of each single voxel shell generated after each dilation. After 15 times dilation applied to all labelled particles, a plateau is reached of the mean grayscale intensity value of 315 (for the 16-bit unsigned converted PXCT dataset). This value was then taken as the mean grayscale intensity value of the background.

4.4.9 Calculation of the Geometrical Parameters of Each Individual Ethylene Polymerized Catalyst Particle

After the marker-based watershed segmentation and subsequent removal of the incompletely reconstructed border particles, 434 separated and completely reconstructed ethylene polymerized catalyst particles remain. For each of these particles several geometrical parameters can be calculated using the label of each particle (meaning a binarized particle with a unique identity). A short explanation on the following geometrical parameters as calculated within either the Avizo software package or MATLAB is given:

1. The volume (V , μm^3) of each particle. This is calculated by simply counting the number of non-zero voxels of each particle's binarized image and multiplying this by the volume of a single voxel ($\sim 9.4 \times 10^{-5} \mu\text{m}^3$).
2. The surface area (SA , μm^2) of each particle. This is calculated in MATLAB using the Crofton formula as described by Lehmann and Legland^[94].

3. The particle's equivalent spherical diameter (ESD in μm). This is calculated simply by assuming the particle to be a perfect sphere and using the following Equation 4.2 based on the volume calculated in 1):

$$ESD = \left(\frac{6 \times V}{\pi}\right)^{\frac{1}{3}} \quad \text{Equation 4.2}$$

4. The particle size distribution (PSD, μm) of each particle. Using the ESD values, the 10, 50 and 90 percentile distribution values referred to as respectively D_{10} , D_{50} and D_{90} can be calculated as well as the span (unitless, Equation 4.1). These values can then be compared to other measurement techniques such as SLS or SEM as well as to the theoretically expected D_{50} based on the polymer yield as discussed in Section 4.4.2.

The particle metrics providing information about the shape of each particle such as sphericity, elongation, and flatness were calculated as it was explained in Section 2.4.16.

4.4.10 K-Means Clustering Algorithm

The histogram of the grayscale intensity values in Figure 4.16 shows a broad distribution where it is difficult to discriminate between a HDPE and Ziegler-catalyst phase. This is most likely the result of the high degree of mixing of HDPE and Ziegler catalyst phases beyond the achieved 3-D spatial resolution of 74 nm. For example, the Ziegler-catalyst shows exclusively mesoporosity with pore sizes between 20-50 nm as discussed in Section 4.4.1. This means that even at the earliest stages of ethylene polymerization where HDPE is forming within the pore network, but the stress exerted on the framework hasn't reach a threshold yet to cause fragmentation, considerable sub-spatial resolution mixing of two chemical phases is expected. The mass density of the HDPE and Ziegler-catalyst phases are assumed to be on the order of $\sim 0.95 \text{ g/cm}^3$ for HDPE and $\sim 2.32 \text{ g/cm}^3$ for anhydrous MgCl_2 (the framework of a Ziegler-catalyst). Therefore, the high degree of mixing of both phases below the achieved spatial resolution and with a high difference in the mass density and therefore the electron density of each material is expected to be the reason for this broadening of the grayscale intensity values.

Applying a manual threshold on the grayscale intensities to what could be considered a HDPE phase and a Ziegler-catalyst phase would be subjective and open for interpretation in this difficult situation. However, the K-means clustering method provides an efficient way to partition each data-point, n , in this case a grayscale intensity value, to the nearest mean position of a cluster K_i . Here the number of K-clusters is chosen manually and the mean of each K, called the centroid, is initialized through a so-called K_{++} -algorithm within MATLAB, which uses an heuristic method to find the centroid seeds for the K-means clustering^[95].

Four K-clusters were chosen, where each K-cluster is expected to represent the following chemical phases in ascending order of mean electron density: K_1 should represent a chemical phase dominant in HDPE since HDPE has the lowest mass density and therefore a lower electron density according to Equation 1.8 than the Ziegler catalyst. K_2 and K_3 both represent highly mixed phases of HDPE and the Ziegler catalyst where in K_2 and K_3 the molar fraction in a voxel is highest for respectively HDPE in K_2 and the Ziegler catalyst in K_3 . Finally, K_4 has the highest mean electron density of all k-means clusters and should therefore represent a chemical phase dominant in the Ziegler catalyst. The result of the partitioning of the PXCT grayscale intensity histogram in these four different K-means clusters is shown in Figure 4.16. Furthermore, the geometrical parameters similar as to those given in Table 4.1 for the full particles are given here for each K-means cluster within each particle in Table 4.3.

The motivation for 4 k-means clusters instead of 3 k-means clusters where one could rationalize only a close-to-pure HDPE cluster, highly mixed HDPE and catalyst cluster and close-to-pure catalyst cluster is based on the calculated ESD of the clusters. As shown in Table 4.3, the ESD for the close-to-pure catalyst K_4 cluster is 3.10 μm , which is 14.8% smaller than that of the pure pristine catalyst D_{50} of 3.64 μm . With 3 instead of 4 k-means clusters, the calculated ESD of the close-to-pure catalyst cluster (K_3 in that case, since there are only 3 clusters) would be 3.66 μm and is practically equal to that of the pristine catalyst. Whereas this might seem logical at first, this would mean that the K_1 and K_2 clusters should both represent a pure HDPE phase since all catalyst is now contained in the K_3 cluster. However, the histogram of the

combined $K_{1,2}$ in the case of 4 clusters is already too broad and non-gaussian in peak-shape to describe a single chemical phase. Therefore, with 3 k-means clusters, a good portion of the highly mixed HDPE-catalyst phase is wrongfully assigned to the close-to-pure catalyst cluster K_3 and therefore overestimates the spatially-resolved catalyst.

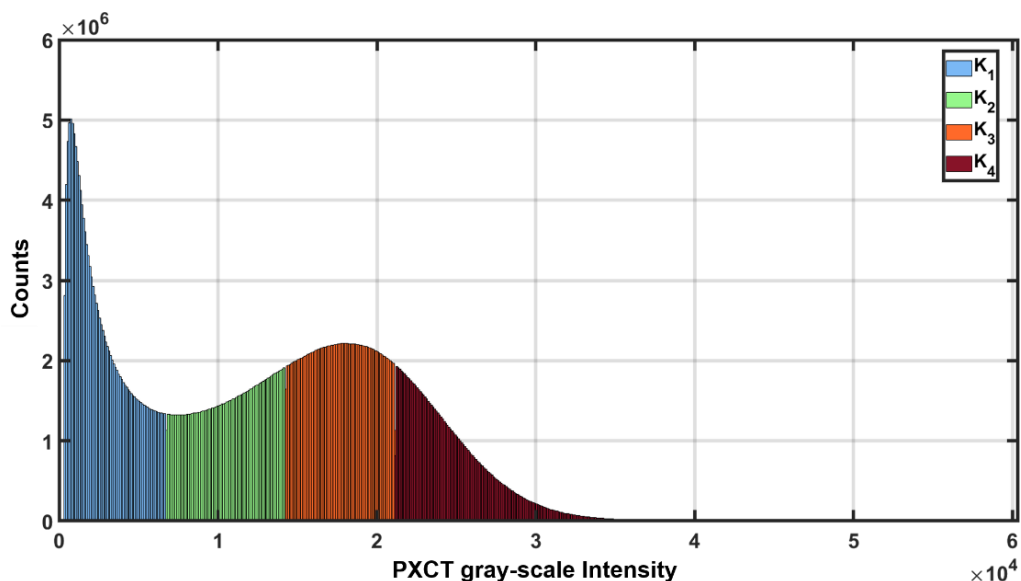


Figure 4.16 Histogram of the 16-bit unsigned converted PXCT grayscale intensity values after applying the 3-D non-local means filter. The color-coding from light blue to light green, orange and dark red correspond to the partitioning of the grayscale intensity values to four clusters (K_1 to K_4) using a k-means clustering algorithm. It should be noted here that the PXCT grayscale intensity values of the x-axis are of a 16-bit unsigned converted dataset (original is 32-bit float). This has no consequences for the data-analysis applied here since the raw data obtained doesn't contain the quantitative mean electron density in each voxel.

Particle Metrics	K-means cluster			
	K_1	K_2	K_3	K_4
V (μm^3)	33.6 ± 18.7	24.6 ± 17.7	31.6 ± 27.3	19.7 ± 20.4
SA (μm^2)	265.3 ± 145.6	304.5 ± 210.8	291.9 ± 239.4	129.2 ± 116.7
ESD (μm)	3.89 ± 0.65	3.46 ± 0.71	3.71 ± 0.89	3.10 ± 0.88
D₁₀ (μm)	3.20	2.69	2.67	2.09
D₅₀ (μm)	3.85	3.40	3.66	3.02
D₉₀ (μm)	4.62	4.25	4.63	4.15
Span	0.37	0.46	0.53	0.68
Ψ	0.20	0.026	0.04	0.08

Table 4.3 Overview of the mean and standard deviation values of the volume (V), surface area (SA) and equivalent spherical diameter (ESD), the 10,50,90 percentile fraction of particle size (D_x) and their span, sphericity (Ψ) for the four k-means clusters of all 434 ethylene polymerized catalyst particles.

4.4.11 Calculation and Comparison of Different Candidate Fragmentation Parameters

Besides the main fragmentation parameter, V_r , used to study the degree of catalyst fragmentation, additional fragmentation parameters can be designed and tried. These additional fragmentation parameters include standard image textural analysis techniques such as calculating the entropy, which is a measurement of the distribution of the greyscale intensity values within a particle, but also the calculation of the total number of spatially resolved catalyst fragments in the K_4 cluster, referred to as N_{NCC} , and the sum distance of these catalyst fragments to the particles center, referred to as $D_{NCC-center}$. Fundamentally speaking both a pure catalyst particle and a pure HDPE particle will have similar low entropy and standard deviation values due to the presence of a narrow greyscale intensity distribution. Therefore, such textural analysis techniques can't distinguish between extreme cases of very low and very high degrees of catalyst fragmentation due to the complete lack of chemical information input. Alternatively, the N_{NCC} and $D_{NCC-center}$ fragmentation parameters are fundamentally more straightforward than V_r as they directly and purely consider the catalyst fragments to study the degree of catalyst fragmentation. However, since both of these fragmentation parameters fully rely on being able to spatially resolve all catalyst fragments in the K_4 cluster to quantify the fragmentation degree it can severely underestimate the catalyst fragmentation degree in this study. The reason for this is that the smallest or also called primary particle size of the $MgCl_2$ support matrix is reported on the order of several to several tens of nm whereas the achieved spatial resolution in this work is 74 nm. Therefore, both catalyst fragments smaller than 74 nm and catalyst fragments in close proximity of each other can be either assigned to a lower k-means cluster and thus removed from the fragmentation parameter or become assigned to a single larger fragment.

The three fragmentation parameters used to study the degree or state of fragmentation of each particle are calculated in MATLAB using in-house written code:

A) The main fragmentation parameter, V_r , used in this Chapter is based on the ratio of the total volume of the $K_{1,2,3}$ clusters, which constitute the formed HDPE and catalyst fragments that couldn't be spatially resolved from the mixing with HDPE, to the mean volume of the catalyst fragments in the K_4 cluster. This V_r value is calculated by summing the $K_{1,2,3}$ volumes up for each particle and dividing this by the mean volume of all non-connected components (NCCs) found in K_4 . These NCCs are found by performing a labelling procedure on K_4 similar as to that performed after the watershed segmentation described in Section 4.4.8.

B) By counting the total number of NCCs in each particle and sort them accordingly in terms of increasing fragmentation degree the N_{NCC} fragmentation parameter is constructed. This N_{NCC} is calculated as described for V_r by counting the total number of NCCs found in K_4 for each particle. N_{NCC} suffers from underestimation of the fragmentation parameter since only spatially resolved catalyst fragments in the K_4 cluster are considered.

C) Finally, by also taking the distance of the NCCs from the center into account, additional spatial information is added to N_{NCC} in the form of the $D_{NCC-center}$ fragmentation parameter. However, $D_{NCC-center}$ suffers from the same shortcoming as N_{NCC} in that it fragments that are spatially unresolved from the HDPE phase are not taken into account. To calculate the sum of the distance of the NCCs in K_4 to the respective particle's center for each particle ($D_{NCC-center}$) the Euclidean distance is measured between the centroid of each NCC and the centroid of a particle.

Using the values obtained from the fragmentation parameter calculations of each particle, a sorting procedure can be made. In this sorting procedure, each particle gets assigned an ID value based on the value obtained from the respective fragmentation parameter in ascending order. For example, imagine a scenario with only two particles imaged. Particle A has a N_{NCC} value of 1 and a V_r value of 10 and particle B has a N_{NCC} value of 10 and V_r value of 1. In this case Particle A would be assigned an ID value of 1 for N_{NCC} since it has a lower N_{NCC} value than particle B. However, particle A would be assigned an ID value of 2 for V_r since it has a larger V_r than particle B. Furthermore, a sorting parameter dispersion is calculated for each particle,

which is simply the standard deviation value of the ID value this particle gets assigned according to each of the four fragmentation parameters. A small sorting dispersion value thus means that all three fragmentation parameters are in good agreement with each other regarding the degree of catalyst fragmentation of that specific particle. A large sorting dispersion value means that there is a weak agreement between these three fragmentation parameters regarding the degree of catalyst fragmentation of that specific composite particle. A weak agreement is typically expected for certain composite particles where the achieved 3-D spatial resolution limits the assessment of one or more of the three fragmentation parameters. In Table 4.4 the sorting ID values of all three fragmentation parameters are shown in an ascending order with respect to the sorting dispersion.

Sorting Dispersion	Fragmentation Parameter			Sorting Dispersion	Fragmentation Parameter		
	V_f	N_{NCC}	$D_{NCC-center}$		V_f	N_{NCC}	$D_{NCC-center}$
0	434	434	434	8.7	406	408	422
0.6	12	13	13	9	261	269	251
1	1	3	2	9.2	140	152	158
1	410	411	412	9.6	43	40	25
1.2	3	1	1	9.6	81	99	96
1.2	427	427	429	9.8	428	409	414
1.5	63	61	60	10	404	415	424
1.5	386	384	387	10.5	155	176	165
1.7	4	7	4	10.8	390	373	393
2.5	5	2	7	11	16	36	18
3.1	2	8	6	11.1	337	328	350
3.5	15	18	22	11.2	307	286	290
3.8	426	433	432	11.2	412	429	433
4.4	409	417	410	11.5	388	377	400
5.2	69	69	78	11.7	20	28	5
5.6	395	388	399	12	327	351	339
5.7	21	24	32	12.1	397	407	421
6.1	27	26	16	12.1	13	22	37
6.4	401	412	401	12.2	25	5	3
6.5	17	4	10	12.2	115	113	135
6.6	400	387	395	12.7	398	414	423
6.7	11	20	24	12.7	403	422	427
7	331	325	317	13	306	305	283
7.4	373	362	376	13	59	33	47
7.4	417	428	431	13.1	389	364	370
7.5	317	324	332	13.5	29	44	56
7.6	411	421	426	13.6	216	217	193
7.8	8	12	23	13.7	7	17	34
7.8	35	50	39	13.7	36	58	61
7.8	91	80	95	13.8	10	15	36
7.8	339	338	352	14	32	39	59
7.8	433	432	419	14.2	28	54	51
8.2	358	374	369	14.4	78	78	103
8.4	24	23	9	14.5	9	11	35
8.5	345	361	348	14.5	137	135	161
8.5	82	91	74	15.3	425	395	415
8.7	405	391	389	15.5	177	160	146

Sorting Dispersion	Fragmentation Parameter			Sorting Dispersion	Fragmentation Parameter		
	V_f	N_{NCC}	$D_{NCC-center}$		V_f	N_{NCC}	$D_{NCC-center}$
15.5	408	425	394	24.4	380	419	425
15.7	37	41	12	24.6	54	16	8
16	123	108	91	24.7	162	210	196
16.3	343	332	364	24.8	366	403	413
16.4	52	30	20	25.1	26	60	11
16.4	424	393	418	25.2	67	62	108
16.5	402	431	430	25.3	97	59	49
16.7	225	196	225	25.4	50	10	57
16.8	383	355	353	26	92	75	126
17	126	107	141	26	55	72	21
17	129	159	130	26	236	234	280
17.2	156	181	189	26	107	82	134
17.2	336	363	331	26.2	241	189	209
17.2	384	389	416	26.7	359	327	306
17.2	34	56	68	26.9	80	130	122
17.5	44	9	26	26.9	321	329	371
18	298	265	294	26.9	361	399	347
18.3	319	292	284	27	256	307	297
18.4	360	349	385	27.2	379	424	428
18.5	72	35	52	27.3	90	124	70
18.6	98	94	128	27.5	18	21	67
18.6	382	367	404	27.5	183	232	229
18.6	416	401	379	27.5	87	42	92
18.9	349	386	374	27.8	190	144	140
19	105	87	125	27.8	224	270	220
19.1	128	165	155	27.8	348	383	403
19.7	351	381	388	28	73	45	17
19.9	285	316	322	28	287	315	259
19.9	292	291	326	28.2	310	297	351
20	41	77	44	28.3	151	207	186
20	323	304	344	28.5	23	49	80
20.1	421	410	382	28.5	154	211	185
20.6	86	119	124	28.6	94	95	144
20.8	46	53	85	28.9	83	83	33
21	423	400	381	28.9	396	396	346
21.5	189	193	228	28.9	61	104	116
21.7	255	254	217	28.9	30	34	82
21.7	249	222	265	29	243	301	271
22.1	110	92	136	29	311	369	338
22.2	329	368	330	29.5	260	208	210
22.3	53	81	97	29.5	101	89	145
22.4	407	371	366	29.6	175	142	201
22.6	6	19	50	29.7	174	118	129
23	418	372	397	29.9	14	71	58
23.1	47	74	28	30.1	85	100	42
23.1	114	73	75	30.1	161	219	204
23.2	45	32	77	30.2	394	418	358
23.3	374	380	417	30.5	280	249	219
23.4	169	161	205	30.7	270	330	289
23.5	33	38	76	31	194	132	164
24	242	220	194	31.1	60	25	87
24.2	57	64	19	31.2	141	129	188

Sorting Dispersion	Fragmentation Parameter			Sorting Dispersion	Fragmentation Parameter		
	V_f	N_{NCC}	$D_{NCC-center}$		V_f	N_{NCC}	$D_{NCC-center}$
50.4	230	313	321	59.3	313	420	411
50.9	232	162	261	59.4	77	174	66
51.3	238	252	333	59.8	168	163	269
51.6	212	277	314	60.2	221	251	337
51.6	305	404	329	60.7	340	221	260
51.7	245	201	304	60.7	357	236	305
52	104	106	195	60.7	172	88	54
52.2	96	155	200	61.5	227	268	147
52.2	422	318	363	61.6	191	314	248
52.2	326	358	256	61.6	56	150	172
52.2	39	76	142	61.7	206	116	234
52.4	378	295	392	61.7	202	300	316
52.6	392	287	345	62	219	242	336
52.6	144	43	119	62.2	121	96	214
52.6	193	187	99	62.2	209	184	302
52.9	142	48	137	62.8	419	294	367
52.9	48	68	148	63	352	226	286
53.1	299	347	241	63.2	258	140	160
53.3	210	166	272	63.2	269	146	182
53.3	314	382	277	63.6	75	133	202
53.3	196	284	292	64.2	160	275	267
53.3	132	175	238	64.5	350	306	223
53.8	414	310	386	65	76	98	198
53.8	295	188	231	65.7	68	111	197
54.1	240	337	247	65.8	150	171	273
54.2	257	154	176	66	413	285	377
54.4	145	216	252	66.6	88	128	218
54.8	179	223	288	66.8	79	110	207
55.2	362	357	264	68.4	429	296	335
55.3	187	225	296	68.4	204	169	72
56.1	203	190	100	68.6	205	194	318
56.3	138	141	237	68.9	122	157	255
56.5	246	320	357	68.9	247	212	114
56.6	62	151	46	69.1	282	394	408
56.7	325	426	420	69.2	158	131	27
56.7	149	173	257	69.4	263	375	390
56.9	304	205	303	70	167	233	307
56.9	371	348	263	70.2	254	365	384
56.9	369	260	343	70.7	277	302	169
57	308	402	299	71.3	42	101	184
57.3	65	172	83	71.6	253	392	293
57.4	293	278	187	71.6	268	334	191
57.6	134	198	249	72	372	240	356
57.6	377	290	268	72.2	148	202	291
57.8	264	350	240	72.5	99	214	233
58.4	250	143	156	72.6	259	120	226
58.4	111	6	14	72.7	130	170	29
58.5	346	356	250	73.3	328	354	216
58.8	117	153	38	74.3	391	398	266
59.1	198	271	315	74.8	271	385	244
59.2	192	218	105	75.3	376	342	232
59.3	178	109	227	75.7	367	239	373

Sorting Dispersion	Fragmentation Parameter			Sorting Dispersion	Fragmentation Parameter		
	V_f	N_{NCC}	$D_{NCC-center}$		V_f	N_{NCC}	$D_{NCC-center}$
31.4	324	266	274	39.6	164	237	174
31.6	152	117	180	39.7	315	390	375
31.6	368	378	319	39.7	218	192	270
31.6	118	57	73	39.9	58	47	121
31.8	387	326	372	40	303	344	383
32.1	338	317	380	40.2	223	145	167
32.2	301	339	365	40.3	431	416	355
32.4	222	177	159	40.3	356	293	368
32.5	139	204	170	40.5	22	46	101
32.5	214	279	245	40.6	170	231	154
32.5	275	336	325	40.6	102	115	178
33.5	226	191	258	40.7	113	183	112
33.5	252	185	221	40.7	124	134	199
33.6	40	84	106	41	228	230	300
33.6	364	370	309	41.1	420	340	396
34.8	294	346	360	41.4	208	127	153
35.1	333	379	402	41.6	163	199	246
35.2	344	405	405	41.7	116	164	81
35.3	235	298	239	41.9	330	397	407
35.4	244	261	312	41.9	153	209	127
35.6	267	283	215	42.5	363	323	278
36.1	84	97	152	42.7	131	186	102
36.1	186	243	253	43	120	206	162
36.2	103	122	173	43	266	235	181
36.4	71	67	132	43	353	267	308
36.5	64	114	43	43.5	31	63	117
36.5	217	148	203	43.5	195	179	113
36.8	286	213	242	43.5	283	241	328
36.8	289	333	362	43.7	211	262	298
37.2	393	413	341	44	143	70	64
37.2	231	244	301	44	176	203	262
37.2	93	29	94	44.2	215	197	281
37.4	109	121	179	44.6	125	138	208
37.6	207	248	282	44.9	135	123	206
37.7	288	308	361	44.9	119	126	45
37.8	415	341	391	46.2	70	149	151
37.8	342	345	409	46.3	106	90	177
38	265	238	313	46.6	347	273	359
38	302	343	378	46.7	335	423	406
38.2	38	55	111	46.8	133	51	53
38.2	399	430	354	48	108	158	62
38.4	279	276	211	48.1	320	224	276
38.5	273	322	349	48.2	100	79	171
38.6	49	105	123	48.3	166	103	71
38.8	296	353	279	48.5	184	281	230
39	284	359	340	48.6	74	93	166
39.1	290	360	295	49.1	316	247	342
39.1	136	86	163	49.1	19	85	115
39.3	159	112	190	49.1	354	258	324
39.5	334	406	398	49.2	51	139	133
39.5	341	264	287	49.8	112	14	48
39.6	157	147	84	49.9	300	299	213

Sorting Dispersion	Fragmentation Parameter		
	V_r	N_{NCC}	$D_{NCC-center}$
76.3	213	65	107
76.6	248	257	120
77.3	181	168	41
77.7	234	253	110
78	291	137	192
78.9	381	289	224
79.4	199	229	79
79.5	251	125	104
79.5	173	331	236
80.4	297	280	150
80.4	237	215	88
83.4	188	309	149
83.4	318	321	175
84.1	89	200	254
84.9	201	167	40
84.9	146	263	311
85.5	180	335	320
85.6	220	288	118
85.6	147	274	310
86.8	385	311	212
87.2	182	180	30
88	430	255	327
88	312	136	222
88.5	66	156	243
88.7	274	312	143
89.5	185	272	93
89.7	197	31	55
90	165	303	334
92.5	233	52	109
93.6	171	256	69
93.9	432	245	323
94.5	375	195	235
95.1	370	246	183
98.1	262	66	157
98.6	239	228	63
100.7	281	227	86
101.4	278	250	90
102.8	229	178	31
103	95	259	285
103.5	200	27	15
103.8	272	182	65
104.8	322	319	139
105.9	332	366	168
113.2	309	352	138
124.2	276	37	98
125.2	127	376	275
137.4	355	282	89
144.2	365	102	131

Table 4.4 Overview of the fragmentation parameter sorting dispersion and the sorting value of all 434 composite particles as assessed by V_r , N_{NCC} and $D_{NCC-center}$. The sorting dispersion is calculated as the standard deviation of the sorting value each particle gets assigned according to these three

fragmentation parameters, V_r , N_{NCC} and $D_{NCC-center}$. The contents of the tables are given in an ascending order of the sorting dispersion. Particles with a low sorting dispersion have a strong agreement in the sorting between all three fragmentation parameters regardless of whether it is sorted in an early or late stage of fragmentation whereas particles with a high sorting dispersion show a weaker agreement between the fragmentation parameters used.

4.4.12 **Radial and Disk Analysis to Study the Fragmentation Behavior**

In Figure 4.5 both the radial distribution of the all k -means clusters as well as a disk analysis on the mean grayscale intensity values is given along the XY plane. For both calculations the PXCT grayscale, PXCT labelled and k -means clustered datasets were imported as 2-D Tiffs and analyzed with in-house developed MATLAB codes.

The radial analysis was performed in the same way as it was explained in Chapter 2, Section 2.4.10. But for the disk analysis, each particle is analyzed along the XY plane starting from one end of the particle's volume to the opposite. Along this XY plane, the particle is build up from certain number of slices where the distance or step size between each slice is defined by the size of a voxel, so 45.4 nm. Then at each slice the mean grayscale intensity is calculated over all voxels present within that slice and tabulated. The final plot gives the grayscale intensity at a slice number going from one end of the particle to the next. Therefore, the center of the plot corresponds to the center of the particle's respective volume.

4.4.13 **Estimating the Distribution of Particles in Fragmentation State**

The histogram of the V_r fragmentation parameter including the k -means clustering analysis to partition the particles as either weak, moderate, or strong degree of catalyst fragmentation is given in Figure 4.17. The methodology of this k -means clustering algorithm is identical to that as described in Section 4.4.10 and here applied on the V_r fragmentation parameter values. However, caution should be taken in interpreting these values as this k -means clustering algorithm will define hard boundaries on whether a particle is classified as weak, moderate, or strong with regards to the fragmentation degree and in reality, one would rather expect a smooth transition. Keeping

this in mind, the k -means clustering algorithm with therefore 3 clusters, estimates that respectively 274, 123 and 37 polymerized catalyst particles show a weak, moderate and strong degree of catalyst fragmentation.

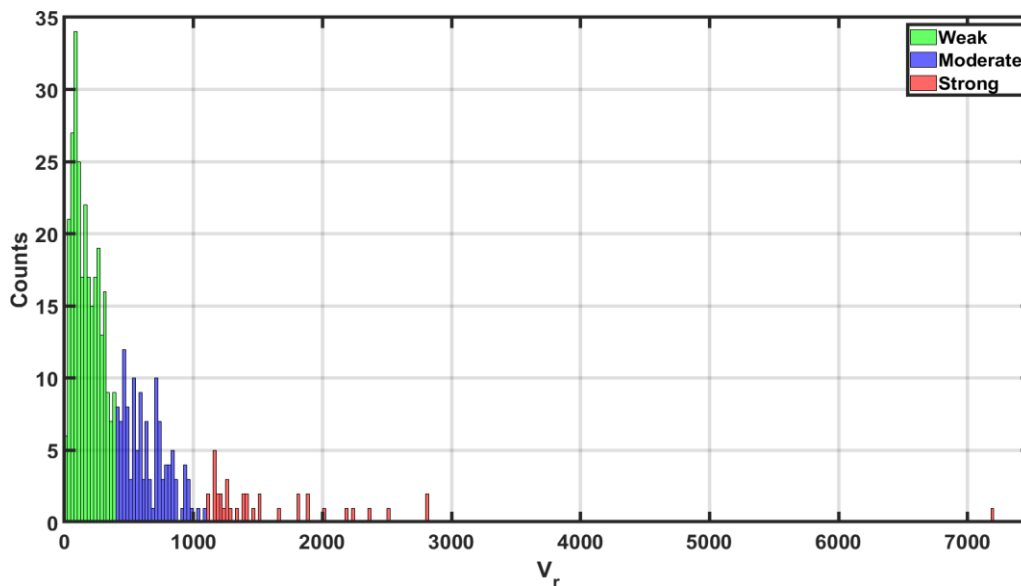


Figure 4.17 Histogram of the V_r fragmentation parameter including the partitioning of the polymerized catalyst particles into either a weak (green), moderate (purple) or strong (red) degree of catalyst fragmentation through a k -means clustering algorithm (3 k -clusters). The hard boundaries give here between these three fragmentation classes are merely an estimation as one would expect a gradual transition from a weak to a strong degree of catalyst fragmentation. 274 particles are assigned to the weak, 123 to the moderate and 37 to the strong classification.

4.5 References

- [1] K. E. Bett, B. Crossland, H. Ford, A. K. Gardner, Review of the Engineering Developments in the High Pressure Polyethylene Process 1933-1983, *Proceedings of the Golden Jubilee Conference, Polyethylenes 1933-1983*, Plastics And Rubber Institute, London, **1983**.
- [2] K. Soga, T. Shiono, *Prog. Polym. Sci.* **1997**, 22, 1503–1546.
- [3] J. R. Severn, J. C. Chadwick, R. Duchateau, N. Friederichs, *Chem. Rev.* **2005**, 105, 4073–4147.
- [4] K. Ziegler, *Angew. Chem.* **1964**, 76, 545–553.
- [5] G. Natta, *Angew. Chem.* **1964**, 76, 553–566.
- [6] W. Kaminsky, *Polyolefins: 50 Years after Ziegler and Natta I: Polyethylene and Polypropylene*, Springer, **2013**.
- [7] L. L. Böhm, *Angew. Chem. Int. Ed.* **2003**, 42, 5010–5030.
- [8] R. Mülhaupt, *Macromol. Chem. Phys.* **2013**, 214, 159–174.
- [9] T. Hees, F. Zhong, M. Stürzel, R. Mülhaupt, *Macromol. Rapid Commun.* **2019**, 40, 1800608.
- [10] I. Vollmer, M. J. F. Jenks, M. C. P. Roelands, R. J. White, T. Harmelen, P. Wild, G. P. Laan, F. Meirer, J. T. F. Keurentjes, B. M. Weckhuysen, *Angew. Chem. Int. Ed.* **2020**, 59, 15402–15423.
- [11] T. F. L. McKenna, A. Di Martino, G. Weickert, J. B. P. Soares, *Macromol. React. Eng.* **2010**, 4, 40–64.
- [12] T. Simonazzi, G. Cecchin, S. Mazzullo, *Prog. Polym. Sci.* **1991**, 16, 303–329.
- [13] M. A. Ferrero, M. G. Chiovetta, *Polym. Eng. Sci.* **1987**, 27, 1448–1460.
- [14] M. A. Ferrero, M. G. Chiovetta, *Polym. Eng. Sci.* **1987**, 27, 1436–1447.
- [15] M. A. Ferrero, M. G. Chiovetta, *Polym. Eng. Sci.* **1991**, 31, 886–903.
- [16] D. A. Estenoz, M. G. Chiovetta, *Polym. Eng. Sci.* **1996**, 36, 2208–2228.
- [17] B. Horáčková, Z. Grof, J. Kosek, *Chem. Eng. Sci.* **2007**, 62, 5264–5270.

- [18] M. Abboud, P. Denifl, K.-H. Reichert, *Macromol. Mater. Eng.* **2005**, 290, 558–564.
- [19] L. Seda, A. Zubov, M. Bobak, J. Kosek, A. Kantzas, *Macromol. React. Eng.* **2008**, 2, 495–512.
- [20] G. A. H. Nooijen, *Catal. Today* **1991**, 11, 35–46.
- [21] M. Hassan Nejad, P. Ferrari, G. Pennini, G. Cecchin, *J. Appl. Polym. Sci.* **2008**, 108, 3388–3402.
- [22] S. Knoke, D. Ferrari, B. Tesche, G. Fink, *Angew. Chemie Int. Ed.* **2003**, 42, 5090–5093.
- [23] J. T. M. Pater, G. Weickert, W. P. M. Van Swaaij, *J. Appl. Polym. Sci.* **2003**, 87, 1421–1435.
- [24] J. T. M. Pater, G. Weickert, J. Loos, W. P. M. van Swaaij, *Chem. Eng. Sci.* **2001**, 56, 4107–4120.
- [25] M. Qi, B. Zhang, Z. Fu, J. Xu, Z. Fan, *J. Appl. Polym. Sci.* **2016**, 133, 43207.
- [26] R. L. Laurence, M. G. Chiovetta, *In Polymer Reaction Engineering*, Hasuer-Verlag, München, **1983**.
- [27] G. A. H. Nooijen, *Eur. Polym. J.* **1994**, 30, 11–15.
- [28] G. Weickert, G. B. Meier, J. T. M. Pater, K. R. Westerterp, *Chem. Eng. Sci.* **1999**, 54, 3291–3296.
- [29] G. Fink, B. Steinmetz, J. Zechlin, C. Przybyla, B. Tesche, *Chem. Rev.* **2000**, 100, 1377–1390.
- [30] H.-L. Rönkkö, T. Korpela, H. Knuutila, T. T. Pakkanen, P. Denifl, T. Leinonen, M. Kemell, M. Leskelä, *J. Mol. Catal. A Chem.* **2009**, 309, 40–49.
- [31] M. Kakugo, H. Sadatoshi, M. Yokoyama, K. Kojima, *Macromolecules* **1989**, 22, 547–551.
- [32] M. Kakugo, H. Sadatoshi, J. Sakai, M. Yokoyama, *Macromolecules* **1989**, 22, 3172–3177.
- [33] L. Noristi, E. Marchetti, G. Baruzzi, P. Sgarzi, *J. Polym. Sci. Part A Polym. Chem.* **1994**, 32, 3047–3059.
- [34] V. M. Egorov, E. M. Ivan'kova, V. B. Kulik, D. V. Lebedev, L. P. Myasnikova, V. A. Marikhin, E. I. Radovanova, M. A. Yagovkina, V. Seydewitz, S. Goerlitz, G. H. Michler, U. Nöchel, F. J. Balta-Calleja, *Polym. Sci. Ser. C* **2011**, 53, 75–88.
- [35] X. Zheng, M. Smit, J. C. Chadwick, J. Loos, *Macromolecules* **2005**, 38, 4673–4678.
- [36] X. Zheng, J. Loos, *Macromol. Symp.* **2006**, 236, 249–258.
- [37] X. Zheng, M. S. Pimplapure, G. Weickert, J. Loos, *Macromol. Rapid Commun.* **2006**, 27, 15–20.
- [38] F. M. Silva, J. P. Broyer, C. Novat, E. L. Lima, J. C. Pinto, T. F. McKenna, *Macromol. Rapid Commun.* **2005**, 26, 1846–1853.
- [39] A. Di Martino, J. P. Broyer, R. Spitz, G. Weickert, T. F. McKenna, *Macromol. Rapid Commun.* **2005**, 26, 215–220.
- [40] F. Machado, E. L. Lima, J. C. Pinto, T. F. McKenna, *Macromol. React. Eng.* **2009**, 3, 47–57.
- [41] T. F. L. McKenna, E. Tioni, M. M. Ranieri, A. Alizadeh, C. Boisson, V. Monteil, *Can. J. Chem. Eng.* **2013**, 91, 669–686.
- [42] C. Jacobsen, *X-Ray Microscopy*, Cambridge University Press, **2019**.
- [43] A. M. Beale, S. D. M. Jacques, B. M. Weckhuysen, *Chem. Soc. Rev.* **2010**, 39, 4656.
- [44] I. D. Gonzalez-Jimenez, K. Cats, T. Davidian, M. Ruitenbeek, F. Meirer, Y. Liu, J. Nelson, J. C. Andrews, P. Pianetta, F. M. F. de Groot, B. M. Weckhuysen, *Angew. Chem.* **2012**, 124, 12152–12156.
- [45] K. H. Cats, I. D. Gonzalez-Jimenez, Y. Liu, J. Nelson, D. van Campen, F. Meirer, A. M. J. van der Eerden, F. M. F. de Groot, J. C. Andrews, B. M. Weckhuysen, *Chem. Commun.* **2013**, 49, 4622.
- [46] A. M. Beale, S. D. M. Jacques, E. K. Gibson, M. Di Michiel, *Coord. Chem. Rev.* **2014**, 277–278, 208–223.
- [47] S. W. T. Price, K. Ignatyev, K. Geraki, M. Basham, J. Filik, N. T. Vo, P. T. Witte, A. M. Beale, J. F. W. Mosselmans, *Phys. Chem. Chem. Phys.* **2015**, 17, 521–529.
- [48] K. H. Cats, J. C. Andrews, O. Stéphan, K. March, C. Karunakaran, F. Meirer, F. M. F. de Groot, B. M. Weckhuysen, *Catal. Sci. Technol.* **2016**, 6, 4438–4449.
- [49] S. W. T. Price, D. J. Martin, A. D. Parsons, W. A. Slawiński, A. Vamvakeros, S. J. Keylock, A. M. Beale, J. F. W. Mosselmans, *Sci. Adv.* **2017**, 3, e1602838.
- [50] F. Meirer, B. M. Weckhuysen, *Nat. Rev. Mater.* **2018**, 3, 324–340.
- [51] A. Vamvakeros, S. D. M. Jacques, M. Di Michiel, D. Matras, V. Middelkoop, I. Z. Ismagilov, E. V. Matus, V. V. Kuznetsov, J. Drnec, P. Senecal, A. M. Beale, *Nat. Commun.* **2018**, 9, 4751.
- [52] A. Vamvakeros, D. Matras, S. D. M. Jacques, M. di Michiel, S. W. T. Price, P. Senecal, M. A. Aran, V. Middelkoop, G. B. G. Stenning, J. F. W. Mosselmans, I. Z. Ismagilov, A. M. Beale, *J. Catal.* **2020**, 386, 39–52.
- [53] T. L. Sheppard, S. W. T. Price, F. Benzi, S. Baier, M. Klumpp, R. Dittmeyer, W. Schwieger, J.-D. Grunwaldt, *J. Am. Chem. Soc.* **2017**, 139, 7855–7863.
- [54] Y. Fam, T. L. Sheppard, A. Diaz, T. Scherer, M. Holler, W. Wang, D. Wang, P. Brenner, A. Wittstock, J.-D. Grunwaldt, *ChemCatChem* **2018**, 10, 2858–2867.
- [55] J. Becher, D. F. Sanchez, D. E. Doronkin, D. Zengel, D. M. Meira, S. Pascarelli, J.-D. Grunwaldt, T. L. Sheppard, *Nat. Catal.* **2021**, 4, 46–53.
- [56] Y. Fam, T. L. Sheppard, J. Becher, D. Scherhauser, H. Lambach, S. Kulkarni, T. F. Keller, A. Wittstock, F. Wittwer, M. Seyrich, D. Brueckner, M. Kahnt, X. Yang, A. Schropp, A. Stierle, C. G. Schroer, J.-D. Grunwaldt, *J. Synchrotron Radiat.* **2019**, 26, 1769–1781.
- [57] J. C. da Silva, K. Mader, M. Holler, D. Haberthür, A. Diaz, M. Guizar-Sicairos, W.-C. Cheng, Y. Shu, J. Raabe, A. Menzel, J. A. van Bokhoven, *ChemCatChem* **2015**, 7, 413–416.

- [58] J. Ihli, D. Ferreira Sanchez, R. R. Jacob, V. Cuartero, O. Mathon, F. Krumeich, C. Borca, T. Huthwelker, W.-C. Cheng, Y. Shu, S. Pascarelli, D. Grolimund, A. Menzel, J. A. van Bokhoven, *Angew. Chem. Int. Ed.* **2017**, 56, 14031–14035.
- [59] J. Ihli, R. R. Jacob, M. Holler, M. Guizar-Sicairos, A. Diaz, J. C. da Silva, D. Ferreira Sanchez, F. Krumeich, D. Grolimund, M. Taddei, W. C. Cheng, Y. Shu, A. Menzel, J. A. van Bokhoven, *Nat. Commun.* **2017**, 8, 809.
- [60] J. Ihli, A. Diaz, Y. Shu, M. Guizar-Sicairos, M. Holler, K. Wakonig, M. Odstrcil, T. Li, F. Krumeich, E. Müller, W.-C. Cheng, J. A. van Bokhoven, A. Menzel, *J. Phys. Chem. C* **2018**, 122, 22920–22929.
- [61] S. R. Bare, M. E. Charochak, S. D. Kelly, B. Lai, J. Wang, Y. C. K. Chen-Wiegart, *ChemCatChem* **2014**, 6, n/a-n/a.
- [62] F. Meirer, D. T. Morris, S. Kalirai, Y. Liu, J. C. Andrews, B. M. Weckhuysen, *J. Am. Chem. Soc.* **2015**, 137, 102–105.
- [63] F. Meirer, S. Kalirai, D. Morris, S. Soparawalla, Y. Liu, G. Mesu, J. C. Andrews, B. M. Weckhuysen, *Sci. Adv.* **2015**, 1, 1–13.
- [64] F. Meirer, S. Kalirai, J. N. Weker, Y. Liu, J. C. Andrews, B. M. Weckhuysen, *Chem. Commun.* **2015**, 51, 8097–8100.
- [65] S. Kalirai, U. Boesenberg, G. Falkenberg, F. Meirer, B. M. Weckhuysen, *ChemCatChem* **2015**, 7, 3674–3682.
- [66] S. Kalirai, P. P. Paalanen, J. Wang, F. Meirer, B. M. Weckhuysen, *Angew. Chem. Int. Ed.* **2016**, 55, 11134–11138.
- [67] A. M. Wise, J. N. Weker, S. Kalirai, M. Farmand, D. A. Shapiro, F. Meirer, B. M. Weckhuysen, *ACS Catal.* **2016**, 6, 2178–2181.
- [68] M. Gambino, M. Veselý, M. Filez, R. Oord, D. Ferreira Sanchez, D. Grolimund, N. Nesterenko, D. Minoux, M. Maquet, F. Meirer, B. M. Weckhuysen, *Angew. Chem. Int. Ed.* **2020**, 59, 3922–3927.
- [69] M. Veselý, R. Valadian, L. M. Lohse, M. Toepperwien, K. Spiers, J. Garreto, E. T. C. Vogt, T. Salditt, B. M. Weckhuysen, F. Meirer, *ChemCatChem* **2021**, 13, 2494–2507.
- [70] W. Curtis Conner, S. W. Webb, P. Spanne, K. W. Jones, W. C. Conner, S. W. Webb, P. Spanne, K. W. Jones, *Macromolecules* **1990**, 23, 4742–4747.
- [71] M. A. Ferrero, R. Sommer, P. Spanne, K. W. Jones, W. C. Conner, *J. Polym. Sci. Part A Polym. Chem.* **1993**, 31, 2507–2512.
- [72] K. W. Jones, P. Spanne, W. B. Lindquist, W. C. Conner, M. Ferrero, *Nucl. Instruments Methods Phys. Res. Sect. B Beam Interact. with Mater. Atoms* **1992**, 68, 105–110.
- [73] S. Boden, M. Bieberle, G. Weickert, U. Hampel, *Powder Technol.* **2008**, 188, 81–88.
- [74] L. Meisterová, A. Zubov, K. Smolná, F. Štěpánek, J. Kosek, *Macromol. React. Eng.* **2013**, 7, 277–288.
- [75] K. W. Bossers, R. Valadian, S. Zanoni, R. Smeets, N. Friederichs, J. Garreto, F. Meirer, B. M. Weckhuysen, *J. Am. Chem. Soc.* **2020**, 142, 3691–3695.
- [76] S. Beucher, F. Meyer, in *Math. Morphol. Image Process.*, CRC Press, **2018**, pp. 433–481.
- [77] M. S. Nielsen, M. B. Munk, A. Diaz, E. B. L. Pedersen, M. Holler, S. Bruns, J. Risbo, K. Mortensen, R. Feidenhans'l, *Food Struct.* **2016**, 7, 21–28.
- [78] C. Huo, X. H. Ren, B. P. Liu, Y. R. Yang, S. X. Rong, *J. Appl. Polym. Sci.* **2003**, 90, 1463–1470.
- [79] H. Hammawa, S. E. Wanke, *Polym. Int.* **2006**, 55, 426–434.
- [80] H. Hammawa, S. E. Wanke, *J. Appl. Polym. Sci.* **2007**, 104, 514–527.
- [81] M. D'Amore, K. S. Thushara, A. Piovano, M. Causà, S. Bordiga, E. Groppo, *ACS Catal.* **2016**, 6, 5786–5796.
- [82] T. F. McKenna, J. B. P. Soares, *Chem. Eng. Sci.* **2001**, 56, 3931–3949.
- [83] A. V. Cheruvathur, E. H. G. Langner, J. W. Niemantsverdriet, P. C. Thüne, *Langmuir* **2012**, 28, 2643–2651.
- [84] D. Liu, J. Yu, in *2009 Ninth Int. Conf. Hybrid Intell. Syst.*, IEEE, **2009**, pp. 344–349.
- [85] N. H. Friederichs, R. Gerlofmsa, *WO Patent 2009112254A1*, **2009**.
- [86] S. Lafleur, R. Berthoud, R. Ensinnck, A. Cordier, G. De Cremer, A. Philippaerts, K. Bastiaansen, T. Margossian, J. R. Severn, *J. Polym. Sci. Part A Polym. Chem.* **2018**, 56, 1645–1656.
- [87] V. A. Solé, E. Papillon, M. Cotte, P. Walter, J. Susini, *Spectrochim. Acta Part B At. Spectrosc.* **2007**, 62, 63–68.
- [88] F. Pfeiffer, *Nat. Photonics* **2018**, 12, 9–17.
- [89] Y. Liu, F. Meirer, P. A. Williams, J. Wang, J. C. Andrews, P. Pianetta, *J. Synchrotron Radiat.* **2012**, 19, 281–287.
- [90] W. van Aarle, W. J. Palenstijn, J. De Beenhouwer, T. Altantzis, S. Bals, K. J. Batenburg, J. Sijbers, *Ultramicroscopy* **2015**, 157, 35–47.
- [91] W. van Aarle, W. J. Palenstijn, J. Cant, E. Janssens, F. Bleichrodt, A. Dabrovolski, J. De Beenhouwer, K. Joost Batenburg, J. Sijbers, *Opt. Express* **2016**, 24, 25129.
- [92] M. van Heel, M. Schatz, *J. Struct. Biol.* **2005**, 151, 250–262.
- [93] R. P. J. Nieuwenhuizen, K. A. Lidke, M. Bates, D. L. Puig, D. Grünwald, S. Stallinga, B. Rieger, *Nat. Methods* **2013**, 10, 557–562.
- [94] G. Lehmann, D. Legland, Insight J., accessed online 01-12-2021 <http://hdl.handle.net/10380/3342>. **2012**.
- [95] A. David, S. Vassilvitskii, D. Arthur, S. Vassilvitskii, in Proc. Eighteenth Annu. ACM-SIAM Symp. Discret. Algorithms, *Society For Industrial And Applied Mathematics*, **2007**, pp. 1027–1035.

5. **Mass Transport Simulation in an Entire Fluid Catalytic Cracking Catalyst Particle**

In this Chapter, mass transport simulations performed on a single fluid catalytic cracking (FCC) particle will be reported. Mass transport through the porous matrix of catalyst bodies plays a key role in heterogeneous catalysis by controlling catalyst efficiency in diffusion limited systems. Simulating diffusion in complex pore structures, such as in solid catalysts, requires information at multiple length scales and across the whole body of the catalyst. Here, X-ray ptychography tomography of a whole single FCC particle was used to map the entirety of its complex macro-pore structure in 3-D. These data were complemented by correlated X-ray fluorescence tomography that allowed identifying the catalytically most active zeolite domains embedded within the catalyst body. Based on these data a computational mass transport simulation was performed, evaluating the diffusion of reactants into the particle, their conversion into products at the zeolite domains, and subsequent outward diffusion of the generated products. The results not only provide a direct measure of catalyst accessibility and catalyst efficiency for diffusion limited systems, but also allow for a time-resolved visualization and quantification of the mass transport behavior of reactants and products inside the catalyst body. This in turn allowed to cross validate FCC catalyst diffusion coefficients reported in literature, which are notoriously hard to determine but represent an important parameter in the rational design of solid catalysts.

This Chapter is based on: Roozbeh Valadian, Amir Raouf, Martin Veselý, Marianna Gambino, Jan Garrevoet, Bert M. Weckhuysen, and Florian Meirer, in preparation.

5.1 Introduction

Synchrotron radiation-based X-ray microscopy techniques, such as X-ray ptychography and micro X-ray fluorescence (μ XRF) tomography, allow mapping of the 3-D pore structure and metals distributions in whole single catalyst particles of up to 100 μ m diameter and at high spatial resolutions^[1]. Specifically, X-ray ptychography tomography achieves 3-D resolutions in the range of a few tens of nanometers^[2] and is therefore able to assess the entire macro-pore structure of a catalyst (pores > 50 nm)^[3]; however, measurement time constraints require a compromise between the imaged field of view (FOV) and the achieved 3-D resolution when a whole catalyst particle needs to be mapped. The latter is indeed necessary when mass transport in an individual catalyst particle should be simulated and quantified based on its real-life pore structure. Mass transport in porous solid catalysts plays a crucial role in catalytic processes where the ability of reactants and products to diffuse into and out of the catalyst body controls overall activity and selectivity – such systems are commonly called diffusion-limited^[4]. However, determining diffusion coefficients for catalyst bodies remains challenging and available experimental methods can only provide average values at the bulk, but not at the single particle level. Moreover, due to the hierarchically complex nature of a catalyst body's pore structure mass transport properties are expected to significantly vary within a single catalyst particle. Understanding these diffusion processes at the single particle level is therefore essential to improve catalyst performance. In this Chapter, an FCC particle was used as an archetypical example of a rationally designed hierarchically porous material.

Different modeling techniques have previously been used to simulate transport phenomena within FCC catalyst particles. Often, idealized continuum models have been used to simulate deactivation and cracking in the riser^[5–10]. However, since inter-particle variations in pore interconnectivity and catalyst particle morphology are neglected in these studies, discrete models, such as a stochastic pore network (PN) model, have been suggested in 2-D^[11–15] and 3-D^[13,16]. To further improve the model and get closer to the real pore structure, scanning electron microscopy (SEM) was used to generate a 2-D PN from a single catalyst particle^[17]. In previous work

our group has also used focused ion beam-scanning electron microscopy (FIB-SEM) to study the pore space at the macro- and mesoscale, track accessibility, and study pore connectivity in several individual particle sub volumes^[18]. However, the lack of information about the location of zeolite domains and the three-dimensional macro-pore structure of the whole catalyst particle prevented insights about the distribution of reactants and products and the accessibility of active sites in the catalyst, that is, factors that ultimately dictate catalyst performance.

Recently, (correlative) X-ray microscopy techniques have become popular for obtaining both the 3-D macro-pore structure and the 3-D element distribution of either FCC catalyst particle sub-volumina^[19] or a whole single FCC catalyst particle at high spatial resolution^[20,21], paving the way for simulations considering those factors. In a first study of that kind, Meirer et al.^[22] used data recorded by transmission X-ray microscopy (TXM) to study the effect of pore clogging by Fe and Ni via simple permeability simulations in selected sub-volumina of an individual catalyst particle. This was later extended by Liu et al.^[20] establishing a resistor network model from correlated 3-D μ XRF and TXM data in turn assessing both zeolite accessibility and the stability of the macro-pore network of a whole FCC particle against pore clogging by poisoning metals. These studies quantified catalyst accessibility at equilibrium conditions and provided valuable information about the contributions of the different processes lowering FCC performance during catalyst ageing, which happens over many process cycles where the catalyst circulates between riser reactor and regenerator. However, to obtain a deeper understanding of catalyst performance one has to assess non-equilibrium mass transport phenomena at the time scale of the catalyst residence time in the riser reactor (a few seconds^[23]), that is, from the moment when the catalyst enters the riser reactors and comes in contact with the feedstock. Moreover, to obtain a more complete picture of the processes involved, the reaction of feedstock molecules at the active sites in the catalyst should also be considered. However, due to the highly complex pore structure of catalyst bodies the use of highly precise continuum models for mass transport simulations is very demanding in terms of computational costs, while discrete models such as PN modeling can be used as a simplified model of the real

macro-pore space of the catalyst particle. When assessing the pore space of a full individual catalyst particle it is therefore necessary to find a compromise between precision of the simulation model and computational costs, analogous to the compromise that has to be made between spatial resolution and imaged FOV when mapping the PN experimentally.

In this Chapter, an analysis of the mass transport properties of an entire single FCC particle was performed based on the 3-D reconstruction of its entire real macro-pore space, which is subsequently used in an effective methodology for simulating diffusion processes. Mass transfer is simulated at the macro-pore level for the whole real-life catalyst particle using PN modeling. Both the 3-D macro-pore space, which is considered the transportation highway for molecules in an FCC catalyst^[23], and the distribution of Fe and Ni poisoning metals, which are known to lower accessibility of an E-cat^[20,22,24–29], were mapped by combined X-ray ptychography and μ XRF tomography (Figure 5.1a,b, Section 5.4.1). To ensure that the FCC catalyst selected here is a representative E-cat particle of high metal loading, the radial distribution profiles of all metals detected by μ XRF tomography was evaluated (Figure 5.11, Section 2.4.10). Also, the morphological parameters of the measured E-cat particle were compared to previous studies as shown in Table 5.1 (further details about particle metrics are provided in Section 2.4.16) and the results were all found to be in the range of values reported in previous studies.

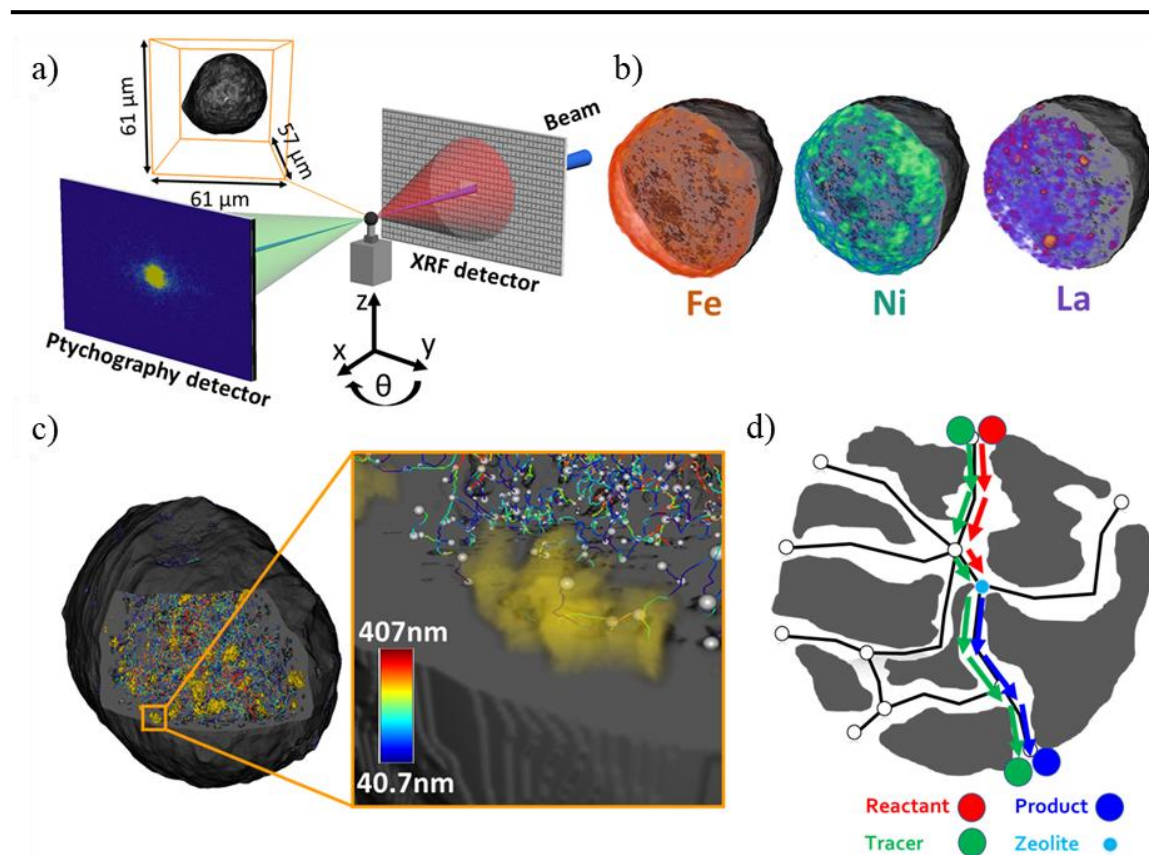


Figure 5.1 Mapping an entire equilibrium FCC particle. (a) X-ray ptychography and X-ray fluorescence microscopy tomography setup used to image the catalyst particle. The bounding box indicates the size of the measured equilibrium catalyst (E-cat) particle. (b) 3-D solid phase of the catalyst (gray) and spatial distributions of iron, nickel, and lanthanum in the catalyst particle. (c) Superposition of the zeolite domains (shown as yellow clusters and identified via the La distribution) on the PN of the catalyst particle. Connections (segments) between nodes (white spheres) indicate the so called ‘skeleton’ of the PN model after skeletonization of the reconstructed pore space. Nodes are defined as segment intersections where more than 2 segments meet. The color scale indicates the different diameters of each segment based on the voxelized pore space (voxel size 40.7 nm). (d) Schematic of the mass transport simulation within the whole single catalyst particle PN (segments are drawn as black lines). Due to the concentration gradient applied between surface and active sites of the particle, reactant and tracer diffuse inside the particle depending on size and connectivity of different pore pathways. When they reach the active (zeolite) domains, the reactants are consumed to create products, which accumulate and diffuse outwards due to the dynamically changing concentration gradients. The tracer on the other hand does not react and remains unchanged while diffusing through the PN, in turn indicating the evolution of the diffusion front.

Metric	
Anisotropy	0.330935
Elongation	0.81876
Flatness	0.81716
Roundness/Sphericity	0.9455
Equivalent Diameter (μm)	43.95
Total Particle Volume (TPV) (μm^3)	44,463.8
Total Particle Surface Area (μm^2)	6419.6
Macro-pore volume (μm^3)	5,466.9
Macro-pore volume (% of TPV)	12.29
Macro-pore surface area (μm^2)	40,402.5
Macro-pore specific surface area ($\mu\text{m}^2/\mu\text{m}^3$)	0.9087

Table 5.1 Single particle metrics of an individual E-cat FCC catalyst particle.

5.2 Results and Discussion

To obtain the location of the catalytically most active zeolite domains in the catalyst the La distribution from μXRF was used as a marker. Only 7 vol% of those domains identified via the lower resolution XRF data were found to not perfectly align with the solid phase obtained via Ptychography tomography, in other words, only 7 vol% of all La domains were ‘leaking’ into the pore space determined by Ptychography tomography data, which shows the excellent alignment that was achieved between XRF and Ptychography data. The small error (7 vol%) can be explained by the difference in spatial resolution of the two data sets^[20].

Using this analysis and a watershed segmentation of the μXRF data that was aided by the average 2-D size of zeolite domains based on FCC cross-sections^[30], a total of 3981 zeolite domains with a total volume of $754 \mu\text{m}^3$ representing 1.7 vol% of the total E-cat particle ($44464 \mu\text{m}^3$) was found. This is in agreement with reports from literature^[23,26]. Of those, 1832 domains were found directly connected to the mapped catalyst’s macro-pore space, while the remaining 2149 domains were buried within the solid phase, that is, in those parts of the catalyst that exhibit pore sizes below the achieved spatial resolution ($<200 \text{ nm}$). Further, 1082 zeolite domains (27 % of all zeolite domains) were connected via the mapped macro-pore space to the surface of the particle, that is, to the outside of the particle. This result is in excellent agreement with the 74% decrease in accessibility reported previously via the commonly used accessibility index (AI) between a fresh catalyst and a catalyst

with high metal loading^[31]. It is interesting to note that these 1082 zeolite domains still represent 66.4 vol% of all zeolite domains. Therefore, while almost $\frac{3}{4}$ of the zeolite domains have become inaccessible, two thirds of their total volume can in principle still be reached by the feedstock via the mapped macro-pore space, albeit with increased diffusion limitations. This suggests that catalyst deactivation must be caused by (the complex interplay of) both, reduced zeolite activity and changes in mass transport properties during ageing and that evaluating accessibility should be complemented by mass transport simulations to evaluate the impact of changes in the pore system of a diffusion limited catalytic solid. In this Chapter, a PN modeling approach was used to simulate the diffusion process within a single FCC catalyst particle.

The PN model which represents the catalyst particle's pore volume as a 3-D geometrical graph was extracted and generated. More than 90% of the nodes found to be within the main sub-graph (largest sub-graph in the network) of the PN model which has a significant influence on the accessibility of nodes within the PN model. Afterwards, the multi directional pore network (MDPN) was generated by applying some filters needed to make the computations feasible (Figure 5.3a). This strategy is justified as solute mixing mainly happens at the locations of pore junctions, and, additionally, the simulated travel distances are much longer than the length of individual pore throats. Using this strategy, a large MDPN of the catalysts pore structure consisting of about 50000 nodes connected by a large number of segments was obtained, which effectively represents the entire complex pore space.

This correlation of the two data sets allowed identifying all nodes of the PN model based on Ptychography data that were connected to, or located within, a zeolite domain (identified via XRF data, Figure 5.1c) – hence, these nodes are in the following referred to as ‘zeolite nodes’. This approach of correlating lower resolution μ XRF data with higher resolution nano-tomography data to obtain a labelled PN model was discussed and analyzed in detail by Liu and Meirer et al.^[20], including an assessment of the effect of merging such data of different spatial resolution on the robustness of the labeled pore network. However, the significantly higher spatial resolution of the μ XRF tomography data achieved here (~ 595 nm) allowed using a more

sophisticated algorithm for identifying zeolite nodes after resampling the XRF data to the voxel size of the ptychography data (the voxel size of the data is always much smaller than the spatial resolution estimate obtained by e.g., Fourier ring correlation). Figure 5.2 shows five cases for how the developed algorithm assigns zeolite nodes, based on the correlated Ptychography and XRF data. Because the skeletonization to establish a PN model was performed twice, once considering zeolite domains as solid (i.e., non-macroporous) phase and once as pore space, cases 1, 2, and 5 represent straightforward results where the zeolite domain contains actual nodes of the network generated from the second skeletonization. The comparison between the PN models obtained from the first and second skeletonization was then used to determine actual connectivity of the respective zeolite domain to the ‘true’ PN model (i.e., the one established considering zeolite domains as non-macroporous phase). For example, cases 1 and 2 are therefore connected to macro-pore space while case 5 is not, as it represents a zeolite domain buried in the solid phase. Cases 3 and 4 represent more complex cases where zeolite domains are located half in the solid and half in the pore phase but do not contain, such as in case 2, segment points or nodes. Here a solid expansion algorithm of the zeolite domain (expanding the domain only in the pore space) was used to determine the nearest node or segment point in the PN model and this point was then used as a zeolite node. Although not actually located in a zeolite domain this node then correctly identified partially buried zeolite domains such as cases 3 and 4 as accessible via the connected macro-pore space.

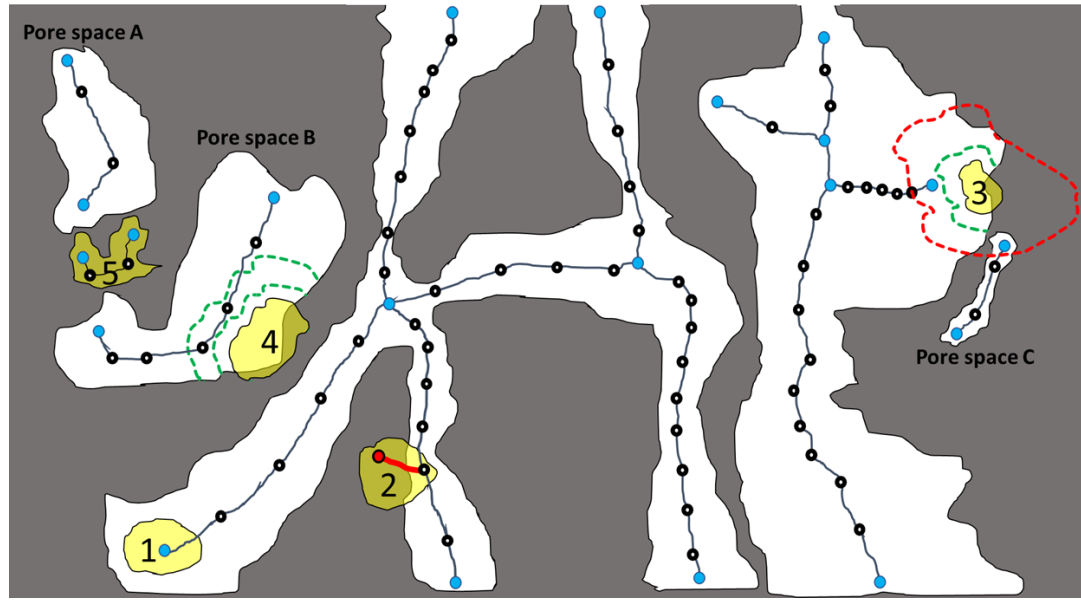


Figure 5.2 Schematic of the 2-D porous structure (pores= white, matter= gray) and the corresponding PN. Nodes, segments, and segment points of the PN are represented by blue dots, solid black lines, and black dots, respectively. The yellow regions show the zeolite domains. The green dashed lines show the expanded domain within the pore space for finding zeolite nodes.

The PN modeling applied in this Chapter^[32] was successfully used to simulate advanced mass transport in several complex porous media in the presence of multiple chemical reactions^[33]. Here, the PoreFlow model generated from the large X-ray ptychography tomography data set ($1497 \times 1497 \times 1400$, i.e., $>10^9$ voxels) consisted of more than 50000 nodes and segments and was used to perform a mass transfer simulation based on Fick's first law. Single phase mass transport simulation (that is, not considering two phase phenomena such as capillary forces) was performed by placing a fixed concentration of reactants at the outer surface ($C_{\text{reactant,outer surface}} = 1$) of the particle, which, upon the start of the simulation, begin to diffuse into the particle pore space due to the generated concentration gradients ($C_{\text{reactant,zeolite domains}} = 0$). When reactants arrive at the zeolite nodes, they react and (immediately) turn into products. Therefore, the concentration of products increases at and next to the zeolite nodes. Due to this increase, products begin to diffuse outwards, ultimately to exit the pore space through the surface nodes. It was assumed that when products exit the particle, they join the bulk flow in the riser and do not accumulate at the surface, that is, the outside product concentration is kept at 0 at all times. As reactants are being consumed

inside the particle, a concentration gradient of reactants is always maintained between the outer surface of the particle (where reactant concentration is kept constant) and inside the particle (where reactants are consumed at the zeolite nodes). This concentration gradient serves as the driving force for the diffusion process, and it becomes clear that this mass transport simulation is dominated by the complex interplay between diffusion pathways, accessibility, and location of the active sites, that is, it is characteristic for the catalyst's composition and pore space morphology. For better visualization and clarity, the concentration of reactant, product, and tracer was normalized by their concentration at the surface of the particle as explained in Section 5.4.6.

It is important to notice that since the transport of mass was simulated directly within the pore space, a binary diffusion coefficient was applied rather than an effective value which is often used by continuum scale models and has a smaller value to compensate for the presence of solid phases and tortuosity of the pore space. A value of $D = 10^{-9} \text{ m}^2/\text{s}$ was chosen based on the range of values reported for FCC catalysts in literature, as seen in Table 5.2.

D [m²/s]	T [K]	Host	Method	Note
9.50×10⁻⁹	307.7	n-octane	PFG-NMR ^[34]	In pellet (3µm zeolite crystals)
5.48×10⁻¹² to 5.00×10⁻¹¹	423-483	di-iPr benzene	ZLC ^[35]	in FCC pellet 0.9µm Y-crystal
2.80×10⁻¹² to 1.71×10⁻¹¹	398-463	tri-iPr benzene	ZLC ^[35]	in FCC pellet 0.9 µm Y-crystal
7×10⁻⁷	623	1,2,4-trimethylcyclohexane	IGC ^[36]	in pellet
1.00×10⁻⁷	623	phenanthrene	IGC ^[36]	in pellet
8×10⁻¹⁴ ± 1×10⁻¹³	293	PDI	SMF ^[37]	in pellet
order of 10⁻¹³	below 773	tri-iPr benzene	Riser ^[38]	in FCC pellet
order of 10⁻¹²	773.15	n-hexadecane	Tracer-Gravimetric uptake ^[39]	in pellet
10⁻¹⁰ to 10⁻⁹	253-363	n-octane	(MAS) Pulsed-field gradient NMR (PFG-NMR) ^[40]	
5×10⁻⁹ to 4×10⁻⁷	303.15	Dagang vacuum residue	(Tracer-) Gravimetric uptake ^[41]	

Table 5.2 Overview of the variety of the diffusion coefficient values obtained by different methods, temperature, and host molecules.

Note that variations in the value of D only causes molecules to move faster or slower; therefore, a scaling factor can be used to predict the reactant, product, and tracer concentrations at any location in the pore network for other D values. The simulation for a time period of ~ 5 min (100 timesteps, each timestep = 2.97s) of diffusion with the above-mentioned D was performed to characterize the macro-pore space of the catalyst particle and observe the diffusion behavior of molecules inside the catalyst pore network over time.

To better evaluate the accessibility of all nodes from the particle surface and interconnectivity of the pore space, which controls the mass transport ability of the catalyst, diffusion of conservative tracer molecules that probe the entire pore network without reacting at the zeolite nodes was simulated. Clearly, due to the complex topology of the pore network, the diffusion path length is a key parameter to define accessibility of the zeolite nodes compared to the Euclidean distance from the particle surface (see Section 5.4.5 for further details). It is important to note that, even when two nodes exhibit the same diffusion path length, they often display different normalized tracer concentration values at a certain time due to the complex network topology of the particle as shown in Figure 5.13. This is because the diffusion path only considers the shortest path and does not take into account the coordination number of the nodes along the path. However, the presence of nodes with higher coordination number (i.e., more branching of the path) lowers the concentration along the path compared to a path with less branches connected to it, since the tracer molecules will be distributed across more nodes. In this context it becomes clear that only a mass transport simulation of the entire particle can capture the complex topology of a pore network that is as highly interconnected as the ones typically found in porous catalyst bodies.

The results of the mass transport simulation are displayed in Figure 5.3a. Panels b,c and d show the normalized concentrations for all three components (i.e., tracer, reactants, and products) over time (i.e., after 5s, 2min and 5min of simulation). The normalized concentration of each component at a certain time is obtained by taking the average of the normalized concentrations of the corresponding component in all nodes. As expected, the normalized tracer and reactant concentrations initially increased rapidly because of the high initial concentration gradient developed between the surface and the interior sections

of the particle. However, after about half a second (Panel b), the normalized reactant concentration levelled off and remained almost constant, while the normalized tracer concentration continued to increase, always showing larger values than reactants and products. This is in line with the fact that the tracer does not react at zeolite nodes and continuously diffuses into the pore network. The normalized reactant concentration on the other hand approached a constant value, which indicates that a steady state condition had been reached, i.e., the state where the influx of reactant from the surface of the particle was equal to its consumption at the zeolite nodes inside the particle.

The rapid initial increase of normalized reactant concentration explains why catalyst deactivation by coke deposits happens in the first 0.15 seconds in the riser reactor^[42]: the final cracking reaction of the reactant molecules at the zeolite nodes takes place during the very early stages of the process facilitated by the highly inter-connected and therefore highly accessible macro-pore structure. Note that the pre-cracking of the reactant molecules within the catalyst matrix, which results in even faster coke formation throughout the catalyst, was not even considered here.

During the first 47 s of our simulation the normalized reactant concentration remained higher than the normalized product concentration since products are only created after reactants have penetrated into the pore space and reached the zeolite nodes. After this time, the normalized concentration of products continued to increase and became higher than that of the reactants. This is because product molecules are generated and accumulate at the zeolite nodes and within the particle, while reactant molecules are being consumed. Generation of the product molecules over time increases their concentration and drives an increasingly larger diffusive flux of these molecules towards the surface of the particle where they exit. The normalized concentration of the product molecules is set and kept at zero at the surface of the particle since they are being transported to the bulk flow in the riser reactor with much lower concentration values. In other words, the product molecules are now probing the same pore space as the tracer molecules but are instead diffusing out of the particle. Because their normalized concentration was averaged over all nodes, the curves of tracer and product displayed in Figure 5.3 naturally show the same trend.

It is also important to mention that even for this simulation that does not even consider coke deposition that can block pores, the steady-state condition for product molecules is never reached – it is only reached after simulation times that are much longer than the 5 minutes used here (Figure 5.3d). This observation shows that the assumption of steady-state conditions for product flow is not valid considering the residence time of the catalyst in the riser reactor, which is only a few seconds.

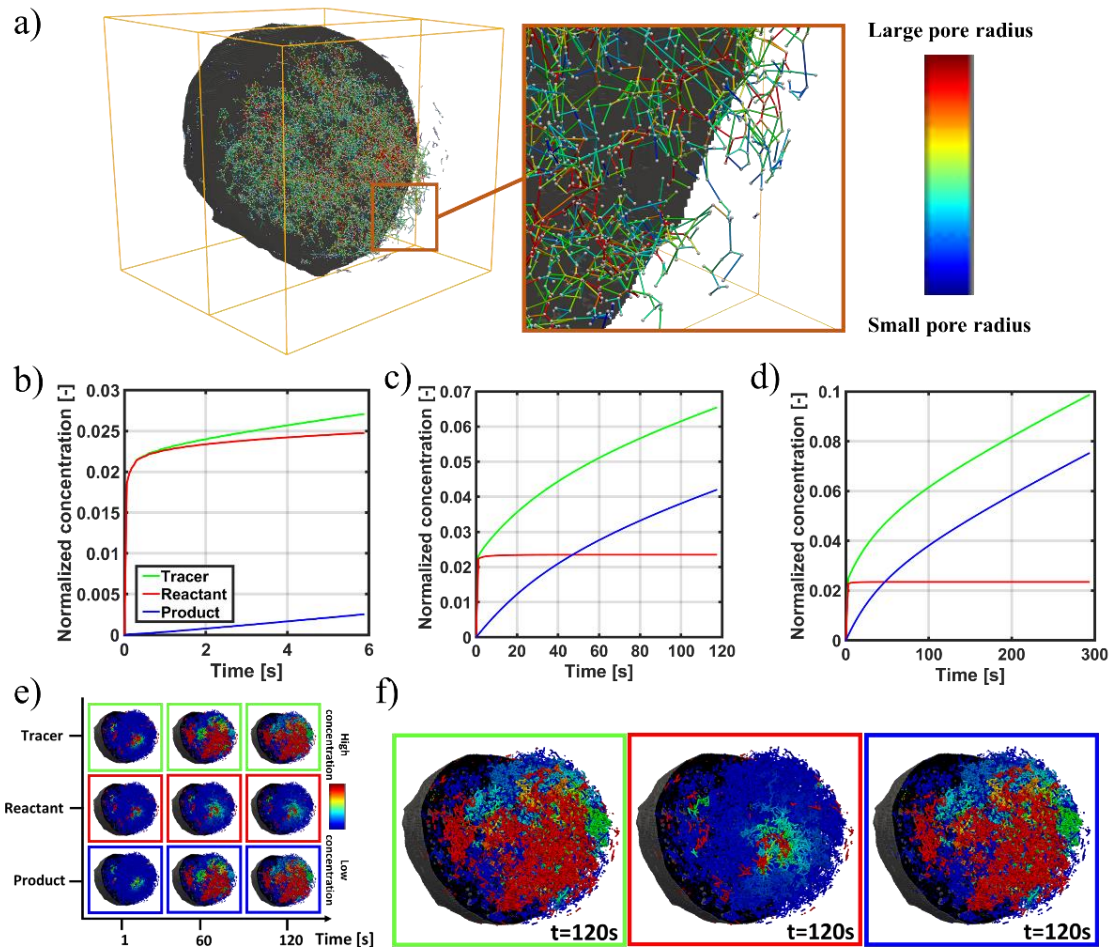


Figure 5.3 Distribution of the three components tracer, reactant, and product inside the catalyst's MDPN as a function of time. (a) The MDPN of the particle. The color of different segments represents their pore radius. (b,c,d) Average single particle normalized concentration profiles of all three components (tracer, reactant, and product) versus time using a diffusion coefficient value of $10^{-9} \text{ m}^2/\text{s}$. This normalized concentration at a certain time is obtained by taking the average over the normalized concentrations of the corresponding component in all nodes. The normalized concentration of all three components is visualized in 3-D in (e) at three different times (1s, 60s, 120s). Here the different colors of the segments indicate the respective normalized concentration of tracer, reactant, and product. Panel (f) shows the distribution of all components within the MDPN at $t=120s$ of the simulation (enlarged from panel e).

While graphs b and c in Figure 5.3 provide information on concentrations averaged over the entire particle, the three-dimensional distribution of tracer, reactant, and product concentrations at various times can be inspected. This allowed to reveal the inhomogeneous site accessibility within the catalyst particle that is responsible for the observed diffusion behavior. Figure 5.3e shows that after 120s the normalized product concentration was only high in one part of the particle which indicates low, or even no connectivity between smaller and larger sub-regions of the macro-pore network. This is in line with previous studies^[20,25] where it was reported that a large number of surface nodes, i.e., the entry points of the catalyst's macro-pore network, were blocked by metal deposits, which made a large fraction of the particle's macro-pore space inaccessible for both in- and out-diffusion processes. Here, it was also found that several surface nodes, which are uniformly distributed over the particle surface were not connected to the main-graph (i.e., largest sub-graph) of the pore network, but to smaller sub-graphs and thus created isolated pore regions. Additional remarkable regions identified from a detailed analysis of the simulation results for this specific E-cat particle are discussed below.

Having information about the three-dimensional concentration distribution of the tracer allowed to plot tracer concentrations at all individual zeolite nodes as a function of time and diffusion path length (Figure 5.4a, Section 5.4.5). This plot directly visualizes zeolite node accessibilities, and its time evolution reveals the presence of three distinct regions within the particle (Figure 5.4b-f): Region 1 is characterized by zeolite nodes at (or very close to) the surface of the particle (shown in magenta in Figure 5.4b-d). This region, which actually consists of several isolated smaller pore volumina in the particle surface, is highly accessible and therefore reached the maximum normalized concentration (i.e., $C_{\max}=1$) already during the early stages of the diffusion simulation. Region 2 (shown in red in Figure 5.4b,c, and e) includes a volume that is still close to the particle surface, which is characterized by less interconnected pores (clearly expressed by the much larger spread of tracer concentration values shown in Figure 5.4b) when compared to the pore connectivity in the deeper, more central parts of the particle. This region formed most likely because the particle is an aged E-cat and many macro-

pores close to the surface are blocked due to metal poisoning as can be seen in Figure 5.11. The radial analysis (see Section 2.4.10 for further details) shown in Figure 5.12a confirms that the porosity close to the surface is smaller than that of regions deeper in the particle. This is in line with the observation that the node density (i.e., the number of nodes in a concentric volume shell that is normalized by the shell volume) increases when moving towards the center of the particle (Figure 5.12b). It is important to note that, particular for the catalyst particle used in this Chapter, the reactant molecules could only enter via the mapped macro-pores on one side of the particle (indicated as Region 2), because all other mapped surface macro-pores were either blocked or belonged to the isolated pores and clusters of Region 1 (magenta). A similar observation was reported in literature for aged E-cat particles^[25]. Such pore clogging in near-surface regions of the particle also caused poor interconnectivity between pores in Region 2. Therefore, Region 2 acts as a bottleneck for reactant molecules to reach the internal space of the particle (i.e., Region 3). This can be seen in the schematic of Figure 5.4c in which Region 2 is connected to Region 3 only through very few connections. Region 3 (blue color scheme in Figure 5.4), however, contained 85 percent of the total pore space of the catalyst particle (evaluated via the sum of segment volumes of the MDPN). This region is characterized by a highly interconnected pore network with higher porosity and pore density compared to Region 2. Therefore, tracer molecules, upon entering this region, almost immediately distributed nearly uniformly over the entire pore space of this region, as evidenced by the very small spread in tracer concentrations in Figure 5.3c. Note that, as flux of molecules into this region was limited by the bottleneck between Region 2 and Region 3, the normalized tracer concentrations in the zeolite nodes of this region were always lower than in the other two regions. The magnitude of the flux into Region 3 was so small that the normalized concentration of tracer molecules at the zeolite nodes increased only very slowly, and equilibrium between the regions was never reached, even when increasing the simulation time to ~5 minutes (Figure 5.3d). As seen in Figure 5.4b, the normalized tracer concentration profiles clearly confirm the presence of these different regions, including the clear separation between Regions 2 and 3.

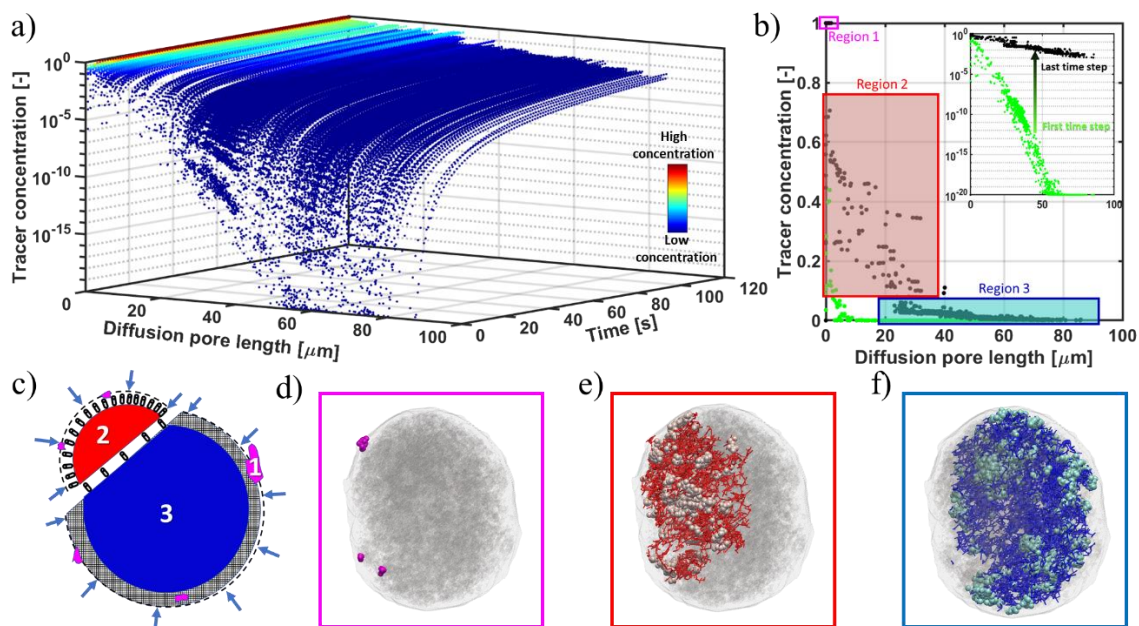


Figure 5.4 Change of tracer normalized concentration in zeolite nodes versus diffusion pore length and simulation time. (a) The normalized concentration of the tracer in all zeolite nodes was plotted against simulation time and diffusion pore length. Dots show the normalized concentration at the corresponding zeolite node with a specific diffusion pore length and at each recorded timestep (for clarity the normalized concentration gradient with time, the color of the dots also shows the tracer normalized concentrations (color bar)). (b) Tracer normalized concentration in all zeolite nodes comparing only the first- and last time steps of the simulation (last time step after 120 s). Zeolite nodes within the catalyst particle can be classified into three regions, each with a different normalized concentration range. The spread in normalized concentration values provides direct evidence for high (regions 1 and 3) and low (region 2) pore interconnectivity. (c) Schematic of the 3 regions detected within the PNM. Blue arrows show the direction of inward diffusion, which can proceed efficiently only from one side of the particle, that is, via region 2 that exhibits many ‘entrance pores’, while entrance pores are blocked on the other side, that is, for region 3. The measured particle is an aged E-cat FCC particle, so metal and coke deposition inside the particle typically causes major macro-pore clogging at the surface of the particle; this explains why region 3 is poorly connected to the surface area and reactant molecules cannot diffuse directly into it. Moreover, the pore connectivity between regions 2 and 3 is severely limited, creating a bottleneck for flux between those regions. Regions shown in magenta (region 1) represent isolated pore space connected the surface of the particle but not to the deeper regions (regions 2 or 3). Panels (d), (e), and (f) show the 3-D volume of the catalyst particle separated into regions 1-3 of the MDPN (nodes and segments represented by spheres and lines), respectively.

In literature a wide range of diffusion coefficient values have been reported for the FCC catalyst (Table 5.2), spanning several orders of magnitude. The diffusion coefficient is, however, an important parameter of the catalyst as it needs to be sufficiently large to allow reactant molecules to reach the majority of zeolite domains embedded in the particle within the

residence time of the catalyst particle inside the riser reactor (often in the range of 3 to 5 seconds^[23]).

Figure 5.5a shows the normalized averaged tracer concentration for all zeolite domains within the MDPN. The normalized averaged tracer concentration for each zeolite domain is defined as the average of normalized tracer concentration for all zeolite node(s) within the corresponding zeolite domain. It is clear that within 5 seconds, by using a diffusion coefficient of 10^{-9} m²/s (blue graph), only a small amount of tracer molecules can reach the zeolite domains ($C_{tracer}^{t=5s} = 5.5 \times 10^{-3}$). However, as can be seen in Figure 5.5b, within this time all accessible zeolite domains (27% of all zeolite domains) can be reached by the tracer.

To explore the effect of different diffusion coefficient values suggested in literature, tracer averaged normalized concentration profiles (in zeolite nodes) were determined for three values of D (Figure 5.5) taken from literature^[34,35,43]. The simulations show that for a small diffusion coefficient (for instance D_4), not only the average tracer normalized concentration in the catalyst was found to be very small, but also the percentage of zeolite domains involved in the cracking reaction was very low (red curve in Figure 5.5a,b) within 5 seconds simulation time. Even by extending the simulation time up to 5 minutes (Figure 5.5c,d, red plot), only 12% of all domains participate in the cracking process after that time. These results highlight the importance of optimized diffusive flux within a catalyst and how it relates to catalyst efficiency.

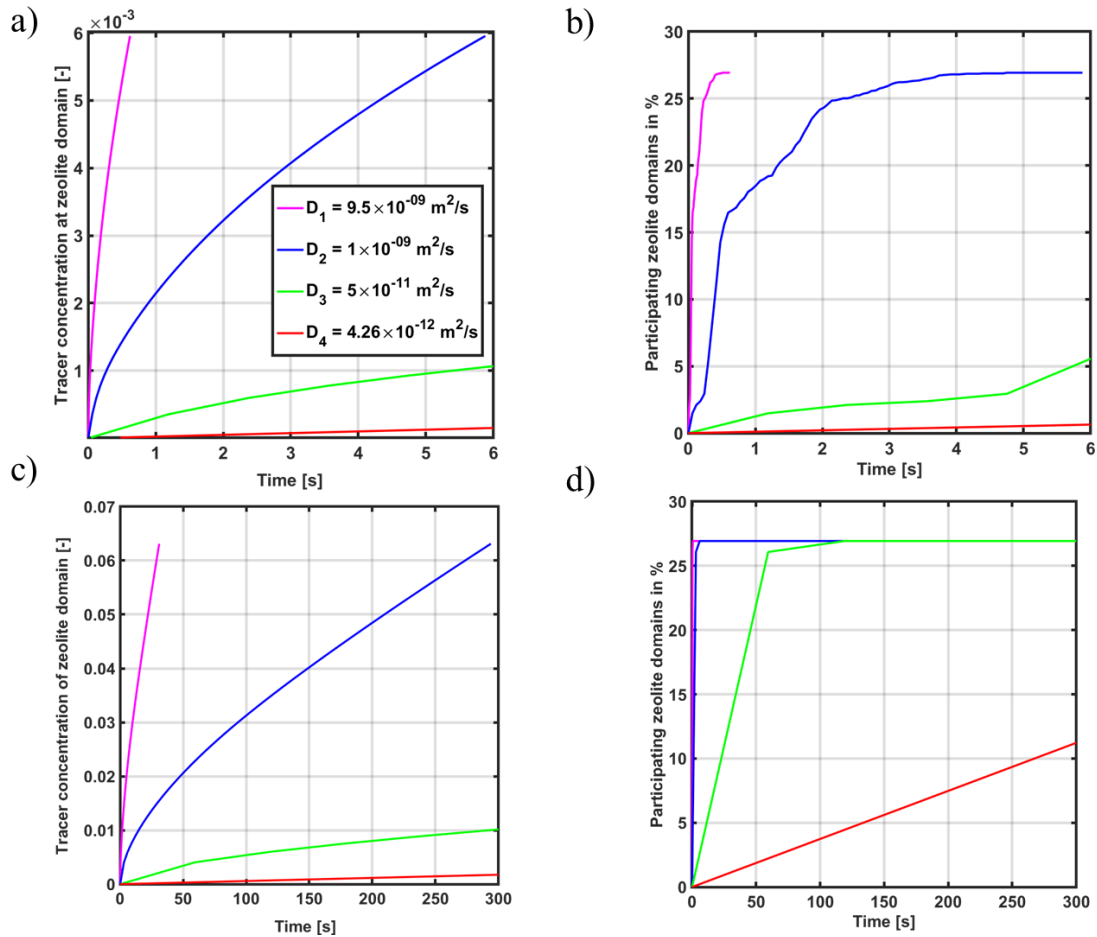


Figure 5.5 The average normalized tracer concentrations at the zeolite domains (the average over concentration of all zeolite domains which contain one or more than one zeolite nodes) together with the number of zeolite domains participating in the cracking reaction using different diffusion coefficients, i.e., $D_1^{[34]}$, $D_2^{[34]}$, $D_3^{[35]}$, $D_4^{[43]}$. (a) and (c) show the concentrations of all accessible zeolite domains versus time. (b) and (d) show the percentage of zeolite domains contributing in the cracking reaction versus time. The y axis shows the percentage of zeolite domains participating actively in the cracking reaction at different times (relative to the total number of zeolite domains located within either solid phase or the pore space).

5.3 Conclusions

In this Chapter, a powerful modeling tool enabling mass transport simulation of an entire real-life catalyst particle containing a complex macropore space topology was presented. Being able to characterize the whole particle at once, the mass transport limited behavior originating from this complex pore structure and its very heterogenous and spatially dependent inter-connectivity was evaluated. Synchrotron-radiation based correlated X-ray fluorescence tomography and ptychography tomography was used to map

both the element distribution and pore structure of a whole individual catalyst particle in 3-D and at high spatial resolution. To be able to perform the mass transport simulation in such a large dataset (ptychographic images with more than 10^9 voxels) with complex morphology/topology, a multi directional pore network was generated to represent the complexity of the macro-pore space and the active sites of a whole individual catalyst particle. This method decreased the computational time of the simulation for the whole particle to less than two days. We have used a representative FCC catalyst particle as a showcase example because it is a well-known diffusion-limited catalyst with a wide range of applications mainly used in oil refinery. It is also applied and explored for processing bio-oil and plastic waste. Development and optimization of this catalyst therefore remains important as it opens up opportunities for its utilization in other refining processes, that is, using feedstocks that are very different from vacuum gas oil (VGO); especially some with higher viscosity such as plastics. Understanding mass transport in the FCC catalyst is crucial for its present and future application and for an improved design tailored towards these new applications.

For this specific particle, the developed tool introduced in this Chapter revealed regions of different inter-connectivity of the macro-pore space that have significant influence on the mass transport behavior of the catalyst. It was found that only 27 % of all zeolite domains within the FCC catalyst particle were accessible (via the mapped macro-pores) from the exterior surface of the catalyst particle, which is in line with the accessibility index value for deactivated FCC catalysts reported in the literature^[31]. Interestingly, the analysis revealed that while almost $\frac{3}{4}$ of the number of zeolite domains had become inaccessible, two thirds of the total zeolite domain volume remained accessible, although less efficiently than expected (e.g., for a fresh FCC catalyst particle). However, mass transport simulations of reactant, product, and tracer within the mapped macro-pore space revealed that only a fraction of those remaining accessible active domains in the catalyst will actually participate in the cracking for typical residence times of the particle in the FCC riser reactor, depending on the diffusion constant used in the simulation.

For all evaluated diffusion coefficient values from literature, a rapid initial increase of normalized reactant concentration at the remaining accessible active domains facilitated by the high interconnectivity of the accessible macro-pore network was seen. This is in line with the reported fast deactivation by coke formation during the first 0.15 s in the riser reactor^[42]. Furthermore, even without considering coke formation that can block pores, the simulation for this aged FCC catalyst particle never reached steady-state condition for product molecules within simulation times (up to 5 min). Based on this and considering the residence time of the catalyst in the riser reactor (a few seconds), the conclusion is that the assumption of steady-state conditions for product flow in FCC is not valid.

Results obtained in this Chapter show and confirm that it is the complex interplay between both reduced zeolite activity and changes in mass transport properties during ageing that result in catalyst deactivation. This only became obvious by combining mass transport simulations and an evaluation of accessibility, which in turn shows that such a combined analysis is essential when studying the pore system of a diffusion limited catalytic solid. The key aspect in this approach is the fact that the mass transport simulation performed for an entire catalytic solid performed here is a characteristic for both pore space morphology and catalyst composition because it is dominated by diffusion pathways, accessibility, and the location of active sites.

Finally, results obtained in this Chapter show that the accessibility of a diffusion limited catalytic solid alone cannot provide a complete picture of the effects of catalyst deactivation caused by changes in the pore system and largely benefits from accompanying mass transport simulations. Specifically, the accessibility of zeolite domains and their contribution to the cracking reaction was quantified and evaluated during typical residence times of the particle in the FCC riser reactor. Moreover, the diffusion front for reactant, product, and tracer molecules was quantified and visualized within the particle. Such an accurate characterization was only possible by exploring the macro-pore space of the entire aged E-cat particle at once since the catalyst particle's performance depends very strongly on the connectivity of the complex pore structure, which was shown to have a very non-uniform distribution. Under this condition, due to the presence of a very heterogenous

and spatially dependent pore connectivity, a sub-volume of the catalyst particle would not reveal the true particle behavior as it is not representative for the whole catalyst particle. All this information together provided a clear process-based understanding of the catalyst performance during its residence time in the riser reactor.

5.4 Experimental Section

5.4.1 Correlative X-ray Ptychography and X-ray Fluorescence Tomography

The simultaneous ptychography and fluorescence tomography were performed at the Hard X-ray Micro/Nano-Probe beamline P06 at PETRA III, DESY, Hamburg (Germany). A hard X-ray beam of 12 keV had $160 \times 140 \text{ nm}^2$ spot size focused by KB-mirror optics. The fluorescence signal was detected using a 384 element Maia detector¹. The far-field diffraction images were recorded by an Eiger detector. The individual particle was mounted on a titanium tip by two component 5-minute epoxy glue. The tip was placed on a goniometer and the particle on the tip was placed in the center of rotation. The data were acquired at $0.5 - 1.8^\circ$ angle steps for 360° rotation, the total number projection angles was 161.

5.4.2 Data Analysis and Image Processing

The data from PILATUS was processed using in-house MATLAB code to produce individual ptychographic projections at all acquired angles. The reconstruction of ptychographic projections were performed by TXM-Wizard software^[44]. First, the stack of the projections was aligned with multiple-featured alignment tool. Secondly, an iterative Algebraic Reconstruction Technique (i-ART) was used to produce virtual slices with pixel size 40.7 nm.

The acquired XRF spectra from the Maia detector were fitted in GeoPIXE^[45] software to determine individual element contribution in each pixel of every single projection. The resulting stack of images for each element was aligned by multiple-featured alignment procedure built in TXM-Wizard software. We used titanium as a reference stack and the calculated misalignment was used for Ca, Cu, Fe, Ga, La, Ni, Pt, Si, V, and Zn. The

volume image for each single element was reconstructed using the i-ART algorithm built-in TXM-Wizard software. The resulting voxel size was 200 nm. We filter out the noise from the 3-D volume images using a diffusion filtering^[46] and we segmented the volume image into pore and solid space using a watershed segmentation. We generated a PN model in Avizo Fire and calculated all image properties using in-house MATLAB code.

In order to segment the zeolite domain, the same method explained in Chapter 2, Section 2.4.14 was used. We tuned the parameters to obtain an average zeolite domain size in the 2-D virtual cuts of $0.5588 \mu\text{m}^2$, which is in perfect agreement with published⁵ values of $0.52 \mu\text{m}^2$ and $0.55 \mu\text{m}^2$ for two E-cat particles.

5.4.3 Estimation of 3-D Resolution of the Ptychography and X-ray Fluorescence Datasets

In order to estimate the effective 3-D resolution of the data set, two methods were used. As a standard method, the Fourier Ring Correlation^[47] (FRC) was used to assess reproducible resolution of volume image (see Section 2.4.4 for further details). We have used the most 500 central reconstructed slices from each subset to calculate individual FRC values. The individual FRC values averaged over the number of slices intersects $2\text{-}\sigma$ criterion in the reproducible resolution value (Figure 5.6) and gives reproducible resolution 203 - 239 nm (221 nm in average). However, the reproducible resolution determined by FRC can be affected by various factors, such as the number of voxels in a Fourier shell, a microstructure symmetry, and the portion of the volume image filled by the microstructure.

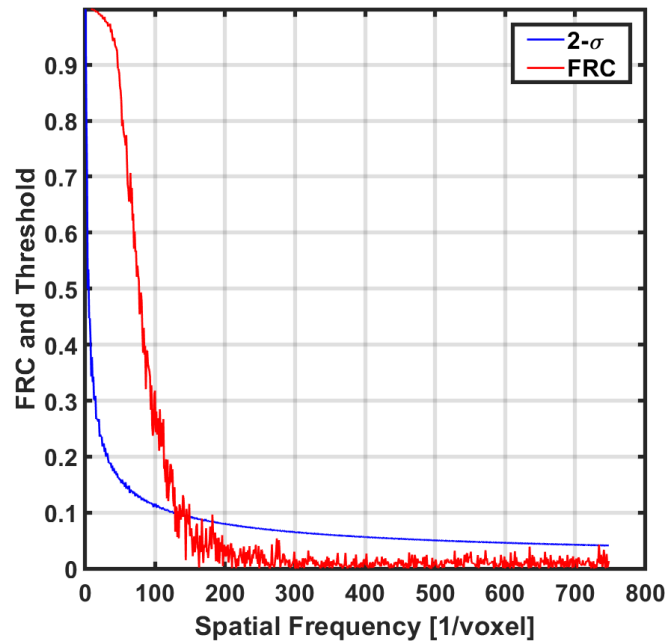


Figure 5.6 FRC for 3-D resolution estimation. The FRC uses 700 slices of reconstructed 3-D data using the $2\text{-}\sigma$ criterion. The final resolution is 221 nm for 40.7 nm/pixel.

As a supplementary method, a platinum marker with known geometry and size was deposited on the particle surface using gas injection system (GIS) in a dual-beam FIB-SEM microscope to evaluate the effect of before mentioned factors.

The platinum marker had a clear contribution in the XRF spectra and the corresponding XRF volume image pinpointed the marker spatial position in the ptychographic volume image enabling to estimate an image resolution from perfectly known marker shape and size. Figure 5.7 shows an image of the surface of the FCC particle including F-shape platinum marker (red squares) deposited on the surface. 100 probe lines through the marker (50 probes over blue arrows and 50 probes over red arrows) were constructed. Every single probe shows the image intensity profile (see example of the probe in blue direction in Figure 5.8) with significant changes on the marker edges. The edge intensity change has usually a gaussian dependency and the resolution can be calculated by the half-width at half maximum of the gaussian fit. To determine the image resolution from the intensity profile, three steps procedure was applied as follow: i) the intensity profile was normalized by the mean intensity value from the most central part of the probe (red line in

Figure 5.9) which has the same length as the marker, ii) the biggest possible rectangle which is fully under the intensity profile and has a side equal to the marker length (green rectangle in Figure 5.9) was constructed (the green rectangle indicates the marker edge). Thirdly, the edge intensity change was fitted by the gaussian curve (purple curves in Figure 5.9). Then the resolution was determined as a distance between the green rectangle and the purple curve at half height of the green rectangle. From the nature of the calculation, 200 resolution values were obtained which varied from 90 to 210 nm and had the average image resolution value of 132 nm.

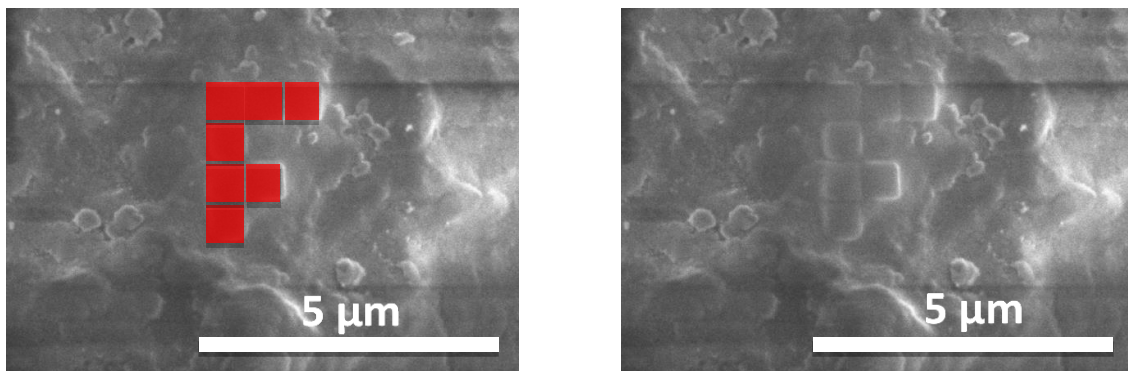


Figure 5.7 The image of the FCC particle surface with the platinum deposited letter F. The pattern used for the deposition is drawn schematically by red squares.

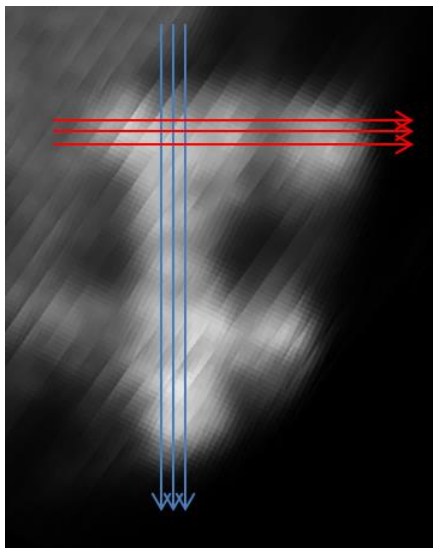


Figure 5.8 The cut through the volume image showing the letter F on the surface of the FCC particle. Red and blue arrows show the probe direction used for obtaining the intensity profile over the markers.

The 3-D spatial resolution of the XRF datasets was also estimated by using line scan method using 10%-90% criterion^[48] (see Section 2.4.4 for further details). The intensity profile of 12 lines obtained from 12 different 2-D slices (reconstructed Fe images) was used to determine the resolution (Figure 5.10). The mean resolution of 595 nm was estimated for the XRF dataset.

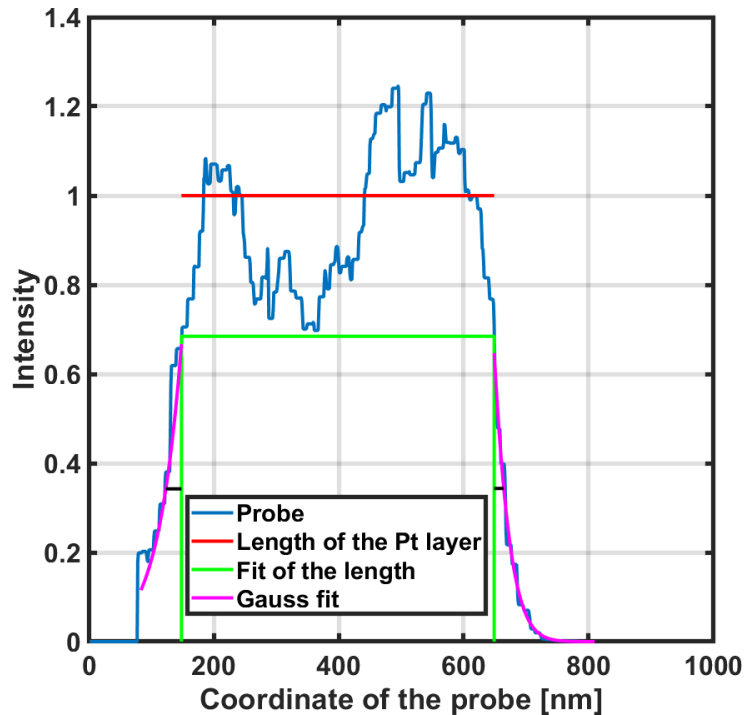


Figure 5.9 Determination of the resolution using the intensity profile of a probe over the marker in letter F deposited on the particle. Blue line shows the intensity profile of the probe over the marker. Red line with length equal to the marker size is located in the most central part of the marker. Sides of the green rectangle shows the marker edge. The intensity changes at the edge of the marker fitted by a Gaussian shown in purple curve. The resolution is defined by the half-width at half maximum of the gaussian fit.

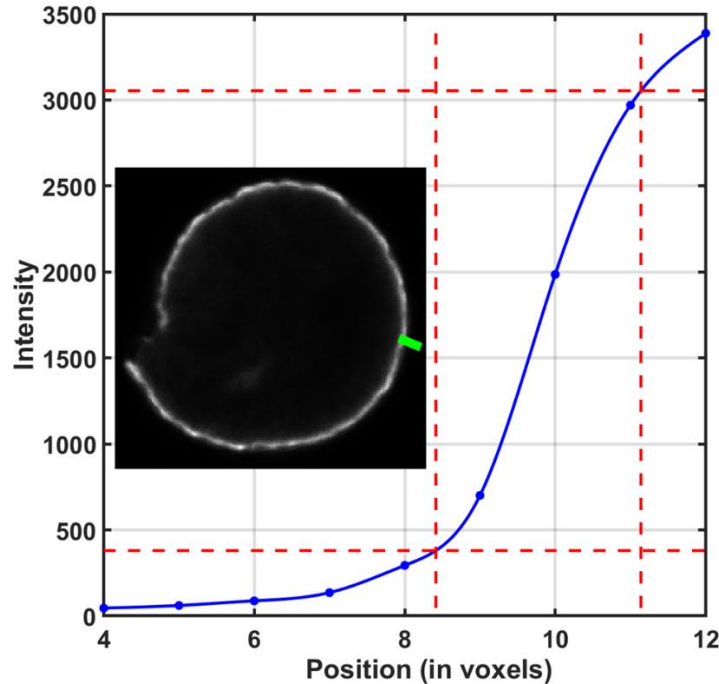


Figure 5.10 Line scan profile and the corresponding reconstructed slice of the XRF dataset. The intensity of each voxel (blue dots) of the green line in the 2-D slice (Fe distribution) was plotted as a function of the position of voxels. Two horizontal red dashed lines show the 10%-90% criteria corresponding to the intensity profile. The mean resolution over 12 lines in different 2-D slices was estimated as 595 nm.

5.4.4 Radial Analysis

The radial analysis was performed in the same way as explained in Chapter 2 (Section 2.4.10). A radial distribution of Fe, Ni, V, La, Cu, Zn, and Ti was analyzed, as shown in Figure 5.11. The ring-shape distribution (sharp peak close to the surface) of the Fe and Ni together with particle metrics shown in Table 5.1 indicate that the studied particle is a typical aged E-cat FCC particle.

The fraction of the void space in a shell (volume of all voxels in the shell belong to pore space) over the total volume of the shell (volume of all voxels in a shell) was determined as porosity. As seen in Figure 5.12, the surface of the aged catalyst particle has lower porosity and nodes density (number of nodes divided by shell volume) compared to the inside since it has high metal deposition at the surface. Also increase of porosity and node density towards the center shows the high interconnectivity of the pores in the region close to the center of the particle (region 3 shown in Figure 5.4).

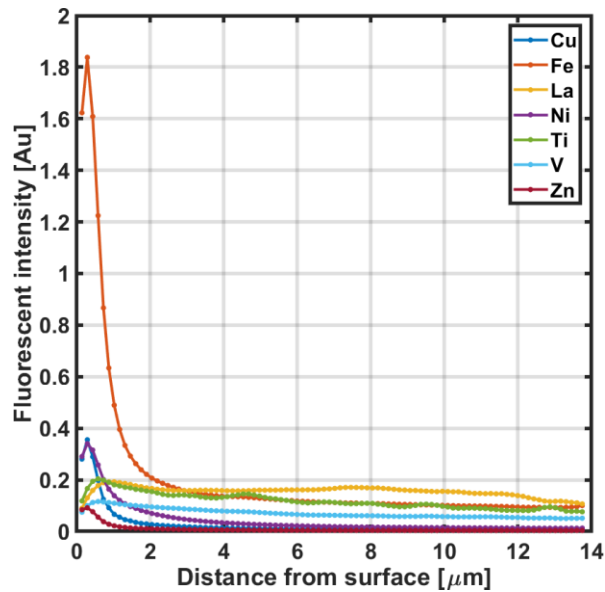


Figure 5.11 Radial distribution of different metals in an individual E-cat FCC catalyst particle.

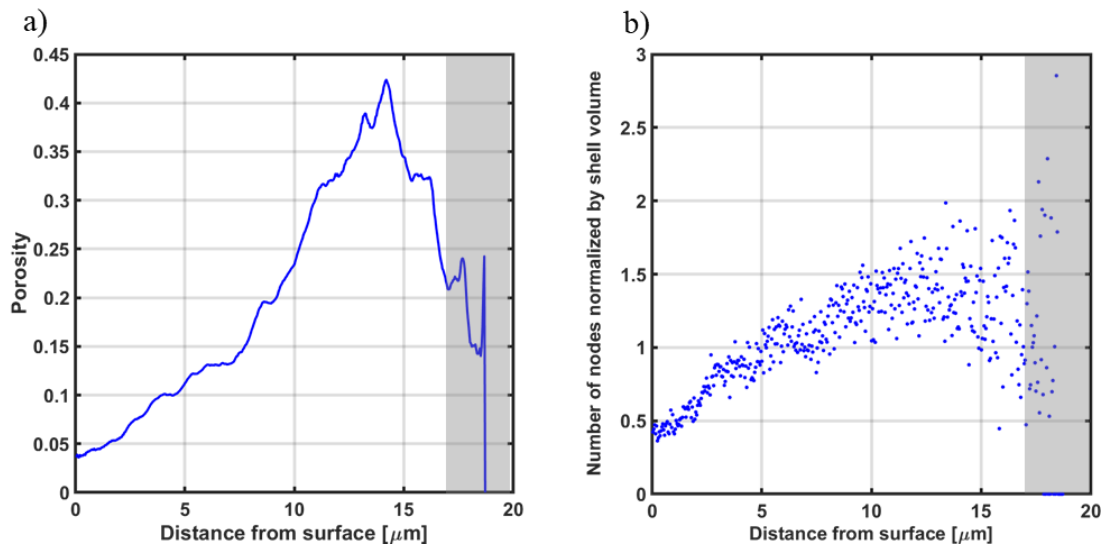


Figure 5.12 Radial analysis of porosity and number of nodes normalized by shell volume. The grey region in both (a) and (b) represents shells with small volume, that is why they have only few nodes and show the scattered data points. Therefore, these regions cannot show the real trend and statistically can be neglected.

5.4.5 Zeolite Domain Sorting and Accessibility

After obtaining the corresponding zeolite domain nodes, all domains were sorted based on their diffusion pore length. The diffusion pore length is the distance from between two points considering the path and its tortuosity. First, the shortest distance of each node inside the MDPN from all surface nodes

was obtained. Then the distance between the node inside MDPN and the certain surface node which has the smallest value (shortest distance) was considered as diffusion pore length. Afterwards, the smallest diffusion pore length of the nodes corresponding to each zeolite domain was assumed as the diffusion pore length of that corresponding domain.

The accessibility of each zeolite domain was evaluated, which represents a crucial parameter that determines whether reactants and products can diffuse to and from the active sites within the residence time of a catalyst particle in the riser reactor, which is typically at the order of seconds^[23]. In order to assess accessibility of the domains within the PN model, each zeolite domain required to contain at least 1 node of the network; otherwise, it was considered an isolated domain, i.e., a region that was not directly connected to the macropore space of the catalyst. With this approach, the connectivity between pores in the zeolite domains and pores located at the surface of the particle was directly described to evaluate the accessibility of each zeolite domain.

5.4.6 Diffusion Simulation in the Catalyst Pore Network

A mass transport simulation was performed by PoreFlow software^[32] by applying a normalized concentration at ‘the outside’ of the particle, i.e., at the surface pores ($C_{tracer}^{out} = C_{Reactant}^{out} = 1$, $C_{Product}^{out} = 0$) which cause a concentration gradient towards ‘the inside’ of the particle, i.e., at zeolite domains with an initial normalized concentration of zero ($C_{tracer}^{in,t=0} = C_{Reactant}^{in,t=0} = 0$). As soon as an inbound reactant reached a (node in a) zeolite domain, immediate cracking into product molecules was simulated based on the fact that FCC undergoes a diffusion limited transport and the cracking in the zeolites happens much faster than the diffusion within the zeolite^[23]. The products, generated at the location of zeolites, diffused within and out of the particle driven by an (increasing) normalized concentration gradient of product molecules between ‘the inside’ and ‘the outside’ sections of the particle. To obtain information on solute arrival time curves, normalized concentrations at single or a selected collection of pores can be averaged at successive times^[49]. After calculation of normalized concentration profiles of all pores, including zeolite domains, the accessibility of each zeolite domain

was studied based on their participation in the cracking reaction. To do so, a threshold was considered for the normalized concentration of tracer molecules at each zeolite domains. The threshold was assumed as the normalized tracer concentration inside the isolated pores ($C = 5 \times 10^{-18}$) which were supposed to have no tracer molecules (for solving the system of equations explained above, the normalized concentration cannot be absolute zero^[49]). If the tracer normalized concentration within the zeolite domain is below the threshold, this means the zeolite domain is not accessible and does not participate in the cracking reaction. While in case of normalized concentration above the threshold, the zeolite domain is considered as accessible and participating in the cracking reaction (Figure 5.5b,d).

It is also important to mention that the size of the probe molecules was neglected in the simulation. In turns, the concentration of nodes can be affected by their diffusion pore length and the interconnectivity of the network which plays an important role in change of concentration within the MDPN. For instance, as shown in Figure 5.13, considering two nodes inside the MDPN, i.e., B and C. These nodes are connected to the surface nodes A and D with exactly the same diffusion pore length. The only difference is that in the path CD, there are extra nodes due to junctions made by red segments. Presence of these extra nodes leads to decrease in concentration of node C and in turn the path BA without any extra nodes/junctions has a higher concentration in node B compared to node C.

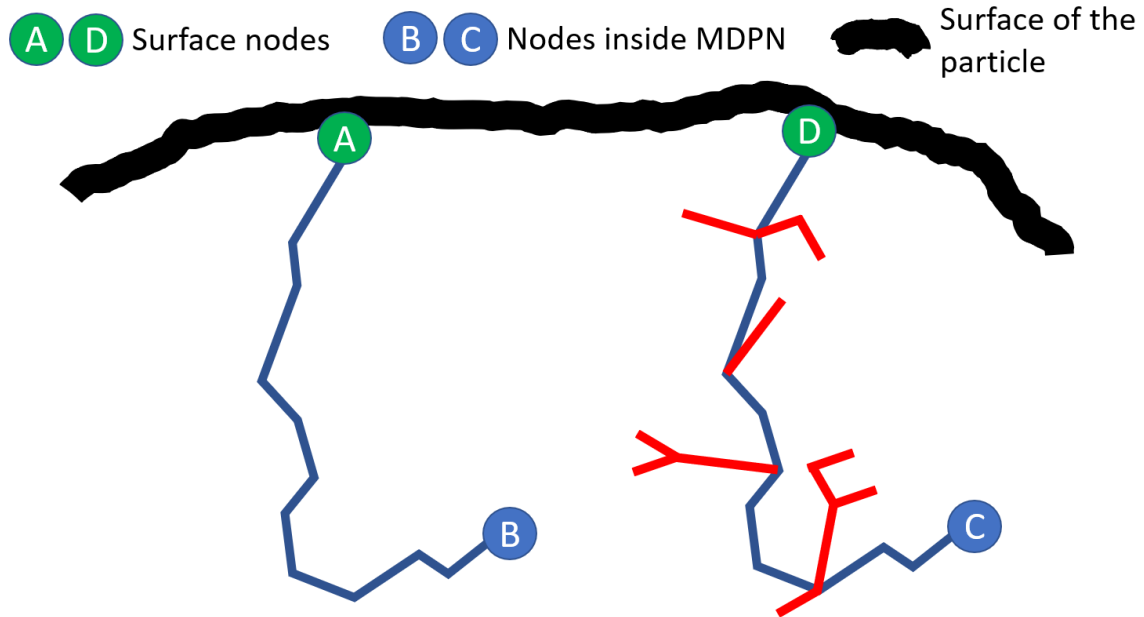


Figure 5.13 Influence of the topology of a pore structure on the concentration profile of nodes within the PNM. Blue and red solid lines represent the segments within the PNM. The red segments in the path CD causes a decrease in the concentration of node C compared to node B since the concentration would be distributed in all nodes within the path.

Solution of the system of equations requires boundary conditions implemented at the surface pores. The morphological information obtained by ptychography tomography was used to identify the nodes that are located at the surface of the FCC and act as the entry points for the feedstock molecules as mentioned above. Progress of solute through the pore network is, in principle, due to the advection and diffusion transport processes. Within our computational scheme, calculations are done by considering each pore element (i.e., a node or a segment) as a control volume. Applying mass balance, the solute concentration in a given node, i , may be written as:

$$V_i \frac{dc_i}{dt} = \sum_{j=1}^{N_{in}^{th}} q_{ij} c_{ij} - Q_i c_i + \sum_{j=1}^{Z_i} D_0 A_{ij} \frac{(c_{ij} - c_i)}{l_{ij}} \quad \text{Equation 5.1}$$

where V_i is the volume of node i , Q_i is the total volumetric volume rate going out of the node i , q_{ij} is the volumetric flow rate within segment ij , A_{ij} is the cross sectional area of the segment, D_0 is the ionic or molecular diffusion coefficient, c_i is the concentration in node i , c_{ij} is the concentration in the segment between nodes i and j , l_{ij} is again the length of that segment, and N_{in}^{th} is the number of segments flowing into the node i .

Assuming that pore body j is the upstream node and pore body i the downstream node, the solute concentration in segment ij may be written as:

$$V_{ij} \frac{dc_{ij}}{dt} = q_{ij}(c_j - c_{ij}) + D_0 A_{ij} \left(\frac{(c_j - c_{ij}) + (c_i - c_{ij})}{l_{ij}} \right) \quad \text{Equation 5.2}$$

Writing Equations 5.1 and 5.2 for each pore provides a system of equations which can be solved to obtain solute concentrations of each pore. In these equations, the advection term is neglected since the flow velocity is zero. To solve the generated system of equations, we have used a fully implicit method introduced by Raouf et al.^[32].

5.5 References

- [1] F. Meirer, B. M. Weckhuysen, *Nat. Rev. Mater.* **2018**, *3*, 324–340.
- [2] J. C. da Silva, K. Mader, M. Holler, D. Haberthür, A. Diaz, M. Guizar-Sicairos, W.-C. Cheng, Y. Shu, J. Raabe, A. Menzel, J. A. van Bokhoven, *ChemCatChem* **2015**, *7*, 413–416.
- [3] M. Nič, J. Jiráť, B. Košata, A. Jenkins, A. McNaught, Eds., *IUPAC Compendium of Chemical Terminology*, IUPAC, Research Triangle Park, **2009**.
- [4] P. E. Hansen, J. B. & Hojlund Nielsen, in *Handb. Heterog. Catal.* (Ed.: Ertl, G., Knözinger, H., Schüth, F. & Weitkamp, J.), Wiley-VCH, Weinheim, **2008**, p. 2920.
- [5] S. Benyahia, H. Arastoopour, T. M. Knowlton, H. Massah, *Powder Technol.* **2000**, *112*, 24–33.
- [6] V. Jiradilok, D. Gidaspow, S. Damronglerd, W. J. Koves, R. Mostofi, *Chem. Eng. Sci.* **2006**, *61*, 5544–5559.
- [7] A. Neri, D. Gidaspow, *AIChE J.* **2000**, *46*, 52–67.
- [8] M. T. Shah, R. P. Utikar, M. O. Tade, V. K. Pareek, *Chem. Eng. J.* **2011**, *168*, 812–821.
- [9] A. M. Lattanzi, M. B. Pecha, V. S. Bharadwaj, P. N. Ciesielski, *Chem. Eng. J.* **2020**, *380*, 122507.
- [10] M. Sahimi, G. R. Gavalas, T. T. Tsotsis, *Chem. Eng. Sci.* **1990**, *45*, 1443–1502.
- [11] O. H. J. Muhammad, E. K. T. Kam, *Catal. Today* **1997**, *38*, 85–95.
- [12] R. Mann, U. A. El-Nafaty, *Stud. Surf. Sci. Catal.* **1996**, *100*, 355–364.
- [13] R. Mann, P. N. Sharratt, G. Thomson, *Chem. Eng. Sci.* **1986**, *41*, 711–718.
- [14] R. Mann, *Catal. Today* **1993**, *18*, 509–528.
- [15] U. A. El-Nafaty, R. Mann, *Chem. Eng. Sci.* **1999**, *54*, 3475–3484.
- [16] E. S. Kikkinides, A. A. Lappas, A. Nalbadian, I. A. Vasalos, *Chem. Eng. Sci.* **2002**, *57*, 1011–1025.
- [17] U. A. El-Nafaty, R. Mann, *Chem. Eng. Sci.* **2001**, *56*, 865–872.
- [18] D. A. Matthijs De Winter, F. Meirer, B. M. Weckhuysen, *ACS Catal.* **2016**, *6*, 3158–3167.
- [19] E. Rautiainen, B. Nelissen, *Hydrocarb. Eng.* **2003**, *8*, 41–47.
- [20] Y. Liu, F. Meirer, C. M. Krest, S. Webb, B. M. Weckhuysen, *Nat. Commun.* **2016**, *7*, 12634.
- [21] K. W. Bossers, R. Valadian, S. Zaroni, R. Smeets, N. Friederichs, J. Garrevoet, F. Meirer, B. M. Weckhuysen, *J. Am. Chem. Soc.* **2020**, *142*, 3691–3695.
- [22] F. Meirer, D. T. Morris, S. Kalirai, Y. Liu, J. C. Andrews, B. M. Weckhuysen, *J. Am. Chem. Soc.* **2015**, *137*, 102–105.
- [23] E. T. C. Vogt, B. M. Weckhuysen, *Chem. Soc. Rev.* **2015**, *44*, 7342–7370.
- [24] I. Union, O. F. Pure, A. Chemistry, J. Rouquerol, D. Avnir, C. W. Fairbridge, D. H. Everett, J. M. Haynes, N. Pernicone, J. D. F. Ramsay, K. S. W. Sing, K. K. Unger, I. Union, O. F. Pure, A. Chemistry, J. Rouquerol, D. Avnir, C. W. Fairbridge, D. H. Everett, J. M. Haynes, N. Pernicone, J. D. F. Ramsay, K. S. W. Sing, K. K. Unger, *Pure Appl. Chem.* **1994**, *66*, 1739–1758.
- [25] F. Meirer, S. Kalirai, D. Morris, S. Soparawalla, Y. Liu, G. Mesu, J. C. Andrews, B. M. Weckhuysen, *Sci. Adv.* **2015**, *1*, e1400199.
- [26] J. Ihli, R. R. Jacob, M. Holler, M. Guizar-Sicairos, A. Diaz, J. C. da Silva, D. Ferreira Sanchez, F. Krumeich, D. Grolimund, M. Taddei, W. C. Cheng, Y. Shu, A. Menzel, J. A. van Bokhoven, *Nat. Commun.* **2017**, *8*, 809.
- [27] M. Gambino, M. Veselý, M. Filez, R. Oord, D. Ferreira Sanchez, D. Grolimund, N. Nesterenko, D. Minoux, M. Maquet, F. Meirer, B. M. Weckhuysen, *Angew. Chem. Int. Ed.* **2020**, *59*, 3922–3927.

-
- [28] F. Meirer, S. Kalirai, J. N. Weker, Y. Liu, J. C. Andrews, B. M. Weckhuysen, *Chem. Commun.* **2015**, 51, 8097–8100.
- [29] J. Ihli, D. Ferreira Sanchez, R. R. Jacob, V. Cuartero, O. Mathon, F. Krumeich, C. Borca, T. Huthwelker, W.-C. Cheng, Y. Shu, S. Pascarelli, D. Grolimund, A. Menzel, J. A. van Bokhoven, *Angew. Chem. Int. Ed.* **2017**, 56, 14031–14035.
- [30] S. Kalirai, P. P. Paalanen, J. Wang, F. Meirer, B. M. Weckhuysen, *Angew. Chem. Int. Ed.* **2016**, 55, 11134–11138.
- [31] D. R. R. Rainer, E. Rautiainen, P. Imhof, *Appl. Catal. A Gen.* **2003**, 249, 69–80.
- [32] A. Raof, H. M. Nick, S. M. Hassanizadeh, C. J. Spiers, *Comput. Geosci.* **2013**, 61, 160–174.
- [33] A. Raof, H. M. Nick, T. K. T. Wolterbeek, C. J. Spiers, *Int. J. Greenh. Gas Control* **2012**, 11, S67–S77.
- [34] J. Kärger, S. Vasenkov, *Microporous Mesoporous Mater.* **2005**, 85, 195–206.
- [35] S. F. Zaman, K. F. Loughlin, S. A. Al-Khattaf, *Ind. Eng. Chem. Res.* **2015**, 54, 4572–4580.
- [36] D. Wallenstein, C. Fougret, S. Brandt, U. Hartmann, *Ind. Eng. Chem. Res.* **2016**, 55, 5526–5535.
- [37] F. C. Hendriks, F. Meirer, A. V. Kubarev, Z. Ristanović, M. B. J. J. Roeffaers, E. T. C. C. Vogt, P. C. A. A. Bruijninx, B. M. Weckhuysen, *J. Am. Chem. Soc.* **2017**, 139, 13632–13635.
- [38] J. A. Atias, H. De Lasa, *Ind. Eng. Chem. Res.* **2004**, 43, 4709–4720.
- [39] C. M. Bidabehere, U. Sedran, *Ind. Eng. Chem. Res.* **2001**, 40, 530–535.
- [40] P. Kortunov, S. Vasenkov, J. Kärger, M. Fé Elía, M. Perez, M. Stöcker, G. K. Papadopoulos, D. Theodorou, B. Drescher, G. McElhiney, B. Bernauer, V. Krystl, M. Kočířik, A. Zikánová, H. Jirglová, C. Berger, R. Gläser, J. Weitkamp, E. W. Hansen, M. Kočířik, A. Zikánová, H. Jirglová, C. Berger, R. Gläser, J. Weitkamp, E. W. Hansen, *Chem. Mater.* **2005**, 17, 2466–2474.
- [41] Z. Liu, S.-L. L. Chen, X. Ge, P. Dong, J. Gao, Z. Xu, *Energy and Fuels* **2010**, 24, 2825–2829.
- [42] M. A. den Hollander, M. Makkee, J. A. Moulijn, *Catal. Today* **1998**, 46, 27–35.
- [43] Y. Qin, X. Gao, H. Zhang, S. Zhang, L. Zheng, Q. Li, Z. Mo, L. Duan, X. Zhang, L. Song, *Catal. Today* **2015**, 245, 147–154.
- [44] Y. Liu, F. Meirer, P. A. Williams, J. Wang, J. C. Andrews, P. Pianetta, *J. Synchrotron Radiat.* **2012**, 19, 281–287.
- [45] C. G. Ryan, D. R. Cousens, S. H. Sie, W. L. Griffin, *Nucl. Inst. Methods Phys. Res. B* **1990**, 49, 271–276.
- [46] P. Perona, J. Malik, *IEEE Trans. Pattern Anal. Mach. Intell.* **1990**, 12, 629–639.
- [47] M. van Heel, M. Schatz, *J. Struct. Biol.* **2005**, 151, 250–262.
- [48] M. Holler, A. Diaz, M. Guizar-Sicairos, P. Karvinen, E. Färm, E. Härkönen, M. Ritala, A. Menzel, J. Raabe, O. Bunk, *Sci. Rep.* **2014**, 4, 3857.
- [49] A. Raof, S. M. Hassanizadeh, *Transp. Porous Media* **2010**, 81, 391–407.

6. Summary, Future Perspectives, and Conclusions

6.1 Summary

This PhD Thesis focuses mainly on the characterization of complex porous materials at the low micrometer and sub-micron length scale. The characterization techniques used in this PhD Thesis can be classified into two synchrotron-based X-ray microscopy (XRM) techniques: i) X-ray holotomography and ii) correlative ptychographic X-ray computed tomography (PXCT) and X-ray fluorescence (XRF) tomography. X-ray holotomography combined with pore network (PN) modeling was used to study deactivation mechanisms caused by coke and metal deposition within a single fluid catalytic cracking (FCC) catalyst particle (Chapter 2). Furthermore, in Chapter 3, the same combination was used for studying the heterogeneity in the fragmentation behavior of a set of metallocene-type catalyst particles at different stages of ethylene polymerization. Correlative PXCT and XRF tomography was used to perform statistical analysis and to quantify the degree of fragmentation of an ensemble of Ziegler-type ethylene polymerization catalyst particles by mapping support, polymer, and mixed phases at high spatial resolution (Chapter 4). Moreover, in Chapter 5, the pore structure as well as the element distribution within a single FCC catalyst particle was mapped using correlative PXCT and XRF tomography. The obtained morphological and elemental information allowed performing a mass transport simulation based on pore network modeling, which revealed invaluable insights into the diffusion behavior of reactant and product molecules as well as active site accessibility within a single FCC catalyst particle. Here, we summarize the findings of Chapters 2 to 5. A summary of the main findings of this PhD Thesis can be found in Figure 6.1.

In **Chapter 2**, we have used differential contrast X-ray holotomography together with other complimentary X-ray microscopy techniques, such as XRF, XRD, SAXS, and WAXS, to identify and map the 3-D distribution of carbon and metal deposits within a single FCC equilibrium catalyst (E-cat) particle. The analytical approach allowed us also to differentiate between the coke located at the surface and inside the E-cat particle using the obtained electron density of coke deposits from X-ray holotomography. It was shown that the dense surface layer of coke deposits (with a thickness of less than 1

μm) blocking the macro-pores at the surface caused a significant decrease in accessibility of the E-cat particle. We have also shown that most of the coke deposits accumulate within the particle rather than on the surface due to the incomplete coke removal during regeneration. We concluded that during the regeneration process, mainly surface-near coke is burnt off because of the short residence time of the catalyst in the regenerator (at the order of minutes^[1]), while coke located deeper in the particle remains.

The spatial correlation between coke deposits and metals, such as Fe, Ni, and La, obtained by XRF tomography was also investigated. We found that La and Ni domains show considerably higher activity for the formation of non-surface coke (less electron dense) compared to Fe and metal-free regions, which is in line with the suggested higher dehydrogenation activity of Ni^[2,3].

Pore network modeling was used to investigate the influence of coke deposits on the macro-pore structure of the catalyst particle. We constructed two pore network models for both the uncalcined (catalyst with coke) and the calcined (catalyst without coke) particle. This enabled us to visualize the pore blockage caused by coke deposits. We observed clear changes in the pore network parameters after calcination, such as an increase of the number of nodes, the number of segments, the mean pore diameter, the number of surface nodes, and a decrease of tortuosity, evidencing the presence of coke in the macro-pore structure of the spent FCC catalyst. It is important to mention that this approach to study coke is not limited to the FCC catalyst, but can also be applied to other porous catalysts used in different catalytic reactions and systems.

In **Chapter 3**, X-ray holotomography as a powerful tool with sub-500 nm spatial resolution and relatively low measurement times was used to map low Z (atomic number) elements within several supported ethylene polymerization catalysts. Quantitative information on the morphological evolution of 12 hafnocene-based catalyst particles at 5 different stages of polymerization (i.e., pristine catalyst and catalysts after 1 min, 10 min, 30 min and 60 min of polymerization) was obtained. We were able to quantify the change of composition and porosity of catalyst particles during the pre-polymerization reaction. Pore space interconnectivity, tortuosity, and pore

size distribution of particles at different stages of polymerization were obtained by pore network modeling. The decrease in porosity and macro-pore space interconnectivity during polymerization showed that the controlled catalyst support fragmentation in overcoming potential mass transfer limitations has great importance. The 3-D distribution of different phases of the catalyst, i.e., support, polymer, and pore space domains, was also visualized within each metallocene-type catalyst. It was shown that the remarkable interparticle heterogeneity in terms of fragmentation degree and pathway can be due to the unique configuration of the particles' respective supports and pore space networks. Moreover, we showed that the homogeneous fragmentation of the support phase in pre-polymerized particles at mild reaction conditions demonstrates the form of a layer-by-layer mechanism.

In **Chapter 4**, correlative PXCT and XRF tomography was used to map the local electron density of 434 ethylene polymerized particles over a large, scanned field of view of $120 \times 120 \times 20 \mu\text{m}^3$, with an achieved 3-D spatial resolution of 74 nm. It enabled us to visualize and analyze the heterogeneity in the fragmentation of these catalyst particles in the early stage of ethylene polymerization (after 5 min) with high catalyst loading and mild reaction conditions. Different geometrical parameters such as volume, surface area, equivalent spherical diameter, sphericity, and elongation were obtained after segmentation of highly connected particles using a supervised marker-based watershed algorithm. The obtained geometrical parameters showed a relatively homogeneous particle morphology within these 434 catalyst particles. The slightly elongated pristine catalyst particles as observed by SEM together with the mean elongation value (0.6) of this ensemble of particles showed that the composite polymer-particles followed the replication phenomena of pristine catalyst particles.

To quantify the degree of fragmentation, by using K-means clustering, each particle was segmented into 4 phases, namely i) a HDPE-rich phase, ii) a highly mixed HDPE-catalyst with more HDPE phase, iii) a highly mixed HDPE-catalyst with more HDPE phase and iv) a catalyst-rich phase. Then, the fragmentation parameter (V_r) was introduced to determine the degree of fragmentation of each particle based on the obtained K-means segmented

dataset. We observed a strong heterogeneity in terms of fragmentation behavior among the entire ensemble of polymer-particles based on the calculated V_r . We found that in all catalyst particles both layer-by-layer and continuous bisection mechanisms were present. For weakly fragmented catalyst particles, the layer-by-layer mechanism was dominant while for moderately and strongly fragmented particles the continuous bisection fragmentation mode became the dominant pathway for fragmentation. This indicates that the diffusion of monomers towards the interior happened without any limitation for moderately and strongly fragmented catalyst particles. It also shows the higher local ethylene polymerization activity of these polymer-catalyst particles.

In **Chapter 5**, we have introduced a powerful modeling toolbox for analysis of mass transport properties of a whole real-life catalyst particle containing a complex macro-pore space topology. The FCC catalyst was used as an archetypical example of a rationally designed hierarchically porous material. The 3-D element distribution as well as macro-pore structure of the E-cat FCC catalyst particle was obtained using correlative PXCT and XRF tomography. 3-D XRF data was used to identify regions of the catalytically most active zeolite domains by recording the lanthanum distribution and using that as a marker for the RE-USY zeolites embedded in the FCC particle matrix. A multi directional pore network (MDPN) model was constructed based on the obtained large ptychographic volume images containing more than 10^9 voxels to represent the complex morphology and topology of the FCC catalyst. This enabled decreasing the computational time of the simulation for the whole particle to less than two days. The mass transport simulation of the whole single FCC catalyst based on the MDPN made use of the concentration gradient between the outside ('surface nodes') and inside ('zeolite nodes') of the particle representing the driving force for diffusion of reactants and products. Due to the diffusion limitations within the FCC particles, the cracking reaction at the La domains can be assumed as instantaneous in this simulation. Based on the simulation results, we were able to quantify and visualize the diffusion front for all components of the simulation, i.e., reactant, product, and tracer molecules.

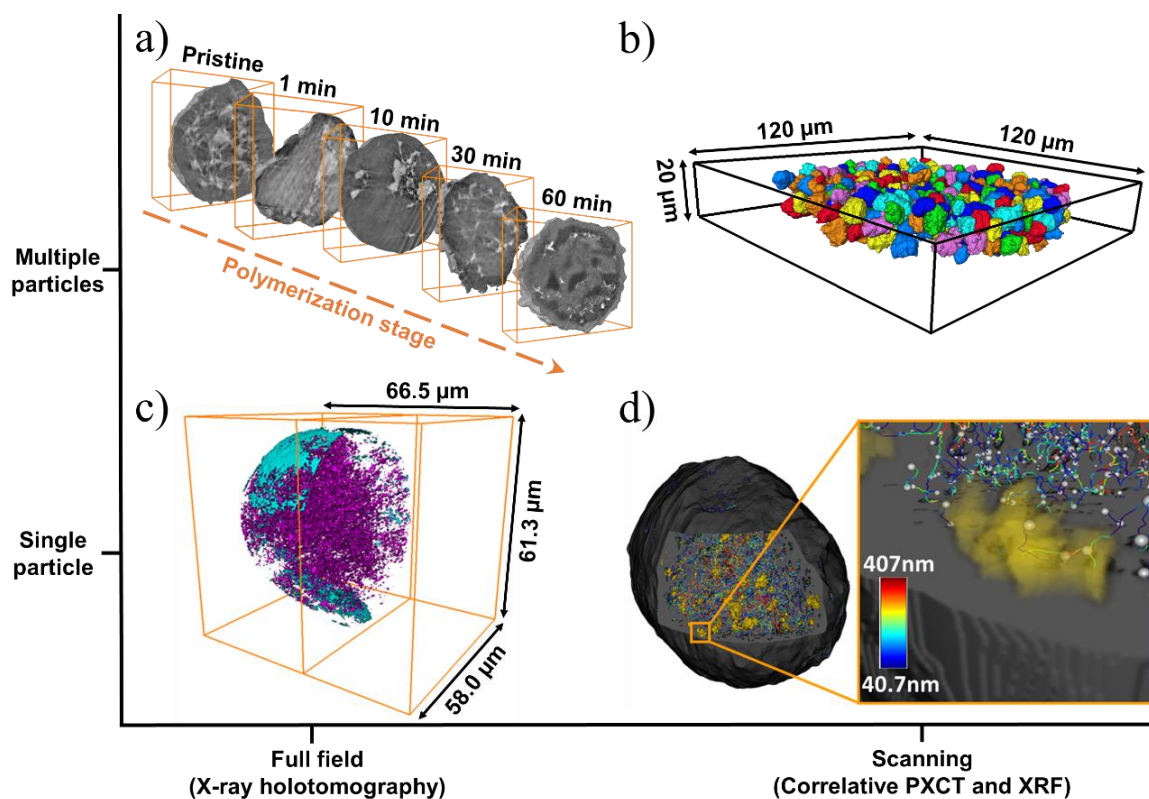


Figure 6.1 Summarizing the main findings of this PhD Thesis. (a) shows the application of X-ray holotomography for characterization of multiple metallocene-type catalyst particles at different stages of ethylene polymerization (studied in Chapter 3) while (b) shows another approach using correlative PXCT and XRF with a large field of view to do statistical analysis on 434 Ziegler-type ethylene polymerization catalyst particles from the same stage of polymerization (after 5 min) (studied in Chapter 4). The application of X-ray holotomography to investigate different carbon deposition mechanisms in a single FCC catalyst particle is shown in (c). Surface and non-surface coke deposits are shown in cyan and magenta colors, respectively (studied in Chapter 2). (d) shows the pore structure, respective pore network model and La distribution (yellow domains) within a single FCC catalyst particle (studied in Chapter 5).

We found that only 27% of all zeolite domains were accessible from the surface of the E-cat FCC particle. The analysis, interestingly, showed that 75 vol. % of zeolite domains remained accessible despite of the fact that almost three fourths of the number of zeolite domains were inaccessible. Although, based on simulation results, depending on the diffusion coefficient used in the simulation, only part of those accessible zeolite domains in the catalyst will contribute in the cracking reaction due to the short residence time of the FCC catalyst particle in the riser reactor (between 3 to 5 s^[1]). We also showed that the steady-state condition for product molecules cannot be reached even by

considering longer simulation time (~5 min, which is almost 60 times longer than the residence time of the FCC catalyst in the riser reactor).

6.2 Future Perspectives

The main focus of this PhD Thesis was on the characterization of complex porous catalysts using high-resolution X-ray microscopy (XRM) techniques. The combination of XRM with pore network modeling allowed assessing catalyst pore space interconnectivity and accessibility during different processes such as fluid catalytic cracking or polymerization.

In Chapter 2, the 3-D spatial distribution of coke (low absorptive element) and its effect on the macro-pore structure of a single FCC catalyst particle was studied using a combination of hard XRM techniques and pore network modeling. Future improvements, such as upgrading to a 4th generation synchrotron, leading to a higher and more coherent photon flux, e.g., Max IV, ESRF EBS, or the planned Petra IV storage ring, as well as improvements in detector technology and phase retrieval algorithms, will be able to push the 3-D spatial resolution down to a few nanometers. This paves the way for studies of the effect of coke depositions not only in macro-pores but also in meso- or even micro-pores. The differential contrast methodology for characterization of low Z elements within a single porous particle introduced in this Chapter can also be applied to any other porous catalysts (or materials) used in different chemical reactions, such as reforming, hydrotreating, and hydrocracking. It can give new insight into the coking process and its relation to deactivation mechanisms, which can lead to an improved catalyst design. In this methodology, a single porous catalyst particle needs to be measured twice, i.e., before and after removing coke. Therefore, the post-processing of the data is highly sensitive to the precision of the alignment procedure as well as experimental parameters/conditions used in both measurements. In this case, *in-situ* X-ray holotomography represents a good alternative for future work to simplify the post-processing (subtraction procedure would be easier since not a complex alignment procedure is needed in case of a stable particle) and the experimental procedure (no need to re-mount the particle on sample holder after calcination). Moreover, despite the fact that synchrotron-based measurements provide high-resolution images thanks to the coherent and high

brilliance X-ray beam, there are some drawbacks for this type of experiments: i) obtaining beamtime at a SR facility is highly competitive and is time consuming, ii) related to point i), synchrotron-based measurements are expensive in terms of operational costs, and iii) there is only limited time granted for running experiments (normally a short period from a few days to a week). On the other hand, lab-based techniques for obtaining morphological information at high-resolution are also being developed (e.g., development of X-ray sources, detectors, and optics) that could be partially represent an alternative for synchrotron-based XRM techniques.

In Chapter 3, the morphological heterogeneity in a silica-supported ethylene polymerization catalyst at different reaction stages was studied using X-ray holotomography and pore network modeling. The divergence in reactivity and fragmentation behavior that is observed within individual catalyst batches (i.e., reaction stages) does underline the need for further studies using 3-D imaging techniques such as holotomography, in which the morphology and fragmentation of a statistically relevant number of catalyst particles is assessed. Besides characterizing larger sample sets, the observed morphological heterogeneity also calls for the implementation of novel support synthesis strategies that lower the divergence in initial catalyst particle morphology. As the resolution of X-ray-based imaging techniques improves, polymer formation in the meso- and micro-pores may also be imaged, thereby yielding vital insights into their respective contributions to the morphological evolution of supported olefin polymerization catalysts. Finally, this Chapter provides the foundation for future *in-situ* studies to directly establish correlations between the initial catalyst particle structure and observed fragmentation pathways. The obtained quantitative data can also be useful for further computational simulation of catalyst support fragmentation, possibly providing means of validating and expanding the computational models.

In Chapter 4, the degree of high-density polyethylene Ziegler-type catalyst fragmentation in the early stages of ethylene polymerization under mild reaction conditions was studied using correlative X-ray ptychography and XRF tomography. In order to determine the degree of fragmentation, a statistical analysis was performed on an ensemble of 434 fully reconstructed

catalyst particles imaged within a large field of view ($120 \times 120 \times 20 \mu\text{m}^3$). With further improvements with respect to photon flux and beam coherency, such as through the upgrading to 4th generation synchrotron facilities^[4-6], as well as detector improvements with higher scan-rates will allow the dwell-time per pixel to be reduced to sub-ms^[4-6]. This would allow for even larger FOV's to be scanned within the limited and precious allocated beam-time. Faster scanning times will further allow incorporating a stable air reference for truly quantitative X-ray phase nano-tomography on polyolefin catalysts that require a large FOV ($>140 \mu\text{m}$ in width if using the same polyimide capillaries). Moreover, with such improvements, the 3-D spatial resolution of PXCT can be pushed below the size of the primary particles of the MgCl_2 -based framework (as small as 5 nm), while maintaining large scanning areas. This will enable a full quantitative approach to study the fragmentation degree of each individual particle with the methodology provided in Chapter 5 and can be extended to study other polyolefin catalyst systems, such as the Phillips-type catalysts.

In Chapter 5, correlative X-ray ptychography and XRF tomography was used to map the macro-pore structure as well as the catalytically most active zeolite domains within an entire FCC catalyst particle. The mass transport simulation at the macro-pore level for the whole catalyst particle based on pore network modeling was performed to study the diffusion limitation originated from the complex pore structure as well as the accessibility of catalyst active sites based on the macro-pore space. Considering feasible simulation times, this methodology can be upscaled for macro-pore space characterization of a particle ensemble (i.e., to the scale of bulk measurements) although the acquisition of high-resolution images using synchrotron-based X-ray imaging techniques is still limited in terms of the field of view, which can, however, be improved in the future as discussed above. Also, synchrotron-based measurements can be replaced by state-of-the-art lab-based techniques that could partially achieve sub-100 nm spatial resolution. Finally, the data collected for the macro-pore space properties of particles can be used for training machine learning algorithms to generate artificial/digital catalyst particles with customized properties. Mass transport simulations on a large number of artificial catalysts can then significantly

enhance the design and performance processes encountered in heterogeneous catalysis.

6.3 Conclusions

In this PhD Thesis, the combination of hard X-ray microscopy techniques with pore network modeling was introduced as a powerful tool to characterize complex porous materials. Phase contrast imaging techniques, such as X-ray holotomography and X-ray ptychography, have been introduced as a suitable method for mapping the 3-D distribution of low atomic number elements such as carbon within a whole porous material. State-of-the-art X-ray microscopy techniques can deliver composition, morphology, and topology of a porous catalyst body, while pore network modeling allows for a quantitative assessment of interconnectivity and accessibility of the pore structure.

6.4 References

- [1] E. T. C. Vogt, B. M. Weckhuysen, *Chem. Soc. Rev.* **2015**, *44*, 7342–7370.
- [2] H. S. S. Cerqueira, G. Caeiro, L. Costa, F. Ramôa Ribeiro, *J. Mol. Catal. A Chem.* **2008**, *292*, 1–13.
- [3] C. A. Trujillo, U. N. Uribe, P.-P. Knops-Gerrits, L. A. Oviedo A, P. A. Jacobs, *J. Catal.* **1997**, *168*, 1–15.
- [4] C. G. Schroer, I. Agapov, W. Brefeld, R. Brinkmann, Y.-C. Chae, H.-C. Chao, M. Eriksson, J. Keil, X. Nuel Gavaldà, R. Röhlsberger, O. H. Seeck, M. Sprung, M. Tischer, R. Wanzenberg, E. Weckert, *J. Synchrotron Radiat.* **2018**, *25*, 1277–1290.
- [5] U. Johansson, U. Vogt, A. Mikkelsen, *Proc. SPIE* **2013**, 8851, 88510L.
- [6] P. Raimondi, *Synchrotron Radiat. News* **2016**, *29*, 8–15.

Back Matter

Appendix A: Influence of 3-D Spatial Resolution on Image Analysis

A simulation was performed to study the effect of binning on the analysis of the grayscale images as well as the pore network model analysis. The original reconstructed holotomography dataset of particle E_0 used in Chapter 4 was binned iteratively using the ‘imresize’ function in MATLAB with bicubic interpolation and at increasing scale factors (2 and 4). The spatial resolution of the data set was thus lowered. Due to the large size of the dataset, the original projections were binned by a factor of 2 prior to phase retrieval (see Chapter 3 and Section 3.4.5 for further details). Therefore, the binning factors used in the simulations and all results are 2 (original image), 4 (two times binned), and 6 (three times binned) in this Chapter. All volume images were converted to an unsigned 16-bit format (i.e., the voxel intensity of images was between 0 and 2^{16}). Then, to better understand the effect of the binning process on image analysis, the different properties were calculated, which are mainly obtained based on i) the grayscale images directly and ii) the pore network model. In the next two sections, the influence of binning of images on these properties will be discussed.

i) Properties based on grayscale images

Grayscale intensity histogram: The histogram of the grayscale intensities was plotted for all binned datasets. As seen in Figure A1, even at a scale factor of 6, the relative distributions of grayscale intensity values remained almost unchanged. Not surprisingly, the count of each intensity value decreases significantly due to the smaller size of the images (i.e., decrease in number of voxels) after binning, while, due to the smoothing via bicubic interpolation, the width of the histogram decreased slightly, mainly reducing the most extreme values with frequencies below 10.

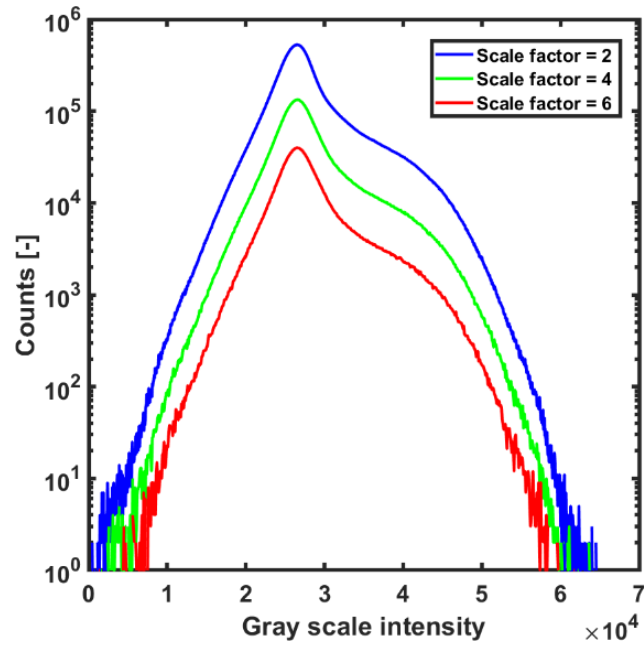


Figure A1 The change in histogram of grayscale intensities after binning with 3 different scale factor of 2, 4 and 6.

Porosity and number of isolated pores: To calculate the porosity of the data sets at each iteration, the grayscale images were binarized and segmented into pore space (PS) and solid phase using interactive thresholding. This means a constant intensity threshold was chosen in a way that voxels with intensity below and above the threshold were assigned to solid and PS phases, respectively. Then, porosity was determined as the number of PS voxels divided by sum of PS and solid phases voxels. Moreover, the number of isolated pores was determined at each scale factor. Isolated pores are defined as a group of connected voxels (voxels assigned to PS) surrounded by solid voxels, which means that there is no connection between two distinct isolated pores.

As seen in Figure A2, the porosity does not change significantly (less than 5% change) even after binning 3 times (scale factor 6), while the number of isolated pores is decreasing notably. The reason is that after segmentation, many small, isolated pores with volumes of one to only a few voxels are present, either due to noise and/or real features of the pore space that are close to or even smaller than the achieved spatial resolution (for example, pores smaller than one voxel will result in ‘partially filled’ voxels that will, based

on the applied segmentation threshold and the noise level in the data, either be classified as a single voxel pore or solid phase). Here it is important to mention that simulations were also performed with different segmentation thresholds, but the results showed the same trend without a notable change after binning. Those small, isolated pores are eliminated from the binarized PS images after binning due to the averaging of voxel intensities in bicubic interpolation. On the other hand, large pores (see Figure A3) and the total interconnectivity of the catalyst particle do not change significantly as defined by the Nodes Connectivity Ratio (NCR) parameter (see ‘Properties based on the pore network model’). This is because those small, mostly single voxel pores do not contribute significantly to the connectivity of the established macro-pore network (defined by the largest pores). This is an important observation because it means that they are in a size regime close to or below the actual spatial resolution of the data set (which is not the voxel size), and therefore appear as isolated very small pores that are mostly randomly distributed over the sample volume.

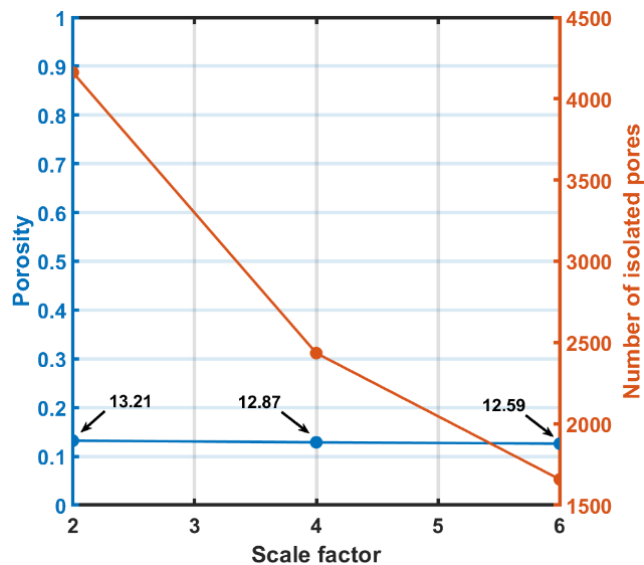


Figure A2 The change in porosity and number of isolated pores after binning with 3 different scale factors of 2, 4 and 6. Arrows in the figure show the porosity for the corresponding scale factor.

Largest isolated pore volume:

The volume of the 5 largest isolated pores accounting for 95% of the total pore space of the catalyst particle was compared after binning with different

scale factors. As for the largest isolated pore, the changes after 6-fold binning were less than 2% which indicates a negligible effect of the binning on the volume of the largest pore space within the catalyst particle (Figure A3a). The same trend can be seen for the 2nd to 5th largest isolated pores (Figure A3b). This is an important finding as it shows the robustness of the evaluation of the macro-pore space against a variation in spatial resolution. Note that this test should be repeated for significantly different catalysts as this robustness is also based on the morphology of the pore space (i.e. a property of the catalyst under study) and cannot be guaranteed for pore spaces of a significantly different nature.

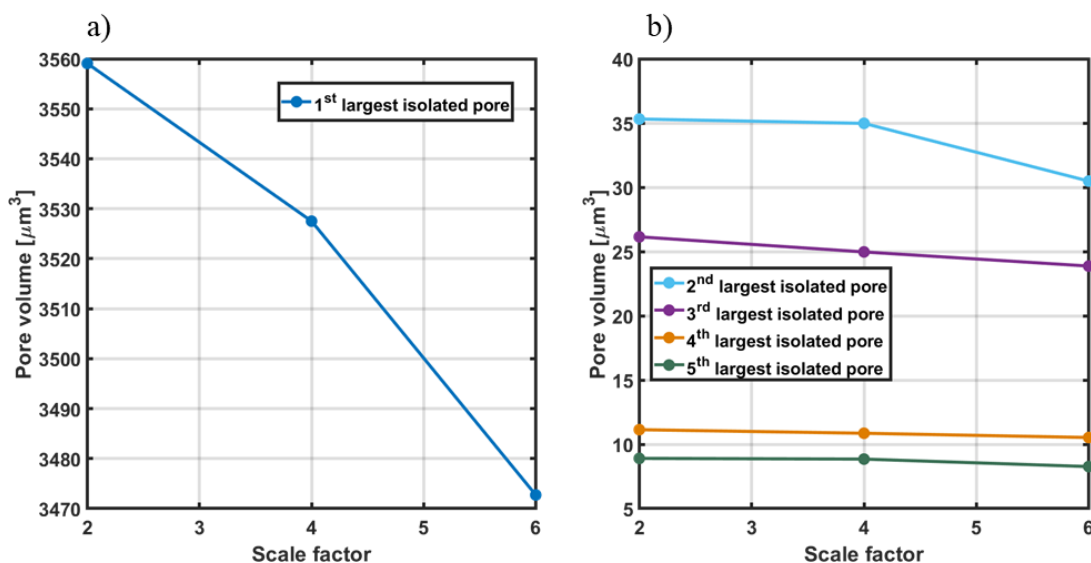


Figure A3 The change in the volume of (a) 1st and (b) 2nd to 5th largest isolated pores within the particle after binning with scale factors of 2, 4 and 6.

Radial analysis:

The radial analysis (see Section 2.4.10 for further details) was performed on the segmented PS dataset and grayscale images. All calculations were carried out in relation to the central voxel of a given particle and the shells are concentrically arranged around the central voxel. Then, the volume fraction of PS voxels (i.e., number of PS voxels in the shell divided by the total number of voxels in the shell) as well as mean grayscale intensity within each shell were determined as a function of shell distance from the surface as shown in Figure A4. In this plot, as always, shells close to the center are not statistically

relevant due to the limited number of voxels in those shells (which approaches one the closer the shell lies to the central voxel).

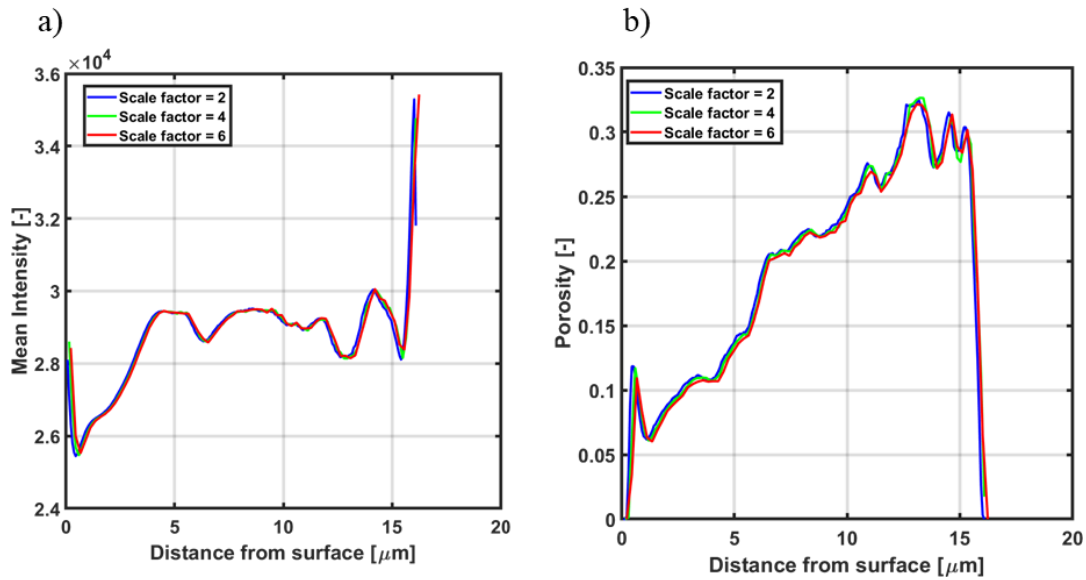


Figure A4 Radial analysis of (a) mean grayscale intensity and (b) porosity for scale factors 2, 4 and 6

As seen in Figure A4, the differences in the radial change of porosity and mean grayscale intensity are negligible after binning the volume images. This is important because such a radial analysis can be used as a fingerprint for the pore space distribution of an individual catalyst particle.

Connectivity to surface:

The change in the volume of the part of the catalyst pore space that is connected to the particle surface is shown in Figure A5. An isolated pore is connected to the surface if it contains at least one voxel that is located within 500 nm from the particle's surface. The threshold (i.e., 500 nm) used for defining the surface of the particle can vary depending on the particle characteristics. In this simulation, the threshold was chosen as $\sim 1\%$ of particle diameter (it was also tested with different surface thickness thresholds and the results showed similar trends). The results show that the changes of pore space volume connected to the surface is not remarkable after binning of the dataset ($<7\%$). This is another important observations as it guarantees the robustness

of any accessibility evaluation using the macro-pore space of the catalyst particle.

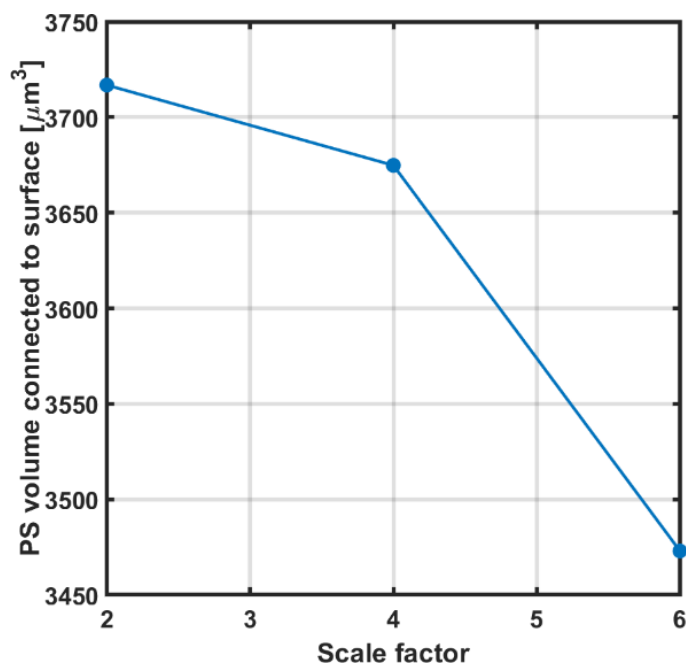


Figure A5 Volume of the pore space connected to the surface of the particle for scale factors 2, 4 and 6.

ii) Properties based on the pore network model

The pore network model was generated applying the procedure explained in Section 1.3. Sub-graphs in the pore network model can be considered as an indicator for the interconnectivity of a catalyst particle's pore space (Table A1), i.e., a pore network with a larger number of sub-graphs is less interconnected than one with a smaller number of sub-graphs. Another metric that can be used to describe the connectivity of the macro-pores is the nodes connectivity ratio (NCR). This number is given by the formula $\text{NCR} = N_c / (n^2 - n)$, where N_c corresponds to the number of connected nodes denoted as '1' in Figure A6b and n represents the total number of nodes in all graphs. A high NCR value indicates extensive macro-pore connectivity. For instance, the NCR of the particular exemplary sub-graph displayed in Figure A6a is equal to 0.33 ($\text{NCR} = 10 / (6^2 - 6) = 0.33$).

For all sets of two connected nodes (denoted as '1' in Figure A6b)) in the connectivity matrix (Figure A6b), the Euclidean distance as well as the

shortest real distance (i.e., the distance between two nodes taking into account the path tortuosity) were calculated. Also, the longest segment in the pore network was considered as a parameter to assess the influence of binning on pore network analysis. As shown in Table A1, pore network interconnectivity and properties did not change significantly even for a scale factor of 6.

Binning factor	2	4	6
Number of sub-graphs	111	106 (-4%)	101 (-9%)
NCR	0.93	0.93 (0%)	0.91 (-2%)
Mean distance between all nodes [μm]	15.226	14.854 (-2%)	14.717 (-3%)
Mean tortuosity between all nodes	1.98	1.91 (-3%)	1.89 (-4%)
Longest segment [μm]	2.33	2.18 (-6%)	2.14 (-8%)

Table A1 Metrics derived from the pore network model for catalyst particle at multiple different scale factors.

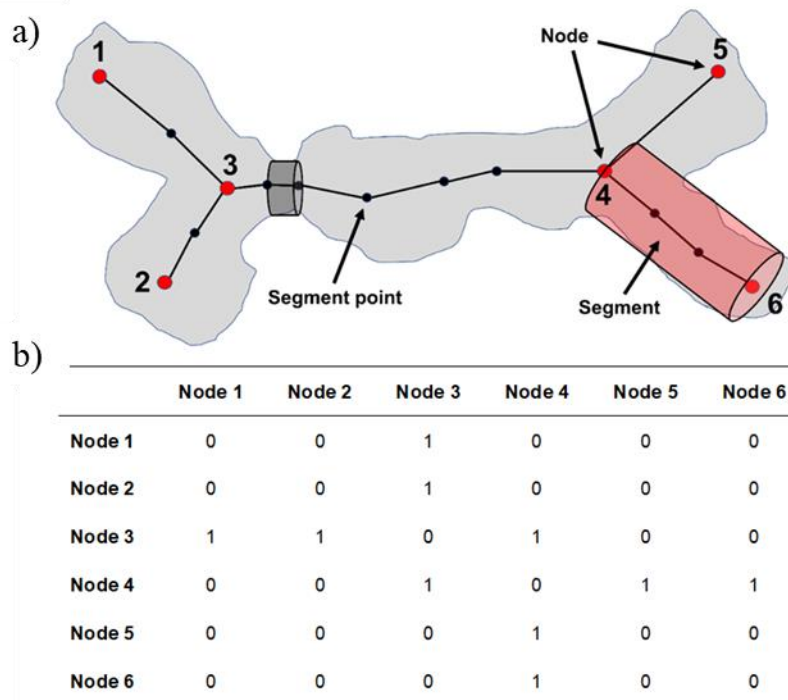


Figure A6 (a) Schematic illustration of a sub-graph consisting of nodes (1–6), segments and segment points. (b) Connectivity matrix for the sub-graph displayed in (a). Connected and disconnected nodes are denoted as ‘1’ and ‘0’, respectively.

Appendix B: Nederlandse Samenvatting

Deze PhD Thesis legt de focus op de karakterisatie van complexe en poreuze materialen in het gebied van de (sub)-micrometer lengteschaal. De karakterisatietechnieken die in deze PhD Thesis zijn gebruikt kunnen geclassificeerd worden in twee verschillende synchrotron-gebaseerde X-ray microscopie (XRM) technieken: i) X-ray holotomografie en ii) gecorreleerde ptychografie X-ray berekende tomografie (PXCT) en X-ray fluorescentie (XRF) tomografie. X-ray holotomografie gecombineerd met porienetwerk modellering (PNM) werd gebruikt om het deactivatie mechanisme, als gevolg van coke en metaal afzettingen, te bestuderen binnen één enkel fluïde katalytisch kraak (FCC) katalysatordeeltje (Hoofdstuk 2). In Hoofdstuk 3 werden dezelfde technieken gebruikt om de heterogeniteit in het fragmentatiegedrag in een set van metalloceen-gebaseerde ethyleen polymerisatie katalysatoren te bestuderen op verschillende tijdstippen in de polymerisatie reactie. Gecorreleerde PXCT en XRF-tomografie werden gebruikt om de mate van fragmentatie statistisch te benaderen en te kwantificeren binnen een ensemble van Ziegler-gebaseerde ethyleen polymerisatie katalysatordeeltjes. Dit maakte het mogelijk om het dragermateriaal, het polymeer en de gemixte fases met grote ruimtelijke resolutie in kaart te brengen (Hoofdstuk 4). Vervolgens werd in Hoofdstuk 5 de poriestructuur en verdeling van elementen binnen één enkel FCC katalysatordeeltje in kaart gebracht met gecorreleerde PXCT en XRF tomografie. Op basis van de verkregen morfologische en element-gerelateerde informatie was het mogelijk massa transport te simuleren door middel van porienetwerk modellering. Hierdoor kwamen waardevolle inzichten over het diffusiegedrag van reactant en productmoleculen alsmede de toegankelijkheid van actieve plaatsen binnen een enkele FCC-katalysatordeeltje naar voren. In dit Hoofdstuk vatten we de bevindingen van Hoofdstukken 2 tot en met 5 samen. Een samenvatting van de belangrijkste bevindingen van deze PhD Thesis is weergegeven in Figuur 6.1.

In **Hoofdstuk 2** hebben we differentiaal-contrast gebaseerde X-ray holotomografie gebruikt samen met andere complementaire X-ray microscopie technieken, zoals X-ray fluorescentie (XRF), X-ray diffractie

(XRD), kleine-hoek X-ray verstrooiing (SAXS) en wijde-hoek X-ray verstrooiing (WAXS). Hiermee zijn koolstof en metaal afzettingen geïdentificeerd en in kaart gebracht binnen één enkel FCC geëquilibreerd katalysatordeeltje (E-cat). Deze analytische benadering stelde ons in staat om een verschil te maken tussen coke dat zich aan de oppervlakte bevond of juist binnen in de kern van het E-cat deeltje bevond dankzij de bemachtigde elektronen-dichtheid van X-ray holotomografie. Zo bleek dat de dichte oppervlaktelaag van coke afzettingen (met een dikte van minder dan 1 micrometer) de macroporiën op het oppervlakte blokkeert, een significante afname in de toegankelijkheid van het E-cat deeltje veroorzaakt. Daarnaast hebben we ook aangetoond dat over tijd de meeste coke afzettingen binnen in het deeltje ophopen in plaats van op het oppervlak, wat wordt veroorzaakt door de onvolledige verwijdering van coke tijdens het regenereren. Hieruit concluderen wij dat gedurende het regeneratieproces, voornamelijk oppervlakte coke wordt verbrand vanwege de korte verblijftijd van de katalysator in de regenerator (in de orde van minuten^[1]) terwijl dit niet het geval is voor coke wat zich dieper in het deeltje bevindt.

De ruimtelijke correlatie tussen de coke afzettingen en de aanwezigheid van metalen, zoals Fe, Ni en La, werd ook bestudeerd met XRF. Hier zagen wij dat La en Ni rijke domeinen, vergeleken met Fe rijke en anderzijds metaal-arme domeinen, een significant hogere hoeveelheid van niet-oppervlakte coke bevatten. Dit komt overeen met de vanuit de literatuur bekende hogere dehydrogenatie activiteit van Ni ^[2,3].

Vervolgens werd het effect van coke afzettingen op de integriteit van het porienetwerk bestudeerd door middel van het modelleren van het porienetwerk. We ontwikkelden twee porienetwerkmodellen voor 1) een niet-gecalcineerd katalysatordeeltje (katalysator met coke afzettingen) en 2) een gecalcineerd katalysatordeeltje (katalysator zonder coke afzetting). Dit stelde ons in staat om porie blokkades veroorzaakt door coke afzettingen te visualiseren. We observeerden duidelijke verschillen in de porienetwerk parameters na calcinatie, zoals een toename in het aantal knooppunten, het aantal segmenten, de gemiddelde poriediameter, het aantal oppervlakte knooppunten en een afname in de tortuositeit. Dit bewees de aanwezigheid van coke in de macroporiën van een gebruikt (niet geregenereerd) FCC-

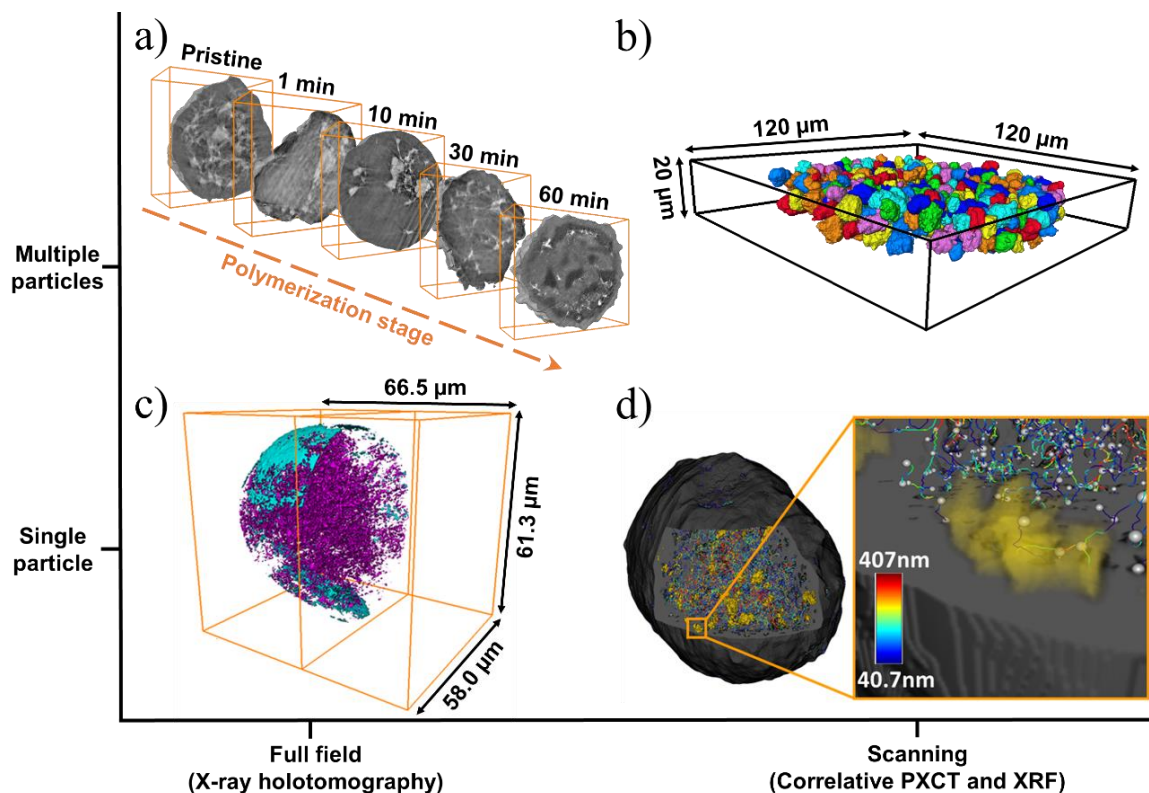
katalysatordeeltje. Het is belangrijk om te vernoemen dat deze methode om coke te bestuderen niet alleen mogelijk is voor FCC-katalysatoren, maar ook toegepast kan worden voor andere poreuze katalysatoren die gebruikt worden in andere katalytische reacties en systemen.

In **Hoofdstuk 3** werd X-ray holotomografie gebruikt als techniek met sub-500 nm ruimtelijke resolutie en relatief korte meettijden om lage Z (atomisch nummer) elementen in kaart te brengen bij meerdere gedragen ethyleen polymerisatiekatalysatoren. Kwantitatieve informatie over de morfologische evolutie van 12 hafnoceen-gebaseerde katalysatordeeltjes werd verkregen over vijf verschillende stadia van polymerisatie (i.e., de oorspronkelijke katalysator en na 1, 10, 30 en 60 minuten polymeriseren). Hiermee konden wij het verschil in de kompositie en porositeit van de katalysatordeeltjes kwantificeren tijdens deze zogezegde pre-polymerisatiereactie. Vervolgens werden aan de hand van het modelleren van het porienetwerk de porieruimte connectiviteit, tortuositeit en poriegrootte distributie van deeltjes tijdens verschillende stadia van polymerisatie verkregen. De afname in porositeit en macroporieruimte connectiviteit tijdens polymerisatie lieten zien dat gecontroleerde fragmentatie van de katalysator belangrijk is in het overkomen van potentiële massa transfer limitaties. De 3-D distributie van verschillende fases van de katalysator, i.e., dragermateriaal, polymeer en porieruimte domeinen werden binnen elk gemeten katalysatordeeltje gevisualiseerd. Hiermee was het mogelijk om de verschillende manieren van fragmentatie te visualiseren als gevolg van de unieke samenstellingen van de verschillende deeltjes. Bovendien lieten wij hier ook zien dat in de milde pre-polymerisatie fase de fragmentatie een laag-bij-laag mechanisme volgt.

In **Hoofdstuk 4**, werden gecorreleerde PXCT en XRF-tomografie gebruikt om de lokale elektronen dichtheid van 434 ethyleen gepolymeriseerde deeltjes over een grote gemeten gebied van $120 \times 120 \times 20 \text{ um}^3$ te meten met een ruimtelijke 3-D resolutie van 74 nm. Dit stelde ons in staat om de heterogeniteit in het fragmentatiegedrag van deze katalysator deeltjes te visualiseren en analyseren tijdens het vroege stadium van ethyleen polymerisatie (na 5 minuten) met een hoge katalysator lading gedurende de polymerisatiereactie die plaats vond onder milde reactie condities.

Verskillende geometrische parameters, zoals volume, oppervlakte, equivalente sferische diameter, sfericiteit en elongatie, werden berekend na de segmentatie van de uiterst verbonden deeltjes door middel van een onder toezicht marker-gebaseerde waterscheiding algoritme. Deze bekomen geometrische parameters lieten een relatief homogene morfologie van de gepre-polymeriseerde katalysatordeeltjes zien binnen het ensemble van 434 katalysator deeltjes. De lichtelijk verlengde oorspronkelijke katalysatordeeltjes, zoals geobserveerd met SEM, samen met een gemiddelde elongatiewaarde van 0.6 van dit ensemble van deeltjes lieten zien dat de komposiet polymeerdeeltjes het replicatie fenomeen volgen van de oorspronkelijke katalysatordeeltjes.

Om de mate van fragmentatie te kwantificeren werd een K-gemiddelde klusteringstechniek gebruikt waarbij elke deeltjes werd gesegmenteerd in 4 fases, namelijk i) een HDPE-rijke fase, ii) een gemengde HDPE-katalysator fase met meer HDPE, iii) een gemengde HDPE-katalysator fase met meer katalysator en iv) een katalysator-rijke fase. Daarna werd de fragmentatie parameter (V_r) geïntroduceerd om de mate van fragmentatie binnen elk deeltje te berekenen gebaseerd op het K-gemiddelde gesegmenteerde dataset. De V_r waarden wezen op een sterk heterogeen fragmentatiegedrag binnen het ensemble van gemeten polymeerdeeltjes. Hier zagen we dat binnen elk katalysatordeeltje zowel de laag-bij-laag en continue bisectionele mechanismes aanwezig waren. Voor zwak gefragmenteerde katalysatordeeltjes bleek de laag-bij-laag fragmentatie modus dominant, terwijl dit voor de middelmatig en sterk gefragmenteerde de de continue bisectionele fragmentatie modus bleek te zijn. Dit laat zien dat massa-transfer van de monomeer naar de actieve plaatsen gemakkelijk verliep voor de middelmatig en sterk gefragmenteerde deeltjes. Daarnaast wijst dit ook op een hogere lokale polymerisatie activiteit voor deze deeltjes.



Figuur 1 Samenvatting van de hoofdbevindingen van deze PhD Thesis. (a) Voorbeeld van de toepassing van X-ray holotomografie voor de karakterisatie van verscheidene metallocen-gebaseerde katalysatordeeltjes tijdens verschillende stages van ethyleen polymerisatie (zoals bestudeerd in Hoofdstuk 3) terwijl (b) een andere benadering laat zien met gecorreleerde PXCT en XRF met een groot gemeten volume voor een statistische analyse van een ensemble van 434 Ziegler-gebaseerde ethyleen polymerisatie katalysatordeeltjes tijdens dezelfde stage van polymerisatie (na 5 minuten) (bestudeerd in Hoofdstuk 4). De toepassing van X-ray holotomografie om verschillende koolstof depositie mechanismes aan te tonen in een enkele FCC katalysatordeeltje is weergegeven in (c). Oppervlakte en niet-oppervlakte coke deposities zijn weergegeven in respectievelijk, licht blauw en roze (bestudeerd in Hoofdstuk 2). (d) laat de poriestructuur, respectievelijke porienetwerk model en La distributie (gele domeinen) zien binnenin een enkele FCC katalysatordeeltje (bestudeerd in Hoofdstuk 5).

In **Hoofdstuk 5** hebben we een modellering gereedschapskist geïntroduceerd voor de analyse van massatransport eigenschappen van één compleet katalysatordeeltje met een complexe macroporie ruimte topologie. De FCC katalysator werd gebruikt als een archetypisch voorbeeld van een rationeel ontworpen hiërarchisch poreus materiaal. De 3-D element distributie alsmede de macroporie structuur van het E-cat (FCC) katalysatordeeltje werd onderzocht met gecorreleerde PXCT en XRF-tomografie. De 3-D XRF data werd gebruikt om de meest actieve regio's te identificeren aan de hand van de Lanthaan distributie, welke als marker diende voor RE-USY zeoliet

domeinen. Een meervoudig directioneel porienetwerk (MDPN) model werd gecreëerd gebaseerd op het grote ptychografische volume, wat uit meer dan 109 voxels bestond, representatief voor de complexe morfologie en topologie van FCC-katalysatordeeltjes. Dit leidde ertoe dat de totale rekentijd voor het gehele deeltje minder dan twee dagen was. De massa transport simulatie van het gehele, enkele FCC-katalysatordeeltje gebaseerd op het MDPN maakte gebruik van een concentratie gradiënt tussen het buitenste ('oppervlakte knooppunten') en binnenste ('zeoliet knooppunten') van het deeltje, wat representatief was voor de drijvende kracht van diffusie en reactanten binnen het deeltje. Door de diffusie limitaties binnen de FCC-deeltjes, kunnen de kraakreacties bij de La domeinen als instantaan verondersteld worden binnen deze simulatie. Gebaseerd op de simulatie resultaten was het mogelijk om het diffusie front te kwantificeren en visualiseren voor alle componenten van de simulatie, i.e., reactant, product en spoorzoeker moleculen.

We vonden dat slechts 27% van alle zeoliet domeinen toegankelijk waren vanaf het oppervlak van het E-cat FCC-deeltje. Interessant genoeg laat de analyse zien dat 75 vol% van de zeoliet domeinen toegankelijk bleven desondanks het feit dat bijna drie vierde van het aantal zeoliet domeinen ontoegankelijk zijn. Alhoewel, gebaseerd op de simulatieresultaten, zal afhankelijk van de diffusie coëfficiënten die gebruikt zijn in de simulatie, slechts een deel van de toegankelijke zeoliet domeinen binnen de katalysator ook daadwerkelijk bijdragen aan de kraakreactie vanwege de korte residentietijd van de FCC katalysatordeeltje in de stijgende reactor (tussen de 3 en 5 seconden). We lieten ook zien dat de stabiele toestand conditie voor productmoleculen niet bereikt kunnen worden, zelfs als we langere simulatietijden overwegen (~5 minuten, wat bijna 60 keer langer is dan de residentietijd van de FCC-katalysator in de stijgende reactor).

Appendix C: List of Abbreviations

APT	Atom probe tomography
ART	Algebraic reconstruction technique
BSE	Backscattered electron
CCD	Charge coupled device
CDI	Coherent diffraction imaging
CFM	Confocal fluorescence microscopy
¹³ C NMR	Carbon-13 nuclear magnetic resonance
CMOS	Complementary metal oxide semiconductor
CP	Cross-polarization
CTF	Contrast transfer function
DCM	Double crystal monochromator
DNP	Dynamic nuclear polarization
DNS	Direct numerical simulation
DSC	Differential scanning calorimetry
DTA	Differential thermal analysis
E-cat	Equilibrium catalyst
ED	Electron density
EELS	Electron energy loss spectroscopy
EM	Electron microscopy
EPR	Electron paramagnetic resonance
ESD	Equivalent spherical diameter
FBP	Filter back projection

FCC	Fluid catalytic cracking
FIB	Focused ion beam
FOV	Field of view
FP	Fragmentation parameter
FRC	Fourier ring correlation
FSC	Fourier shell correlation
FTIR	Fourier-transform infrared
GIS	Gas injection system
HDM	Hydrodemetallization
HDPE	High-density polyethylene
HGO	Heavy gas oil
HVGO	Hydrogenated vacuum gas oil
KB	Kirkpatrick-Baez
LB	Lattice-Boltzmann
LDPE	Low-density polyethylene
LLDPE	Linear low-density polyethylene
MALDI-TOF-MS	Matrix-assisted laser-desorption/ionization time-of-flight mass spectroscopy
MAO	Methylaluminoxane
MAS	Magic-angle spinning
MAT	Micro activity test
MC	Metallocene-type
MDPE	Medium-density polyethylene

MDPN	Multi-directional pore network
MS	Mass spectrometry
MMT	Million metric tons
NCC	Non-connected component
NCR	Nodes connectivity ratio
NEXAFS	Near edge X-ray absorption fine structure
NLM	Non-local means
NRA	Nuclear reaction analysis
OD	Optical density
PE	Polyethylene
PET	Positron emission tomography
PIXE	Proton-induced X-ray emission
PNM	Pore network model
PP	Polypropylene
PSD	Pore size distribution
PXCT	Ptychographic X-ray computed tomography
RE	Rare-earth
REV	Representative elementary volume
SAXS	Small angle X-ray scattering
SDD	Silicon drift detector
SEM-EDX	Scanning electron microscopy combined with energy dispersive X-rays spectroscopy
SFE	Supercritical fluid extraction

SIFT	Scale-invariant feature transform
SIMS	Secondary ion mass spectroscopy
SPH	Smoothed particle hydrodynamics
SR	Synchrotron-radiation
STXM	Scanning transmission X-ray microscopy
TAP	Temporal analysis of product
TLD	Through the Lens Detector
TPH	Temperature programmed hydrogenation
TPO	Temperature-programmed oxidation
TPV	Total particle volume
TXM	Transmission X-ray microscopy
USY	Ultra-stable Y
VGO	Vacuum gas oil
WAXS	Wide angle X-ray scattering
XANES	X-ray absorption near edge structure
XAS	X-ray absorption spectroscopy
XCT	X-ray computed tomography
XPS	X-ray photoelectron spectroscopy
XRD	X-ray diffraction
XRF	X-ray fluorescence microscopy
XRM	X-ray microscopy

Appendix D: Publications and Presentations

D.1. List of Publications appearing in this PhD Thesis:

“3-D X-ray Nanotomography Reveals Different Carbon Deposition Mechanisms in a Single Catalyst Particle” M. Vesely, R. Valadian, L. Merten Lohse, M. Toepperwien, K. Spiers, J. Garrevoet, E. Vogt, T. Salditt, B. M. Weckhuysen and F. Meirer, *ChemCatChem* **2021**, 13, 2494-2507.

“Heterogeneity in the State of Fragmentation Within an Ensemble of Ziegler Catalyst Particles Using X-ray Nano-Tomography” R. Valadian, K. W. Bossers, J. Garrevoet, S. van Malderen, R. Chan, N. Friederichs, J. Severn, A. Wilbers, S. Zanoni, M. K. Jongkind, B. M. Weckhuysen, and F. Meirer, *JACS Au* **2021**, 1, 852-864.

“X-Ray Nanotomography Uncovers Morphological Heterogeneity in a Silica-Supported Ethylene Polymerization Catalyst at Multiple Reaction Stages” R. Valadian, M. J. Werny, L. Merten Lohse, A. Robisch, S. Zanoni, C. Hendriksen, N. Friederichs, B. M. Weckhuysen, and F. Meirer, *Chem Catalysis* **2021**, doi: <https://doi.org/10.1016/j.checat.2021.10.008>.

“Simulation of Mass Transport in an Entire Catalyst Particle Based on High-resolution X-ray Microscopy and Pore Network Modeling” R. Valadian, A. Raoof, M. Veselý, M. Gambino, J. Garrevoet, B. M. Weckhuysen, and F. Meirer, in preparation.

D.2. Other Publications by the Author:

“Correlated X-ray Ptychography and Fluorescence Nano-Tomography on the Fragmentation Behavior of an Individual Catalyst Particle during the Early Stages of Olefin Polymerization” K. W. Bossers, R. Valadian, S. Zanoni, R. Smeets, N. Friederichs, J. Garrevoet, F. Meirer, and B. M. Weckhuysen, *JACS* **2020**, 142(8), 3691-3695.

“Visualizing Defects and Connectivity within Metal Organic Frameworks by X-ray Transmission Tomography” R. Mayorga- González, M. Rivera-Torrente, N. Nikolopoulos, K. W. Bossers, R. Valadian, J. Yus, B. Seoane, B. M. Weckhuysen, F. Meirer, *Chemical Science* **2021**, 12, 8458-8467.

D.3. Oral Presentations by the Author:

“Simulation of Mass Transport in a Single FCC Catalyst Particle Based on High-Resolution X-ray Microscopy and Pore Network modeling”, The Netherlands Catalysis and Chemistry Conference, **2020**, Noordwijkerhout, The Netherlands.

“Carbon Deposits in a Single Catalyst Particle as Studied by Correlated 3-D X-ray Microscopy and Pore Network Modeling”, Catalysis and Green chemistry Conference, **2018**, Tokyo, Japan.

D.4. Poster Presentations by the Author:

“Macro-pore Diffusion in Individual Catalyst Particles: From X-ray Imaging to Mass Transport Simulation By Means Of Pore Network Modeling”, Post EuropaCat, **2019**, Utrecht, The Netherlands.

“The effect of carbon deposits in an individual catalyst particle as studied by pore network modeling”, The Netherlands Catalysis and Chemistry Conference, **2018**, Noordwijkerhout, The Netherlands.

Appendix E: Acknowledgments

I still cannot believe that this long journey is over! Moving from Germany to the Netherlands was pretty exciting. I enjoyed experiencing a new life and new culture, while working in such an amazing team with so many nice people. It might be sad/difficult to be a bit far from this nice environment, but I am pretty sure that friendships with strong bonds always stay with me and I will do my best to keep all treasures that I obtained during my PhD period. At the moment I am so excited to close this great chapter of the book of life and to get ready for the new chapter! Within this Chapter, I learned, I experienced, I grew, and I formed a network with amazing people. Here, I want to use the opportunity to thank people who helped and taught me in this amazing life chapter!

Before starting with people from Utrecht university, I would like to say that I am so lucky to have such a family who are the real supporter. My mom, my dad, and my brothers always gave me energy and did their best to make me happy. They tried to help me reaching my goals in my life. They let me live my life, they let me decide, they let me fail, they let me laugh and cry! They did not want to shape me in the way they wanted, but they helped me more to be able to shape myself by myself. I admire having them in my life and I wish them all a healthy and happy life! **I LOVE YOU ALL AND THANKS A LOT!**

I would like to start with you, **Bert**. Indeed, this chapter could have not been done without you. I am so thankful that you gave me this opportunity to work/grow in your group. I still remember the first week of my PhD that I guessed the number of your PhD students (honestly it was just a random number 😊) during the group meeting and I won a fancy bottle of wine from you. That was indeed a nice starting point for such a journey. Also, it was a great honor for me to have your guidance and leadership through this difficult but valuable period of time. I am so happy that we worked together, and I could learn and gain all these experiences from you regarding science and life. I always remember your short but sharp quotes you gave me in our meetings. Particularly, I like the term ‘Helicopter View’ that you always used. That helped me a lot not only in science, but also in my life to have a bigger picture

of events! I am trying to keep this ‘Helicopter View’ for the rest of my life. Thank you so much, Bert.

It is difficult for me to wrap it up here, **Florian**. It was such a short but great time of working together. I remember how you motivated me when I started my PhD, how smartly I have been given enough time to learn and grab information about X-ray microscopy, pore network modeling, beamtrips, catalysis, and so on. I never forget how humble you were when you talked about your coding skills in the beginning of my PhD. The way you said it was much different from the way it was! When I read the complex codes you wrote, I was so surprised and indeed happy that I am going to work directly with someone like you. I was/am also always inspired by your creative/innovative ideas and EXTREMELY fast data processing in our meetings with different topics! It is great that you can switch topics and discussions within few minutes. I could just come to your office and ask my question with minimum explanation. It was not so difficult to understand that I can fill in my backpack during this PhD period with so many precious experiences. I think beside all scientific subjects that I discussed with you and learned from you, your commitment and patience was something that inspired me a lot. It was so nice for me to have a supervisor who is so sharp during the meeting regardless of subject, but also someone that I can grab a beer with him like a real friend during the conferences and borrels and talk with him about different topics (such as astrophysics 😊)! Oh, I should not forget that next to science, we are also a good team in kicker. Florian, you are such a great supervisor but also an amazing friend. I will definitely keep in touch with you and there are still much more to learn from you! Many thanks, Florian.

Meeting **Amir Raouf** during my PhD interview! There we started to know each other although I knew you before by reading your great articles about pore network modeling. I already understood during the interview that you are so smart and sharp with your detailed questions. It was a great pleasure for me to start diffusion simulation project with you which is my fifth chapter in this PhD Thesis. I got so much knowledge, while I was working with you. I also so much enjoyed meetings with you since you are always open for

discussion and indeed very helpful as well. Although I know that I disturbed you a lot during the diffusion paper by coming back to you with new problems 😊, but I am so happy that you cared about science, and you were always in for better results. I hope that we come up with new projects and work together more in the future! Thank you so much, **Amir**.

Here we go! **Martin (Vesely)** we both started our work together at the same time. I even remember the first meeting you came with your luggage, and I can remember how friendly you were. It is not possible to name all things you taught me, but I have to emphasize (as I did in all presentations) that you made me an expert specifically in image processing. Without your guidance and help, I am sure I could not learn that much dense information in such a short time. Thanks for all your help, **Martin**.

Moreover, I would like to say thanks to **Prof. dr. E.T.C. Vogt** for his fruitful discussion about the project in Chapter 2 and his great guidance particularly in the FCC field. Many thanks to **Prof. Tim Saldit** because of his valuable help during the holotomography measurement for both Chapters 2 and 3. Indeed, it was not possible to finish those projects without his support. Also, many thanks to his team members, such as **Marieke , Anna-Lena, and Leon** for all their amazing support and energy in holotomography experiments as well as post-processing of the datasets. I would like to say special thanks to **Dr. Jan Garrevoet** and his team at DESY, where they helped us a lot to perform ptychography and XRF measurements, which I used in Chapters 4 and 5. It was great to meet and work with you during my PhD. Thank you all.

As I said I grew a whole network of amazing people and it is so tough to talk about all of them, but I am trying to sort them based on the time that I got to know them:

Koen and Laurens, real brother/buddy? Okay let's start with **Lau Lau!** It was so much fun to meet you in the first week of my PhD. Lau, you are such a kind person and now such a kind father. How can I forget the time with you in Hofman, Tivoli, NCCC and so on. How can I explain our serious discussion about life in the morning and during coffee breaks. It is amazing to have such

a friend who constantly takes care of you and your life. We will be friends and we will have more fun together man! Many thanks, **Lau**.

I think it is the time to talk about **koenie**. Man, during my first borrel, you were so drunk but still you were able to invite me for having a lunch together the day after the borrel. I mean I need to write a book about you and the things you have done! Hopefully, one day I will do it 😊. But indeed, I think it is SOOOOO important to thank you since you were not only a good friend, but also you were such a great team worker. I am so sad we did not start working together from the beginning, but still so happy that we started the collaboration in the middle of my PhD period. I think I should not mention how fruitful it was to work with you since it is such a clear story. Thanks for everything you taught me Mr. Chemist! It was amazing to have such an intelligent person and incredible writer during my PhD. The majority of an joint memories are not allowed to be shared here :D, so I will end it up like this. Thanks a lot, **Koen**.

Gorgi is my hero! Great in science, great in communication, and great in music. Man, what a gorgeous time we had together. What a useful set of Italian vocabularies I learned from you 😊. What a temper that Neapolitan has 😊!!!! Please, do not forget that you promised me to visit Italy together with Frani. I am writing it here since we have to do it! Also, we need to make a music band and play all together '**Lasciatemi cantare con la chitarra in mano**'. Gorgi, I am honestly so thankful to have you in my life and I am pretty sure we will have more stories together. Thanks a lot, **Gorgi!**

There is another guy called **Franni**. He is from Italy! This guy has a lovely heart!!! Man, I remember the first day we met next to the coffee machine, and you were about to start your master thesis with Gorgi. Sometimes, I just trust some people from the first glance since they are direct, honest, and reliable. You were such a guy in my life. I don't know even how I can give a summary of our memories about discussions, parties, dinners and so on. You inspired me a lot man, a lot! You are such a perfect friend. Also, I would like to thank Emma as well. I always enjoyed meeting you guys since you are such a lovely and kind couple. I wish you all the best and we keep in touch! Thanks a lot, **Franni and Emma**.

Another Italian! **Silvia!** I thought in the beginning that we might not be a match to make a friendship, but I am pretty happy that I did not believe it. Now I have such an amazing person in my life! Never forget the night shifts in the beamtrip. I hope I did not disturb you with my weird challenging (sometimes stupid) philosophical questions! I appreciate having you in my life and many thanks for all the good time we had, and we will have, **Sil!**

Marteen, it was great to see you in Schiermonnikoog. I believe it was a epic trip although I got sick in the beginning of the course 😊. I think we had so many memories together in beamtrips, bars and clubs which I cannot mention all here. Just want to say that you are such an amazing guy with a kind heart. Never forget your great help to prepare the Samenvatting of this Thesis together with Koen. I am super happy to have such a nice friend in my life. Many thanks, **Marteen**.

Max, it was really nice to meet you. We started a challenging project together and I am pretty happy that we could do a great job together besides all the hard time we had. Also, I really enjoyed the trip with you to Göttingen. We had such a fancy Italian food there with a fair price I think 😊. I am so pleased that we had so much fun together and we made a great piece of science as well. Many thanks, **Max**.

Our lunch group was amazing. Started with few people and then in less than a year, it grew and expanded into a big group of people. It was lovely to send a message in the WhatsApp group everyday, to wait for people to join, and have a lunch with lovely people such as **Koeni, LauLau, Gorgi, Frani, Remi, Laura, Rafa, Basi, Maarten, Fouad, Nikos, Oscar D, Chris (habibti), Savvie, Abi, Valerio, Livan, and Nathan**.

Furthermore, without amazing colleagues I could not finish this chapter. Here, I would like to say thanks to all lovely friends and colleagues in Inorganic Chemistry and Catalysis (ICC) group such as **Yadi, Marianna, Anna-eva, Albaraa, Caroline, Ellen, Erik, Ilse, Iris, Jim, Joren, Kordula, Mark, Michael, Romy, Sebastian, Sophi, Stijn, Guusje, Matteo, Charli, Thomas, Peter, Yadi, Katinka, Khaled, Ramon, Nienke, Roy, Bea, Miguel, Petra, Sam, Donglong, Zoran, Pierre, Ozgun, Freddy, Ward**,

Rolf, Oscar, Jochum, Jochem, Egor, Frederique, Inna, Kai, Robert, Wirawan, Suzanne, Luke, Johan, Lars, Pascal and the rest that I might forget to add here.

Next to friends and colleagues from ICC group, I want to also thank my old friends that they always helped me to grow. These people are so valuable for me since it is not indeed easy to find friends with whom you can easily share, talk, and enjoy life with them. To say how important they are for me, I need to write a book for each of them! I would appreciate having these lovely people in my life. Thanks a lot, **Alish, Ali, Pourya, Soheil, Nima, Peyman, Elmira, Behzad, Behrang, Arash.**

Appendix F: Curriculum Vitae

Roozbeh Valadian was born on the 22nd of May 1989 in Tehran, Iran. After obtaining his high school diploma in 2007, he enrolled in an undergraduate study in chemical engineering at Tehran University in Iran. In 2011 he graduated with a Bachelor of Science degree with a specialization in chemical process design. His Undergraduate Thesis project was entitled “Molecular dynamics simulation (MDS) of adsorption and diffusion of light gases in carbon nanotubes.” In October 2012, Roozbeh started his Master’s studies in Chemical and Energy Engineering under Dr. Attari Moghaddam and Dr. Kharaghani. In July 2016, he graduated as a Master of Science with the Thesis entitled “Macroscopic parameters of drying porous media in gravity-capillary regime obtained from pore network simulations.” In February 2017, Roozbeh continued to work under the supervision of Prof. dr. ir. Bert M. Weckhuysen and Dr. Florian Meirer as a PhD candidate in the group of Inorganic Chemistry and Catalysis, Utrecht University, The Netherlands. The objective of his PhD project was about characterization of porous materials based on high-resolution X-ray microscopy techniques and pore network modeling. The main results of this project are described within this PhD Thesis and are published in scientific journals. Besides research, Roozbeh plays guitar and also has a great interest in the relationship between philosophy and astrophysics.

